

Advances in GIS and remote sensing the landscape pattern of land cover on urban climate and urban ecology

Edited by

Pedzisai Kowe, Cletah Shoko and Steven Jerie

Published in

Frontiers in Ecology and Evolution

Frontiers in Earth Science

Frontiers in Environmental Science



FRONTIERS EBOOK COPYRIGHT STATEMENT

The copyright in the text of individual articles in this ebook is the property of their respective authors or their respective institutions or funders. The copyright in graphics and images within each article may be subject to copyright of other parties. In both cases this is subject to a license granted to Frontiers.

The compilation of articles constituting this ebook is the property of Frontiers.

Each article within this ebook, and the ebook itself, are published under the most recent version of the Creative Commons CC-BY licence. The version current at the date of publication of this ebook is CC-BY 4.0. If the CC-BY licence is updated, the licence granted by Frontiers is automatically updated to the new version.

When exercising any right under the CC-BY licence, Frontiers must be attributed as the original publisher of the article or ebook, as applicable.

Authors have the responsibility of ensuring that any graphics or other materials which are the property of others may be included in the CC-BY licence, but this should be checked before relying on the CC-BY licence to reproduce those materials. Any copyright notices relating to those materials must be complied with.

Copyright and source acknowledgement notices may not be removed and must be displayed in any copy, derivative work or partial copy which includes the elements in question.

All copyright, and all rights therein, are protected by national and international copyright laws. The above represents a summary only. For further information please read Frontiers' Conditions for Website Use and Copyright Statement, and the applicable CC-BY licence.

ISSN 1664-8714
ISBN 978-2-8325-3949-1
DOI 10.3389/978-2-8325-3949-1

About Frontiers

Frontiers is more than just an open access publisher of scholarly articles: it is a pioneering approach to the world of academia, radically improving the way scholarly research is managed. The grand vision of Frontiers is a world where all people have an equal opportunity to seek, share and generate knowledge. Frontiers provides immediate and permanent online open access to all its publications, but this alone is not enough to realize our grand goals.

Frontiers journal series

The Frontiers journal series is a multi-tier and interdisciplinary set of open-access, online journals, promising a paradigm shift from the current review, selection and dissemination processes in academic publishing. All Frontiers journals are driven by researchers for researchers; therefore, they constitute a service to the scholarly community. At the same time, the *Frontiers journal series* operates on a revolutionary invention, the tiered publishing system, initially addressing specific communities of scholars, and gradually climbing up to broader public understanding, thus serving the interests of the lay society, too.

Dedication to quality

Each Frontiers article is a landmark of the highest quality, thanks to genuinely collaborative interactions between authors and review editors, who include some of the world's best academicians. Research must be certified by peers before entering a stream of knowledge that may eventually reach the public - and shape society; therefore, Frontiers only applies the most rigorous and unbiased reviews. Frontiers revolutionizes research publishing by freely delivering the most outstanding research, evaluated with no bias from both the academic and social point of view. By applying the most advanced information technologies, Frontiers is catapulting scholarly publishing into a new generation.

What are Frontiers Research Topics?

Frontiers Research Topics are very popular trademarks of the *Frontiers journals series*: they are collections of at least ten articles, all centered on a particular subject. With their unique mix of varied contributions from Original Research to Review Articles, Frontiers Research Topics unify the most influential researchers, the latest key findings and historical advances in a hot research area.

Find out more on how to host your own Frontiers Research Topic or contribute to one as an author by contacting the Frontiers editorial office: frontiersin.org/about/contact

Advances in GIS and remote sensing the landscape pattern of land cover on urban climate and urban ecology

Topic editors

Pedzisai Kowe — Midlands State University, Zimbabwe

Cletah Shoko — University of the Witwatersrand, South Africa

Steven Jerie — Midlands State University, Zimbabwe

Citation

Kowe, P., Shoko, C., Jerie, S., eds. (2023). *Advances in GIS and remote sensing the landscape pattern of land cover on urban climate and urban ecology*.

Lausanne: Frontiers Media SA. doi: 10.3389/978-2-8325-3949-1

Table of contents

04	Editorial: Advances in GIS and remote sensing the landscape pattern of land cover on urban climate and urban ecology Pedzisai Kowe, Cletah Shoko and Steven Jerie
06	Landscape ecological risk assessment and driving mechanism of coastal estuarine tidal flats—A case study of the liaohhe estuary wetlands Haifu Li, Fangli Su, Chengjiu Guo, Linlin Dong, Fei Song, Chao Wei and Yunlong Zheng
22	Characterizing urban growth and land surface temperature in the western himalayan cities of India using remote sensing and spatial metrics Rajman Gupta, Mani Sharma, Garima Singh and Rajendra Kr Joshi
37	GIS integrated RUSLE model-based soil loss estimation and watershed prioritization for land and water conservation aspects Mahesh Chand Singh, Koyel Sur, Nadhir Al-Ansari, Prashant Kumar Arya, Vipin Kumar Verma and Anurag Malik
54	Urban expansion impacts on agricultural land and thermal environment in Larkana, Pakistan Ghani Rahman, Noor Hussain Chandio, Muhammad Farhan Ul Moazzam and Nadhir Al Ansari
68	Evaluating land use/cover change associations with urban surface temperature via machine learning and spatial modeling: Past trends and future simulations in Dera Ghazi Khan, Pakistan Muhammad Sajid Mehmood, Adnanul Rehman, Muhammad Sajjad, Jinxi Song, Zeeshan Zafar, Zhai Shiyan and Qin Yaochen
84	Large-scale measurement of urban streets' space health based on the spatial disorder theory—A case study on the old urban area of Daoli District of Harbin City Ting Wan and Mingxue Wang
96	Landscape ecological risk assessment and influencing factor analysis of basins in suburban areas of large cities – A case study of the Fuchunjiang River Basin, China Xiaomeng Cheng, Yaping Zhang, Guofu Yang, Wenbin Nie, Yinyi Wang, Jing Wang and Bin Xu
114	Relationships between microplastic pollution and land use in the Chongqing section of the Yangtze River Sheng Ye and Desheng Pei
126	The evolution of spatiotemporal patterns and influencing factors of high-level tourist attractions in the Yellow River Basin Rentian Shu, Jingyi Xiao, Yanxia Yang and Xiangdan Kong
142	Study on the spatial variability of thermal landscape in Xi'an based on OSM road network and POI data Jiang Wu, Shenshan Han, Leijie Shi and Qun Hui



OPEN ACCESS

EDITED AND REVIEWED BY
Alexander Kokhanovsky,
German Research Centre for Geosciences,
Germany

*CORRESPONDENCE
Pedzisai Kowe
✉ Kowemuso5@gmail.com

RECEIVED 07 October 2023
ACCEPTED 23 October 2023
PUBLISHED 01 November 2023

CITATION
Kowe P, Shoko C and Jerie S (2023)
Editorial: Advances in GIS and remote
sensing the landscape pattern of land
cover on urban climate and urban ecology.
Front. Ecol. Evol. 11:1308710.
doi: 10.3389/fevo.2023.1308710

COPYRIGHT
© 2023 Kowe, Shoko and Jerie. This is an
open-access article distributed under the
terms of the [Creative Commons Attribution
License \(CC BY\)](#). The use, distribution or
reproduction in other forums is permitted,
provided the original author(s) and the
copyright owner(s) are credited and that
the original publication in this journal is
cited, in accordance with accepted
academic practice. No use, distribution or
reproduction is permitted which does not
comply with these terms.

Editorial: Advances in GIS and remote sensing the landscape pattern of land cover on urban climate and urban ecology

Pedzisai Kowe^{1,2,3*}, Cletah Shoko⁴ and Steven Jerie¹

¹Department of Geography, Environmental Sustainability and Resilience Building, Faculty of Social Sciences, Midlands State University, Gweru, Zimbabwe, ²Geomatics Department, Tshwane University of Technology, Pretoria, South Africa, ³Research and Training, Biomedical Research and Training Institute, Harare, Zimbabwe, ⁴School of Geography, Archaeology and Environmental Studies, University of the Witwatersrand, Johannesburg, South Africa

KEYWORDS

spatial and temporal distribution, earth observation (EO) data, urban growth patterns, socio-ecological patterns, urban thermal environment, geospatial information, landscape architecture, spatial analytical methods

Editorial on the Research Topic

Advances in GIS and remote sensing the landscape pattern of land cover on urban climate and urban ecology

Globally, more than half of the urban population is facing severe social-economic and ecological challenges. These challenges are especially those relating to growing urban heat islands, land cover conversions, land encroachment, informal settlements, traffic congestion, land and water pollution (Ye and Pei), decline in landscape connectivity, green infrastructure fragmentation, soil erosion (Singh et al.) and environmental degradation, due to rapid urban expansion. These changes affect urban climate and landscape ecology, thereby compromising the provision of ecosystem services and human livelihoods. Advances in Geographic Information Systems (GIS), Remote Sensing technologies and other robust spatial analytical and quantitative methods are urgently and routinely required in managing these socio-economic and environmental challenges.

Existing, new sources of data (i.e., OpenStreetMap road network data) (Wu et al.), emerging and advanced Geospatial Information Systems technologies and remote sensing offer great opportunities to acquire ubiquitous spatial data over time and space. These approaches enable the monitoring and detection of the spatial-temporal patterns of changes in the landscape and urban climate at various spatial and temporal scale, as well as to make predictions and scenarios for future landscape ecology and urban surface temperature trends. Containing contributions from various researchers and experts around the world based on a collection of original research articles, this Research Topic documents the Remote Sensing and GIS applications in tackling the challenges of urban climate and landscape ecology research from local scale (urban, suburban areas, urban fringes) to national spatial scales, but with more focus on urban areas.

Furthermore, the Research Topic showcases the applications of various remote sensing data and Geospatial techniques including Landscape metrics (Spatial metrics),

Geodetector, Machine Learning (ML), Spatial Autocorrelation Methods (Global Moran I and Local Indicator of Spatial Association (LISA) of local Moran's index and Hot Spot Analysis tool (Getis-Ord Gi*), Landscape Ecological Risk, Nearest Neighbor Index (NNI) and Kernel Density analytical techniques. Over the years, Landscape metrics have been widely used for generating fragmentation metrics using categorical land cover maps derived from classified remote sensing data for quantifying landscape structure and composition. Their application has been largely due to their effectiveness as evidenced in previous work in relating them to underlying biophysical or ecological processes. Spatial Metrics combined with GIS have proved to be useful technologies in spatial and temporal mapping and analysis of landscape fragmentation, urban sprawl, agglomeration, and different morphological aspects of urban growth patterns (Gupta et al.).

In this Research Topic, Geodetector tools have been demonstrated as vital tools in analysing the relationship between landscape pattern and factors influencing landscape ecological risks in city suburbs (Cheng et al.) and coastal estuarine tidal flats (Li et al.). The tools were also able to detect spatial heterogeneity and influencing factors of High-Level Tourist Attractions (HLTAs) (Shu et al.). Similarly, in landscape ecology, second-order statistics have emerged as important tools in assessing spatial autocorrelation of landscape ecological risks (LER) and HLTAs at a global and local scale by employing the Global Moran's I, local Moran's index, and Hot Spot Analysis tool (Getis-Ord Gi*) methods (Cheng et al.; Shu et al.). However, as demonstrated by Shu et al. within the Yellow River Basin in China, the integration of spatial autocorrelation indices with other techniques, such as the Nearest Neighbour Index (NNI) and Kernel density, is crucial for accurately estimating and visualizing the spatial distribution and agglomeration patterns of High-Level Tourist Attractions.

There is also a growing concern over significant land cover changes and unplanned urban expansion (urban sprawl, which usually displaces natural areas with impervious and built-up areas). These changes are responsible for inducing the sensible heat rather than latent heat thereby increasing land surface temperature and affecting the urban thermal environment (Gupta et al.; Mehmood et al.; Rahman et al.). With the advancement in Artificial Intelligence (AI) and Machine Learning (ML)-based modelling techniques and approaches such as Support Vector Machine (SVM), Gradient Boosting (GB), AdaBoosting, and Random Forest (RF), combined with freely available multispectral remote sensing data like Landsat and Sentinel 2, it has become possible to analyse, spatially simulate and predict future land surface temperatures associated with different spatial patterns of land cover (e.g., water, built-up areas, vegetation cover) and land use (e.g., agriculture land, residential, industrial and commercial areas) changes and urban growth patterns with higher accuracy (Mehmood et al.). Furthermore, ML methods can serve as useful tools to evaluate the spatial disorder, a large-scale measurement of different street space health (Wan and Wang).

In addition, in recent years, ML algorithms have become popular in land cover classification (Rahman et al.) because they are powerful, reliable, more adaptable, faster, and less expensive in quantifying and extracting accurate information. Similarly, recent remote sensing

studies have showed that the open-source Google Earth Engine (GEE) cloud computing platform is rapidly growing with the use of advanced machine learning algorithms. GEE has shown invaluable capabilities in processing large remote sensing and other spatial datasets for land cover and land use detection and monitoring (Mehmood et al.; Rahman et al.). The GEE renders the much-required long-term time records (i.e., Landsat imagery) and access to advanced machine learning to complement the user training dataset. Rahman et al. employed the RF algorithm in GEE to quantify Land surface temperature using a series of Landsat images. The integration of new and existing datasets remains promising for the geospatial analysis and remote sensing of urban climate and landscape ecology. As highlighted in a study that analysed the impact range of thermal landscape footprint of various types of functional blocks (Wu et al.), the integration of new and existing datasets remains promising for the geospatial analysis and remote sensing of urban climate and landscape ecology. The study used a combination of Landsat 8 remote sensing imagery, OpenStreetMap (OSM) road network data, and kernel density analysis (Wu et al.).

Author contributions

PK: Writing – review & editing. CS: Writing – review & editing. SJ: Writing – review & editing.

Funding

The author(s) declare that no financial support was received for the research, authorship, and/or publication of this article.

Acknowledgments

We would like to thank the Frontiers Editorial team, all the authors who have contributed in submitting and writing the manuscripts, and also thank the reviewers for their valuable comments and suggestions that greatly improved the quality of the manuscripts.

Conflict of interest

The authors declare that the research was conducted in the absence of any commercial or financial relationships that could be construed as a potential conflict of interest.

Publisher's note

All claims expressed in this article are solely those of the authors and do not necessarily represent those of their affiliated organizations, or those of the publisher, the editors and the reviewers. Any product that may be evaluated in this article, or claim that may be made by its manufacturer, is not guaranteed or endorsed by the publisher.



OPEN ACCESS

EDITED BY
Pedzisai Kowe,
Midlands State University, Zimbabwe

REVIEWED BY
Tatenda Musasa,
Midlands State University, Zimbabwe
Ming Jiang,
Northeast Institute of Geography and
Agroecology (CAS), China

*CORRESPONDENCE
Fangli Su,
syaulhf@syau.edu.cn

SPECIALTY SECTION
This article was submitted to
Environmental Informatics and Remote
Sensing, a section of the journal
Frontiers in Environmental Science

RECEIVED 14 October 2022
ACCEPTED 14 November 2022
PUBLISHED 28 November 2022

CITATION
Li H, Su F, Guo C, Dong L, Song F, Wei C
and Zheng Y (2022), Landscape
ecological risk assessment and driving
mechanism of coastal estuarine tidal
flats—A case study of the liaohe
estuary wetlands.
Front. Environ. Sci. 10:1070009.
doi: 10.3389/fenvs.2022.1070009

COPYRIGHT
© 2022 Li, Su, Guo, Dong, Song, Wei and
Zheng. This is an open-access article
distributed under the terms of the
Creative Commons Attribution License
(CC BY). The use, distribution or
reproduction in other forums is
permitted, provided the original
author(s) and the copyright owner(s) are
credited and that the original
publication in this journal is cited, in
accordance with accepted academic
practice. No use, distribution or
reproduction is permitted which does
not comply with these terms.

Landscape ecological risk assessment and driving mechanism of coastal estuarine tidal flats—A case study of the liaohe estuary wetlands

Haifu Li^{1,2}, Fangli Su^{1,2*}, Chengjiu Guo^{1,2}, Linlin Dong³,
Fei Song^{1,2}, Chao Wei^{1,2} and Yunlong Zheng^{1,2}

¹College of Water Conservancy, Shenyang Agricultural University/Liaoning Panjin Wetland Ecosystem National Observation and Research Station, Shenyang, Liaoning, China, ²Liaoning Shuangtai Estuary Wetland Ecosystem Research Station, Panjin, Liaoning, China, ³Yellow River Engineering Consulting Co., Ltd., Zhengzhou, Henan, China

Estuarine tidal flats are located in the land-sea crisscross-sensitive zone. The degraded and shrinking state of major tidal flat landscapes weakens their ecological role in maintaining the safety of coastal wetlands in the world. However, little attention has been paid to tidal flat landscape evolution and ecological risks due to the tidal flats being located in the periphery of estuarine wetlands. This study was conducted in the tidal flats of the Liaohe estuary wetlands. The GIS spatial analysis and a transition matrix were combined to explore the tidal flat landscape evolution characteristics. The ecological risk faced by the tidal flats was evaluated by a landscape ecological risk model constructed by landscape indexes. The key driving factors and threshold values that affect the ecological risks were clarified using geographical detectors and regression analysis methods. The results showed that the tidal flats mainly evolved into a natural wetland before 2000 and rapidly changed into an artificial landscape between 2000 and 2010; the proportion of artificial landscapes then began to decline after 2010. Over the past 30 years, the landscape ecological risk in this area has generally been at a medium risk level. The ecological risk index showed a decreasing trend with the increases in landscape diversity. The low-risk artificial plaques have gradually replaced high-risk and medium-risk plaques of exposed tidal flats and natural wetlands. The study showed that human development activities were the key factors affecting the landscape ecological risks of the tidal flats. River sediment discharge was the key natural factor in maintaining the landscape ecological risk at a stable level. Therefore, the human development activities should be controlled within an appropriate limit, and the material supply of the upstream basin should be guaranteed to maintain the stability of the tidal flat landscape form in the protection and utilization of estuarine tidal flats in the future.

KEYWORDS

coastal estuary, tidal flats, landscape evolution, ecological risk, impact thresholds

1 Introduction

Estuary tidal flats are important land–sea material exchange belts, and are located at the outermost periphery of coastal estuarine wetlands (Yao, 2013; Li et al., 2021a). Tidal flats play an important ecological role in the security of estuarine wetland ecosystems, shoreline stability, reserving coastal land, and conserving biodiversity (Kim and Ryu, 2020; Bao and Gao, 2021; Costanza et al., 2021; Jackson et al., 2021). However, 16% of the world's tidal flats were lost between 1984 and 2016 due to natural and human factors such as watershed climates, water conservancy construction, and industrial and agricultural production weakening the buffering capacity of tidal flats as a defense against coastal erosion (Murray et al., 2019; Liu et al., 2020). This phenomenon leads to the structural degradation of coastal wetland ecosystems and the reduction of ecological functions (Sun et al., 2017; Cui et al., 2021), which is not conducive to the sustainable development of coastal cities (Ma et al., 2014). Thus, of importance to maintaining the stability of estuarine wetland shorelines and wetland ecological security is exploring the spatial evolution of, and ecological risks to, tidal flats.

The temporal and spatial evolution of wetlands has been the result of changes in regional landscape patterns (Jiang et al., 2017; Murray et al., 2019). Landscape patterns reflect a combination of different ecological processes, climate, land-use changes, and biodiversity changes (Zhan et al., 2019; Zhang et al., 2021). Studies have shown that wetland landscape patterns depend on the geographical distribution and composition of wetland resources, and are closely related to the robustness to disturbance, resilience, stability, and biodiversity of wetland ecosystems (Fu, 1995). External disturbance is an important ecological and landscape-scale process, and a key driving force affecting landscape structure and spatial organization (Li et al., 2021b; Duan et al., 2022). Nearly three-quarters of the global ecological landscape has been altered by human disturbance over the past millennium (Dadashpoor et al., 2019; Grafius et al., 2020; Winkler et al., 2021). For example, the transfer rate of the tidal flats landscape around the Nile Estuary to the ocean waters reaches 30 m/a (Zucker et al., 2021), and other tidal flats landscapes such as the Mississippi, Ebro, and Colorado have been showing a trend in shifting to marine waters due to the intensification of external disturbances (Walling, 2006; Xu et al., 2019). In the coastal areas of China, almost 53% of the tidal flats along the coast were lost due to land reclamation (Zhou et al., 2020). In particular from 2000 to 2010, the area of coastal tidal flats transformed into such artificial landscapes as construction land and cultivated land reached 320,000 hm² (Yu and Zhang, 2020), and the area of tidal flats was reduced by 25.2% (Ma et al., 2019). Changes in natural factors, such as river conditions, estuary size, and estuary hydrodynamic environments have also had an important impact on the evolution of coastal tidal flats landscapes (Paul et al., 2002; Strayer et al., 2003). For

example, 5.2 km² of the coastal tidal flats landscape in South Korea transformed into marine waters due to the reduction of river sediment input from 2013 to 2018 (Kim et al., 2021). The tidal flats landscape of the Yangtze River estuary has also been continuously turned into marine waters due to the decline of the annual sediment discharge from the Yangtze River after 2000 (Shen et al., 2013; Liu et al., 2020). In addition to Qingbacha, the tidal flats landscapes of the Yellow River estuary have been transforming into marine waters due to the reduction of river runoff and thus sediment discharge (Wang et al., 2017).

Ongoing landscape changes have caused a range of environmental and ecological problems globally, including habitat destruction, soil degradation, primary productivity decline, and biodiversity loss (Imhoff et al., 2004; Guida Johnson and Zuleta, 2013; Zhang et al., 2016; Zhou et al., 2018). Especially in recent decades, the dominant landscape of coastal wetlands has been gradually replaced by artificial landscapes with the expansion of construction land, resulting in regional ecosystem changes and the formation of more scattered and complex landscape patterns (Dadashpoor et al., 2019; Roussel and Alexandre, 2021). This makes landscape fragmentation a common feature of the evolution of coastal tidal flats landscapes (Plexida et al., 2014; Pace et al., 2017; Skilleter et al., 2017). These problems have greatly curtailed the ability of wetland ecosystems to provide ecological services for humans, and have brought serious threats to the sustainable development of human society (Jiyuan et al., 2010; Zhou et al., 2018). Therefore, it is crucial to assess the ecological risks arising from the current evolution of wetland landscapes correctly to alleviate the conflict between regional sustainable development and environmental protection. Landscape ecological risk is a landscape pattern-based perspective that reflects the possible adverse effects of human activities or natural conditions on landscape composition, structure, function, and processes comprehensively (McEachran et al., 2018). It can characterize comprehensive ecological risks from multiple stressors through landscape features, and provides an ecological risk mitigation pathway based on landscape pattern optimization (Goussen et al., 2016; Wang et al., 2021). Landscape ecological risk analyzes the impact of ecological risk on landscape composition and function, emphasizing the spatiotemporal heterogeneity of that risk (Wang et al., 2021; Zhang et al., 2022). Landscape ecological risk is used in watersheds, coastal wetlands, and for the ecological risk assessment of ecologically fragile areas and cities. However, there is still a lack of research based on ecological risk assessments of tidal flats landscapes around estuarine wetlands, and research on landscape patterns, ecological risks, and their driving factors is limited.

In summary, the landscape patterns of estuarine wetlands are in continuous evolution under the influence of human or natural environment factors, which affects the ecological security and ecological functions of regional wetlands. Relevant studies mainly focus on the ecological degradation and restoration of

wetlands within tidal flats, ignoring that tidal flats are an important peripheral defense line of estuarine wetlands, and thus there is a lack of understanding of the ecological role of tidal flats on coastal wetlands security. Therefore, since findings from the research to date on the evolution of estuarine tidal flats landscapes are unclear, the present study was conducted at the tidal flats in the Liaohe estuary wetlands (abbreviated as LEW), representing a typical international estuarine wetland, to achieve the following objectives: 1) Analyze the tidal flats landscape pattern around the estuary wetland; 2) quantitatively assess the ecological risks faced by estuarine tidal flats; 3) clarify the key driving forces and thresholds of ecological risks affecting tidal flats landscapes, and provide a theoretical basis for the protection and utilization of estuarine wetlands. The results will provide a theoretical basis for the protection and utilization of estuarine wetlands.

2 Materials and methods

2.1 Study area

This study was conducted on the tidal flats at the boundary between the land and sea of the LEW in Panjin City, northern China (Figure 1). This area is an important zone of material exchange in Bohai Bay, which is both boundaries of the wetlands and the city. The tidal flat area identified in this study is the area before the boundary of the vegetation zone and the boundary of the ocean low tide in the LEW. To discover the evolution of the estuary tidal flats landscape, the study area was chosen as

between the upper and lower boundaries of the tidal flats of the LEW in 1985 and 2017. The area of the tidal flats was 223.30 km² in 2017. The main material source of the continuous tidal flats deposition in the LEW is the sediment discharge of the Liaohe River. The study area was in a warm, temperate continental, semi-humid monsoon climate zone with four distinct seasons, including rain and high temperatures in the same season, and also dry and cold weather in the same period. The annual average temperature was 8.40°C, the annual average precipitation was 623.20 mm, and the annual average evaporation was 1669.60 mm.

2.2 Data sources

The main indicators and data sources involved in this study are shown in Table 1.

2.3 Landscape ecological risk assessment

The main methods and technical processes used in the current research to explore the ecological risks to tidal flat landscapes were shown in Figure 2. The research was completed through the following steps: step 1, obtain remote sensing images of the study area, and apply GIS spatial analysis and a transition matrix comprehensively to explore landscape evolution characteristics; step 2, calculate and analyze the relevant indices based on the results of landscape interpretation: 1) calculate the landscape

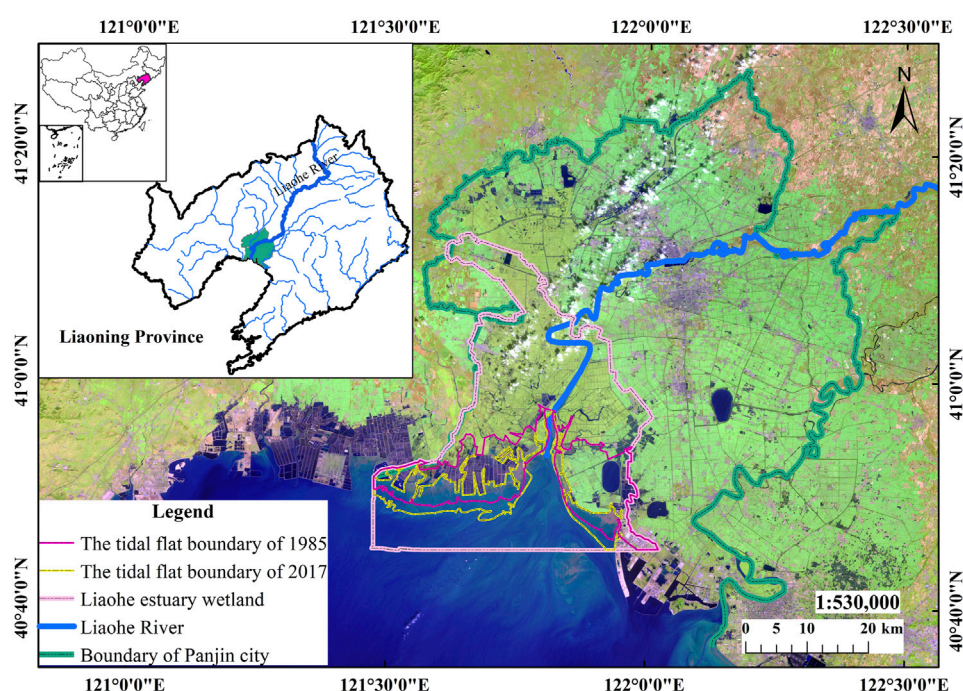
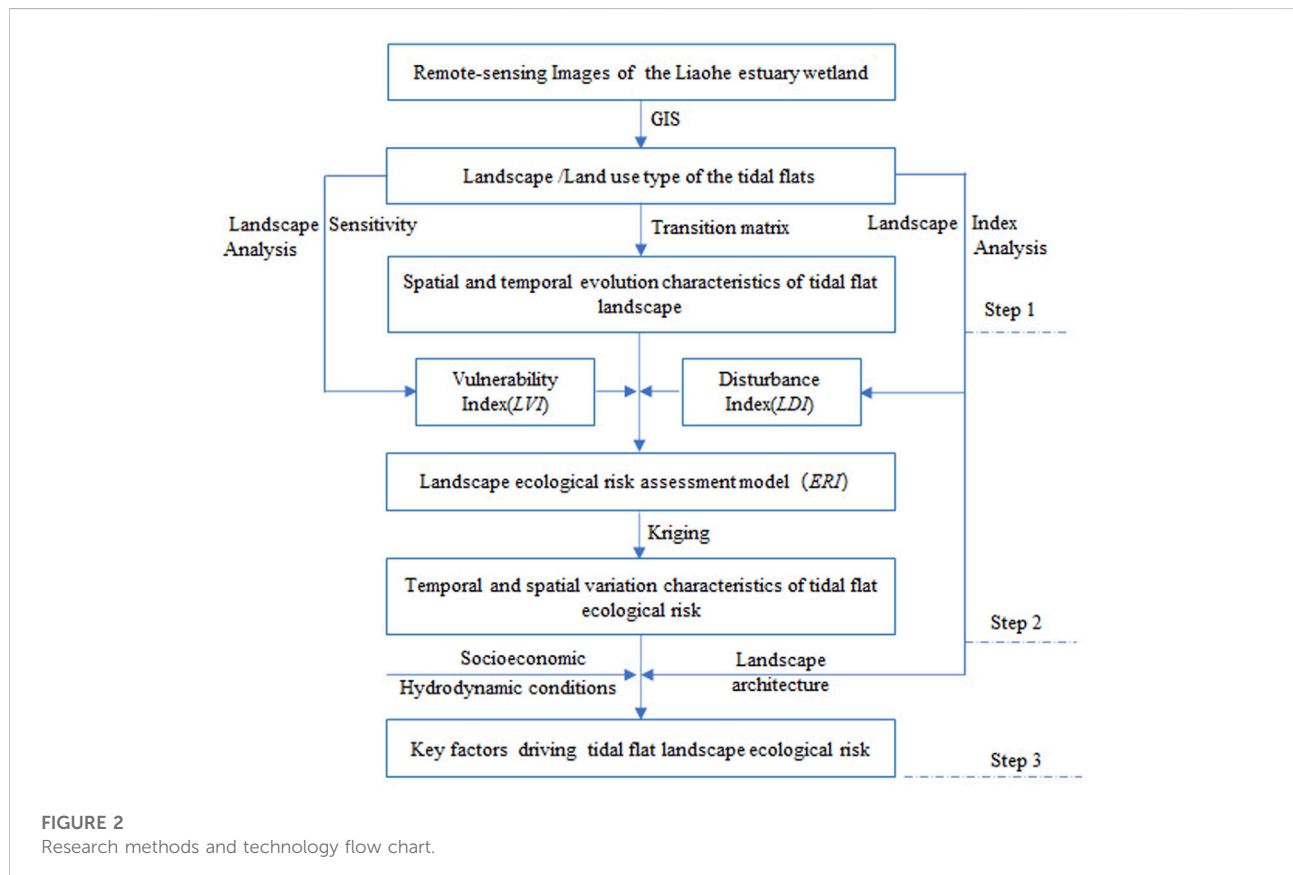


FIGURE 1
The location of the research area.

TABLE 1 Research indicators and data sources.

Type	Index/Elements	Data source
Landscape composition	Landscape area	The remote-sensing image data were downloaded from the China Geospatial Data Cloud (http://www.gscloud.cn) and the website of USGS (http://earthexplorer.usgs.gov/). RS image resolution was 30 m. The landscape was divided into exposed tidal flats, natural waters, natural wetlands (Suaeda salsa and reeds), paddy fields, mariculture, oil and gas exploitation, roads, towns, reservoirs, and construction land; based on GIS. The overall accuracy of image interpretation was 85.62%
	Landscape architecture	The landscape index was calculated using Fragstats_V4.2 (Chen et al., 2014; Plexida et al., 2014; Wang et al., 2020) based on the interpreted landscape-type data of the study area Net Shoreline Movement (NSM) represents the interannual migration distance of tidal flats shorelines in horizontal space and is an indicator characterizing tidal influence. The data were calculated by the baseline cross-sectional method based on the digital shoreline analysis system
Landscape ecological risk	Landscape disturbance	he index value was calculated by the formula $LDI_i = \alpha C_i + \beta S_i + \gamma F_i$ based on the interpreted patch data of landscape types. The specific calculation formulas and parameter explanations are provided in the supplementary materials
	Landscape sensitivity	Landscape sensitivity was divided into five levels based on a comprehensive analysis of related studies (Chen et al., 2020; Ran et al., 2022) and the state of the tidal flats in the LEW. Level 1: towns, roads, oil and gas exploitation, construction land; Level 2: mariculture, reservoirs, paddy fields; Level 3: natural waters; Level 4: natural wetlands; Level 5: exposed tidal flats. According to the landscape type in the study area, the landscape vulnerability index was calculated based on sensitivity level assignment and data normalization of different landscape types
Influencing factors	Socioeconomic	The index value was calculated based on the interpreted landscape patch data. The method of calculation is provided in the supplementary materials Annual data for 1985–2017 were obtained from the “Panjin Statistical Yearbook.”
	Watershed hydrology	The daily observation data were obtained for 1985 to 2017 from the “Liaohu Hydrological Yearbook”

FIGURE 2
Research methods and technology flow chart.

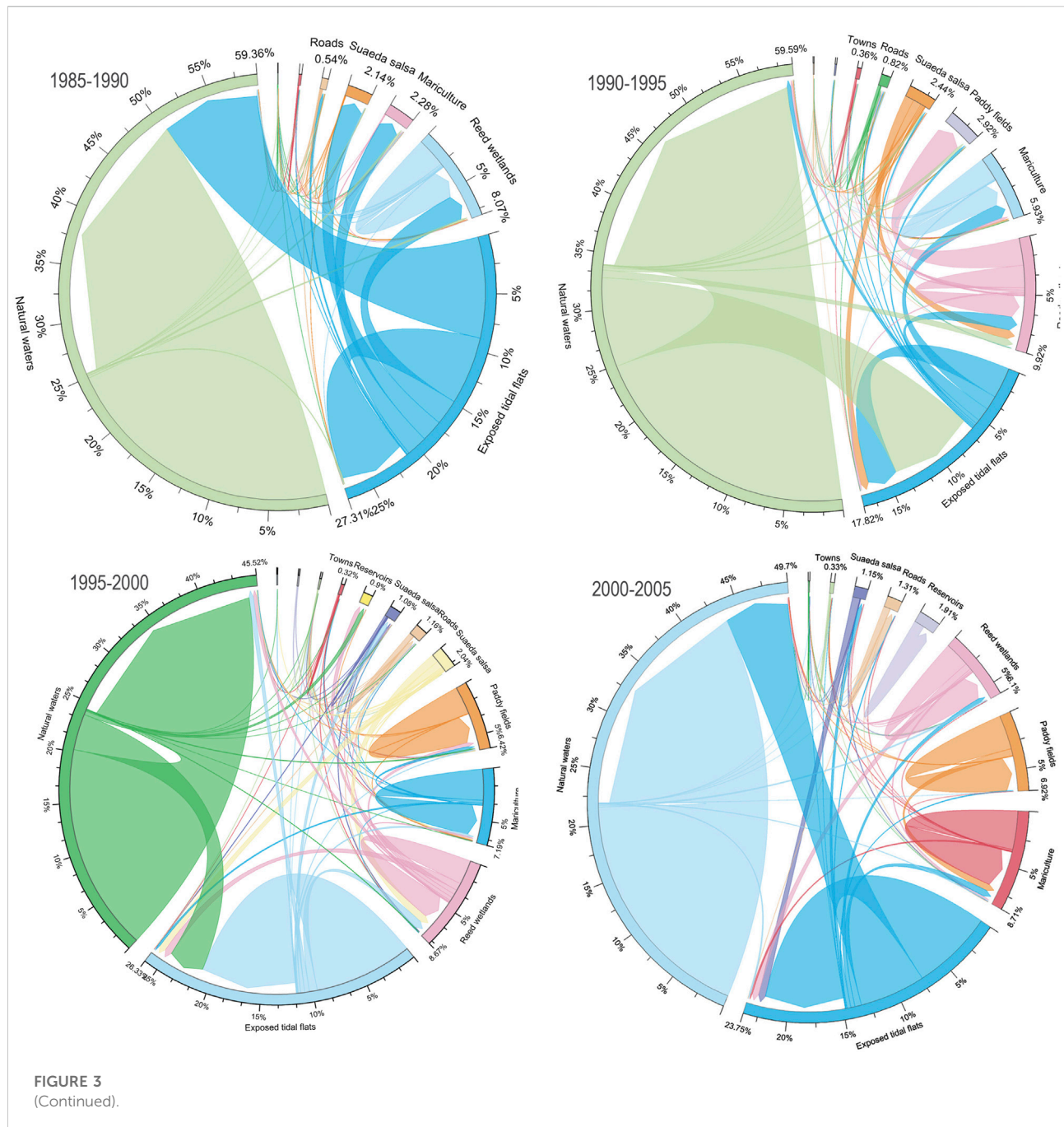
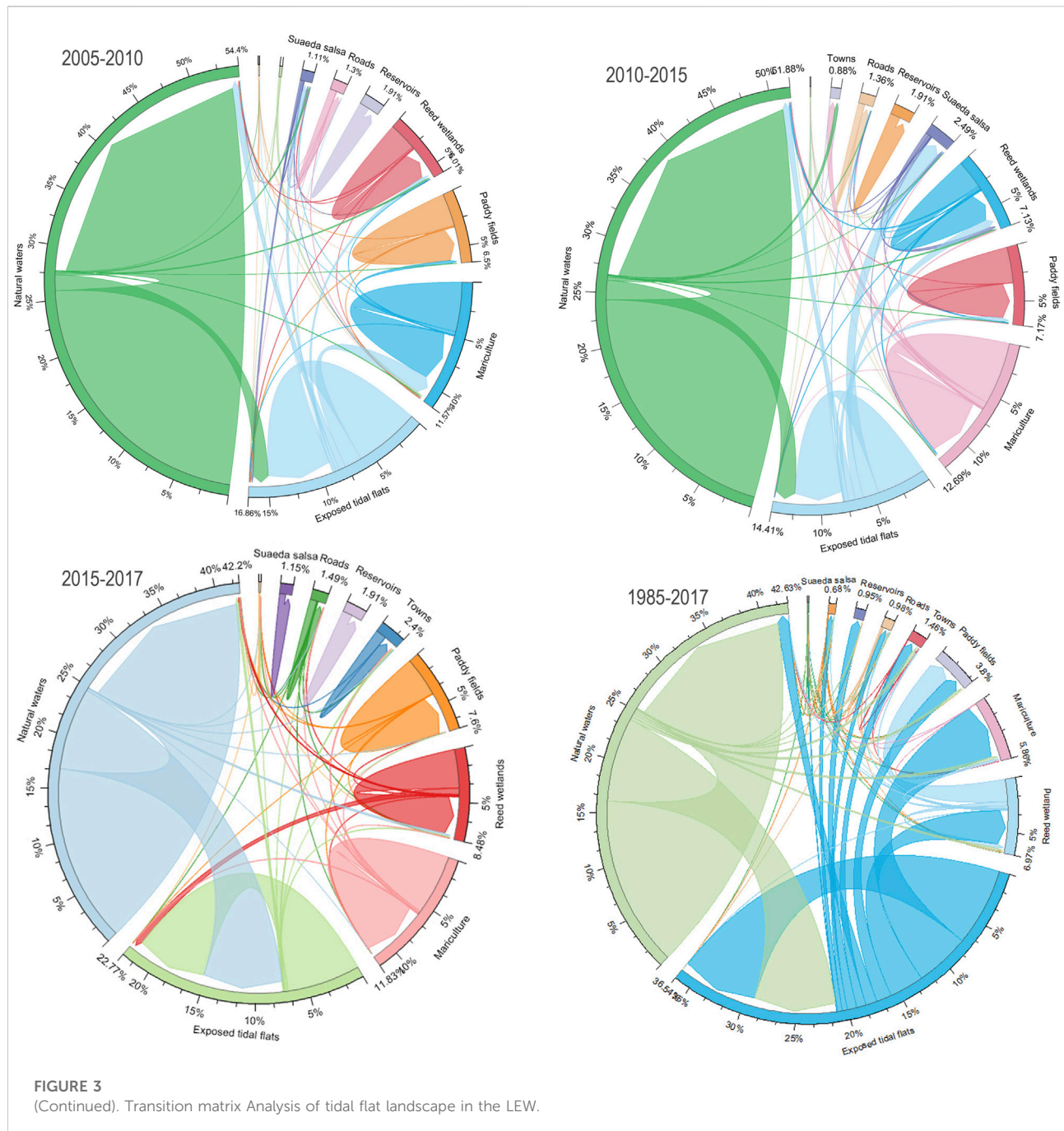


FIGURE 3
(Continued).

vulnerability index (*LVI*) through sensitivity analysis; 2) calculate the landscape disturbance index (*LDI*) using Fragstats_V4.2 (Chen et al., 2014; Plexida et al., 2014; Wang et al., 2020); 3) construct a landscape ecological risk model based on integrating the two parameters, and evaluate the ecological risk of the study area; step 3, explore the key driving factors that affect ecological risk. Specifics about the methods of analysis and calculations undertaken are presented in the [Supplementary Materials](#).

To finely evaluate the ecological risks to this regional landscape, this study established a 500×500 m grid according to the spatial distribution characteristics of the landscape patches, and divided the study area into 2,963 grid evaluation units. The values of the landscape disturbance index (*LDI*) and the landscape vulnerability index (*LVI*) for each evaluation unit were calculated and then the landscape ecological risk index (ERI_k) of the corresponding grid assessment unit was calculated using the following formula.



$$ERI_k = \sum_{i=1}^n \frac{A_{ki}}{A_k} (LDI_i \times LVI_i) \quad (1)$$

In the formula, ERI_k is the landscape ecological risk index of the k th evaluation unit; LDI_i is the landscape disturbance index; LVI_i is the landscape vulnerability index; n is the number of landscape types; A_{ki} is the area of the i th landscape type of the k th evaluation unit; A_k is the total area of the k th evaluation unit. The larger the ERI_k value, the higher the ecological risk of the corresponding grid.

To analyze the spatial and temporal distribution differences of the ERI , the values of ERI were divided into low ecological risk areas, medium ecological risk areas, and high ecological risk areas using the Jenks natural breaks classification method (Chen et al., 2013; Gong et al., 2021). Then, the spatial distribution characteristics of the ERI were analyzed using the kriging interpolation method, and the spatial distribution changes of the number of high-risk, medium-risk, and low-risk grids were statistically analyzed.

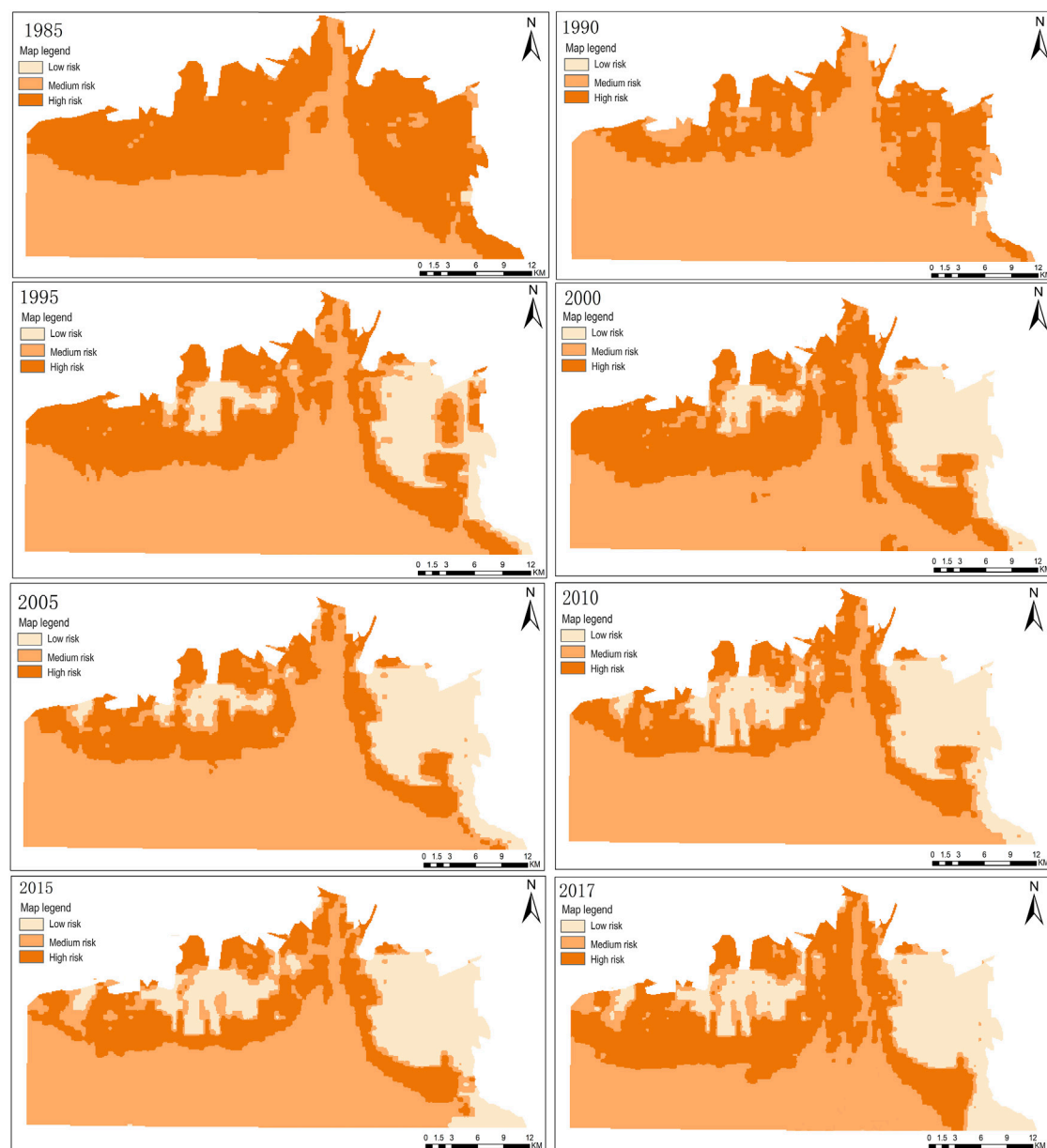


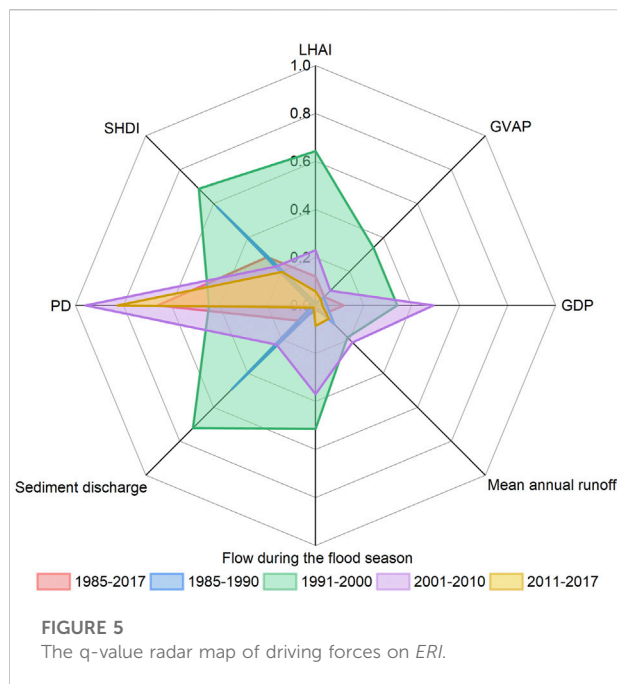
FIGURE 4
Landscape Ecologic risk index Spatial distribution in the LEW.

2.4 Driving factors analysis

According to the current environmental status of the tidal flats in the LEW, the eight main driving factors of patch density (PD), landscape diversity (*SHDI*), artificial disturbance intensity index (*LHAI*), Gross Domestic Product (GDP), Gross Value of Agricultural Production (GVAP), mean annual flow, flow during the flood season, and annual sediment discharge were screened out by principal component analysis based on a comprehensive

analysis of the 14 impact indicators shown in [Table 1](#). Among them, the *LHAI*, GDP, GVAP, *PD*, and *SHDI* in the first principal component had factor loads greater than 0.8, while the mean annual flow, flow during the flood season, and annual sediment discharge in the second principal component had factor loads greater than 0.8.

Based on the main initiating factors screened, the factor detector in the geographic detector ([Wang et al., 2010, 2016](#)) was used to analyze the effect of the main driving factors affecting the



ERI on the tidal flats landscape in the LEW, based on the main initiating factors that were screened. Then, the q value was used to judge and explain the driving force of each index with regards the range of change of the ERI. Regression analysis was used to explore the relationship between each driving factor and the ERI, and to analyze the effect of different driving factors on the ecological risk to the regional landscape.

3 Results

3.1 The evolution of the tidal flats landscape

The tidal flats of the LEW has been silting up to the sea gradually over the past 30 years, meanwhile, the tidal flats landscape has evolved into natural wetlands and artificial landscapes such as roads, towns, and aquaculture (Figure 3). From 1985 to 2017, 16.11% of the natural waters gradually evolved into tidal flats in the study area. 17.66% of the tidal flats have evolved into natural wetlands, of which 15.44% and 2.22% have evolved into reed and *Suaeda salsa* wetlands respectively; 24.47% of the tidal flats have been developed into mariculture, and 6.85% have been developed into paddy fields. 11.08% evolved into other artificial landscapes. In terms of artificial landscape, 24.47%, 6.85%, and 11.08% of the tidal flats were developed into mariculture, paddy fields, and other artificial landscapes, respectively. Of the natural wetlands, 68.72% were developed into paddy fields, of which 70.71% and 11.01% of the reed and *Suaeda salsa* wetlands were

transformed into paddy fields, respectively. In addition, 7.38% of the natural wetlands were developed for aquaculture, of which 13.40% and 7.17% of the *Suaeda salsa* and reed wetlands were developed for aquaculture, respectively.

The characteristics of landscape change can be roughly divided into the natural evolution period (1985–2000), the artificial landscape rapid increase period (2000–2010), and the ecological restoration period (2010–2017). In terms of the period 1985 to 2000, the tidal flats in the LEW mainly turned to *Suaeda salsa* and reed wetlands by natural succession, and the average proportion of artificial landscapes such as marine aquaculture and roads was 2.30%. The proportion of natural wetlands being developed into paddy fields increased year by year. From 2000 to 2010, the proportion of artificial landscapes increased rapidly. 6.40% of tidal flats turned into natural wetlands, 13.72% was developed for mariculture, and only 0.2% was turned into other artificial landscapes. Of the natural wetlands, 7.18% were turned into such artificial landscapes such as for mariculture, roads, and other artificial landscapes. During this period, the area that can be developed for mariculture reached its limit, and the scale of mariculture accounted for 13.18% of the study area, which was the largest artificial landscape. At this time, the tidal flats were in a state of erosion, and 35.06% of the area was transformed into natural water, while 57.82% and 14.79% of *Suaeda salsa* and reed wetlands, respectively, were degraded into the exposed tidal flats. From 2010 to 2017, 28.29% of the tidal flats were transformed into natural wetlands, of which 18.65% were transformed into *Suaeda salsa* wetlands. The proportion of tidal flats developed for aquaculture was reduced to 1.17%, and 5.47% of the tidal flats were developed. In paddy fields, the proportion of other artificial landscapes was reduced to 0.83% during the period, and 9.72% of the aquaculture landscapes were cleared and restored to natural wetlands, of which 8.41% of aquaculture was transformed into *Suaeda salsa* wetlands. The results show that the implementation of the “Environmental Grayscale Project around the Bohai Bay” has promoted improvement of the landscape pattern in the study area, and the increased rate of the artificial landscape has begun to decline. However, during this period, the tidal flats were still eroded, shrinking by 6.84%, and 5.84% of *Suaeda salsa* degenerated into exposed tidal flats.

In general, the proportion of tidal flats transformed into such artificial landscapes as paddy fields and aquaculture between 1985 and 2017 was greater than that of natural wetlands such as reeds and *Suaeda salsa*. The regional tidal flats landscape generally showed a tendency to transform into an artificial landscape, in which, in 2017, the average increase in rate of mariculture reached 11.39%, the proportion of mariculture reached 11.55%, and the natural wetlands accounted for 8.02%. The reed and *Suaeda salsa* natural wetlands in the region were mainly developed into paddy fields, and the transfer rate increased to 7.60% in 2017.

3.2 The ecological risk of the tidal flats landscape

The tidal flats of the estuary have evolved into salt marsh wetlands and reed wetlands through the gradual but continuous process of silting, and swelling towards the sea. The landscape of the estuary has evolved from a single tidal flats landscape into a

variety of wetlands. The landscape diversity has increased, but with the impact of human activities, the evolution of the tidal flats has gradually been replaced by the artificial landscape. The ecological risk faced by the regional landscape has changed with the evolution of the landscape. The evaluation results of ecological risk in the study area over the past 30 years are shown in Figure 4.

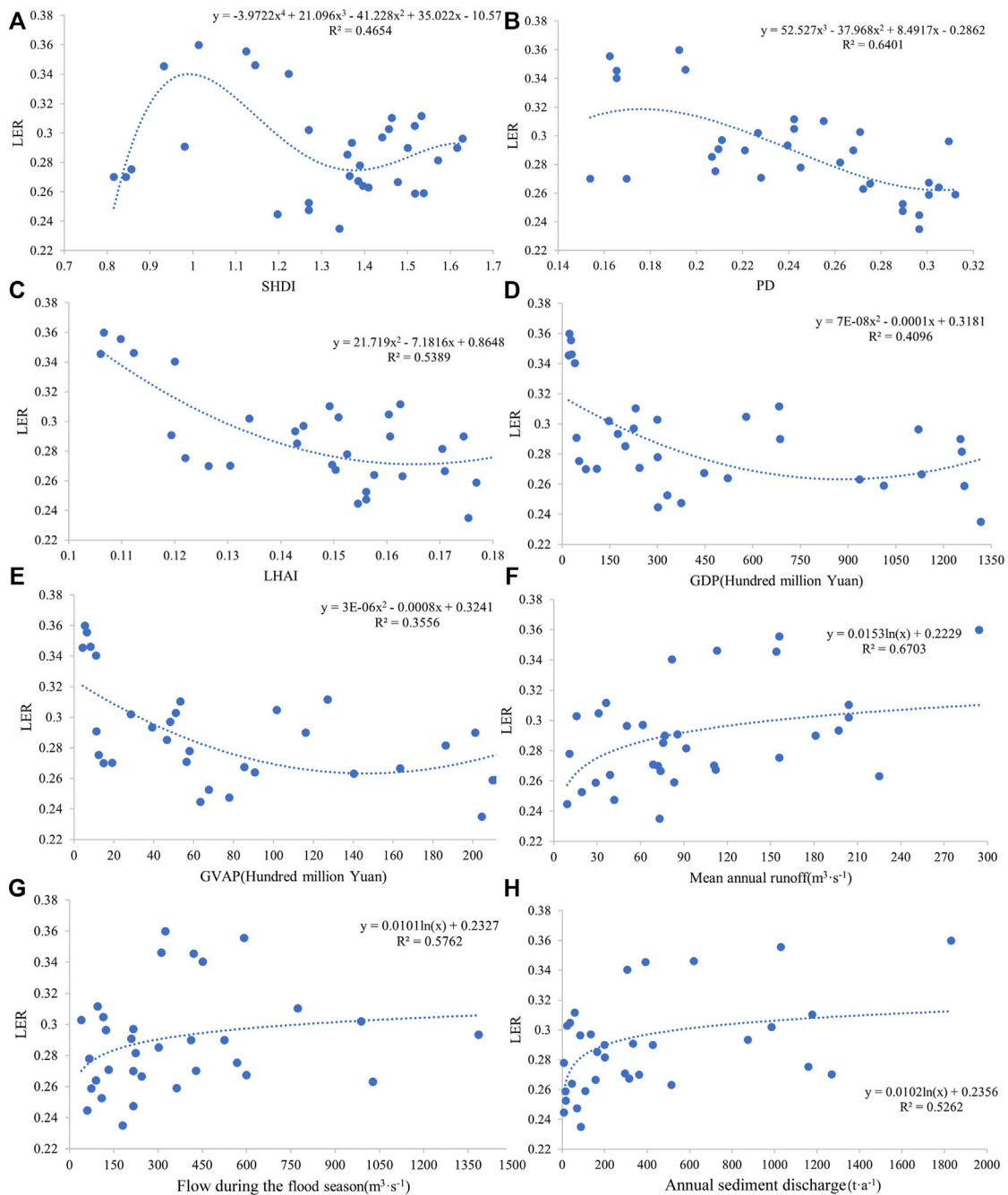


FIGURE 6

Different kinds of driving forces on Ecological risk in the tidal flat: the labels (A–H) represent SHDI, PD, LHAI, GDP, GVAP, mean annual flow, flow during the flood season, and annual sediment discharge respectively.

The change of the *ERI* reflects the superposition effect of the changes of various types of landscape utilization in the region (Ran et al., 2022). With the evolution of landscape patterns, the spatial distribution of the *ERI* in the study area was different (Figure 4). The *ERI* fluctuated with changes in the distribution of exposed tidal flats, with high ecological sensitivity. From 1985 to 2017, the high ecological risk zones were mainly distributed in the exposed tidal flats located outside of the LEW; the medium ecological risk zones were mainly distributed in the largest natural waters; the low-risk zones were mainly distributed in the artificial landscapes with strong anti-interference capacity, and the low-risk zones increased to a certain extent with the increase in landscape diversity. This demonstrates that the increase of regional landscape types can alleviate ecological risk to a certain extent.

From 1985 to 1990, the high ecological risk and medium ecological risk zones dominated the study area, with a small proportion of low-risk zones. This shows that the regional landscape type was dominated by exposed tidal flats at the beginning of the research period. The overall landscape type also had high ecological sensitivity and thus the study area suffered from high landscape ecological risk. After 1990, as the tidal flats silted up to the sea, the areas of high ecological risk increased. From 1995 to 2005, the high ecological risk areas increased, spreading from the periphery to the inside of the study area, and the value of the *ERI* increased. The low-risk areas were mainly in mariculture, paddy fields, and reservoir landscapes, and the medium-risk areas decreased. Since 2005, the natural water landscape has evolved into medium ecological risk zones, indicating that the continuous strengthening of artificial developments has increased the ecological risk of natural waters. By 2010, the area of high ecological risk was decreasing, and mainly distributed in the peripheral areas of the tidal flats. The low ecological risk zones were mainly distributed in artificial landscapes with strong robustness against interference such as paddy fields, mariculture, and reservoirs. Since 2010, the spatial distribution of the *ERI* has not changed much, the area of high-risk zones has decreased, and the medium-risk and low-risk zones have not changed significantly. The area of high-risk zones increased by 2017, however, which may be related to the large-scale degradation of salt marsh wetlands caused by the disconnection of tidal flats waterways which in turn were caused by tourism developments from 2015 to 2017.

Considering the changes in the spatial distribution of the *ERI* in the study area from 1985 to 2017, in the process of natural succession of the tidal flats from a single landscape to a natural wetland landscape, with the increase of landscape diversity, the *ERI* decreased. Later in this period, with the increase in the proportion of artificial landscapes and the influence of tidal flats erosion, the *ERI* showed a fluctuating trend of increasing and decreasing. Overall, the ecological risk of the tidal flats landscape in the LEW has been at a medium-risk level over the past

30 years, the high-risk and medium-risk zones have declined to some extent, and the low-risk zones have been slowly increasing. The results of this study have showed that the stability of the estuarine wetland landscape can be improved when the regional landscape evolved from a single exposed tidal flats landscape to a diverse landscape structure. The ability of ecologically fragile areas to resist ecological risks also improved. This landscape evolution improves its ability to resist ecological risks in ecologically fragile areas.

3.3 The driving factors affecting the ecological risk of the tidal flats

3.3.1 Screening of key factors

The staged comprehensive analysis by the factor detection method (Figure 5) showed that the order of explanatory power of the driving factors affecting the changes of the tidal flats *ERI* in the LEW was $PD > SHDI > LHAI > GDP > \text{sediment discharge} > \text{GVAP} > \text{mean annual runoff} > \text{flow during the flood season}$. The results showed that the *PD*, *SHDI*, and *LHAI* have a greater impact on the landscape ecological risk index in the study area, indicating that the change in structure of the tidal flats was the key process that caused changes in landscape ecological risk. However, the main force driving the change in regional landscape structure was human development (Jat et al., 2008; Bryan et al., 2018). On the whole, the *q* value of the socioeconomic driving factor reflecting the influence of human activities was greater than that of the natural factors, which indicates that human development activities were the key factors driving the changes in ecological risk of the tidal flats landscape in the LEW.

3.3.2 Effects of changes in landscape spatial structure on ecological risks

The *ERI* increased first and then decreased with the increase of *SHDI* (Figure 6A). The *ERI* increased when the *SHDI* changed when the *SHDI* value was less than 1.0. The *ERI* decreased when the *SHDI* increased from a value changed from 1.0 to 1.4. The *ERI* increased again when the *SHDI* continued to increase after exceeding 1.4. The *ERI* slowly decreased with the increase of the *PD* (Figure 6B). The influence of the *PD* on the *ERI* stabilized with no obvious change beyond a *PD* of 0.3. The results showed that the environmental risks faced by a single landscape patch were decreased when the tidal flat landscape evolved from a single landscape patch to multiple other landscape patches. Thus, the *ERI* decreased to a certain extent as the *SHDI* and *PD* increased. However, the ecological risk of the landscape tended to be stable or increase when this changing trend exceeded a certain limit. This indicates that the continuous increase of *SHDI* and *PD* will be unfavorable to reducing the ecological risk of the regional landscape. This limitation may be related to the increase of landscape diversity in the study area mainly due to the contribution of the artificial landscape.

However, the increase of artificial landscapes will exacerbate the fragmentation of regional landscapes (Zhou et al., 2018), making the landscape pattern unstable and affecting the regional landscape and its ecological security.

3.3.3 The impact of human disturbance activities on ecological risks

The LHAI, GDP, and GVAP all have a quadratic polynomial relationship with the *ERI* (Figures 6C–E). The regional *ERI* decreased with increases in the LHAI, when the value was less than 0.15. This indicates that the ecological risk faced by the single landscape of tidal flats would be reduced if the single tidal flats landscape was transformed into an artificially developed landscape. The *ERI* became stable when human disturbance continued to increase. However, the *ERI* changed to a trend of increasing with increasing LHAI when the LHAI value was greater than 0.17. The *ERI* decreased with increases in regional GDP and GVAP but once economic development exceeds a certain limit, the *ERI* switched to increasing with increases in GDP and GVAP. These results show that the environmental risks faced by a single tidal flats landscape would be reduced to a certain extent in the face of human development controlled within a certain range.

3.3.4 The impact of watershed hydrology on landscape ecological risk

The Liaohe River flowing into the estuary has a logarithmic relationship between the mean annual flow, flow during the flood season, annual sediment discharge, and the *ERI* (Figures 6F–H). The *ERI* increased rapidly with changes in the mean annual flow and the flow during the flood season when the mean annual flow was less than $90 \text{ m}^3 \text{ s}^{-1}$ and the flow during the flood season was less than $300 \text{ m}^3 \text{ s}^{-1}$ in the low runoff years. The *ERI* tended to be stable with no obvious change when the mean annual flow and the flow during the flood season continued to increase beyond

$180 \text{ m}^3 \text{ s}^{-1}$ and $600 \text{ m}^3 \text{ s}^{-1}$, respectively. The regional *ERI* clearly increased with the change of the sediment discharge when the annual sediment discharge of the Liaohe River was less than 400 t y^{-1} . Beyond this, The *ERI* tended to be stable when the annual sediment discharge further increased. In addition, there was little effect on the *ERI* when the annual sediment discharge was greater than $1,200 \text{ t y}^{-1}$.

4 Discussion

4.1 The evolution of estuarine tidal flats landscapes

The estuary tidal flats are located in the land–ocean interlaced, sensitive zone, which is the most vulnerable type of landscape in coastal estuaries (Li et al., 2021a; Xie et al., 2021). They are potential development areas for reeds, salina, and other types of wetlands that exist in coastal estuaries. The coastal and estuarine tidal flats have mainly evolved into salt marsh wetlands under the dominant action of certain natural factors. Regional landscape diversity has increased, which has improved the anti-disturbance ability of coastal estuarine wetland ecosystems (Cao et al., 2020; Liu et al., 2020; Zhao et al., 2020). However, tidal flats in coastal estuaries are an important element of the land reserve resources of coastal cities, and the evolution of this landscape has been deeply affected by human activities (Lin et al., 2018), which have intensified the evolution of natural tidal flats into diversified artificial landscapes (Zhang et al., 2022). This has led to the fragmentation of wetland landscapes, reducing the connectivity between patches of landscape types (Zhou et al., 2018), and increasing the complexity and heterogeneity of patch shapes (Liu et al., 2016).

The research showed that the tidal flats and natural water landscapes of coastal wetlands were mainly transformed into

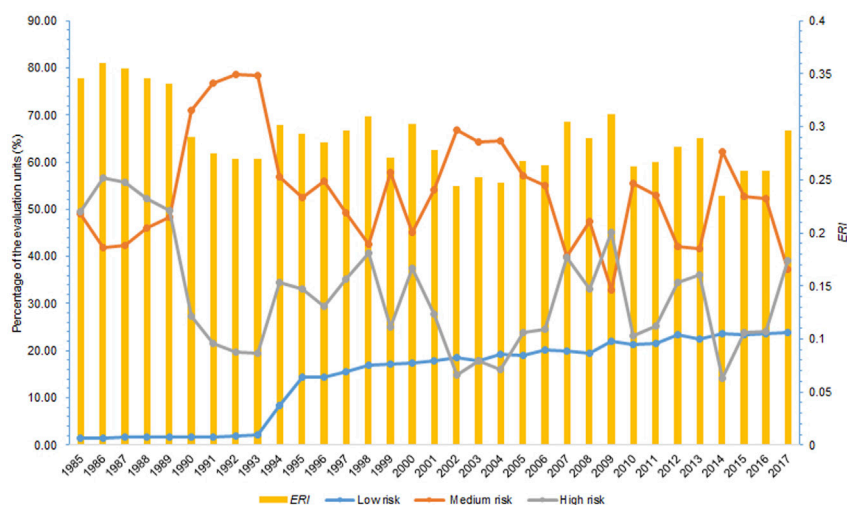


FIGURE 7

Interannual changes in *ERI* and percentage of assessment units with different ecological risk levels.

construction land and aquaculture land, the natural wetlands were turned into artificial wetlands and aquaculture, and the artificial wetlands were transformed into construction land (Lin et al., 2018). These results were consistent with the results of the tidal flats in the LEW. The tidal flats landscape has mainly evolved into a natural wetland landscape under the influence of natural factors. In contrast, the tidal flats landscape has rapidly turned into an artificial landscape due to human interference, which causes the fragmentation of the regional landscape pattern. In general, the evolution of the landscape pattern of coastal estuarine tidal flats indicated that landscape types with a high degree of human disturbance replaced various landscape types with low and medium levels of human disturbance (Li et al., 2017; Zhou et al., 2018), and the intensity of human disturbance was the main reason for the instability of the landscape pattern in the study area. It showed that the continuous increase of human disturbance intensity was the main reason for the rapid changes in the estuarine tidal flat landscape pattern.

4.2 Ecological risks faced by estuarine tidal flats landscape evolution

In terms of time dynamics, the *ERI* of the tidal flats landscape in the study area changed in stages, and the *ERI* level differed at different stages of landscape evolution. The *ERI* was established based on the landscape index, and its value was determined by the change in the combination of landscape type and its vulnerability (Xu and Kang, 2017; Lin et al., 2019). Therefore, the degree of transfer between the patches with different ecological risk levels was different in the process of landscape evolution of the tidal flats. The LEW was mainly affected by agricultural production at the beginning of the study period when the main landscape type was exposed tidal flats (Figure 7). The *ERI* was relatively high due to the exposed tidal flats with a high degree of vulnerability. Whereafter, with the increase of landscape diversity, the tidal flats landscape evolved into natural wetlands such as reeds and *Suaeda salsa*. As a result, the *ERI* has decreased, and the high-risk zones have shifted to become medium and low-risk zones. More recently, with the implementation of China's reform and development policy, the Liaohe Estuary region experienced rapid urbanization and social and economic development, which promoted the rapid transformation of such landscapes of exposed tidal flats, natural waters, natural wetlands, and others to artificial landscapes with low vulnerability (Cheng et al., 2019). By the end of the study period, the overall *ERI* decreased due to the area of high-risk and medium-risk patches decreasing by 24.90% and 16.83% respectively, and the area of low-risk patches increasing by 20.24%.

Previous studies concluded that urban sprawl and increased land fragmentation were the main driving factors leading to

increased ecological risks in regional landscapes (Tang et al., 2018; Lin et al., 2021). However, in terms of the environmental conditions, the artificial reclamation of coastal tidal flats has played a role to some extent in protecting the fragile ecological environment of the islands and the coastal tidal flats (Lin et al., 2018). The expansion of artificial landscapes increased landscape diversity and reduced landscape sensitivity (Yang et al., 2022). It showed that there has a double nature of the impact of human disturbance on the ecological landscape structures. The anti-interference ability of the fragile ecosystem will be improved due to the increase in landscape diversity of the regional ecosystem under moderate interference. Nevertheless, the ecological risk of the regional ecosystem will be increased due to the destruction and imbalance of landscape structures under excessive artificial interference (Osman, 2008, 2015). The overall distribution of the *ERI* in the tidal flats of the LEW (Figure 7) exhibited a shift from high-risk patches with high sensitivity to medium-risk patches with low sensitivity and low-risk ones with strong robustness against interference. The *LER* values decreased to a certain extent with the increase of artificial landscape components generally. But a continued increase in artificial disturbance would lead to an increase in regional ecological risk.

4.3 The impact thresholds of driving factors

The results showed that in the evolution of the tidal flats landscape in the LEW, there seems to be a critical value for the impact of human disturbance factors and natural factors on the *ERI* in the study area. Studies on the Yellow River Estuary and Yancheng Beach showed that the main artificial disturbance activities should be controlled within a reasonable threshold to ensure the stability and ecological security of the estuary and the pattern of the tidal flats landscape (Tian et al., 2022; Yang et al., 2022). Other studies determined that the vehicular roads in the tidal flats of the LEW should be limited to at or below 770.92 hm² to ensure the ecological stability of the tidal flat structure (Li et al., 2021a). This study found that the LHAI should be controlled to be no higher than 0.17 in the development of the tidal flats, otherwise, if the LHAI exceeds this value, the *ERI* will increase due to the continuous artificial disturbance. It showed that the management of the estuarine tidal flat landscape should follow the guidance of the intermediate disturbance hypothesis (Lubchenco and Sousa, 2020; Murdoch and Sousa, 2020). The proportion of artificial landscapes can be increased appropriately in the development of tidal flat resources. But to take maximum advantage of human interference to increase the heterogeneity and diversity of regional landscapes its development needs to be controlled within a reasonable limit. As such, the ecological risks faced by a single landscape structure will be reduced (Molino and Sabatier, 2001; Sasaki et al., 2009; Liu et al., 2019).

A local government in Italy dredged $10 \times 10^4 \text{ m}^3$ of sand from Viareggio to nourish the tidal flats in order to maintain the relative stability of the Tuscan estuary landscape (Pranzini et al., 2020). Research on the Hudson River estuary clarified that the upstream sediment input to the estuary of the Mohawk and Hudson Rivers should not be less than 36.13×10^4 and $10.95 \times 10^4 \text{ t}\cdot\text{y}^{-1}$, respectively, to maintain the stability of the tidal flats landscape (Ralston and Geyer, 2009). Research into the Yellow River Estuary showed that to maintain the stability of the tidal flats landscape, the sediment discharge of the Yellow River should not be less than 441×10^6 and $167 \times 10^6 \text{ t}\cdot\text{y}^{-1}$ before and after artificial water and sediment regulation, respectively (Kong et al., 2015). Previous studies proposed that the river sediment transported to the tidal flats should be no less than $792.91 \times 10^4 \text{ t}\cdot\text{y}^{-1}$ to maintain the stability of the landscape macro-structure of the Liaohe Estuary wetlands (Li et al., 2021a). It showed that the material supply of the upstream basins restricted the stability of the morphological structure of the estuarine tidal flat landscape (Giosan et al., 2014). If the material supply of the basins was insufficient, the tidal flat landscape ecosystem will be degraded directly, hence the ecological risk level aggravated faced by the estuary tidal flats (Wei et al., 2020; Yu et al., 2021). This paper also found that there was a threshold range for the impact of changes in sediment input upstream of the Liaohe River in terms of the ecological risk to tidal flats landscapes. The annual sediment discharge, the mean annual flow, and the flow during the flood season should not be less than $400 \text{ t}\cdot\text{y}^{-1}$, $180 \text{ m}^3\cdot\text{s}^{-1}$, or $600 \text{ m}^3\cdot\text{s}^{-1}$, respectively. If any of these factors are below these thresholds, the ecological risk index increases rapidly. The results showed that the sediment and water input from the upstream of the Liaohe River was an important material source to ensure the stability of the estuary tidal flat landscape structure, which can alleviate the ecological risk pressure of the tidal flat landscape effectively. Therefore, to maintain the ecological risk of tidal flat landscapes within an available range, two aspects should be paid attention to in the protection and utilization of estuary tidal flat resources in the future. The regional human development activities should be controlled within an appropriate range. On the other hand, it was necessary to coordinate the allocation of water and sediment material supply from upstream to ensure the stability of the estuary tidal flat landscape morphology.

5 Conclusion

The evolution of the tidal flats landscape in the LEW has changed in stages, and seems to be turning into mainly an artificial landscape. Between 1985 and 2000, the exposed tidal

flats landscape mainly evolved into natural wetlands such as *Suaeda salsa* and reeds. In the period 2000 to 2010, the exposed tidal flats landscape rapidly transformed into paddy fields and aquaculture, and landscape fragmentation continued to intensify. From 2010 to 2017, the proportion of artificial landscapes began to decrease, changing into natural landscapes, and the tidal flats landscapes in the study area developed naturally due to ecological restoration projects.

The landscape pattern of tidal flats in the LEW has generally been at a medium level of ecological risk over the past 30 years. The ecological risk tended to decrease as the single exposed tidal flats landscape evolved into a diverse landscape. The areas of high-risk and medium-risk patches decreased to a certain extent, and the areas of low-risk patches gradually increased. The high ecological risk patches were mainly distributed in the exposed tidal flats zones, with high sensitivity in the periphery of the estuary.

The key factors affecting the landscape ecological risk of the tidal flats were *PD*, *SHDI*, *LHAI*, *GDP*, and sediment discharge. Among them, the *PD*, *SHDI*, and *LHAI* were the key processes that caused changes in landscape ecological risk. Human disturbance was the key factor affecting changes to landscape ecological risk. In regional wetland management, the *LHAI* should be controlled to be no higher than 0.17, and the *SHDI* and *PD* should be kept within 0.14 and 0.3, respectively, to preserve a reasonable landscape structure and the ecological security of regional tidal flats. River sediment input was a key natural factor affecting landscape ecological risk, to ensure the continuing evolution of the regional tidal flats landscape.

Data availability statement

The original contributions presented in the study are included in the article/Supplementary Materials, further inquiries can be directed to the corresponding author.

Author contributions

Writing—original draft preparation, HL; writing—review and editing, HL and FS; investigation, HL and LD; data curation, FS and CW; supervision, CG; project administration, FS.

Funding

This research was funded by the National Key Research and Development Program of China (2022YFF1301004); the China Postdoctoral Science Foundation (2021MD703856); the Liaoning

Science and technology innovation leader projects (XLYC2002054).

Acknowledgments

Thanks to all the teachers who participated in the research process for their technical guidance, the master and doctoral students for their help in data collection and interpretation, and the support of Liaoning Panjin Wetland Ecosystem National Observation and Research Station and Liaoning Shuangtai Estuary Wetland Ecosystem Research Station.

Conflict of interest

LD was employed by the Yellow River Engineering Consulting Co., Ltd.

The remaining authors declare that the research was conducted in the absence of any commercial or financial

relationships that could be construed as a potential conflict of interest.

Publisher's note

All claims expressed in this article are solely those of the authors and do not necessarily represent those of their affiliated organizations, or those of the publisher, the editors and the reviewers. Any product that may be evaluated in this article, or claim that may be made by its manufacturer, is not guaranteed or endorsed by the publisher.

Supplementary material

The Supplementary Material for this article can be found online at: <https://www.frontiersin.org/articles/10.3389/fenvs.2022.1070009/full#supplementary-material>

References

- Bao, J., and Gao, S. (2021). Wetland utilization and adaptation practice of a coastal megacity: A case study of chongming island, shanghai, China. *Front. Environ. Sci.* 9, 627963. doi:10.3389/fenvs.2021.627963
- Bryan, B. A., Gao, L., Ye, Y., Sun, X., Connor, J. D., Crossman, N. D., et al. (2018). China's response to a national land-system sustainability emergency. *Nature* 559, 193–204. doi:10.1038/s41586-018-0280-2
- Cao, W., Zhou, Y., Li, R., and Li, X. (2020). Mapping changes in coastlines and tidal flats in developing islands using the full time series of Landsat images. *Remote Sens. Environ.* 239, 111665. doi:10.1016/j.rse.2020.111665
- Chen, A., Yao, L., Sun, R., and Chen, L. (2014). How many metrics are required to identify the effects of the landscape pattern on land surface temperature? *Ecol. Indic.* 45, 424–433. doi:10.1016/j.ecolind.2014.05.002
- Chen, J., Dong, B., Li, H., Zhang, S., Peng, L., Fang, L., et al. (2020). Corrigendum to 'Study on landscape ecological risk assessment of Hooded Crane breeding and overwintering habitat' [Volume 187, August 2020, 109649]. *Environ. Res.* 191, 110076. doi:10.1016/j.envres.2020.110076
- Chen, J., Yang, S., Li, H., Zhang, B., and Lv, J. (2013). "Research on geographical environment unit division based on the method of natural breaks (jenks)," in *Isprs/igu/ica joint workshop on borderlands modelling and understanding for global sustainability 2013*. Editors J. Chen, Y. Ge, and Y. Cheng (Göttingen: Copernicus Gesellschaft MbH), 47–50. doi:10.5194/isprsarchives-XL-4-W3-47-2013
- Cheng, R., Chen, W., Wu, S., and Lin, J. (2019). Spatiotemporal variation characteristics of ecosystems and their driving forces in the min delta urban agglomeration. *IRSPSD. Int.* 7, 177–194. doi:10.14246/irspda.7.1_177
- Costanza, R., Anderson, S. J., Sutton, P., Mulder, K., Mulder, O., Kubiszewski, I., et al. (2021). The global value of coastal wetlands for storm protection. *Glob. Environ. Change* 70, 102328. doi:10.1016/j.gloenvcha.2021.102328
- Cui, L., Li, G., Chen, Y., and Li, L. (2021). Response of landscape evolution to human disturbances in the coastal wetlands in northern jiangsu province, China. *Remote Sens.* 13, 2030. doi:10.3390/rs13112030
- Dadashpoor, H., Azizi, P., and Moghadas, M. (2019). Land use change, urbanization, and change in landscape pattern in a metropolitan area. *Sci. Total Environ.* 655, 707–719. doi:10.1016/j.scitotenv.2018.11.267
- Duan, H., Yu, X., Zhang, L., Xia, S., Liu, Y., Mao, D., et al. (2022). An evaluating system for wetland ecological risk: Case study in coastal mainland China. *Sci. Total Environ.* 828, 154535. doi:10.1016/j.scitotenv.2022.154535
- Fu, B. (1995). The spatial pattern analysis of agricultural landscape in the loess are. *Acta Ecol. Sin.* 15, 113–120. doi:10.2307/2997695
- Giosan, L., Syvitski, J., Constantinescu, S., and Day, J. (2014). Climate change: Protect the world's deltas. *Nature* 516, 31–33. doi:10.1038/516031a
- Gong, J., Cao, E., Xie, Y., Xu, C., Li, H., and Yan, L. (2021). Integrating ecosystem services and landscape ecological risk into adaptive management: Insights from a Western mountain-basin area, China. *J. Environ. Manage.* 281, 111817. doi:10.1016/j.jenvman.2020.111817
- Goussen, B., Price, O. R., Rendal, C., and Ashauer, R. (2016). Integrated presentation of ecological risk from multiple stressors. *Sci. Rep.* 6, 36004. doi:10.1038/srep36004
- Grafius, D. R., Edmondson, J. L., Norton, B. A., Clark, R., Mears, M., Leake, J. R., et al. (2020). Estimating food production in an urban landscape. *Sci. Rep.* 10, 5141. doi:10.1038/s41598-020-62126-4
- Guida Johnson, B., and Zuleta, G. A. (2013). Land-use land-cover change and ecosystem loss in the Espinal ecoregion, Argentina. *Agric. Ecosyst. Environ.* 181, 31–40. doi:10.1016/j.agee.2013.09.002
- Imhoff, M. L., Bounoua, L., DeFries, R., Lawrence, W. T., Stutzer, D., Tucker, C. J., et al. (2004). The consequences of urban land transformation on net primary productivity in the United States. *Remote Sens. Environ.* 89, 434–443. doi:10.1016/j.rse.2003.10.015
- Jackson, M. V., Fuller, R. A., Gan, X., Li, J., Mao, D., Melville, D. S., et al. (2021). Dual threat of tidal flat loss and invasive *Spartina alterniflora* endanger important shorebird habitat in coastal mainland China. *J. Environ. Manage.* 278, 111549. doi:10.1016/j.jenvman.2020.111549
- Jat, M. K., Garg, P. K., and Khare, D. (2008). Modelling of urban growth using spatial analysis techniques: A case study of ajmer city (India). *Int. J. Remote Sens.* 29, 543–567. doi:10.1080/01431160701280983
- Jiang, W., Lv, J., Wang, C., Chen, Z., and Liu, Y. (2017). Marsh wetland degradation risk assessment and change analysis: A case study in the zoige plateau, China. *Ecol. Indic.* 82, 316–326. doi:10.1016/j.ecolind.2017.06.059
- Jiyuan, L., Zengxiang, Z., Xinliang, X., Wenhui, K., Wancun, Z., Shuwen, Z., et al. (2010). Spatial patterns and driving forces of land use change in China during the early 21st century. *J. Geogr. Sci.* 20, 483–494. doi:10.1007/s11442-010-0483-4
- Kim, J.-H., Kim, S.-Y., and Yoo, S.-H. (2021). South Koreans' willingness to pay for restoration of gomsoman tidal flat. *Ocean Coast. Manage.* 199, 105388. doi:10.1016/j.ocecoaman.2020.105388
- Kim, K.-L., and Ryu, J.-H. (2020). Mapping oyster reef distribution using kompsat-2/3 and linear spectral unmixing algorithm - a case study at hwangdo tidal flat. *J. Coast. Res.* 102, 246–253. doi:10.2112/SI102-030.1

- Kong, D., Miao, C., Wu, J., Jiang, L., and Duan, Q. (2015). Bi-Objective analysis of water-sediment regulation for channel scouring and delta maintenance: A study of the lower Yellow River. *Glob. Planet. Change* 133, 27–34. doi:10.1016/j.gloplacha.2015.07.007
- Li, H., Li, L., Su, F., Wang, T., and Gao, P. (2021a). Ecological stability evaluation of tidal flat in coastal estuary: A case study of Liaohe estuary wetland, China. *Ecol. Indic.* 130, 108032. doi:10.1016/j.ecolind.2021.108032
- Li, H., Peng, J., Yanxu, L., and Yi'na, H. (2017). Urbanization impact on landscape patterns in Beijing city, China: A spatial heterogeneity perspective. *Ecol. Indic.* 82, 50–60. doi:10.1016/j.ecolind.2017.06.032
- Li, Y., Mao, D., Wang, Z., Wang, X., Tan, X., Jia, M., et al. (2021b). Identifying variable changes in wetlands and their anthropogenic threats bordering the Yellow Sea for water bird conservation. *Glob. Ecol. Conservation* 27, e01613. doi:10.1016/j.gecco.2021.e01613
- Lin, J., Lin, M., Chen, W., Zhang, A., Qi, X., and Hou, H. (2021). Ecological risks of geological disasters and the patterns of the urban agglomeration in the Fujian Delta region. *Ecol. Indic.* 125, 107475. doi:10.1016/j.ecolind.2021.107475
- Lin, W., Cen, J., Xu, D., Du, S., and Gao, J. (2018). Wetland landscape pattern changes over a period of rapid development (1985–2015) in the ZhouShan Islands of Zhejiang province, China. *Estuar. Coast. Shelf Sci.* 213, 148–159. doi:10.1016/j.ecss.2018.08.024
- Lin, Y., Hu, X., Zheng, X., Hou, X., Zhang, Z., Zhou, X., et al. (2019). Spatial variations in the relationships between road network and landscape ecological risks in the highest forest coverage region of China. *Ecol. Indic.* 96, 392–403. doi:10.1016/j.ecolind.2018.09.016
- Liu, X., Liu, X., Wu, L., and Tian, Z. (2019). Diversity in phytoplankton communities: A field test of the intermediate disturbance hypothesis. *Ecol. Eng.* 129, 54–60. doi:10.1016/j.ecoleng.2018.12.009
- Liu, Y.-F., Ma, J., Wang, X.-X., Zhong, Q.-Y., Zong, J.-M., Wu, W.-B., et al. (2020). Joint effect of spartina alterniflora invasion and reclamation on the spatial and temporal dynamics of tidal flats in Yangtze River Estuary. *Remote Sens. (Basel)* 12, 1725. doi:10.3390/rs12111725
- Liu, Y., He, Q., Tan, R., Liu, Y., and Yin, C. (2016). Modeling different urban growth patterns based on the evolution of urban form: A case study from Huangpi, central China. *Appl. Geogr.* 66, 109–118. doi:10.1016/j.apgeog.2015.11.012
- Lubchenco, J., and Sousa, W. P. (2020). Joseph H. Connell (1923–2020). *Nature* 586, 670. doi:10.1038/d41586-020-02990-2
- Ma, Z., Chen, Y., David, S. M., Fan, J., Li, J., Dong, J., et al. (2019). Changes in area and number of nature reserves in China. *Conserv. Biol.* 33, 1066–1075. doi:10.1111/cobi.13285
- Ma, Z., Melville, D. S., Liu, J., Chen, Y., Yang, H., Ren, W., et al. (2014). Rethinking China's new great wall. *Science* 346, 912–914. doi:10.1126/science.1257258
- McEachran, Z. P., Slesak, R. A., and Karwan, D. L. (2018). From skid trails to landscapes: Vegetation is the dominant factor influencing erosion after forest harvest in a low relief glaciated landscape. *For. Ecol. Manage.* 430, 299–311. doi:10.1016/j.foreco.2018.08.021
- Molino, J. F., and Sabatier, D. (2001). Tree diversity in tropical rain forests: A validation of the intermediate disturbance hypothesis. *Science* 294, 1702–1704. doi:10.1126/science.1060284
- Murdoch, W. W., and Sousa, W. P. (2020). Joseph H. Connell (1923–2020). *Science* 370, 410. doi:10.1126/science.abe8992
- Murray, N. J., Phinn, S. R., DeWitt, M., Ferrari, R., Johnston, R., Lyons, M. B., et al. (2019). The global distribution and trajectory of tidal flats. *Nature* 565, 222–225. doi:10.1038/s41586-018-0805-8
- Osman, R. W. (2008). "Intermediate disturbance hypothesis," in *Encyclopedia of ecology*. Editors S. E. Jørgensen and B. D. Fath (Oxford: Academic Press), 1986–1994. doi:10.1016/B978-0-08-008045-0.4.00510-3
- Osman, R. W. (2015). "The intermediate disturbance hypothesis," in *Encyclopedia of ecology* (Second Edition), ed. B. Fath (Oxford: Elsevier), 441–450. doi:10.1016/B978-0-12-409548-9.09480-X
- Pace, M., Borg, J. A., Galdies, C., and Malhotra, A. (2017). Influence of wave climate on architecture and landscape characteristics of Posidonia oceanica meadows. *Mar. Ecol. Berl.* 38, e12387. doi:10.1111/maec.12387
- Paul, K. I., Polglase, P. J., Nyakuengama, J. G., and Khanna, P. K. (2002). Change in soil carbon following afforestation. *For. Ecol. Manage.* 168, 241–257. doi:10.1016/S0378-1127(01)00740-X
- Plexida, S. G., Sfougaris, A. I., Ispikoudis, I. P., and Papanastasis, V. P. (2014). Selecting landscape metrics as indicators of spatial heterogeneity-A comparison among Greek landscapes. *Int. J. Appl. Earth Obs. Geoinf.* 26, 26–35. doi:10.1016/j.jag.2013.05.001
- Pranzini, E., Cinelli, I., Cipriani, L. E., and Anfuso, G. (2020). An integrated coastal sediment management plan: The example of the tuscany region (Italy). *JMSE* 8, 33. doi:10.3390/jmse8010033
- Ralston, D. K., and Geyer, W. R. (2009). Episodic and long-term sediment transport capacity in the Hudson River Estuary. *Estuaries Coasts* 32, 1130–1151. doi:10.1007/s12237-009-9206-4
- Ran, P., Hu, S., Frazier, A. E. E., Qu, S., Yu, D., and Tong, L. (2022). Exploring changes in landscape ecological risk in the Yangtze River Economic Belt from a spatiotemporal perspective. *Ecol. Indic.* 137, 108744. doi:10.1016/j.ecolind.2022.108744
- Russel, F., and Alexandre, F. (2021). Landscape ecological enhancement and environmental inequalities in peri-urban areas, using flora as a socio-ecological indicator-The case of the greater Paris area. *Landsc. Urban Plan.* 210, 104062. doi:10.1016/j.landurbplan.2021.104062
- Sasaki, T., Okubo, S., Okayasu, T., Jamsran, U., Ohkuro, T., and Takeuchi, K. (2009). Management applicability of the intermediate disturbance hypothesis across Mongolian rangeland ecosystems. *Ecol. Appl.* 19, 423–432. doi:10.1890/08-0144.1
- Shen, F., Zhou, Y., Li, J., He, Q., and Verhoef, W. (2013). Remotely sensed variability of the suspended sediment concentration and its response to decreased river discharge in the Yangtze estuary and adjacent coast. *Cont. Shelf Res.* 69, 52–61. doi:10.1016/j.csr.2013.09.002
- Skilleter, G. A., Loneragan, N. R., Olds, A., Zharikov, Y., and Cameron, B. (2017). Connectivity between seagrass and mangroves influences nekton assemblages using nearshore habitats. *Mar. Ecol. Prog. Ser.* 573, 25–43. doi:10.3354/meps12159
- Strayer, D. L., Beighley, R. E., Thompson, L. C., Brooks, S., Nilsson, C., Pinay, G., et al. (2003). Effects of land cover on stream ecosystems: Roles of empirical models and scaling issues. *Ecosystems* 6, 407–423. doi:10.1007/pl00021506
- Sun, X., Li, Y., Zhu, X., Cao, K., and Feng, L. (2017). Integrative assessment and management implications on ecosystem services loss of coastal wetlands due to reclamation. *J. Clean. Prod.* 163, S101–S112. doi:10.1016/j.jclepro.2015.10.048
- Tang, L., Wang, L., Li, Q., and Zhao, J. (2018). A framework designation for the assessment of urban ecological risks. *Int. J. Sustain. Dev. World Ecol.* 25, 387–395. doi:10.1080/13504509.2018.1434570
- Tian, P., Cao, L., Li, J., Pu, R., Liu, Y., Zhang, H., et al. (2022). Ecosystem stability assessment of Yancheng coastal wetlands, a world natural heritage site. *Land* 11, 564. doi:10.3390/land11040564
- Walling, D. E. (2006). Human impact on land-ocean sediment transfer by the world's rivers. *Geomorphology* 79, 192–216. doi:10.1016/j.geomorph.2006.06.019
- Wang, H., Liu, X., Zhao, C., Chang, Y., Liu, Y., and Zang, F. (2021). Spatial-temporal pattern analysis of landscape ecological risk assessment based on land use/land cover change in Baishuijiang National nature reserve in Gansu Province, China. *Ecol. Indic.* 124, 107454. doi:10.1016/j.ecolind.2021.107454
- Wang, H., Wu, X., Bi, N., Li, S., Yuan, P., Wang, A., et al. (2017). Impacts of the dam-orientated water-sediment regulation scheme on the lower reaches and delta of the Yellow River (huanghe): A review. *Glob. Planet. Change* 157, 93–113. doi:10.1016/j.gloplacha.2017.08.005
- Wang, J.-F., Zhang, T.-L., and Fu, B.-J. (2016). A measure of spatial stratified heterogeneity. *Ecol. Indic.* 67, 250–256. doi:10.1016/j.ecolind.2016.02.052
- Wang, J., Li, X., Christakos, G., Liao, Y., Zhang, T., Gu, X., et al. (2010). Geographical detectors-based health risk assessment and its application in the neural tube defects study of the heshun region, China. *Int. J. Geogr. Inf. Sci.* 24, 107–127. doi:10.1080/13658810802443457
- Wang, L., Wang, S., Zhou, Y., Zhu, J., Zhang, J., Hou, Y., et al. (2020). Landscape pattern variation, protection measures, and land use/land cover changes in drinking water source protection areas: A case study in danjiangkou reservoir, China. *Glob. Ecol. Conserv.* 21, e00827. doi:10.1016/j.gecco.2019.e00827
- Wei, W., Dai, Z., Pang, W., Wang, J., and Gao, S. (2020). Sedimentary zonation shift of tidal flats in a meso-tidal estuary. *Sediment. Geol.* 407, 105749. doi:10.1016/j.sedgeo.2020.105749
- Winkler, K., Fuchs, R., Rounsevell, M., and Herold, M. (2021). Global land use changes are four times greater than previously estimated. *Nat. Commun.* 12, 2501. doi:10.1038/s41467-021-22702-2
- Xie, W., Wang, X., Guo, L., He, Q., Dou, S., and Yu, X. (2021). Impacts of a storm on the erosion process of a tidal wetland in the Yellow River Delta. *Catena* 205, 105461. doi:10.1016/j.catena.2021.105461
- Xu, J., and Kang, J. (2017). Comparison of ecological risk among different urban patterns based on system dynamics modeling of urban development. *J. Urban Plan. Dev.* 143, 04016034. doi:10.1061/(ASCE)UP.1943-5444.0000365
- Xu, K., Bentley, S. J., Day, J. W., and Freeman, A. M. (2019). A review of sediment diversion in the Mississippi River Deltaic Plain. *Estuar. Coast. Shelf Sci.* 225, 106241. doi:10.1016/j.ecss.2019.05.023

- Yang, D., Zhang, P., Jiang, L., Zhang, Y., Liu, Z., and Rong, T. (2022). Spatial change and scale dependence of built-up land expansion and landscape pattern evolution—case study of affected area of the lower Yellow River. *Ecol. Indic.* 141, 109123. doi:10.1016/j.ecolind.2022.109123
- Yao, H. (2013). Characterizing landuse changes in 1990–2010 in the coastal zone of Nantong, Jiangsu province, China. *Ocean Coast. Manag.* 71, 108–115. doi:10.1016/j.ocecoaman.2012.09.007
- Yu, D., Han, G., Wang, X., Zhang, B., Eller, F., Zhang, J., et al. (2021). The impact of runoff flux and reclamation on the spatiotemporal evolution of the Yellow River estuarine wetlands. *Ocean. Coast. Manag.* 212, 105804. doi:10.1016/j.ocecoaman.2021.105804
- Yu, X., and Zhang, L. (2020). *Green paper of China's coastal wetland conservation*. Beijing, China: Science Press.
- Zhan, J., Zhang, F., Chu, X., Liu, W., and Zhang, Y. (2019). Ecosystem services assessment based on emergy accounting in Chongming Island, Eastern China. *Ecol. Indic.* 105, 464–473. doi:10.1016/j.ecolind.2018.04.015
- Zhang, S., Zhong, Q., Cheng, D., Xu, C., Chang, Y., Lin, Y., et al. (2022). Landscape ecological risk projection based on the PLUS model under the localized shared socioeconomic pathways in the Fujian Delta region. *Ecol. Indic.* 136, 108642. doi:10.1016/j.ecolind.2022.108642
- Zhang, X., Wang, G., Xue, B., Zhang, M., and Tan, Z. (2021). Dynamic landscapes and the driving forces in the Yellow River Delta wetland region in the past four decades. *Sci. Total Environ.* 787, 147644. doi:10.1016/j.scitotenv.2021.147644
- Zhang, Y., Wang, T., Cai, C., Li, C., Liu, Y., Bao, Y., et al. (2016). Landscape pattern and transition under natural and anthropogenic disturbance in an arid region of northwestern China. *Int. J. Appl. Earth Obs. Geoinf.* 44, 1–10. doi:10.1016/j.jag.2015.06.013
- Zhao, Y., Liu, Q., Huang, R., Pan, H., and Xu, M. (2020). Recent evolution of coastal tidal flats and the impacts of intensified human activities in the modern radial sand ridges, east China. *Int. J. Environ. Res. Public Health* 17, 3191. doi:10.3390/ijerph17093191
- Zhou, Y., Dou, Y., Yu, X., Zhang, L., Huang, C., Wang, Y., et al. (2020). Examining health of wetlands with multiple ecosystem services as targets in China's coastal regions. *Chin. Geogr. Sci.* 30, 600–613. doi:10.1007/s11769-020-1137-9
- Zhou, Y., Ning, L., and Bai, X. (2018). Spatial and temporal changes of human disturbances and their effects on landscape patterns in the Jiangsu coastal zone, China. *Ecol. Indic.* 93, 111–122. doi:10.1016/j.ecolind.2018.04.076
- Zucker, E., Gvirtzman, Z., Granjeon, D., Garcia-Castellanos, D., and Enzel, Y. (2021). The accretion of the Levant continental shelf alongside the Nile Delta by immense margin-parallel sediment transport. *Mar. Petroleum Geol.* 126, 104876. doi:10.1016/j.marpetgeo.2020.104876



OPEN ACCESS

EDITED BY

Cletah Shoko,
University of the Witwatersrand, South
Africa

REVIEWED BY

Polina Lemenkova,
Université libre de Bruxelles, Belgium
Gui Jin,
China University of Geosciences Wuhan,
China

*CORRESPONDENCE

Rajendra Kr Joshi,
✉ rajendrkrjo@gmail.com
Rajman Gupta,
✉ rajmangupta61@gmail.com

SPECIALTY SECTION

This article was submitted to
Environmental Informatics and
Remote Sensing,
a section of the journal
Frontiers in Environmental Science

RECEIVED 13 December 2022

ACCEPTED 11 January 2023

PUBLISHED 19 January 2023

CITATION

Gupta R, Sharma M, Singh G and Joshi RK
(2023), Characterizing urban growth and
land surface temperature in the western
himalayan cities of India using remote
sensing and spatial metrics.
Front. Environ. Sci. 11:1122935.
doi: 10.3389/fenvs.2023.1122935

COPYRIGHT

© 2023 Gupta, Sharma, Singh and Joshi.
This is an open-access article distributed
under the terms of the [Creative Commons
Attribution License \(CC BY\)](https://creativecommons.org/licenses/by/4.0/). The use,
distribution or reproduction in other
forums is permitted, provided the original
author(s) and the copyright owner(s) are
credited and that the original publication in
this journal is cited, in accordance with
accepted academic practice. No use,
distribution or reproduction is permitted
which does not comply with these terms.

Characterizing urban growth and land surface temperature in the western himalayan cities of India using remote sensing and spatial metrics

Rajman Gupta*, Mani Sharma, Garima Singh and Rajendra Kr Joshi*

School of Environmental Sciences, Jawaharlal Nehru University, New Delhi, India

Urban heat islands (UHI) are developing due to increasing urbanization and loss of vegetation in major cities in India. Increased urbanization modifies the urban microclimate that leads to significant land-use changes resulting in surface conversion and heat release, which poses serious risks to human health, environment and the ecosystem of the Himalayan ecosystem. Hence, mitigating UHI becomes important and requires a better understanding of underlying associated biophysical processes. In the study an attempt has been made to demonstrate the impact of urbanization on land surface temperature (LST) in Shimla and Dehradun, capitals of the Western Himalayan states, India using satellite data and spatial metrics. The process was analyzed using urban coverage patterns obtained from Landsat 5, 7, and 8 and corresponding sensors from TM, ETM⁺, and OLI. The Built-up and Non-Built-up areas were extracted and the biophysical parameters NDVI, NDBI, NDWI and LST were calculated to capture different features of urban growth. The result indicated, that the built-up area increased from 32.19 km² (2000) to 68.37 km² (2016) in Dehradun and from 12.38 km² (2000) to 29.47 km² (2016) in Shimla during the study period, resulting in an increase in NDBI and LST and Reduction and NDVI and NDWI. Results showed that temperature hotspots were largest in urban areas, followed by vegetation and water bodies. A significant correlation ($p < 0.05$) was observed between LST and biophysical parameters -NDVI, NDBI, NDWI. Spatial metrics at the class and landscape levels show that increased urban growth from 2000 to 2016 has made the landscape fragmented and more heterogeneous. The Identified trends and changes in landscape patterns and their impact on heterogeneous urban areas suggest that the study is feasible to estimate LST, NDVI, NDBI and NDWI with reasonable accuracy that will likely have influence on policy interventions.

KEYWORDS

urban sprawl, normalized difference vegetation index (NDVI), normalized difference water index (NDWI), normalized difference built-up index (NDBI), land surface temperature (LST), spatial metrics

1 Introduction

An increase in surface temperature on account of the reduction in vegetated surface and its conversion into impervious surfaces in urban areas is one of the most pressing issues cities confront nowadays (Mallick et al., 2008). These changes affect numerous aspects of cities, including land use, transportation, infrastructure and the environment (Weng et al., 2004;

Mallick et al., 2008). Urbanization being a global process and is occurring at an escalating rate in developing countries and continuously modifying the land use pattern (Sharma and Joshi, 2012). Increased urbanization contributes to environmental degradation, one of the primary drivers of climate change (Chen et al., 2006; McCarthy et al., 2010). Large-scale urbanization has a distorting effect on the climate in cities and the areas around them (Liu et al., 2018). Conversion of vegetated surfaces to urban land use categories and urban areas experienced an increase in surface temperature and on the verge of developing urban heat islands (Giridharan et al., 2004; Neteler, 2010; Ogashawara and Bastos, 2012; Grover and Singh, 2015).

An important factor in comprehending the land-surface process at both the regional and global scales is the land surface temperature (LST), which serves as a primary indication of the Earth's energy balance (Dewan et al., 2009; Peng et al., 2018). LST is influenced by vegetation and the amount of water in the soil, which provide important information about how numerous environmental systems are operating (Weng et al., 2004; Rashid et al., 2022). Using meteorological data to predict long-term land surface temperature (LST) change is challenging because of the insufficient and sparse availability of meteorological stations in these regions (Zhou et al., 2019). Remote sensing has proved to be one of the vital technologies for providing valuable information such as temporal land cover change analysis and risk analysis at various scales (Punia and Singh, 2012; Guha et al., 2020) and modeling the urban growth patterns (Bhatta, 2009). Satellite images are frequently utilizing to investigate the rate and scope of urbanization on a global and regional scale (Keles et al., 2007; Mishra et al., 2020; Ashwini and Sil, 2022). It provides more detailed view of the human landscape (Carlson, 2003) when superimposed on demographic or geographic data (Joshi et al., 2001; Roy and Tomar, 2001; Rawat and Kumar, 2015).

Several researches have been conducted on assessing the urban built-up and the relationship of NDVI, NDWI, NDBI on LST in foreign nations. There have not been many studies done in India, and those that have been done have primarily focused on megacities like Delhi (Mallick et al., 2013), Mumbai (Grover and Singh, 2015), Chennai (Lilly Rose and Devadas, 2009), Jaipur (Jalan and Sharma, 2014), Bangalore (Ramachandra et al., 2012b), and Hyderabad (Wakode et al., 2014). In the Himalayan foothills, new urban areas are growing at the expense of agricultural and forested land, changing the region's environment (Munsi et al., 2009). However, a few studies have been conducted for cities in the Himalayan region that determined the degree of relationship between water, vegetation, and built-up areas on LST (Kuldeep and Kamlesh, 2011; Pal and Ziaul, 2017). These human activities have resulted into modification of the environment and consequent habitat loss and fragmentation of landscape (Midha et al., 2010). The anthropogenically caused urban development patterns and their effects on forest health are characterized by means of landscape metrics (Munsi et al., 2010; Srinivasan et al., 2022). Many scholars have used landscape spatial analysis in conjunction with geographic information systems as a useful method for tracking urban planning and growth (Pham and Yamaguchi, 2011; Triantakoustantis and Stathakis, 2015; Annes et al., 2018).

Therefore, it's become critical to minimize the rise in land surface temperature and consequent emergence of UHI through monitoring and implementing appropriate land-use plans. In view of this, the present study examines the relationship between surface biophysical

parameters and surface temperature variation (LST) which have occurred in the mountain regions in the past few decades, and also to estimate the role played by the urbanization on LST in space and time. The study is primarily focused on the dynamics of urban growth using Landsat TM, ETM, OLI satellite data and spatial metrics for two Indian Himalayan cities Dehradun and Shimla from 2000 to 2016. These two cities have witness drastic changes in land use categories primarily on account of increased built-up areas, conversion of agriculture and forest land, and economic developmental projects in the last 2–3 decades. Moreover, we assessed how vegetation (NDVI), Hydrology (NDWI) and Built-up (NDBI) have an impact on LST. Spatial and temporal fragmentation of these two cities have also been studied using landscape metrics to quantify the structure of the landscape. The findings of this study may prove beneficial for city planners and policymakers for the sustainable management of these two Himalayan cities.

2 Material and methodology

2.1 Study area

Dehradun, the capital of Uttarakhand, is 450 m above sea level and situated in the Doon valley in the Garhwal region of northern India between the latitudes of 29°58'N and 31°2'N and 77°34'E and 78°18'E. (Figure 1). The area is home to important national parks and wildlife refuges such Rajaji National Park, Benog Wildlife Sanctuary, and Asan Conservation Reserve. It falls within the category of a humid subtropical climate. While the average winter temperature ranges from 1–20°C, the summer temperature can reach 44°C for a few days. Dehradun had 1,696,694 residents in 2011 according to the census conducted in India (<http://censusindia.gov.in>). The state of Himachal Pradesh in northern India, which is situated in the foothills of the Himalayas, has Shimla as its capital. Seven distinct hills in total comprise Shimla and is located between 31.61 N and 77.10 E. The district, which is located at an elevation of 2206 m and is surrounded by Mandi, Kullu, Kinnaur, and Uttarakhand state (Figure 1). According to the Koppen's climate classification, it has a subtropical highland climate. In the summer, the average temperature ranges from 19°C–28°C, and in the winter, it ranges from –1–10°C. Shimla city had an estimated 814,010 residents as per the 2011 India census (<http://censusindia.gov.in>). The two cities being states capitals and also a tourist place have undergone remarkable changes in land use categories resulting into conversion of forested and agriculture lands into built-up areas. This necessitated having a scientific understanding of current land use categories so as to formulate proper policy framework for sustainable management of the two Himalayan cities.

2.2 Acquisition of satellite data

The United States Geological Survey (USGS) Earth Explorer (<http://earthexplorer.usgs.gov/>) was used to collect data for the Landsat series satellites over a 16-year period (2000–2016). Table 1 lists the path/row and other characteristics of the satellite data. Landsat data were chosen because of their wider availability in the public domain-spatially and temporally at medium resolution besides containing thermal bands that were used in calculating land surface

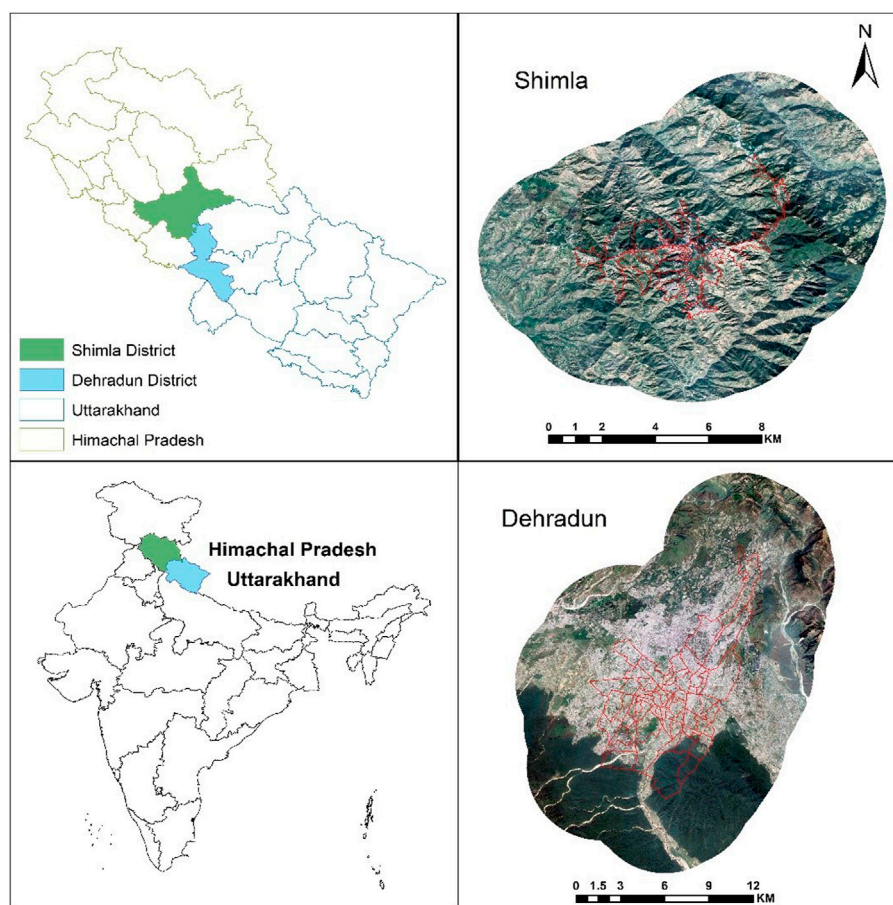


FIGURE 1
Study area location map with buffer zone of 5 Km.

TABLE 1 List of cities with specifications of satellite data.

City	Date	Satellite/Sensor	Path/Row	Resolution (m)
Dehradun	25-Nov-2000	Landsat 7/ETM+	146/39	30
Shimla	15-Oct-2000	Landsat 7/ETM+	147/38	30
Dehradun	12-Oct-2008	Landsat 5/TM	146/39	30
Shimla	15-Oct-2008	Landsat 5/TM	147/38	30
Dehradun	12-Oct-2016	Landsat 8/OLI	146/39	30
Shimla	04-Nov-2016	Landsat 8/OLI	147/38	30

temperature to understand urban dynamics and thermal behavior of the environment focusing on surface physical characteristics in the form of temperature. Google Earth images were additionally employed in the study for visual interpretation and confirmation.

2.3 Image processing

Satellite data when taken has some form of errors associated with it. This error should be removed by using appropriate algorithms for scene matching and change detection analysis. Satellite data

pre-processing include atmospheric correction, geometric correction, and radiometric correction. The acquired data were geometrically and atmospherically corrected and layer stacked using ERDAS IMAGINE 9.1. The boundary layer of Shimla and Dehradun city was procured and a buffer of 5 km was created and clipped for each image from their respective stacked images using the Arc GIS 10.3. Later on and false color composite (FCC) images were created. All the clipped images were classified using the unsupervised nearest neighborhood classification technique wherein the software dispartate a large number of obscure pixels based on the reflectance values into classes without direction from the user (Tou Gonzalez,

1974). The statistical groupings in the data were controlled by a clustering algorithms application. Each image was divided into five classes: forest, agriculture, open land, water body, and urban area. The classified images were afterwards adjusted with Google Earth, recoded with the ERDAS recode option, and then divided into two classes, Built-up and Non-Built up areas. According to the following equations, biophysical parameters including LST, NDVI, NDWI, and NDBI as well as spatial matrices were calculated.

2.4 Calculation of LST from thermal bands

2.4.1 Conversion from DN to spectral radiance (L_λ)

Every object above absolute zero (K), emits electromagnetic radiation in the form of Thermal Energy. Spectral radiance was calculated using Eq. 1 (Landsat Project Science Office, 2002; Chander et al., 2009).

$$L_\lambda = \text{Gain} \times \text{DN} + \text{Bias} = \left(\frac{L_{\max} - L_{\min}}{255} \right) \times \text{DN} + \text{Bias} \quad (1)$$

where, Gain = Slope of radiance/DN conversion function, L_λ = Spectral radiance at the sensor's aperture ($\text{Wm}^{-2}\text{sr}^{-1}\mu\text{m}^{-1}$), Bias = L_{\min} , L_{\max} and L_{\min} = Spectral radiance maximum and minimum for band 6 at DN 0 and 255 respectively (obtained from the metadata file), DN = digital number or pixel value or brightness value.

2.4.2 Conversion of radiance to top of atmosphere reflectance (TOA)

The depletion in between-scene variability was achieved by the normalization process for solar irradiance by changing spectral radiance to the top of atmosphere reflectance. The combined surface and atmospheric reflectance of the image was calculated following Eq. 2 (Chander et al., 2009).

$$\rho_p(\lambda_i) = \frac{\pi \times d^2 \times L_\lambda}{\text{ESUN} \times \cos \theta} \quad (2)$$

where, $\rho_p(\lambda_i)$ = Planetary TOA reflectance, L_λ = spectral radiance at the sensor's aperture, d = Earth-Sun distance in astronomical units (0.9967616), ESUN = Mean Exoatmospheric solar irradiance and θ = solar zenith angle in degrees (45.240).

2.4.3 Calculation of at-sensor brightness

The effective at-sensor brightness temperature (T_b) also known as black body temperature was derived from the spectral radiance using Planck's inverse function. At-sensor brightness temperature under the assumption of uniform emissivity was calculated following (Weng and Lu, 2008).

$$T_b = \frac{K_2}{\ln\left(\frac{K_1}{L_\lambda} + 1\right)} \quad (3)$$

Where, T_b = brightness temperature in Kelvin, L_λ = radiance of thermal band and K_1 and K_2 are the pre-launched calibration constants.

2.4.4 Calculation of NDVI

For calculation of LST, emissivity corrected images were required which were calculated using a modified NDVI threshold method using Eq. 4 (Sobrino et al., 2004).

$$\text{NDVI} = \frac{\lambda_{\text{NIR}} - \lambda_{\text{RED}}}{\lambda_{\text{NIR}} + \lambda_{\text{RED}}} \quad (4)$$

where, λ_{NIR} = Wavelength of NIR band (band 4 of TM and ETM + and OLI band 5) and λ_{RED} = Wavelength of Red band (band 3 of TM and ETM + and OLI band 4)

Values between 0 and 1 indicate vegetation cover, nearer to 1 indicate higher vegetation density.

2.4.5 Emissivity correction

The temperature readings from above are expressed in terms of a black body. As a result, spectral emissivity (ϵ) modifications were required based on the kind of land cover. The thermal band data was transformed from effective at-sensor brightness temperature to at-sensor spectral radiance. Therefore, emissivity effects are taken into account if the Earth's surface is a blackbody and includes air effects (absorption and emission along the path). The method for emissivity adjustment that is most frequently employed is the NDVI threshold method. Using a spatial model maker in the ERDAS, the NDVI generated pictures were applied for the emissivity adjustment.

2.4.6 Calculation of LST from emissivity

The land surface temperature was calculated using Eq. 5 (Artis and Carnahan., 1982)

$$\text{LST} = \frac{T_b}{\ln \epsilon \left(\frac{\sigma T_b}{hc} \right) + 1} \quad (5)$$

where, T_b = Brightness temperature, ϵ = Final Emissivity, λ = Effective wavelength, σ = Boltzmann constant (1.38×10^{-23} J/K), h = Planck's constant (6.626×10^{-24} Js) and c = velocity of light in vacuum (2.998×10^8 m/s).

Finally, to comprehend easily, the derived LST was converted to $^{\circ}\text{C}$ using the relation $0^{\circ}\text{C} = 273.15$ K.

2.5 Normalized difference built-up index (NDBI)

NDBI automatically maps built-up features of urban areas which were computed following the method devised by Zha et al., 2003). The method takes advantage of the spectral feature of built-up areas and other land covers (He et al., 2010).

$$\text{NDBI} = \frac{\lambda_{\text{MIR}} - \lambda_{\text{NIR}}}{\lambda_{\text{MIR}} + \lambda_{\text{NIR}}} \quad (6)$$

Where, λ_{NIR} and λ_{MIR} are the wavelengths of Near-Infrared (TM band 4, ETM + band 4 and OLI band 5) and Middle Infrared band (TM band 5, ETM + band 7 and OLI band 6) respectively.

2.6 Normalize difference water index (NDWI)

NDWI is an index that estimates the moisture content of the vegetation canopy. It uses two NIR channels (Gao et al., 1996). It provides important information regarding the conversion of a vegetated area to a non-vegetated area.

$$\text{NDWI} = \frac{\lambda_{\text{NIR}} - \lambda_{\text{SWIR}}}{\lambda_{\text{NIR}} + \lambda_{\text{SWIR}}} \quad (7)$$

TABLE 2 Details of class and landscape level metrics used in the study, following (McGarigal, 2015).

Metrics	Formula	Range	Description
Edge Density	$ED = \frac{\sum_{k=1}^m e_{ik}}{A} (10,000)$ (class level) or $ED = \frac{E}{A} (10,000)$ (landscape level)	ED > 0, No limit	ED equals the sum of the lengths (m) of all edge segments involving the corresponding patch type (class level) or the landscape level divided by the total landscape area (m ²), multiplied by 10,000 to convert into hectare. Higher value indicate the increasing fragmentation of corresponding class
	e_{ik} = total length (m) of edge in landscape involving patch type (class) i; includes landscape boundary and background segments involving patch type i		
	E = total length (m) of edge in landscape A = total landscape area (m ²)		
Contiguity Index	$CONTIG = \frac{\sum_{r=1}^z c_{ijr} - 1}{V - 1}$	0 ≤ CONTIG ≤ 1	CONTIG equals the average contiguity value for the cells in a patch minus 1, divided by the sum of the template value minus 1. It assesses the spatial connectedness, of cells within a grid-cell patch to provide an index on patch boundary configuration and thus shape (LaGro 1991)
	C_{ijr} = Contiguity value for pixel r in patch ij, V = Sum of the value in 3 by 3 cell template a_{ij} = area of patch ij in terms of number of cells		
Total Edge	$TE = \sum_{k=1}^m e_{ik}$	TE > 0 Without limits	TE equal the sum of the lengths (m) of all edge segments involving the corresponding patch type. TE at class level is an absolute measure of the total edge length of a particular patch type
	E_{ik} = total length (m) of edge in landscape involving patch type (class) i, includes landscape boundary and background segments involving patch type i		
Perimeter area ratio	$PARA = \frac{P_{ij}}{a_{ij}}$	PARA > 0	PARA equals the ratio of the patch perimeter (m) to area (m). It is measures of shape complexity
	Pi = perimeter (m) of patch ij		
	a _{ij} = area (m) of patch of ij	No limits	
Shape Index	$SHAPE = 0.25 \frac{P_{ij}}{\sqrt{a_{ij}}}$	SHAPE ≥ 1 Without limits	SHAPE equals patch perimeter (m) divided by the square roots of patch area (m ²), adjusted by a constant for a square standard. It is 1 when the patch is square and increases without limit as patch shape becomes more irregular
	Pi = perimeter (m) of patch ij		
	a _{ij} = area (m) of patch of ij		
Shannon's Diversity	$SHDI = -\sum_{i=1}^m (P_i \ln P_i)$	SHDI ≥ 0 No limit	SHDI equal minus times the sum, across all patch types, of the proportional abundance of each patch type multiplied by that proportion. Higher value indicates higher landscape diversity
	Pi = Proportion of the landscape occupied by class i, m = NP types (classes) present in the landscape		
Simpson's Diversity	$SIDI = 1 - \sum_{i=1}^m P_i^2$	0 ≤ SIDI < 1	SIDI equals 1 minus the sum, across all patch types, of the proportional abundance of each patch type squared. It is 0 when the landscape contains only 1 patch. SIDI approaches 1 as the number patch types increases and the proportional distribution of area among patch type become more equitable
	Pi = Proportion of the landscape occupied by patch type (class) i		
Simpson's Evenness Index	$SIEI = \frac{1 - \sum_{i=1}^m P_i^2}{1 - (\frac{1}{m})}$	0 ≤ SIEI ≤ 1	SIEI equals 1 minus the sum, across all patch types, of the proportional abundance of each patch types squared, divided by the number of patch types. It is expressed such that an even distribution of area among patch types results in maximum evenness
	Pi = Proportion of the landscape occupied by patch type (class) i		
	m = number of patch types (classes) present in the landscape, excluding the landscape border if present		

Where, λ_{NIR} and λ_{SWIR} are the wavelengths of the near-infrared (band 4 of TM and ETM + and OLI band 5) and short-wave infrared (band 5 of TM and ETM + and OLI band 6) band respectively.

2.7 Degree of association between NDBI, NDVI, NDWI and LST

More than 100 points from the LST image were randomly picked, and the NDVI, NDBI, and NDWI values associated with those points were calculated in order to assess the association between LST and

these metrics. Analysis of correlations between LST values and each biophysical parameter's related values was done. Additionally, regression analysis for NDVI, NDBI, and NDWI was performed to determine how variations in land-use intensity through time and space affect LST.

2.8 Spatial metrics analysis

Spatial metrics are a crucial tool for measuring and quantifying urban sprawl (Herold et al., 2005) and have been used to explicitly

capture spatial variation and the morphological aspects of urban formations (Herold et al., 2003; Prastakos et al., 2012). It is a spatial pattern analysis application for quantifying landscape structure, created for category maps to work with geospatial data and assist the user in categorizing landscape patterns and metrics as well as identifying the region where land use activities have led to fragmentation (Martin Balej, 2012). At the patch, class, and landscape levels in landscape ecology, spatial metrics measures offer valuable numerical descriptions (Yu and Ng, 2006; Martin Balej, 2012; McGaral, 2013). Utilizing FRAGSTATS 4.2 (McGaral and Mark, 1995), landscape metrics were computed at the landscape and class level to better understand the factors influencing urban transitions. Altogether six metrics were used for landscape-level (Table 2) namely Total Edge (TE), Edge density (ED), Shape Index (SHAPE), Shannon's index (SHDI) (Shannon and Weaver, 1949), Simpson's index (SIDI), Simpson's Evenness Index (SIEI) and five metrics at class level namely Contiguity Index (CONTIG), Perimeter area ratio (PARA), Edge density (ED), Total Edge (TE) and shape index (SHAPE) are computed to know land-use changes which can be correlated with the degree of urbanization (Dasgupta et al., 2009). The specified parameters are helpful in locating the primary factors that represent urban dynamics. Edge density (ED) is the length of the edge per unit area. The best way to think of edge metrics is as a representation of the landscape. CONTID is used to create the landscape aggregate (Herold et al., 2002). The total number of edges in a landscape is correlated with its level of spatial variability. The shape index (SI) measures the complexity of the patch shape with a standard shape. Landscape composition is quantified through diversity measures. SHDI, SIDI and SIEI were computed to understand the fragmentation because of urban sprawl (Joshi et al., 2006; Fenta et al., 2017). Simpson's index gives the likelihood that any two patches when selected at random will be of different types. The higher the SIDI value, the greater would be the diversity.

2.9 Method adopted for validation

500 testing points that were uniformly dispersed over the whole region of interest chosen at random and used to evaluate the accuracy of the data. These measurement locations points were employed for each time period, NDBI, NDVI, NDWI, built-up and non-built-up conditions. A field survey and Google Earth were used as the foundation for the validation. We estimated overall accuracy (Story and Congalton, 1986) for validation as we had two classes to validate. The overall accuracy was computed as overall accuracy (%) = Number of correct samples/total samples \times 100% (Congalton and Green, 1999). Based on the meteorological station data obtained from the World Meteorological Station Climate Explorer data (<https://climexp.knmi.nl/start.cgi>), the Land Surface Temperature Model for both Dehradun and Shimla was validated. The daily temperature data was selected for October and November for the years 2000, 2008 and 2016 and compared against the mean temperature derived from the land surface temperature model. The LST model was also verified from the climate research unit (CRU) time series high resolution ($0.5^\circ \times 0.5^\circ$) gridded temperature datasets (Harris et al., 2020). The monthly temperature data from the CRU was retrieved for the respective month and year of satellite data collection and compared against the mean LST model derived temperature.

3 Result and discussion

3.1 Land cover change analysis

Considering the interest of the study two classes i.e. built-up and Non-built up have been generated for the two cities. Dehradun has ascribed the conversion of non-urban regions including forests, grasslands, fallow land, and agricultural land to built-up areas over a sixteen-year period to an increase in population (Figure 2A). The area that was considered to be urbanized in 2000 was 32.19 km², and that area expanded to 55.94 km² in 2008 and then to 68.37 km² in 2016. In the city's center, the built-up area became more concentrated. The sprawl surrounding the city's center continued in 2008 and reached the outside of the city limits. Urban areas clearly grew between 2000 and 2008, which is linked to the rise in population. However, in 2016 both the central city and the surrounding areas saw a concentration of urban expansion. The center of the city now has a higher concentration of built-up areas. Shimla's urban sprawl map divides the area into two categories: built-up and non-built-up (Figure 2B). The built-up area underwent a leapfrogging effect between 2000 and 2008, which indicates a quick transformation. The pattern of urbanization has become more dispersed and less concentrated throughout the central area. Urbanization was calculated for an area of 12.38 km² in 2000. By 2008, that area had nearly doubled to 23.63 km², and by 2016, it had grown even more to 29.47 km². Several studies in the Himalaya highlighted similar changes in land use land cover changes by Gautam et al. (2002); Mishra et al. (2020); Ashwini and Sil, (2022). Bhatt et al. (2017) have also found significant land use changes to urban area during 2004–2014 in the Dehradun city resulting in sharp decline in agriculture, fallow and vacant land.

Based on a random selection of 500 testing points for each city and time period, the accuracy of the classified images, LST, and other biophysical parameters such as NDVI, NDBI, and NDWI were verified and compared. Overall accuracy was determined to be 93.2% (2000), 94.8% (2008), and 96.7% (2016) for Dehradun and Shimla, respectively, and to be 95% (2000), 96.6% (2008), and 97% (2016) for Dehradun. Overall NDVI accuracy was found to be 92.72% (2000), 94.72% (2008), and 95.81% (2016) for Dehradun, and 95.2% (2000), 93.4% (2008), and 92.2% (2016) for Shimla. In terms of overall accuracy, NDBI was reported to be 91.81% in 2000, 96.18% in 2008, and 95.27% in 2016. For Shimla, it was 96% in 2000, 94.4% in 2008, and 94.2% in 2016. The NDWI accuracy for Dehradun was 95.81% (2000), 96.72% (2008), and 96.54% (2016), and that it was 92.8% (2000), 92.4% (2008), and 93.6% (2016) for Shimla. The accuracy of the classified map shows increasing trend over time for both the cities possibly because of the availability of higher resolution imageries in recent times. The Pearson's correlation between the temperature deduced from LST and the daily temperature data for October and November was calculated for LST validation and assessed at the 0.01 level of significance. Dehradun's correlation coefficient values were determined to be 0.4602, 0.562, and 0.634 in 2000, 2008, and 2016 correspondingly, while Shimla's values were 0.485, 0.62, and 0.586 in those same years. At the 0.01 level, each of these values was significant. Additionally, a 2–4°C temperature disparity was noted between the LST model and meteorological station temperature. Additionally, it was discovered that the monthly temperature obtained from gridded climatic records varied by 3–6°C. It can be

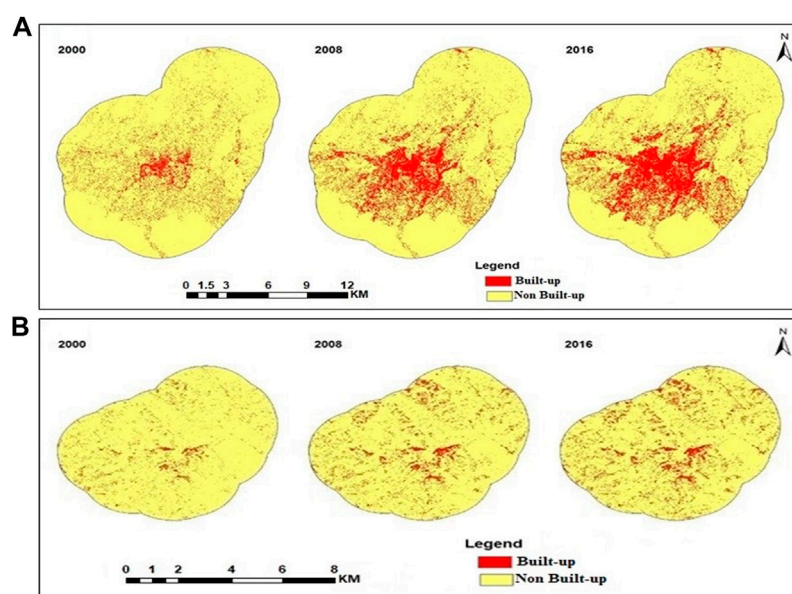


FIGURE 2
Classified map of Dehradun (A) Shimla (B).

TABLE 3 Pearson's correlation between LST and biophysical parameters.

Parameters	Dehradun			Shimla		
	2000	2008	2016	2000	2008	2016
NDBI	0.512**	0.527**	0.692**	0.170	0.682**	0.320**
NDVI	−0.405**	−0.463**	−0.730**	−0.164	−0.708**	−0.330**
NDWI	−0.077	−0.297*	−0.242*	−0.39	−0.596*	−0.186

*Correlation is significant at 0.05 level of confidence.

**Correlation is significant at 0.01 level of confidence.

inferred that LST-derived temperature is reliable as a result of these strong correlations.

3.2 Degree of association of different biophysical parameters with LST

The association between LST and various biophysical factors (Table 3) was examined in order to statistically characterize the variation in LST. At 5% and 1% confidence levels, the Pearson's correlation values were considered significant. The built-up areas have the most influence over LST, according to the correlation coefficient (R) between various LST deriving factors and LST (R of LST vs. NDBI ranges from 0.57 to 0.69 for Dehradun and from 0.17 to 0.68 for Shimla), followed by water bodies (R of LST vs. NDWI ranges from −0.07 to −0.29 for Dehradun and from −0.17 to −0.68 (R of LST vs. NDVI range from −0.45 to −0.73 for Dehradun and from −0.1 to −0.70 for Shimla). Therefore, it is clear that the LST is positively connected with NDBI and negatively correlated with NDVI and NDWI. As a result, greater land surface temperatures are observed in places with less vegetation and water, whereas higher built-up areas suffer lower LST.

3.3 Change in land surface temperature (LST)

The regional distribution of the surface temperature in Dehradun is depicted in Figure 3A. The LST for Dehradun varies from 11.68°C to 32.64°C in 2000 (mean 23.68°C and SD 1.58), 11.42°C–32.85°C in 2008 (mean 26.49°C and SD 4.26) and 13.67°C–33.41°C in 2016 (mean 24.54°C and SD 1.16). According to Figure 3B, the temperature in Shimla ranged from 11.2°C to 28.34°C (mean 33.67°C and SD 5.80) in 2000, 13.0°C–30.6°C (mean 32.31°C and SD 4.74) in 2008, and 11.5°C–32.8°C (mean 24.78°C and SD 2.49) in 2016. It has been noted that the central region has high temperatures, which may be related to the area's dense urbanization, while the forested regions saw moderate temperatures. The radiant temperature is lowered by natural plants or forests because they decrease the amount of heat that is absorbed into the soil through evapotranspiration. Shimla has seen similar patterns as more and more forested areas are turned into urban areas, which has led to an increase in temperature. LST is impacted by a variety of other factors in addition to changes in land use, which together cause changes in LST. These factors are natural and human. Natural factors that influence the LST include changes in the local hydrological cycle, global climate change, and a wide range of others. In terms anthropogenic, population growth has been a significant factor in addition to economic activities. In the past 2 decades, the population of the Dehradun and Shimla has multiplied, increasing both the urban population and urban clusters.

3.4 Association of NDBI with LST

Figures 4A, 5A in the NDBI classifications for Dehradun and Shimla, respectively, demonstrate the spatial distribution and intensity of urban areas for the years 2000, 2008, and 2016, respectively. Both the spatial extent and intensity of urbanization were reported to have

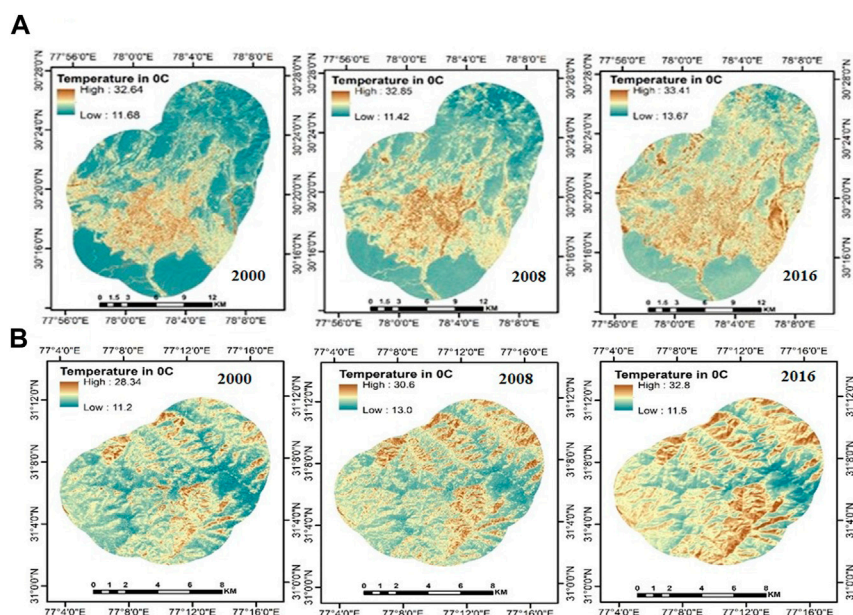


FIGURE 3
Change in LST of Dehradun (A) and Shimla (B).

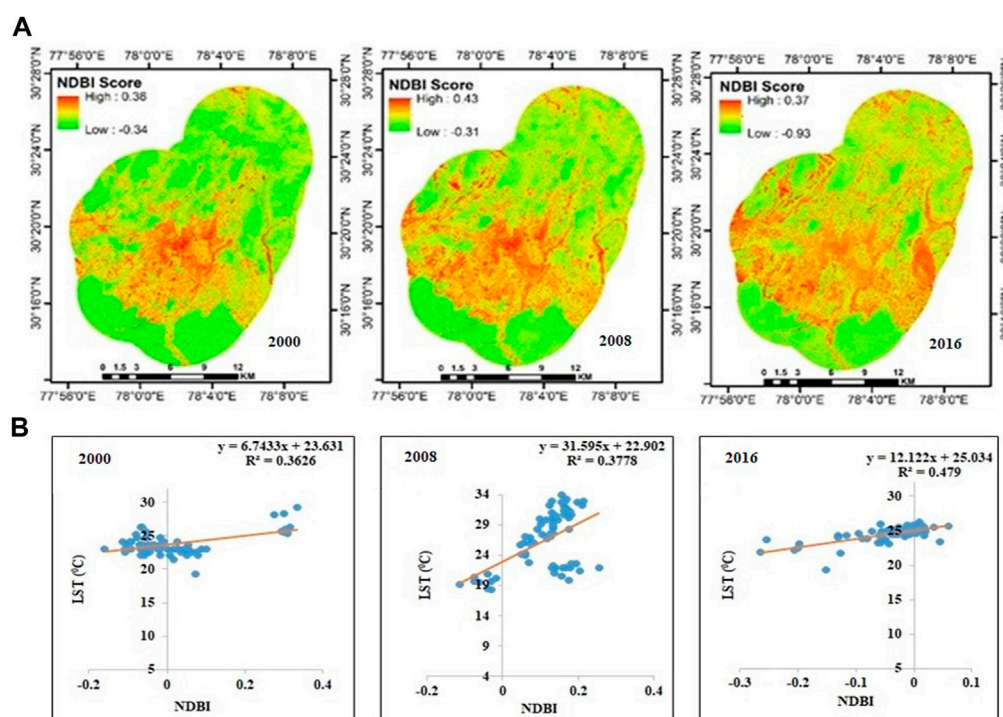


FIGURE 4
Change in NDBI (A) and degree of association of NDBI with LST (B) for Dehradun.

increased temporally. The patterns shown supported the findings that urbanized areas retain the most LST. Similar results were determined by Weng and Yang (2004) wherein they argued that less vegetation covers leads to increased LST. Xiao and Weng, 2007 have also reported

that built-up area positively correlates with land surface temperature in Beijing, China.

The obtained coefficient of determination (R^2) for Dehradun was $R^2 = 0.26$ in 2000, increased to $R^2 = 0.27$ in 2008, and further increased

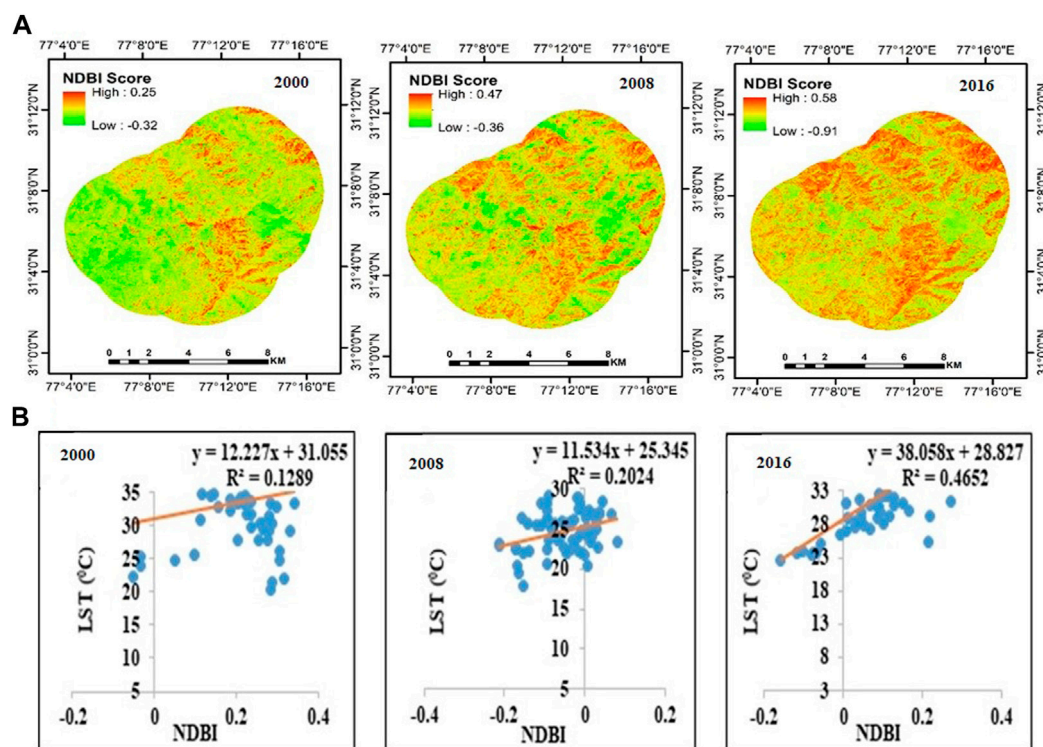


FIGURE 5
Change in NDBI (A) and degree of association of NDBI with LST (B) for Shimla.

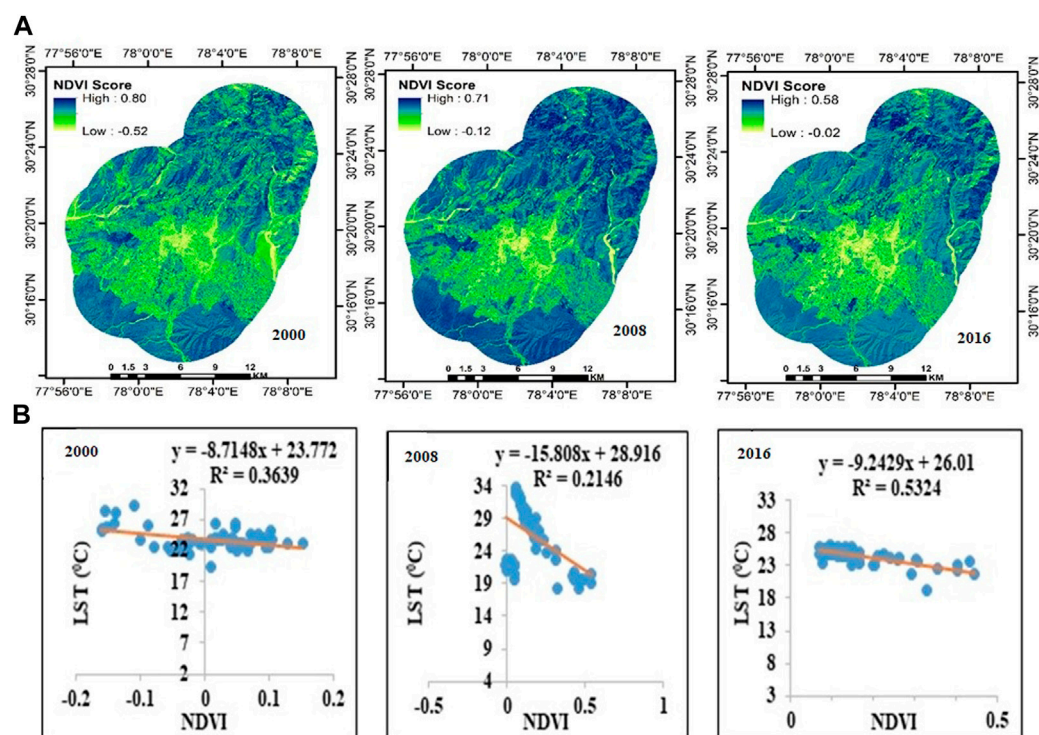


FIGURE 6
Change in NDVI (A) and degree of association of NDVI with LST (B) for Dehradun.

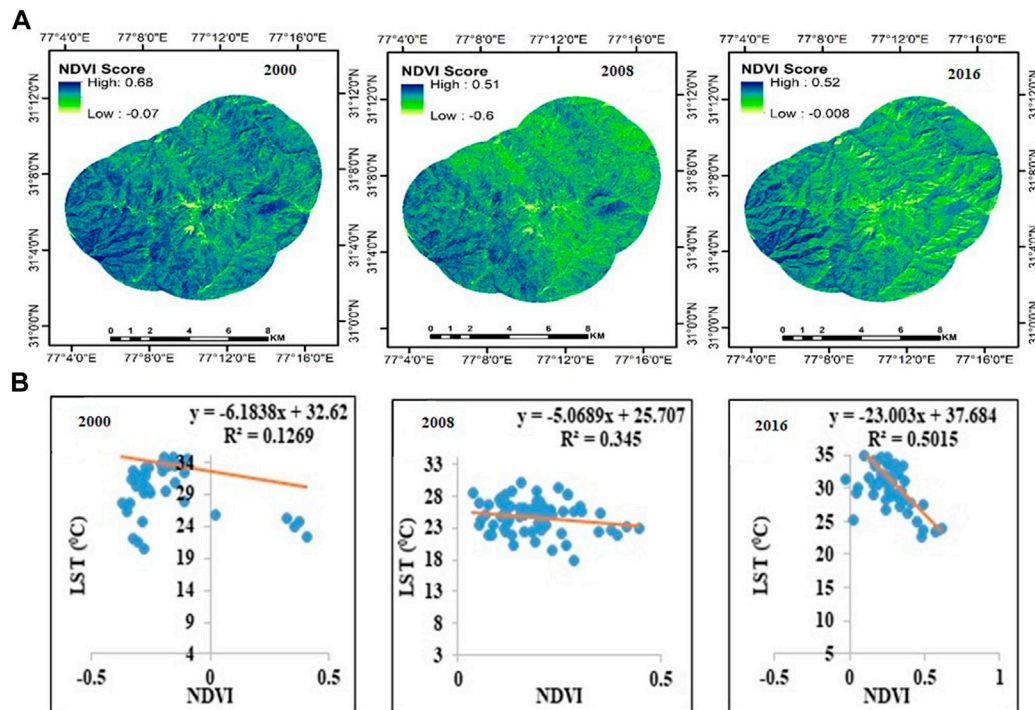


FIGURE 7
Change in NDVI (A) and degree of association of NDVI with LST (B) for Shimla.

to $R^2 = 0.47$ in 2016. Linear regression models between the NDBI and LST were fitted (Figure 4B). Similar trends were seen in Shimla, where the R^2 value in 2000 was $R^2 = 0.02$ and grew to $R^2 = 0.10$ in 2008 and then to $R^2 = 0.46$ in 2016 (Figure 5B). According to the coefficient of determination, LST and NDBI scores positively influenced each other over the study period.

3.5 Association of NDVI with LST

NDVI was utilized to distinguish between vegetated and non-vegetated areas in order to characterize the effect of changes in land cover on temperature trends. For Dehradun (Figure 6A) and Shimla, the geographical pattern and distribution of NDVI computed from Landsat images are displayed in Figure 7A. The NDVI measurements for Dehradun were found to range from -0.52 to 0.80 for 2000, with a mean of 0.00959 and a standard deviation of 0.0738 ; from -0.12 to 0.71 for 2008; from 0.1534 and 0.1356 ; and from -0.02 to 0.58 for 2016, with a mean of 0.1584 and a standard deviation of 0.0921 . A low NDVI value (Yellowish area) indicates high and densely populated areas, mostly in the city's central region, which increased steadily between 2008 and 2016. High NDVI values (dark blue) are seen close to the buffer area's edge. On the outskirts of Dehradun, medium NDVI values (yellowish blue) are seen. The NDVI values for Shimla were found to range from -0.07 to 0.68 in 2000, with a mean of -0.170 and a standard deviation of 0.1541 ; from -0.6 to 0.51 in 2008; and from -0.02 to 0.58 in 2016, with a mean of 0.182 and a standard deviation of 0.091 . Shimla and Dehradun both show similar NDVI trend lines. Due to the presence of steep slopes in the city, which forces people to relocate to nearby hilly areas, the difference in those densely

built-up areas was more concentrated in smaller areas that were decentralized to the outer area in 2008 and 2016. This is explained by the fact that vertical expansion is not desirable up to a certain extent in these situations. As documented earlier, NDVI and LST trend negatively for both the cities and for all the years during the study period as indicated by the R^2 value for Dehradun (Figure 6B) and Shimla (Figure 7B). Mallick et al., 2008 documented a strong relationship between NDVI and LST while studying land surface temperature in Delhi, India and established that LST can be predicted through NDVI values. The study area has undergone significant changes in land use categories and LST over the past 16 years, from 2000 to 2016, as indicated above in the results section. The Normalized Difference Vegetation Index showed similar changes (NDVI). The rapid economic development and shifting economic structure of Dehradun and Shimla, population growth and the ensuing rise in settlements and infrastructure activities, and to some extent the absence of government policies regarding land use change are primarily to blame for these rapid changes.

3.6 Association of NDWI with LST

The spatial pattern and distribution of NDWI for Dehradun and Shimla are shown in Figures 8A, 9A, respectively. NDWI provides the moisture content in areas where the temperature is typically lower than in other land uses (Zhang & Huang, 2015). The LST of water body in general lower than other kind of land use categories (Rao and Pant, 2001; Zhang & Huang, 2015). The level of NDWI control over LST for both cities throughout all time periods is shown in Figures 8B,

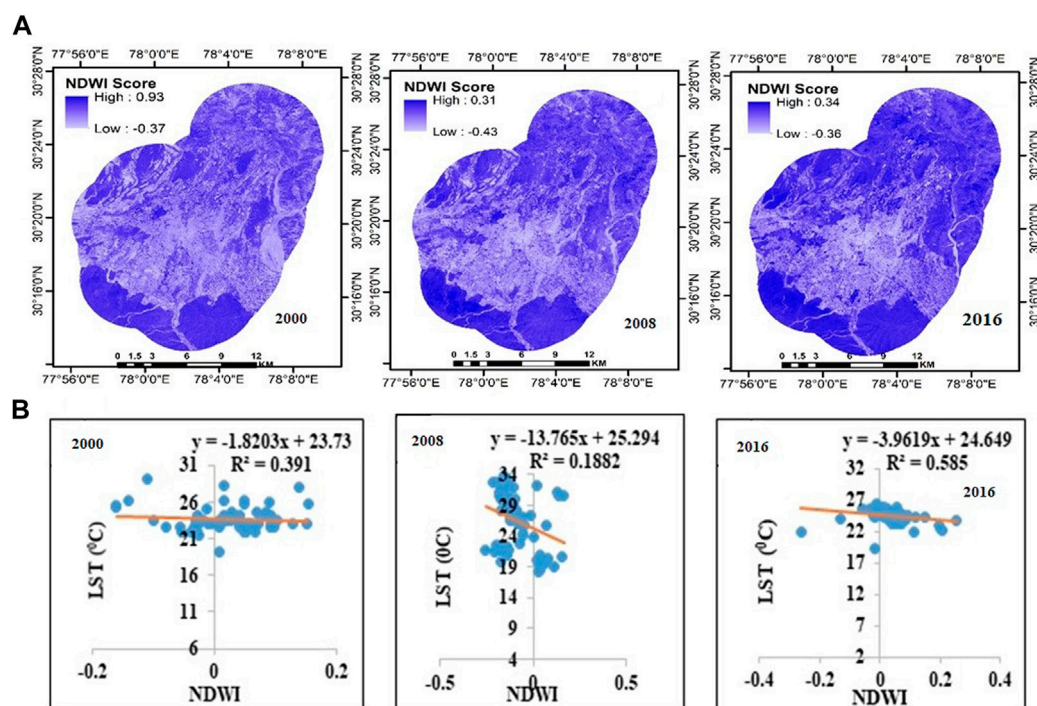


FIGURE 8
Change in NDVI (A) and degree of association of NDVI with LST (B) for Dehradun.

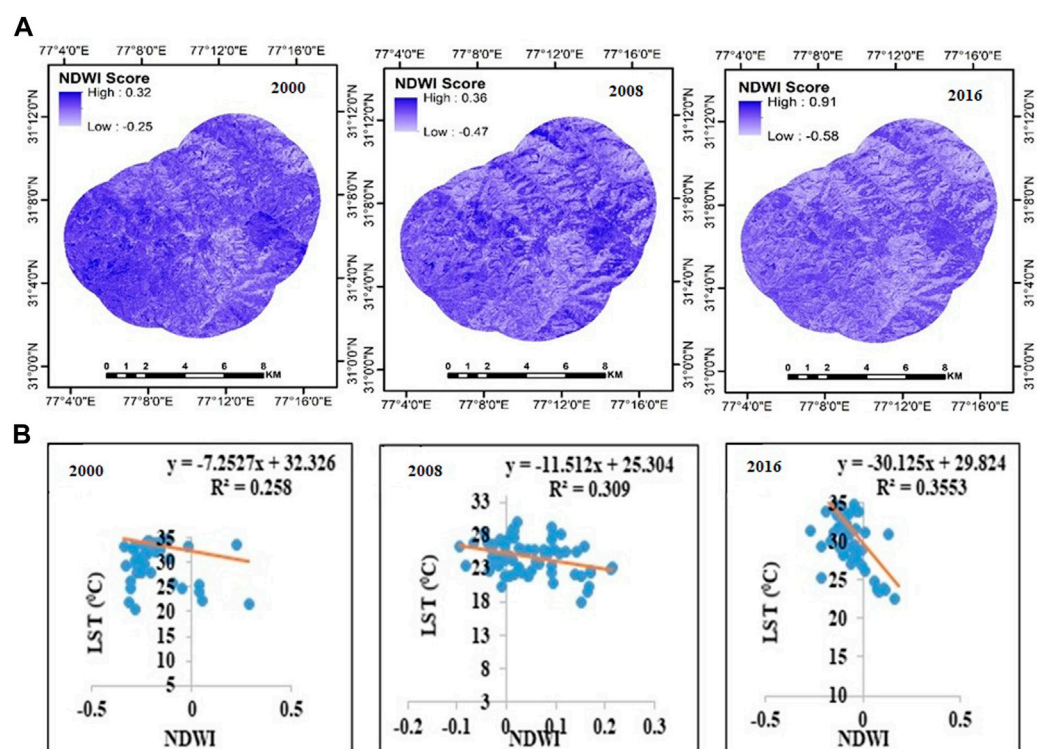


FIGURE 9
Change in NDVI (A) and degree of association of NDVI with LST (B) for Shimla.

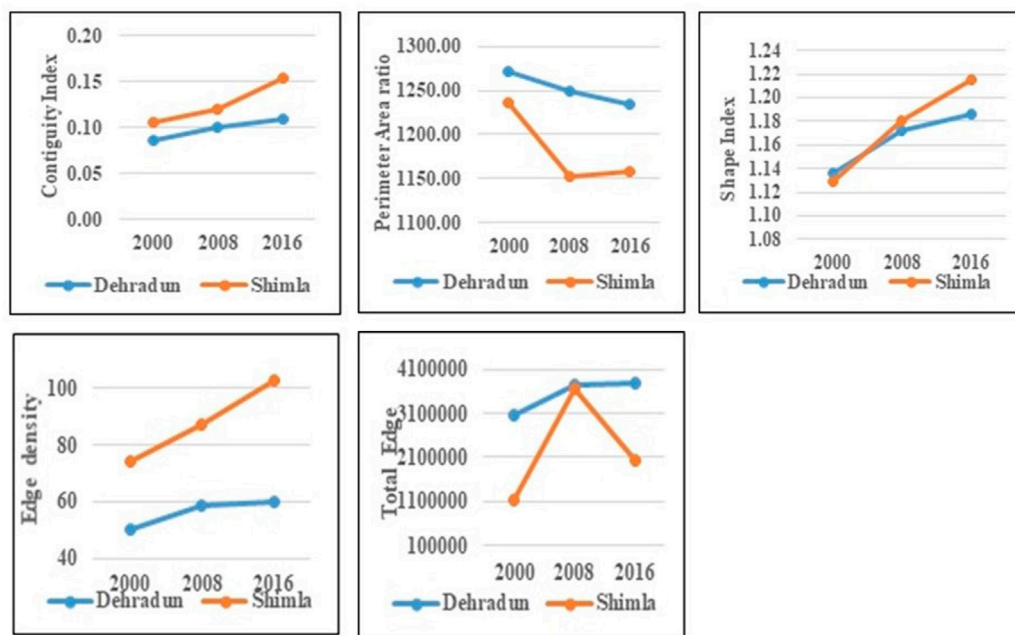


FIGURE 10
Changes in spatial metrics at Class level for Dehradun and Shimla.

9B. It was discovered that NDWI adversely controls LST in every instance. For Dehradun, the R^2 value increased from $R^2 = 0.05$ in 2000 to $R^2 = 0.08$ in 2008 and then to $R^2 = 0.58$ in 2016. Like this, Shimla's R^2 value exhibits rising patterns from 2000 ($R^2 = 0.02$) to 2008 ($R^2 = 0.10$) and further in 2016. ($R^2 = 0.35$). In the city's center, a lower NDWI value was discovered, demonstrating the masking impact of built-up characteristics. Higher NDWI was noticed outside the core zone in all the periods for both cities.

3.7 Spatial metrics

3.7.1 Landscape fragmentation analysis at class level

A solid conceptual and theoretical foundation for evaluating landscape structure, function, and change is quantified through the examination of class- and landscape-level measures. Landscape metrics allow to establish the relationship between the spatial properties of patches or landscapes and biological processes by focusing on changes in the area's geometry, class size and land cover fragmentation (Nagendra et al., 2004). Area and edge metrics are concerned with the size of the patches and the amount of edge that each patch makes up. The lengths of all edge segments involving the relevant patch type are roughly added up to form Total Edge (TE). Figure 10 provides the class-level indicators for Dehradun and Shimla. To determine the shape complexity of the classified maps, the Shape Index was calculated. Greater shape complexity and hence greater changeability are indicated by a higher shape index. The patch is more susceptible to the edge effect as the shape index rises. Shimla's ED, which measures the total edge of any class relative to the entire landscape (Seto and Fragkias, 2005), rises significantly from 2000 to 2016, while Dehradun's rises strongly from 2000 to 2008 and then slowly from 2008 to 2016. This is caused by an

increase in urban edge pixels, which shows the development of new urban edges and intricate structures. The total edge of any patch type at the class level or of all patch types at the landscape level is measured by TE (McGarigal and Mark, 1995). TE for Dehradun has increased during the study period showing the rapid expansion of the city with an increase in built-up structures while for Shimla it increases from 2000 to 2008 due to expansion of the city and then decreases which may be attributed to aggregation of built up structures as horizontal expansion can't take place due to steep slopes of the hilly region. CONTIG measures the degree of spatial connectedness and urban dispersion. High CONTIG means low sprawling as it is related to the discontinuity of urban growth (Triantafyllidis and Stathakis, 2015). Over the course of the study period, CONTIG displays increased tendencies for both cities that show an increase in the connection of urban structures and a corresponding decline in sprawl. Although SI and PARA both measure shape complexity, SI is more representative of shape complexity because the former lacks uniformity. The SI for both cities has increased over the course of the study, which shows that urban areas are developing more intricate patterns. An increase in anthropogenic disturbances will result in increased fragmentation, which will indirectly result in a reduction in the area's forest cover (Aditya et al., 2018).

3.7.2 Landscape fragmentation analysis at landscape level

SHDI is a metric for gauging a community's diversity. It rises as there are more and more varieties of patch. Figure 11 provides the landscape-level measures (SHDI, SIDI, and SIEI) for Dehradun and Shimla. For the years 2000–2016, the SHDI, SIDI, and SIEI showed rising trends for Dehradun and Shimla. The accelerated rate of urban sprawl may be to blame for this. This makes reference to the sprawling

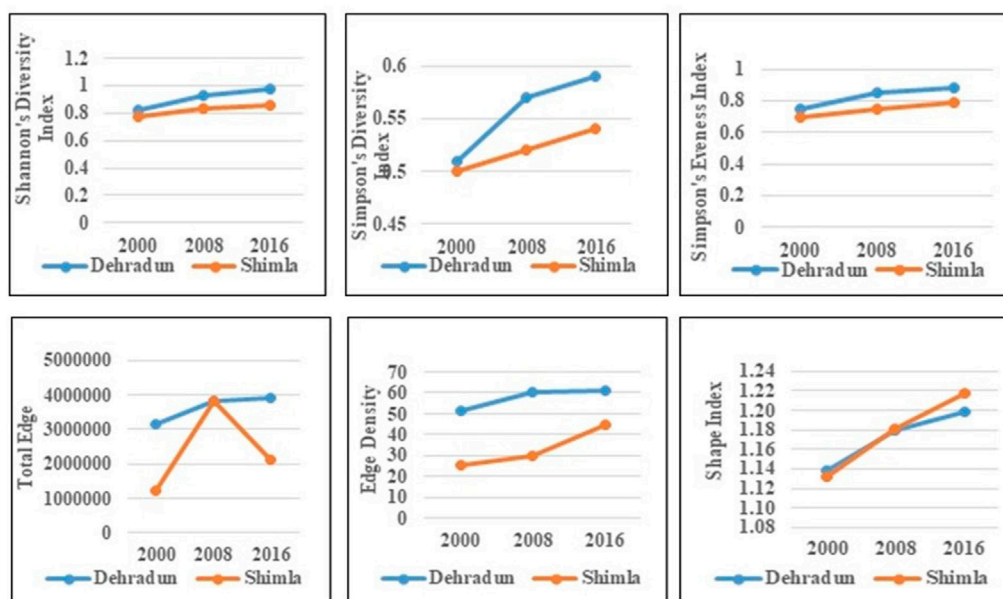


FIGURE 11
Changes in spatial metrics at landscape level for Dehradun and Shimla.

pattern as well. The build-up of Dehradun city has increased quickly and unevenly. This holds true over the course of the investigation. Although the development in built-up areas in Shimla is spatially scattered, it has also led to an increase in size and density. Shimla's built-up area has been steadily expanding, followed by its size and population density.

4 Conclusion

Using change detection and landscape metrics, this study sought to understand and document how urbanization has affected the LST across Dehradun and Shimla. The two Himalayan cities of Uttarakhand and Himachal Pradesh in India are rapidly becoming urbanized. Land surface temperatures are rising as a result of the increased urbanization, which is causing land surfaces to be fragmented and covered in concrete and other impermeable materials. These cities are now experiencing higher temperatures than usual. The LST of the study area has increased as result of decline in land use classes such as forest, agriculture land and waterbodies and increase in concretization in the form of settlement. Increased urbanization impacts the general health of the landscape and makes it more vulnerable to fragmentation, which could significantly alter the area's ecological functions and processes. We noticed urbanization and landscape fragmentation were occurring haphazardly. The outcome showed that the landscape in the research area was fragmented and heterogeneous from 2000 to 2008, after which it has aggregated and grown more heterogeneous. Except for aquatic bodies, lower LST were observed in areas with higher NDVI values, whereas greater LST were found in populated areas. Similar to other Indian cities, urban heat islands are emerging in the Himalayan cities too. According to this study, these changes were primarily attributable to shifts in natural variables like climate and

anthropogenic changes such as population growth and its pressure, a rapidly expanding and structurally changing economy, a lack of land use planning, and ineffective implementation of existing policies. Decentralizing urban built-up areas and population distribution by radical urban infrastructure development policies toward the outskirts of the city can greatly mitigate the consequences of rising temperatures. The findings of this study demonstrate that, especially over the past few decades, human intervention in natural systems has multiplied. Even ecologically delicate ecosystems, like those in the Himalayas, are experiencing these massive human-environmental interactions, which have huge ramifications. In order to reduce population pressure and the strain on land resources, there is an urgent need to transition from horizontal to vertical housing construction. Laws that oppose the haphazard conversion of land resources particularly the conversion of forested land, should be introduced. The analysis of LST, land use and landscape fragmentation directed meticulous planning and policy implementation by concern authorities in order to preserve and maintain the rich ecological diversity of the two Himalayan cities.

Data availability statement

The raw data supporting the conclusions of this article will be made available by the authors, without undue reservation.

Author contributions

RG, MS and GS conceived the idea; RG, MS and GS, designed and analyzed the data; RG, MS, GS and RJ contributed materials/analysis tools; RG, wrote the manuscript and RJ, MS and GS edited the manuscript.

Funding

The author RG is thankful to the University Grant Commission, Govt. of India for providing the necessary financial support under Junior Research Fellowship scheme (NTA ref 190510396571).

Acknowledgments

The author acknowledges Spatial Analysis and Informatics Laboratory (SAIL), School of Environmental Science, Jawaharlal Nehru University, New Delhi, India, for providing the necessary facilities and expertise.

References

- Aditya, S. K., Smitha, A. V., Jenitha, J., and Rajesh, R. (2018). *Landscape analysis using GIS and remote sensing for assessing spatial pattern in forest fragmentation in Shendurney Wildlife Sanctuary*. India: Western Ghats, 299–304.2
- Anees, M. M., Sajjad, S., and Joshi, P. K. (2018). Characterizing urban area dynamics in historic city of Kurukshetra, India, using remote sensing and spatial metric tools. *Geocarto Int.* 34, 1584–1607. doi:10.1080/10106049.2018.1499819
- Artis, D. A., and Carnahan, W. H. (1982). Survey of emissivity variability in thermography of urban areas. *Remote Sens. Environ.* 12, 313–329. doi:10.1016/0034-4257(82)90043-8
- Ashwini, K., and Sil, B. S. (2022). Impacts of land use and land cover changes on land surface temperature over cachar region, northeast India—a case study. *Sustainability* 14 (21)–14087. doi:10.3390/su142114087
- Bhat, P. A., ul Shafiq, M., Mir, A. A., and Ahmed, P. (2017). Urban sprawl and its impact on landuse/land cover dynamics of Dehradun City, India. *Int. J. Sustain. Built Environ.* 6 (2), 513–521. doi:10.1016/j.ijsbe.2017.10.003
- Bhatta, B. (2009). Analysis of urban growth pattern using remote sensing and GIS: A case study of Kolkata, India. *Int. J. Remote Sens.* 30 (18), 4733–4746. doi:10.1080/01431160802651967
- Carlson, T. (2003). Applications of remote sensing to urban problems. *Remote Sens. Environ.* 86, 273–274. doi:10.1016/s0034-4257(03)00073-7
- Chander, G., Markham, B. L., and Helder, D. L. (2009). Summary of current radiometric calibration coefficients for Landsat MSS, TM, ETM+, and EO-1 ALI sensors. *Remote Sens. Environ.* 113, 893–903. doi:10.1016/j.rse.2009.01.007
- Chen, X. L., Zhao, H. M., Li, P. X., and Yin, Z. Y. (2006). Remote sensing image-based analysis of the relationship between urban heat island and land use/cover changes. *Remote Sens. Environ.* 104 (2), 133–146. doi:10.1016/j.rse.2005.11.016
- Congalton, R. G., and Green, K. (1999). *Assessing the accuracy of remotely sensed data: Principles and practices*. Boca Raton: Lewis Publishers.
- Dasgupta, A., Kumar, U., and Ramachandra, T. V. (2009). “Urban Landscape analysis through spatial metrics,” in Proceedings of International Conference on Infrastructure, Sustainable Transportation and Urban Planning, (CISTUP@ CiSTUP), Indian Institute of Science, Bangalore, India, 18–20.
- Dewan, A. M., and Yamaguchi, Y. (2009). Using remote sensing and GIS to detect and monitor land use and land cover change in Dhaka Metropolitan of Bangladesh during 1960–2005. *Environ. Monit. Assess.* 150, 237–249. doi:10.1007/s10661-008-0226-5
- Fenta, A. A., Yasuda, H., Haregeweyn, N., Belay, A. S., Hadush, Z., Gebremedhin, M. A., et al. (2017). The dynamics of urban expansion and land use/land cover changes using remote sensing and spatial metrics: The case of mekelle city of northern Ethiopia. *Int. J. Remote Sens.* 38, 4107–4129. doi:10.1080/01431161.2017.1317936
- Gao, B. C. (1996). NDWI—A normalized difference water index for remote sensing of vegetation liquid water from space. *Remote Sens. Environ.* 58 (3), 257–266. doi:10.1016/s0034-4257(96)00067-3
- Gautam, A. P., Webb, E. L., and Eiumnoh, A. (2002). GIS assessment of land use/land cover changes associated with community forestry implementation in the Middle Hills of Nepal. *Mt. Res. Dev.* 22 (1), 63–69. doi:10.1659/0276-4741(2002)022[0063:gaolul]2.0.co;2
- Giridharan, R., Ganesan, S., and Lau, S. S. Y. (2004). Day time urban heat island effect in high-rise and high-density residential developments in Hong Kong. *Energy Build.* 36 (6), 525–534. doi:10.1016/j.enbuild.2003.12.016
- Grover, A., and Singh, R. B. (2015). Analysis of urban heat island (UHI) in relation to normalized difference vegetation index (NDVI): A comparative study of Delhi and Mumbai. *Environments* 2015 (2), 125–138. doi:10.3390/environments2020125
- Guha, S., Govil, H., Dey, A., and Gill, N. (2020). *A case study on the relationship between land surface temperature and land surface indices in Raipur City, India*. Beijing China: Geogr Tidsskr. doi:10.1080/00167223.2020.1752272
- Harris, I., Osborn, T. J., Jones, P., and Lister, D. (2020). Version 4 of the CRU TS monthly high-resolution gridded multivariate climate dataset. *Sci. Data* 7, 109. doi:10.1038/s41597-020-0453-3
- He, C., Shi, P., Xie, D., and Zhao, Y. (2010). Improving the normalized difference built-up index to map urban built-up areas using a semiautomatic segmentation approach. *Remote Sens. Lett.* 1 (4), 213–221. doi:10.1080/01431161.2010.481681
- Herold, M., Couclelis, H., and Clarke, K. C. (2005). The role of spatial metrics in the analysis and modeling of urban land use change. *Comput. Environ. Urban Sys* 29, 369–399. doi:10.1016/j.compenvurbsys.2003.12.001
- Herold, M., Liu, X., and Clarke, K. C. (2003). Spatial metrics and image texture for mapping urban land use. *Photogram Eng. Remote Sens.* 69, 991–1001. doi:10.14358/pers.69.9.991
- Herold, M., Scepan, J., and Clarke, K. C. (2002). The use of remote sensing and landscape metrics to describe structures and changes in urban land uses. *Environ. Plan. A* 34, 1443–1458. doi:10.1068/a3496
- Jalan, S., and Sharma, K. (2014). Spatio-temporal assessment of land use/land cover dynamics and urban heat island of Jaipur city using satellite data. *Int. Arch. Photogramm. Remote Sens. Spat. Inf. Sci. XL- 8*, 767–772. doi:10.5194/isprsarchives-xl-8-767-2014
- Joshi, P. K., Lele, N., and Agarwal, S. P. (2006). Entropy as an indicator of fragmented landscape. *Curr. Sci.* 91, 276–278.
- Joshi, P. K., Singh, S., Agarwal, S., and Roy, P. S. (2001). Forest cover assessment in Western Himalayas, Himachal Pradesh using IRS 1C/1D WiFS data. *Curr. Sci.* 80 (8), 941–947.
- Keles, S., Sivrikaya, F., and Cakir, G. (2007). Temporal changes in forest landscape patterns in Artvin forest planning unit, Turkey. *Environ. Monit. Assess.* 129, 483–490. doi:10.1007/s10661-006-9380-9
- Kuldeep, T., and Kamlesh, K. (2011). Land use/land cover change detection in Doon valley (Dehradun tehsil), uttrakhand: Using GIS and remote sensing technique. *Int. J. Geomatics Geosciences* 2 (1), 34–41.
- Landsat Project Science Office (2002). Landsat 7 science data user's handbook Washington, DC. URL:Goddard Space Flight Center, NASA http://ftpwww.gsfc.nasa.gov/IAS/handbook/handbook_toc.html (last date accessed: September 10, 2003).
- Lilly Rose, A., and Devadas, M. D. (2009). *Analysis of land surface temperature and land use/land cover types using remote sensing imagery - a case in Chennai city, India, the seventh international conference on urban clim.* Yokohama, Japan. held on 29 June – 3 July 2009.
- Liu, H., Zhan, Q., Yang, C., and Wang, J. (2018). Characterizing the spatio-temporal pattern of land surface temperature through time series clustering: Based on the latent pattern and morphology. *Remote Sens.* 10, 654. doi:10.3390/rs10040654
- Mallick, J., Kant, Y., and Bharath, B. D. (2008). Estimation of land surface temperature over Delhi using Landsat-7 ETM+. *J. Ind. Geophys. Union* 12 (3), 131–140.
- Mallick, J., Rahman, A., and Singh, C. K. (2013). Modeling urban heat islands in heterogeneous land surface and its correlation with impervious surface area by using night-time ASTER satellite data in highly urbanizing city, Delhi-India. *Adv. Space Res.* 5252 (4), 639639–655655. doi:10.1016/j.asr.2013.04.025
- Martin, Balej (2012). Landscape metrics as indicators of the structural landscape changes – two case studies from the Czech Republic after 1948. *J. Land Use Sci.* 7 (4), 443–458. doi:10.1080/1747423X.2011.597443
- McCarthy, M. P., Best, M. J., and Betts, R. A. (2010). Climate change in cities due to global warming and urban effects. *Geophys. Res. Lett.* 37–L09705. doi:10.1029/2010gl042845

Conflict of interest

The authors declare that the research was conducted in the absence of any commercial or financial relationships that could be construed as a potential conflict of interest.

Publisher's note

All claims expressed in this article are solely those of the authors and do not necessarily represent those of their affiliated organizations, or those of the publisher, the editors and the reviewers. Any product that may be evaluated in this article, or claim that may be made by its manufacturer, is not guaranteed or endorsed by the publisher.

- McGarial, K. (2013). Fragstats, v.4 help. Available from: <http://www.umass.edu/landeco/research/Fragstats/documents/fragstats.help.4.2.pdf>.
- McGarial, K., and Marks, B. (1995). Fragstat: Spatial pattern analysis program for quantifying landscape structure. Portland (OR): U.S. Department of Agriculture, Pacific Northwest Research Station. p. 12.
- McGarigal, K. (2015). *FRAGSTATS help*. Amherst (MA): University of Massachusetts.
- Midha, N., and Mathur, P. K. (2010). Assessment of forest fragmentation in the conservation priority Dudhwa landscape, India using FRAGSTATS computed class level metrics. *J. Indian Soc. Remote Sens.* 38 (3), 487–500. doi:10.1007/s12524-010-0034-6
- Mishra, P. K., Rai, A., and Rai, S. C. (2020). Land use and land cover change detection using geospatial techniques in the Sikkim Himalaya, India. *Egypt. J. Remote Sens. Space Sci.* 23 (2), 133–143. doi:10.1016/j.ejrs.2019.02.001
- Munsi, M., Malaviya, S., Oinam, G., and Joshi, P. K. (2009). A landscape approach for quantifying land-use and land-cover change (1976–2006) in middle Himalaya. *Reg. Environ. Change*, [Online] Volume 10(2), p. 145–155. doi:10.1007/s10113-009-0101-0
- Munsi, M., Areendran, G., Ghosh, A., and Joshi, P. (2010). Landscape characterisation of the forests of Himalayan foothills. *Journal of the Indian Society of Remote Sensing* 38 (3), 441–452. doi:10.1007/s12524-010-0046-2
- Nagendra, H., Munroe, D., and Southworth, K. (2004). From pattern to process: Landscape fragmentation and the analysis of land use/land cover change. *Elsevier J. Agric. Ecosyst. Environ.*, [Online] Volume 101(2-3), p. 111–115. doi:10.1016/j.agee.2003.09.003
- Neteler, M. (2010). Estimating daily land surface temperatures in mountainous environments by reconstructed MODIS LST data. *Remote Sens.* 2, 333–351. doi:10.3390/rs1020333
- Ogashawara, I., and Bastos, V. D. S. B. (2012). A quantitative approach for analyzing the relationship between urban heat islands and land cover. *Remote Sens.* 4 (11), 3596–3618. doi:10.3390/rs4113596
- Pal, S., and Ziaul, S. K. (2017). Detection of land use and land cover change and land surface temperature in English Bazar urban Centre. *Egypt. J. Remote Sens. Space Sci.* 20 (1), 125–145. doi:10.1016/j.ejrs.2016.11.003
- Peng, J., Ma, J., Liu, Q., Liu, Y., Hu, Y., Li, Y., et al. (2018). Spatial-temporal change of land surface temperature across 285 cities in China: An urban-rural contrast perspective. *Sci. Total Environ.* 635, 487–497. doi:10.1016/j.scitotenv.2018.04.105
- Prastakos, P., Chrysoulakis, N., and Kochilakis, G. (2012). “Spatial metrics for Greek cities using land cover information from the Urban Atlas,” in *Proceedings of the AGILE’2012 international conference on geographical information science; april 24–27; multidisciplinary research on geographical information in europe and beyond*. Editors J. Gensel, D. Josselin, and D. Vandenbroucke (Avignon, 261–266).
- Punia, M., and Singh, L. (2012). Entropy approach for assessment of urban growth: A case study of Jaipur, India. *J. Indian Soc. Remote Sens.* 40 (2), 231–244. doi:10.1007/s12524-011-0141-z
- Ramachandra, T. V., Bharath, H., and Durgappa, D. (2012b). Insights to urban dynamics through landscape spatial pattern analysis. *Int. J. Appl. Earth Obs. Geoinf* 18, 329–343. doi:10.1016/j.jag.2012.03.005
- Rao, K. S., and Pant, R. (2001). Land use dynamics and landscape change pattern in a typical micro watershed in the mid elevation zone of central Himalaya, India. *Agric. Ecosyst. Environ.* 86 (2), 113–124. doi:10.1016/s0167-8809(00)00274-7
- Rashid, N., Alam, J. M., Chowdhury, M. A., and Islam, S. L. U. (2022). Impact of landuse change and urbanization on urban heat island effect in narayanganj city, Bangladesh: A remote sensing-based estimation. *Environ. Challenges* 8–100571. doi:10.1016/j.envc.2022.100571
- Rawat, J. S., and Kumar, M. (2015). Monitoring land use/cover change using remote sensing and GIS techniques: A case study of hawalbagh block, district almor, Uttarakhand, India. *Egypt. J. Remote Sens. Space Sci.* 18, 77–84. doi:10.1016/j.ejrs.2015.02.002
- Roy, P. S., and Tomar, S. (2001). Landscape cover dynamics pattern in Meghalaya. *Int. J. Remote Sens.* 22 (18), 3813–3825. doi:10.1080/01431160010014008
- Seto, K. C., and Fragkias, M. (2005). Quantifying spatiotemporal patterns of urban land-use change in four cities of China with time series landscape metrics. *Landscape Ecol.* 20, 871–888. doi:10.1007/s10980-005-5238-8
- Shannon, C. E., and Weaver, W. (1949). *The mathematical theory of information*. NY: China
- Sharma, R., and Joshi, P. K. (2012). Monitoring urban landscape dynamics over Delhi (India) using remote sensing (1998–2011) inputs. *J. Indian Soc. Remote Sens.* 41 (3), 641–650. doi:10.1007/s12524-012-0248-x
- Sobrino, J. A., Jimé‘nez-Muoz, J. C., and Paolini, L. (2004). Land surface temperature retrieval from Landsat TM5. *Remote Sens. Environ.* 90 (4), 434–440. doi:10.1016/j.rse.2004.02.003
- Srinivasan, K., Sebastian, A., Menachery, M. P., and Pant, G. (2022). Landscape fragmentation analysis in and around Rajaji national park, Uttarakhand, India. *Indian J. Ecol.* 49 (2), 590–595.
- Story, M., and Congalton, R. G. (1986). Accuracy assessment: A user’s perspective. *Photogramm. Eng. Remote Sens.* 52, 397–399.
- Tou, J. T., and Gonzalez, R. C. (1974). Analysis of urban growth pattern using remote sensing and GIS: A case study of Kolkata, India. *Int. J. Remote Sens.* 30 (18), 4733–4746. doi:10.1080/01431160802651967
- Wakode, H. B., Baier, K., Jha, R., and Azzam, R. (2014). Analysis of urban growth using Landsat TM/ETM data and GIS-a case study of Hyderabad, India. *Arab. J. Geosci.* 7, 109–121. doi:10.1007/s12517-013-0843-3
- Weng, Q., and Lu, D. (2008). A sub-pixel analysis of urbanization effect on land surface temperature and its interplay with impervious surface and vegetation coverage in Indianapolis, United States. *Int. J. Appl. Earth Observation Geo-information* 10, 68–83. doi:10.1016/j.jag.2007.05.002
- Weng, Q., Lu, D., and Schubring, J. (2004). Estimation of land surface temperature–vegetation abundance relationship for urban heat island studies. *Remote Sens. Environ.* 89 (4), 467–483. doi:10.1016/j.rse.2003.11.005
- Weng, Q., and Yang, S. (2004). Managing the adverse thermal effects of urban development in a densely populated Chinese city. *J. Environ. Manag.* 70, 145–156. doi:10.1016/j.jenvman.2003.11.006
- Xiao, H., and Weng, Q. (2007). The impact of land use and land cover changes on land surface temperature in a karst area of China. *J. Environ. Manag.* 85, 245–257. doi:10.1016/j.jenvman.2006.07.016
- Yu, X., and Ng, C. (2006). An integrated evaluation of landscape change using remote sensing and landscape metrics: A case study of panyu, guangzhou. *Int. J. Remote Sens.* 27 (6), 1075–1092. doi:10.1080/01431160500377162
- Zha, Y., Gao, J., and Ni, S. (2003). Use of normalized difference built-up index in automatically mapping urban areas from TM imagery. *Int. J. Remote Sens.* 24 (3), 583–594. doi:10.1080/01431160304987
- Zhang, W., and Huang, B. (2015). Land use optimization for a rapidly urbanizing city with regard to local climate change: Shenzhen as a case study. *J. Urban Plan. Dev.* 141 (1)–05014007. doi:10.1061/(asce)up.1943-5444.0000200
- Zhou, D., Xiao, J., Bonafoni, S., Berger, C., Deilami, K., Zhou, Y., et al. (2019). Satellite remote sensing of surface urban heat islands: Progress, challenges, and perspectives. *Remote Sens.* 11, 48. doi:10.3390/rs11010048



OPEN ACCESS

EDITED BY

Faisal Mumtaz,
Aerospace Information Research Institute
(CAS), China

REVIEWED BY

Subodh Chandra Pal,
University of Burdwan, India
Wani Suhail Ahmad,
Aligarh Muslim University, India

*CORRESPONDENCE

Anurag Malik,
✉ amalik19@pau.edu
Mahesh Chand Singh,
✉ msrawat@pau.edu

SPECIALTY SECTION

This article was submitted
to Land Use Dynamics,
a section of the journal
Frontiers in Environmental Science

RECEIVED 02 January 2023

ACCEPTED 21 February 2023

PUBLISHED 03 March 2023

CITATION

Singh MC, Sur K, Al-Ansari N, Arya PK,
Verma VK and Malik A (2023), GIS
integrated RUSLE model-based soil loss
estimation and watershed prioritization
for land and water conservation aspects.
Front. Environ. Sci. 11:1136243.
doi: 10.3389/fenvs.2023.1136243

COPYRIGHT

© 2023 Singh, Sur, Al-Ansari, Arya, Verma
and Malik. This is an open-access article
distributed under the terms of the
[Creative Commons Attribution License](#)
(CC BY). The use, distribution or
reproduction in other forums is
permitted, provided the original author(s)
and the copyright owner(s) are credited
and that the original publication in this
journal is cited, in accordance with
accepted academic practice. No use,
distribution or reproduction is permitted
which does not comply with these terms.

GIS integrated RUSLE model-based soil loss estimation and watershed prioritization for land and water conservation aspects

Mahesh Chand Singh^{1*}, Koyel Sur², Nadhir Al-Ansari³,
Prashant Kumar Arya⁴, Vipin Kumar Verma² and Anurag Malik^{5*}

¹Department of Soil and Water Engineering, Punjab Agricultural University, Ludhiana, Punjab, India,
²Punjab Remote Sensing Centre, Ludhiana, Punjab, India, ³Civil, Environmental and Natural Resources
Engineering, Lulea University of Technology, Lulea, Sweden, ⁴Institute of Human Development, Eastern
Regional Centre, Ranchi, India, ⁵Punjab Agricultural University, Regional Research Station, Bathinda,
Punjab, India

Land degradation has become one of the major threats throughout the globe, affecting about 2.6 billion people in more than 100 countries. The highest rate of land degradation is in Asia, followed by Africa and Europe. Climate change coupled with anthropogenic activities have accelerated the rate of land degradation in developing nations. In India, land degradation has affected about 105.48 million hectares. Thus, modeling and mapping soil loss, and assessing the vulnerability threat of the active erosional processes in a region are the major challenges from the land and water conservation aspects. The present study attempted rigorous modeling to estimate soil loss from the Banas Basin of Rajasthan state, India, using GIS-integrated Revised Universal Soil Loss Equation (RUSLE) equation. Priority ranking was computed for different watersheds in terms of the degree of soil loss from their catchments, so that appropriate conservation measures can be implemented. The total area of Banas basin (68,207.82 km²) was systematically separated into 25 watersheds ranging in area from 113.0 to 7626.8 km². Rainfall dataset of Indian Meteorological Department for 30 years (1990–2020), FAO based Soil map for soil characterization, ALOS PALSAR digital elevation model for topographic assessment, and Sentinel-2 based land use and land cover map were integrated for modeling and mapping soil erosion/loss risk assessment. The total annual soil loss in the Banas basin was recorded as 21,766,048.8 tons. The areas under very low (0–1 t ha⁻¹ year⁻¹), low (1–5 t ha⁻¹ year⁻¹), medium (5–10 t ha⁻¹ year⁻¹), high (10–50 t ha⁻¹ year⁻¹) and extreme (>50 t ha⁻¹ year⁻¹) soil loss categories were recorded as 24.2, 66.8, 7.3, 0.9, and 0.7%, respectively, whereas the respective average annual soil loss values were obtained as 0.8, 3.0, 6.0, 23.1, and 52.0 t ha⁻¹ year⁻¹. The average annual soil loss among different watersheds was recorded in the range of 1.1–84.9 t ha⁻¹ year⁻¹, being highest (84.9 t ha⁻¹ year⁻¹) in WS18, followed by WS10 (38.4 t ha⁻¹ year⁻¹), SW25 (34.7 t ha⁻¹ year⁻¹) and WS23 (17.9 t ha⁻¹ year⁻¹), whereas it was lowest for WS8 (1.1 t ha⁻¹ year⁻¹). Thus, WS18 obtained the highest/top priority rank in terms of the average annual soil loss (84.9 t ha⁻¹ year⁻¹) to be considered as the first priority for land and water conservation planning and implementation. The quantitative results of this study would be useful for implementation of land and water conservation measures in

the problematic areas of the Banas basin for controlling soil loss through water erosion.

KEYWORDS
banas basin, prioritization, soil loss, RUSLE, GIS

1 Introduction

Land and water resources are vital for the sustainable management of the ecosystem (Prävälíe, 2021). Damage of top soil can reduce soil fertility leading to threat and food security (Pal et al., 2021). Land degradation has become one of the serious threats across the globe in terms of decreasing agricultural productivity, reducing soil health, depleting groundwater storage, a capacity loss of reservoirs due to silt inflow, worsening water quality, poverty and distorting ecological balance (Sur and Chauhan, 2019; Eniyew et al., 2021; Kaur et al., 2022). Globally, around 85% of

degraded land is causing a 17% decline in crop yield (Borrelli et al., 2020). As per the global climatic projection, disruption in the hydrological cycle is continuously magnifying the problem of land degradation (Ahmad et al., 2020), which in turn intensifies the scale of soil erosion through the water as one of the agent from 30% to 66% (Sharda and Ojasvi, 2016). As per Global Soil Partnership reports of the Food and Agriculture Organization (FAO), about 75 billion tons of soil are at high risk of erosion every year from productive agricultural lands across the globe, which may result in an estimated financial loss of 400 billion US Dollar per year (Kayet et al., 2018).

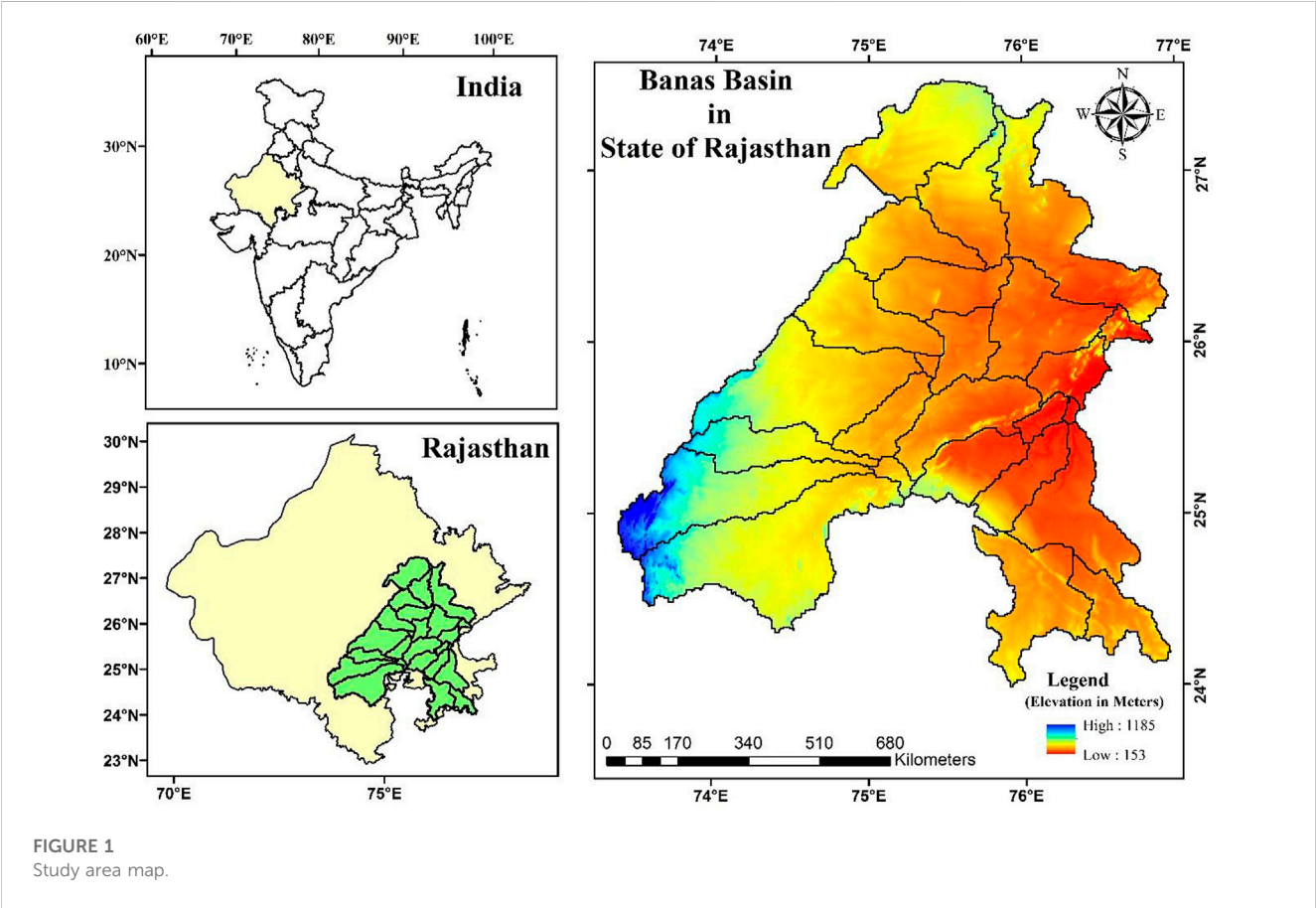


TABLE 1 The database used for estimating soil loss using the RUSLE model.

Database	Purpose	Duration	Scale resolution	Source
Rainfall	Rainfall Erosivity Factor	1990–2020	Station Dataset	India Meteorological Department (IMD)
Soil	Soil Erodibility Factor	2012	30arc Second	Food and Agriculture Organization (FAO)
Elevation	Slope Length Steepness Factor	2021	12.5 m	ALOS PALSAR (DEM)
LULC	Support and Conservation Practices Factor	2021	10 m	Sentinal-2A Google Earth Engine

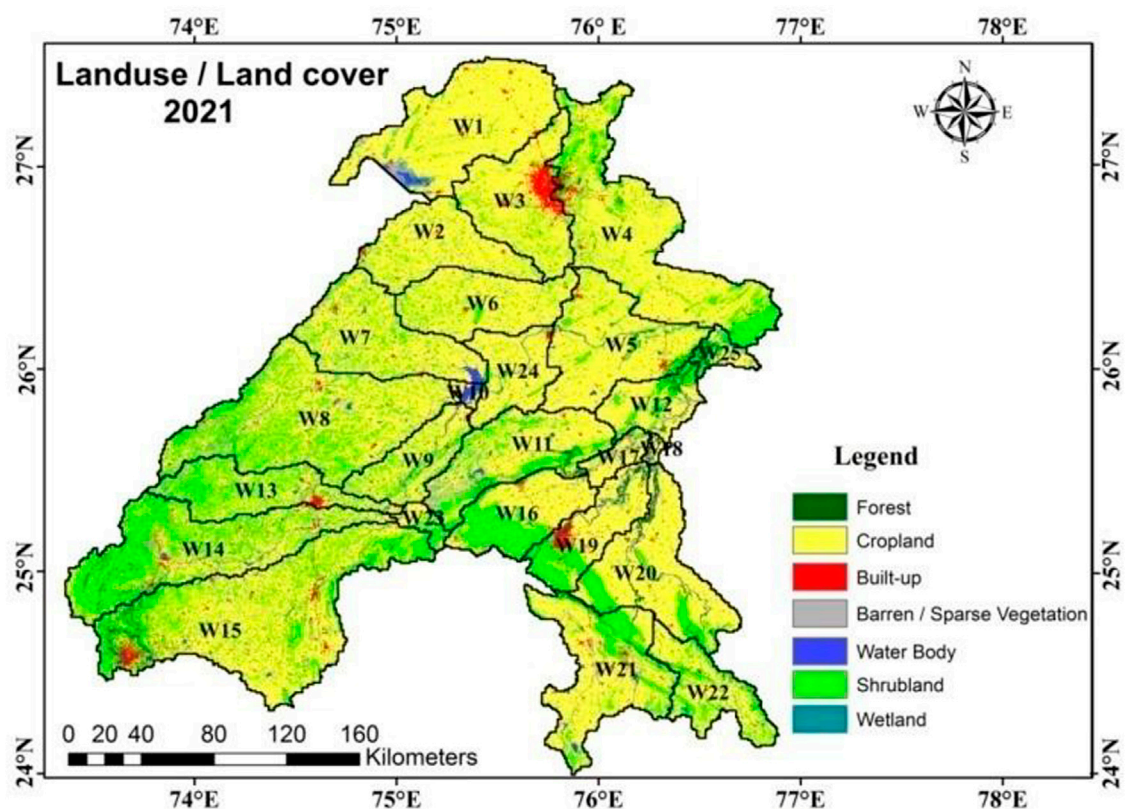


FIGURE 2
LULC map of the Banas basin.

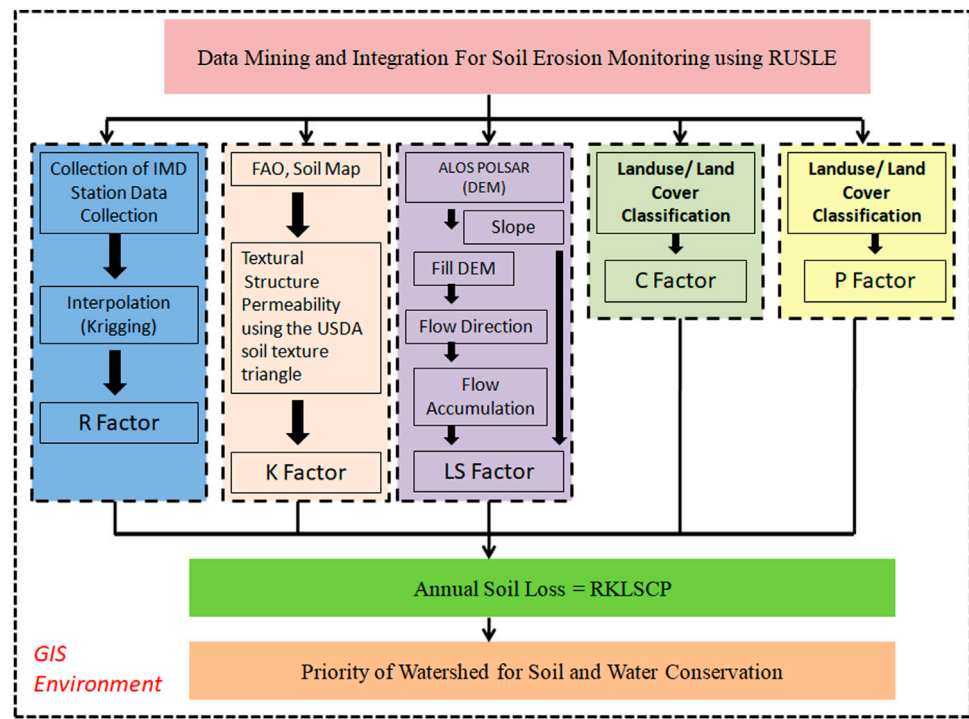


FIGURE 3
Complete work flow diagram of the adopted methodology.

TABLE 2 C and p factors for different LULC.

LULC	C- value	p-value
Forest	0.003	0.8
Cropland	0.63	0.5
Built-up	0.09	1.0
Barren/Sparse Vegetation	0.50	1.0
Water Bodies	0.28	1.0
Scrubland	0.001	1.0
Wetland	0.28	1.0

Land degradation is a major challenge in Asia, where about 663 Mha of the total area is affected by soil erosion and is highest when compared to other continents (Rao et al., 2016). In India, the soil loss is estimated to be 1,559 Mg km⁻² year⁻¹ (Reddy, 2003). About 1,100 Mha of land is affected by rainwater erosion, whereas about 550 Mha is affected by wind erosion in India (Dubey and Sharma, 2018; Kumar et al., 2022). Soil erosion accelerated by water and wind affect the production (≈7.2 million tons) of the staple crops, which in turn results in a reduction of GDP in the country by about 1.0%–1.7% (Lal, 2019). This affects the socioeconomic status of the country negatively (Dubey and Sharma, 2018). Previously, Reddy (Reddy, 2003) reported a loss of about 74 million tons of key

nutrients in the soil due to soil erosion. From the above facts, it is clear that the systematic assessment of soil erosion is the key solution to saving the Earth’s surface from land degradation.

Banas basin drains into Banas river, which is one of the main tributaries of Chambal. It is located in the South-Eastern part of Rajasthan state of India. It is one of the most crucial sites because it falls under five types of climate zones viz. Semi-arid eastern plains, flood-prone Eastern plains, sub-humid Southern plains, humid Southern plains, and humid South-Eastern plains (Chahar and Dhaka, 2013). Banas River remains almost dry in the summer season, as it is a rain-fed river. Major parts of the Banas River Basin have low rainfall and high evapotranspiration rate, leading to a decrease in soil moisture, which affects plant growth ultimately causing low production of biomass (Pham et al., 2018).

For effective implementation of land and water conservation practices in a watershed, the assessment of soil loss through water erosion and its spatial distribution is significant. In past, numerous empirical and physical models viz. USLE: universal Soil Loss Equation (Park et al., 2011), RUSLE: Revised universal Soil Loss Equation (Tiwari et al., 2000; Ouyang et al., 2010), WEPP: Watershed Erosion Prediction Project (Beasley et al., 1980), SWAT: Soil and Water Assessment Tool (Gosain et al., 2009), ANSWERS: Areal Non-Point Source Watershed Environment Response Simulation (Angima et al., 2003), European Soil Erosion Model, Rule Based Expert System, Hybrid Approach, Sediment Concentration Graph, Renard–Laursenn Model, Unit Sediment Graph, and Instantaneous Unit Sediment Graph (24)

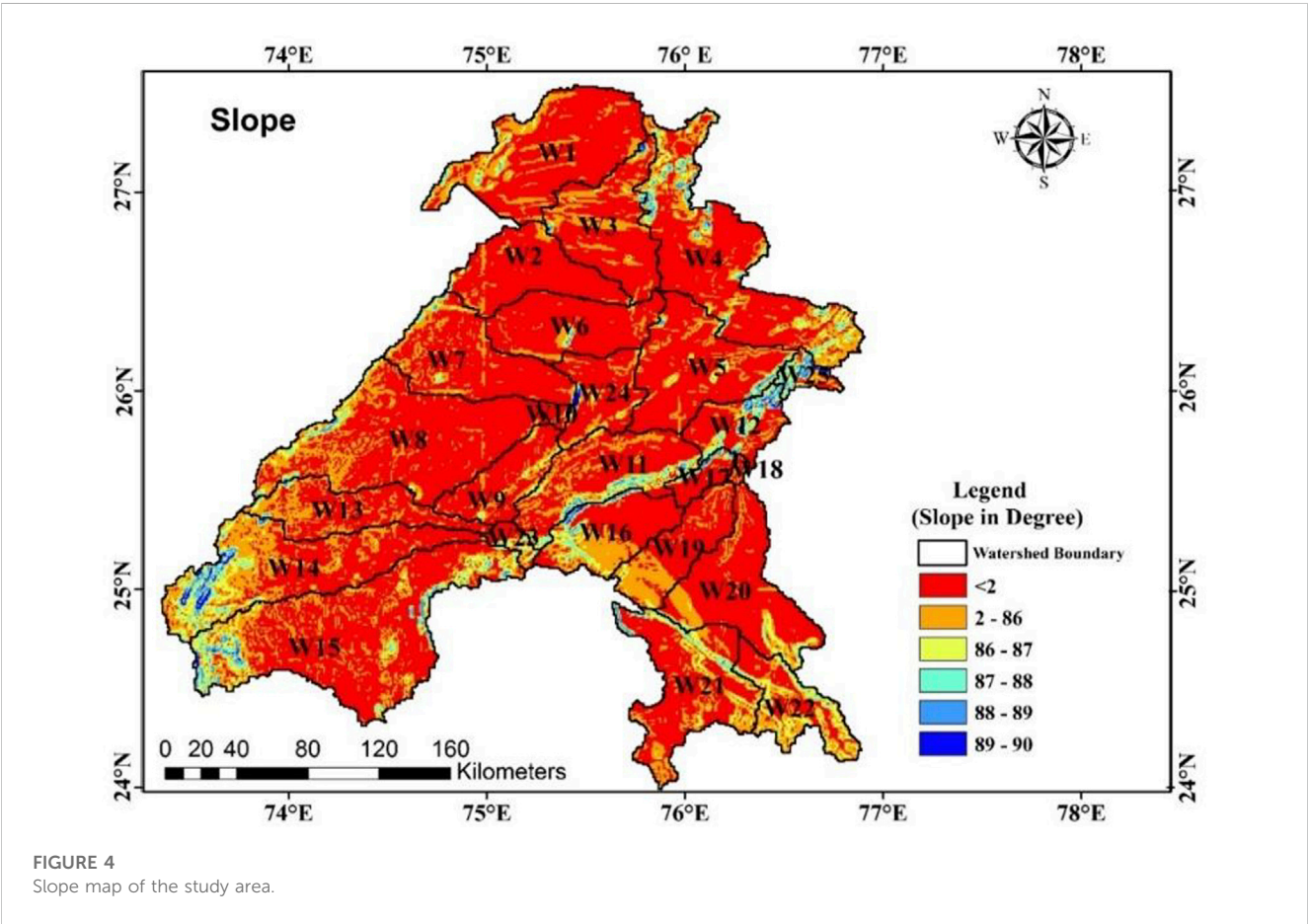


TABLE 3 LULC status in different watersheds in the study area.

WS	Forest		Shrubland		Grassland		Cropland		Built-up		Barren/sparse vegetation	Water body			Wetland	
	Area (ha)	Area (%)	Area (ha)	Area (%)	Area (ha)	Area (%)	Area (ha)	Area (%)	Area (ha)	Area (%)	Area (ha)	Area (%)	Area (ha)	Area (%)	Area (ha)	Area (%)
WS1	176.72	0.04	11412.53	2.54	9651.05	2.15	388863.96	86.64	9725.16	2.17	20875.46	4.65	6202.21	1.38	1938.19	0.43
WS2	319.23	0.13	4634.56	1.85	21918.67	8.76	207768.45	83.03	5677.76	2.27	8773.17	3.51	1145.81	0.46	0.00	0.00
WS3	940.59	0.32	3990.39	1.37	28884.76	9.94	218924.45	75.30	30036.27	10.33	7690.06	2.65	262.23	0.09	0.00	0.00
WS4	9405.93	1.63	25464.42	4.41	105055.69	18.18	405600.82	70.19	17854.17	3.09	12353.12	2.14	1636.06	0.28	473.15	0.08
WS5	5677.76	1.61	8168.91	2.32	29203.99	8.28	286145.50	81.15	8014.99	2.27	10483.34	2.97	4349.53	1.23	575.76	0.16
WS6	513.05	0.20	2109.21	0.82	29243.89	11.42	211445.31	82.55	4281.12	1.67	7165.61	2.80	1390.94	0.54	0.00	0.00
WS7	1408.04	0.44	8721.86	2.75	48426.29	15.30	227543.71	71.87	6869.18	2.17	17449.43	5.51	6190.81	1.96	0.00	0.00
WS8	5763.27	0.94	43352.79	7.06	148072.15	24.10	361854.69	58.91	14832.87	2.41	33935.46	5.52	6458.74	1.05	17.10	0.00
WS9	2553.85	1.53	9098.10	5.43	30840.05	18.42	108031.39	64.53	3351.93	2.00	9166.51	5.48	4378.03	2.62	0.00	0.00
WS10	381.94	2.32	524.45	3.18	507.35	3.08	8670.56	52.59	108.31	0.66	256.53	1.56	6036.90	36.62	0.00	0.00
WS11	10722.76	3.55	38079.77	12.61	43837.34	14.52	173713.28	57.53	4395.13	1.46	26598.83	8.81	4606.06	1.53	0.00	0.00
WS12	9417.33	6.82	17227.10	12.47	12854.77	9.30	86335.04	62.48	1596.16	1.16	8402.63	6.08	2109.21	1.53	228.02	0.17
WS13	3249.32	1.41	19558.63	8.48	76074.02	32.99	108515.93	47.05	8049.20	3.49	12706.56	5.51	2474.04	1.07	0.00	0.00
WS14	19131.09	3.98	65647.69	13.65	152490.08	31.71	200933.47	41.79	13778.26	2.87	21206.10	4.41	7650.16	1.59	0.00	0.00
WS15	38062.66	4.99	46784.53	6.13	159507.48	20.91	464863.88	60.95	27750.34	3.64	19051.28	2.50	6663.96	0.87	0.00	0.00
WS16	2941.49	1.35	9109.50	4.18	76376.15	35.06	118184.09	54.25	4685.86	2.15	5626.46	2.58	917.79	0.42	0.00	0.00
WS17	2069.30	3.94	2496.85	4.75	2331.53	4.44	36147.28	68.81	986.20	1.88	7883.88	15.01	615.66	1.17	0.00	0.00
WS18	1647.46	14.57	0.00	0.00	0.00	0.00	7764.17	68.68	165.32	1.46	1128.71	9.98	598.56	5.30	0.00	0.00
WS19	9252.02	4.78	4936.69	2.55	44817.83	23.17	109245.61	56.47	11275.72	5.83	9998.79	5.17	3933.39	2.03	0.00	0.00
WS20	13345.02	3.83	6065.40	1.74	46904.24	13.45	261866.80	75.07	5558.05	1.59	8374.13	2.40	6720.96	1.93	5.70	0.00
WS21	8425.43	2.32	16907.87	4.65	60665.40	16.68	246697.60	67.83	8505.24	2.34	14582.04	4.01	7923.78	2.18	5.70	0.00
WS22	5016.50	2.73	13447.63	7.33	36774.34	20.04	115818.36	63.11	1972.40	1.07	7861.08	4.28	2639.36	1.44	0.00	0.00
WS23	467.45	1.31	3329.13	9.36	10973.59	30.85	18367.22	51.64	467.45	1.31	1408.04	3.96	552.95	1.55	0.00	0.00
WS24	1607.56	0.99	2257.42	1.39	11566.44	7.12	135656.32	83.47	3927.69	2.42	4543.35	2.80	2964.29	1.82	0.00	0.00
WS25	7159.91	15.57	7302.42	15.88	9177.91	19.96	16406.22	35.69	290.73	0.63	4839.78	10.53	438.94	0.95	359.14	0.78

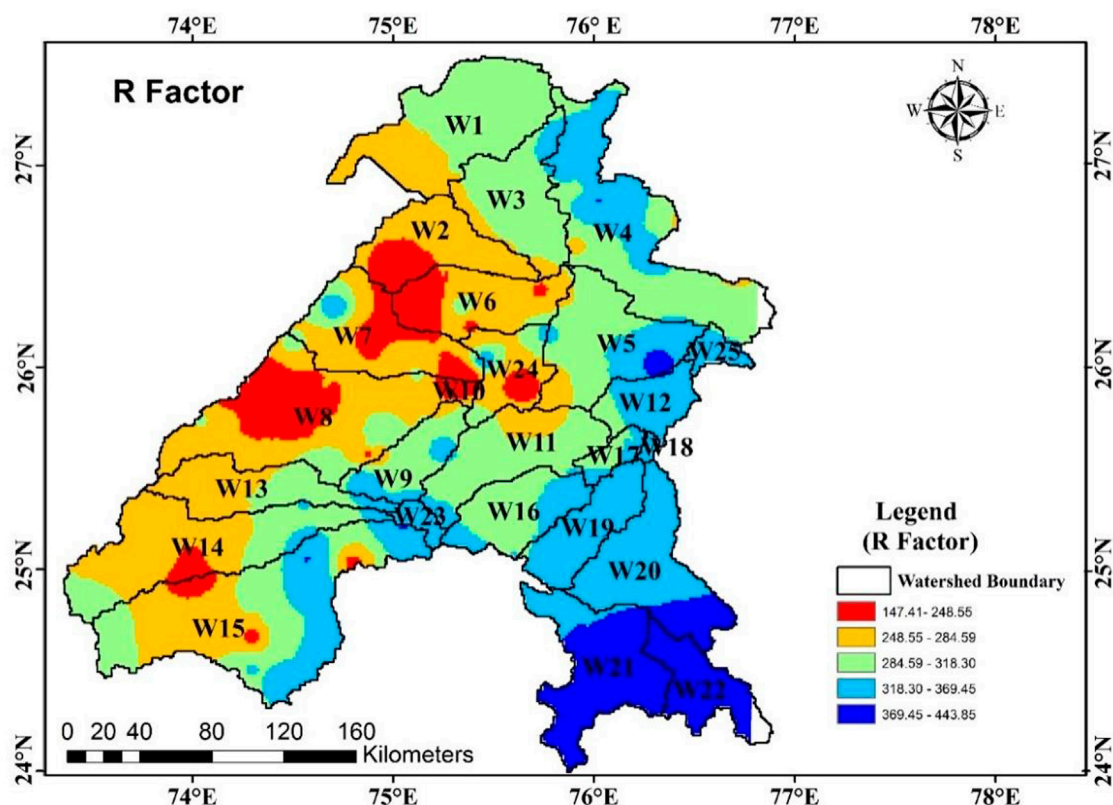


FIGURE 5
R factor map of the study basin.

have been used for predicting soil loss through water erosion. The empirical models significantly reduce the inputs, and therefore commonly applied for predicting soil loss through water erosion. Whereas, the physical models use non-linear partial differential equations for representing several hydrological processes and involve huge input data (Abdelwahab et al., 2018). Within the above-mentioned models for predicting soil loss through water erosion, RUSLE is the most widely applied empirical model for assessing soil erosion rate/loss. This model computes the soil loss in relation to the prevailing climatic conditions and several features of a watershed (Boufala et al., 2020).

Several authors have tested the performance of RUSLE with other models (Tiwari et al., 2000; Mondal et al., 2016; Chen et al., 2019; Safwan et al., 2021). Tiwari et al. (Tiwari et al., 2000) reported statistically similar results of soil loss using RUSLE and WEPP models. While comparing the performance of the USLE, RUSLE, and WEPP models, Ubierna et al. (Tiwari et al., 2000) reported soil loss estimates of the RUSLE model very close to the actual data. Recently, Safwan et al. (Safwan et al., 2021) also confirmed a good agreement in the soil loss results of RUSLE with the WEPP model. While testing the performance of USLE, RUSLE, and modified Morgan-Morgan-Finney (MMF) models, Mondal et al. (Mondal et al., 2016) also reported the soil loss data of the RUSLE model in close agreement with the actual data. Later on, Abdelwahab et al. (Abdelwahab et al., 2018) reported the soil loss results of RUSLE quite closer to that obtained using SWAT and Agricultural non-point source pollution (AGNPS). Similarly, Boufala et al. (Boufala et al., 2020) confirmed a close agreement in the soil loss results of RUSLE and SWAT

models. Thus, it can be said that the RUSLE model, which is as good as WEPP and SWAT models should be integrated with the GIS platform for precise estimation of soil loss. This would be a time- and labor-efficient approach to estimating erosion rate or soil loss from a large area.

Nowadays, remote-sensing and geographic information systems (GIS) are being widely applied for identifying areas susceptible to water erosion and estimating soil erosion. A hydrological model when jointly used with remote sensing and GIS techniques offers great potential in identifying the erosion-prone hotspots, spatial spread of erosion, and estimating soil loss. Remote sensing and GIS applications have made it possible to estimate erosion from a large expanse in a smaller period of time. A digital elevation model (DEM) is useful for extracting the topographical features viz. Slope, flow direction, flow accumulation, and drainage networking of a watershed for assessing the soil loss through water erosion (Mondal et al., 2016). The Remote Sensing and GIS-coupled application of RUSLE is a cost-effective and can be applied over a large area with improved consistency.

RUSLE when combined with GIS, helps to identify the erosion-prone hotspots, predict the cell-by-cell soil erosion/loss, and prioritize the sub-watersheds in a big watershed in relation to the amount of soil loss from their catchments (Chen et al., 2019). The integrated applications of RUSLE with the GIS platform have already been made in past (Renard et al., 1991; Sharma, 2010; Ranzi et al., 2012; Wijesundara et al., 2018; Thapa, 2020). While estimating soil erosion through the integration of RUSLE with the GIS platform, Farhan et al. (Farhan et al., 2014) reported about 31.2% area of the WadiKufanja

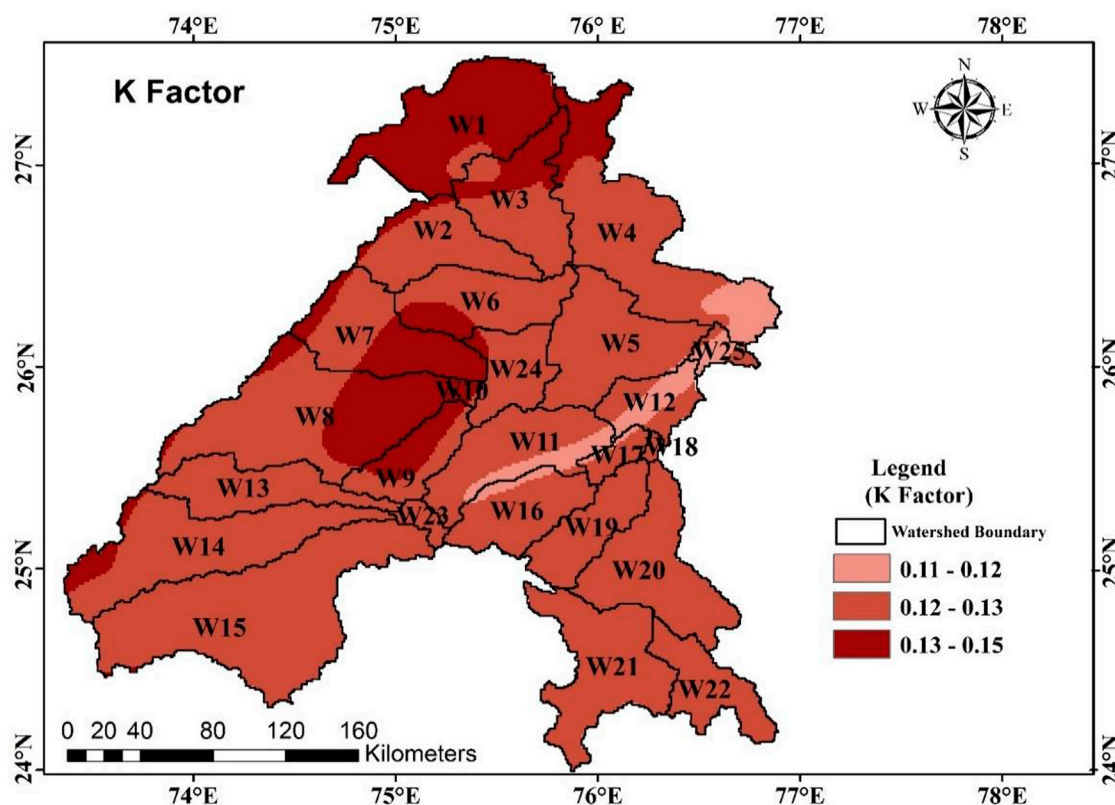


FIGURE 6
K factor map of the study basin.

watershed in Jordan was under severe erosion. Similarly, using RUSLE and GIS jointly, Marondedze and Schütt (Marondedze and Schütt, 2020) reported about 40% of the Epworth district of Zimbabwe is under severe soil erosion. Recently, Amellah and Morabiti (Amellah and El Morabiti, 2021) also used RUSLE jointly with remote sensing and GIS for identifying erosion-prone zones and estimating the soil loss in the OuedLaou basin, Morocco. Using RUSLE and the GIS platform jointly, Srinivasan et al. (Srinivasan et al., 2021) reported about 8.9, 55.0, and 35.0% of areas under severe, medium, and low erosion risk, respectively, in Deccan Plateau, India. Pal and Chakraborty (2019a); Pal and Chakraborty (2019b) reported a strong correlation between amount of actual soil loss on ground and estimated soil loss by RUSLE.

Banas River has a length of about 512 km. It is the most important river, as it is one of the major natural water supply sources of arid Rajasthan. It provides water to the entire forest land of Rajasthan, therefore often referred to as “Van ki Asha” by local people. The soil loss through water erosion from the upstream ends of a watershed may adversely affect the storage capacities of the water bodies (dams or reservoirs) located in the downstream areas in relation to silt inflow or sedimentation. Thus, it becomes imperative to assess the soil loss from a watershed for implementation of appropriate land and water conservation measures starting from the area/watershed of the highest priority rank. However, no effort has been made in past to estimate the soil loss from the Banas basin and identify the most water-erosion-affected zones. Thus, the present study was undertaken with the objectives 1) to estimate the soil loss from twenty-five watersheds of

Banas Basin (comprising fourteen districts) in Rajasthan state, 2) to study the spatial distribution of soil erosion/loss, and 3) to perform prioritization of the watersheds for implementing land and water conservation practices starting from areas with higher priority in terms of soil erosion/loss.

2 Materials and methods

2.1 Brief description of the study area

The Banas River Basin is located between 24° and 27° N latitude and 73°–77° E longitude in the East South-Central region of Rajasthan (Mundetia et al., 2018; Sharma et al., 2018). Banas River is also colloquially named “Van Ki Asha”. The Banas River is seasonal and often remains dry in the summer months. It has a tropical type of climate. The average maximum and minimum temperature in summer are 40°C and 25.8°C, respectively, whereas in winter the maximum and minimum values are 22°C and 8.3°C, respectively (Everard et al., 2018). The Banas River Basin receives an average annual rainfall of 637 mm compared to all India’s average of 1,100 mm. The humidity level reaches the level of 90% during the monsoon month. It is a major tributary of the Chambal River, which is also a tributary of the Ganga River. The total catchment area (Figure 1) of Banas River Basin is 68207.82 km² and the river has a length of about 512 km and flows

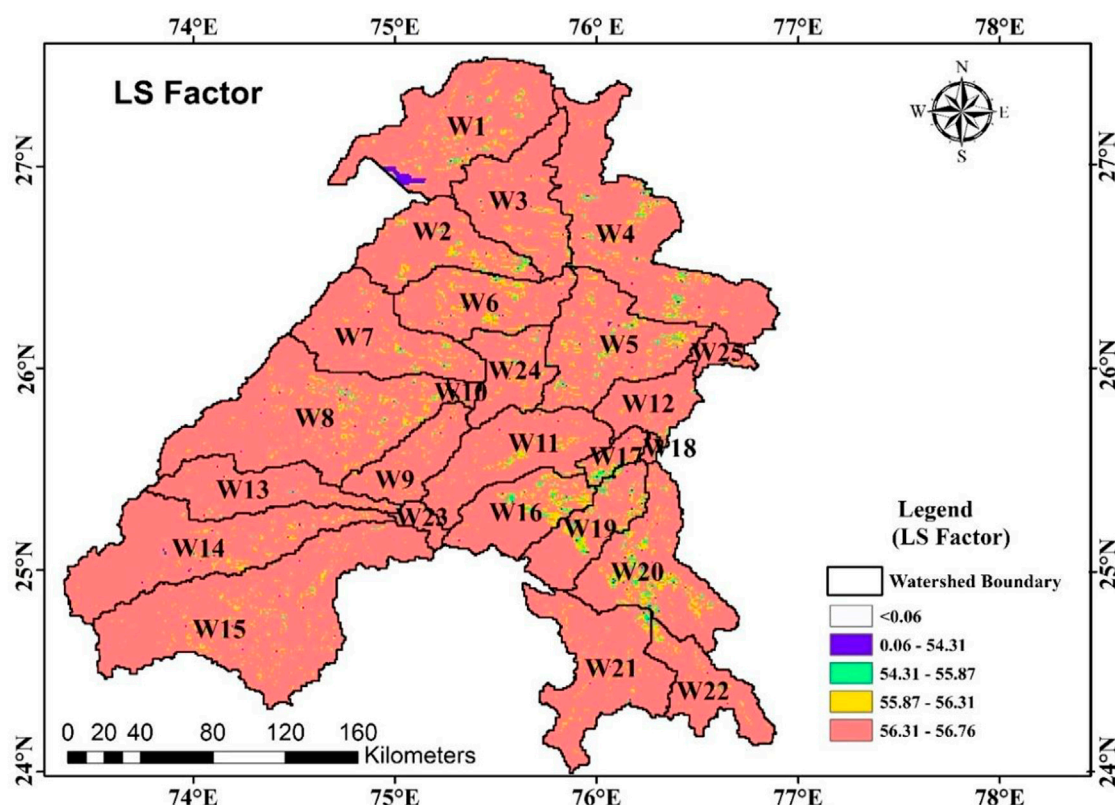


FIGURE 7
LS factor map of the study basin.

entirely within Rajasthan. The Banas River Basin covers 14 districts namely Sikar, Jaipur, Ajmer, Nagaur, Rajsamand, Chittaurgarh, Bundi, Sawai Madhopur, Bhilwara, Dausa, Udaipur, Tonk, Neemuch, and Karauli (Dubey et al., 2015).

2.2 Watershed delineation

The Banas basin of Rajasthan state was demarcated into 25 watersheds by defining their outlet points (pour points) at appropriate places.

2.3 Data collection

The station rainfall data for the 31 years (1990–2020) of the study region was obtained from the Indian Meteorological Department (IMD) for computing rainfall erosivity index/factor. Soil data of 30 arcs second resolution for the year 2012 of FAO was used for computing soil erodibility index/factor. For the computation of the slope length-steepness factor (LS), the elevation data of 12.5 m-spatial resolution for the year 2021 was used. For the computation of support/conservation practices factor (p), LULC data of 10 m spatial resolution using Sentinel-2A Google Earth Engine for the year 2021 was used as mentioned in Table 1.

2.3.1 Land use land cover (LULC) of banas basin

Sentinel-2A based Google Earth Engine product of 10 m-spatial resolution was used for LULC analysis of the Banas basin. The LULC of the study area was categorized into eight classes viz. Forest, shrubland, grassland, cropland, built-up, barren/sparse vegetation, waterbody, and wetland. The LULC classified map was produced by a deep learning model trained using over 5 billion hand-labeled Sentinel-2 pixels, sampled from over 20,000 sites distributed across all major biomes of the world. The underlying deep learning model was supported by information on 6 bands of Sentinel-2 surface reflectance data: visible blue, green, red, near-infrared, and two shortwave infrared bands (Du et al., 2021). Figure 2 shows the LULC map of the Banas basin. This region has prominent seven classes which distinctly show that the area is an agriculturally dominant area with one big city (Jaipur) in the North and a few small cities in the Southern part. The region is covered by small patches of forest land in the Eastern part. Shrubland is a major class covering apart from agriculture in the region. The spread of scrubland in the region proves that the land is not very fertile and therefore not suitable for cultivation and prone to water and wind erosion.

2.3.2 Slope of the basin

Soil erosion/loss is greatly affected by the slope in relation to its direct impact on the hydrological response of the watershed. For a better understanding of the causes of erosion, soil loss, and risk analysis, the topographical data of the watershed is required (Everard et al., 2018). In

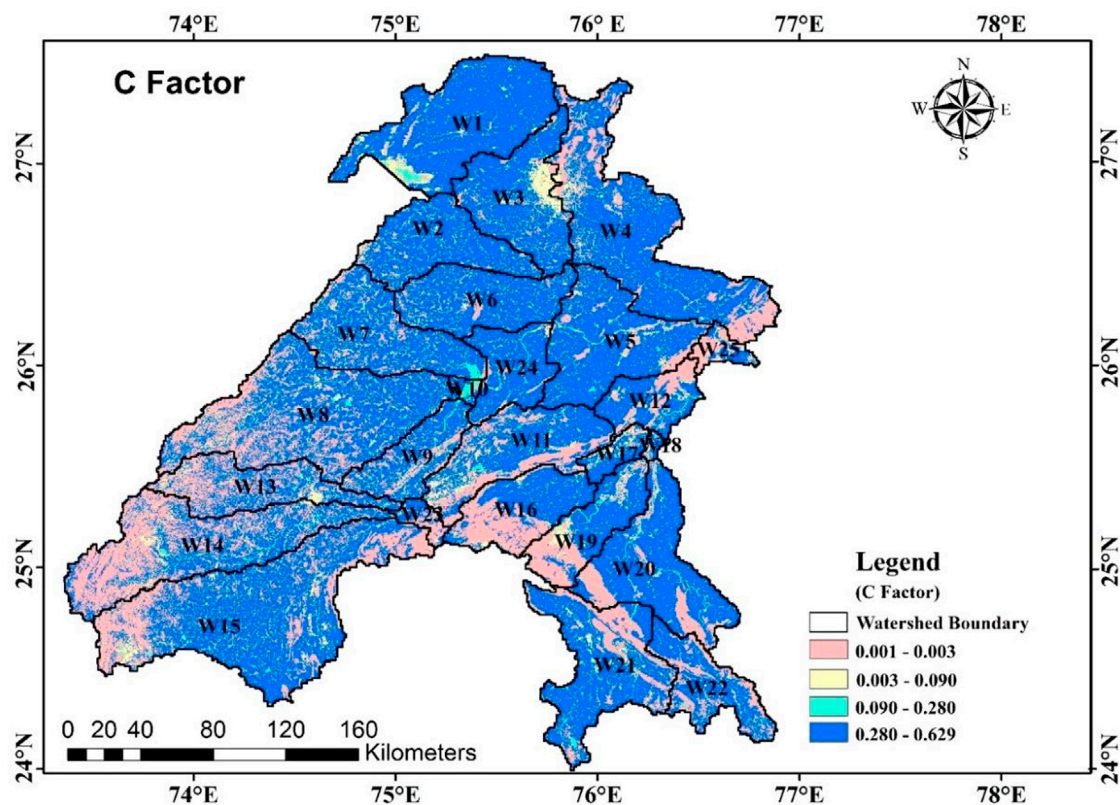


FIGURE 8
C factor map of the study basin.

the present study, the ALOS PALSAR digital elevation model (DEM) of 12.5 m-spatial resolution was used for generating the slope map of the Banas basin in GIS software (Arc GIS Pro 2.8.7).

2.3.3 Estimating parameters of revised universal Soil Loss Equation (RUSLE)

RUSLE is a widely applied empirical model for estimating the average annual soil loss or erosion rate (Sujatha and Sridhar, 2021). Collected datasets were assembled using various data mining techniques coupled with machine learning algorithms to generate thematic layers which served as the input for the RUSLE model (Ruidas et al., 2021; Ruidas et al., 2022a; Ruidas et al., 2022b; Ruidas et al., 2022c; Jaydhar et al., 2022). This model incorporates five factors related to rainfall/precipitation, soil/land, topography/landscape, LULC, and conservation practices. Mathematically, RUSLE is expressed as:

$$A = R.K.LS.C.P \quad (1)$$

where, A = average annual soil loss ($\text{t.ha}^{-1} \text{ year}^{-1}$), R = rainfall erosivity index/factor ($\text{MJ.mm.ha}^{-1} \cdot \text{h}^{-1} \text{ year}^{-1}$), K = soil erodibility index/factor ($\text{t.ha.h.MJ}^{-1} \text{ mm}^{-1}$), LS = slope length and steepness factor (-), C = crop/cover management factor (-), and p = support and conservation practices factor (-).

2.3.4 Rainfall erosivity index/factor (R)

This parameter designates the capability/erosive power of raindrops to detach soil due to high impact force or kinetic

energy (Nampak et al., 2018). It has been recognized as the foremost power accountable for higher soil erosion rate/soil loss (Fenta et al., 2016). Here, the mean annual rainfall of 31 years (1990–2020) was utilized for computing R-value using the equation

$$R = 79.0 + 0.363P \quad (2)$$

Where, p = mean annual rainfall (mm).

2.3.5 Soil erodibility index/factor (K)

This index (K value) designates the susceptibility of soil to get erode (Das et al., 2021). It is mainly dependent on the land/soil features, the texture of the soil, organic matter content, and unsaturated hydraulic conductivity. Normally, it varies from 0.0 to 1.0. For the present study, the K value was obtained using the FAO soil map. The soil data of the study site was obtained from a digital soil map of the world published by FAO using GIS software. The textural class of the soil, structural code (S), and permeability (p) were obtained from the soil texture triangle of USDA. As reported by Das et al. (Sujatha and Sridhar, 2021), the K value was obtained using the equation given below:

$$K = 2.8 \times 10^{-7} \times (12 - OM) \times M^{1.14} + 4.3 \times 10^{-3} \times (S - 2) + 3.3 \times 10^{-3} \times (P - 3) \quad (3)$$

$$M = (\% \text{ silt} + \% \text{ very finesand}) \times (100 - \% \text{ clay}) \quad (4)$$

Where, K = soil erodibility factor ($\text{t.ha.h.MJ}^{-1} \cdot \text{mm}^{-1}$), M = particle size parameter (-), OM = organic matter (%), S = soil structure code (1 for very fine granular, 2 for fine granular, 3 for medium and coarse

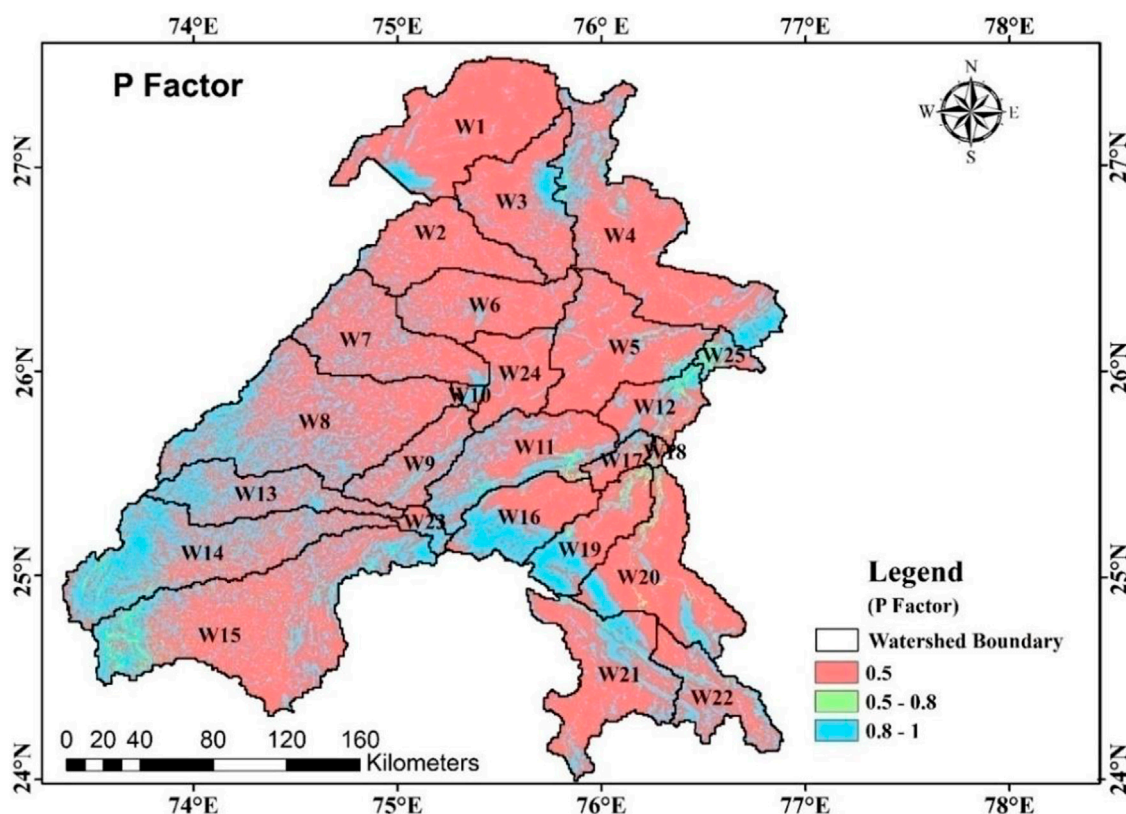


FIGURE 9
p factor map of the study basin.

granular, and 4 for blocky, platy or massive), and p = profile permeability class (1 for rapid, 2 for moderate to rapid, 3 for moderate, 4 for slow to moderate, 5 for slow and 6 for very slow).

2.3.6 Slope length steepness factor (LS)

This is a combined factor for indicating the joint effect of slope length (L) and slope steepness (S) on soil erosion rate/soil loss (Amsalu and Mengaw, 2014). The LS factor was appraised using the “flow accumulation” raster, which contains data on the cumulative number of pixels contributing to flow into a specific cell. The flow direction matrix was used for obtaining the flow accumulation matrix. The “flow direction matrix” governs the natural drainage direction/path for all cells in a DEM. On the basis of the low accumulation matrix, the size of each pixel and pixel slope, and LS factor were computed using a raster calculator in GIS based environment. The equation for computing the LS factor as reported by Panagos et al. (Panagos et al., 2015) is given below:

$$LS = (\text{flowaccumulation} \times \text{cell size}/22.13)^{0.20} \times (0.0065 \times \text{slope}^2 + 0.045 \times \text{slope} + 0.065) \quad (5)$$

Where, flow accumulation = accumulate dup-slope contributing area for a given cell, cell size = size of a grid cell (i.e., 12.5 m × 12.5 m in the present case), and slope = cell slope (%).

2.3.7 Cover/crop management factor (C)

This parameter governs the effect of LULC on soil erosion rate or soil loss in relation to the kinetic energy and impact of raindrops

on land/soil surface (Sujatha and Sridhar, 2018). The crop/plant cover on the ground/land surface prevents splash/raindrop erosion through a reduction in raindrop impact force. It is dependent on plant type, stage of growth, and extent of land use cover. The C-value varies from 0.0 to 1.0. The higher C-value (nearly 1.0) designates a higher vulnerability of the soil to erosion (Ganasri and Ramesh, 2016). Here, the C-value was allocated as per the type of land use as given in Table 2 (USDA, 1972; Marondedze and Schütt, 2020). The map of the C-factor was created by reclassifying the LULC map.

2.3.8 Support and conservation practices factor (P)

This parameter (p) shows the effect of different conservation practices such as contouring, strip cropping, and bunding on soil erosion/loss rate. It is termed as a ratio of soil loss from a piece of land under a particular support/conservation practice to the equivalent soil loss with no support/conservation practice. The p -value varies from 0.0 to 1.0, being highest for up and down cultivation. The databases used to formulate input files for the RUSLE model are presented in Table 1. The p -value in the present case was allotted on the basis of land use types (Table 2).

2.3.9 Soil loss (A)

Considering the appraised factors of RUSLE as different layers in the map calculator, the average soil loss was estimated on annual basis, along with its dispersal in the region under consideration. For

TABLE 4 The area under different severity classes (very low, low, medium, high, and extreme) of soil loss.

Watershed	Very low		Low		Medium		High		Extreme		Total area
	Area		Area		Area		Area		Area		ha
	ha	%	ha	%	ha	%	ha	%	ha	%	
WS1	28450.0	1.7	381941.5	8.4	35134.6	7.0	1185.4	1.9	2133.8	4.4	448845.3
WS2	25842.1	1.6	210530.1	4.6	13391.2	2.7	474.2	0.8	0.0	0.0	250237.7
WS3	31057.9	1.9	228785.6	5.0	29225.7	5.8	1659.6	2.7	0.0	0.0	290728.8
WS4	100523.4	6.1	421060.3	9.2	51755.1	10.3	2845.0	4.6	1659.6	3.4	577843.4
WS5	39830.0	2.4	291612.7	6.4	16435.4	3.3	1659.6	2.7	3082.1	6.3	352619.8
WS6	53343.8	3.2	195356.8	4.3	5551.9	1.1	1659.6	2.7	237.1	0.5	256149.1
WS7	67331.7	4.1	218116.8	4.8	26656.2	5.3	4504.6	7.2	0.0	0.0	316609.3
WS8	215034.7	13.0	353491.5	7.8	40070.8	8.0	5452.9	8.7	237.1	0.5	614287.1
WS9	38170.4	2.3	110243.8	2.4	12367.3	2.5	1422.5	2.3	5215.8	10.7	167419.9
WS10	5452.9	0.3	4741.7	0.1	1312.7	0.3	4978.8	8.0	0.0	0.0	16486.0
WS11	92699.6	5.6	175678.9	3.9	29544.2	5.9	3319.2	5.3	711.3	1.5	301953.2
WS12	36036.7	2.2	84638.8	1.9	13464.4	2.7	0.0	0.0	4030.4	8.3	138170.3
WS13	102657.2	6.2	107635.9	2.4	17252.6	3.4	2133.8	3.4	948.3	2.0	230627.7
WS14	238743.1	14.4	202706.4	4.4	34408.6	6.9	3793.3	6.1	1185.4	2.4	480836.9
WS15	238268.9	14.4	469899.5	10.3	47877.4	9.6	3793.3	6.1	2845.0	5.9	762684.1
WS16	94596.3	5.7	114511.3	2.5	8022.5	1.6	0.0	0.0	711.3	1.5	217841.3
WS17	5927.1	0.4	37222.1	0.8	9144.4	1.8	0.0	0.0	237.1	0.5	52530.7
WS18	2133.8	0.1	6875.4	0.2	1346.7	0.3	0.0	0.0	948.3	2.0	11304.2
WS19	55951.7	3.4	110006.7	2.4	24419.5	4.9	0.0	0.0	3082.1	6.3	193460.0
WS20	59982.1	3.6	265059.3	5.8	15026.7	3.0	1659.6	2.7	7112.5	14.6	348840.3
WS21	51684.2	3.1	264111.0	5.8	25394.9	5.1	12802.5	20.5	9720.4	20.0	363713.1
WS22	15884.6	1.0	128499.3	2.8	29662.5	5.9	6164.2	9.9	3319.2	6.8	183529.7
WS23	14225.0	0.9	20152.1	0.4	951.6	0.2	0.0	0.0	237.1	0.5	35565.8
WS24	15410.4	0.9	137271.3	3.0	6759.2	1.4	2845.0	4.6	237.1	0.5	162523.1
WS25	24419.6	1.5	15410.4	0.3	5433.8	1.1	0.0	0.0	711.3	1.5	45975.0
Total	1653657.3	100.0	4555559.3	100.0	500610.0	100.0	62353.0	100.0	48602.1	100.0	6820781.7

the factors R , K , C , and p , the raster layers were created in $10\text{ m} \times 10\text{ m}$ resolution, whereas, for the LS factor, it was in $12.5\text{ m} \times 12.5\text{ m}$ resolution. Further, the DEM was resampled into $10\text{ m} \times 10\text{ m}$ resolution using the “bilinear method” for creating the LS map for carrying out the perfect overlay analysis. The average annual soil loss was estimated using pixel-based information of all the factors of the $RUSLE$ model for each pixel having a spatial resolution of $10\text{ m} \times 10\text{ m}$. For developing erosion severity map of the study area, the assessed soil loss was characterized as very low ($0.0\text{--}1.0\text{ t ha}^{-1}\text{ year}^{-1}$), low ($1.0\text{--}5.0\text{ t ha}^{-1}\text{ year}^{-1}$), medium ($5.0\text{--}10.0\text{ t ha}^{-1}\text{ year}^{-1}$), high ($10.0\text{--}50.0\text{ t ha}^{-1}\text{ year}^{-1}$) and extreme ($>50.0\text{ t ha}^{-1}\text{ year}^{-1}$). This classification was adopted by Pham et al. (Pham et al., 2018).

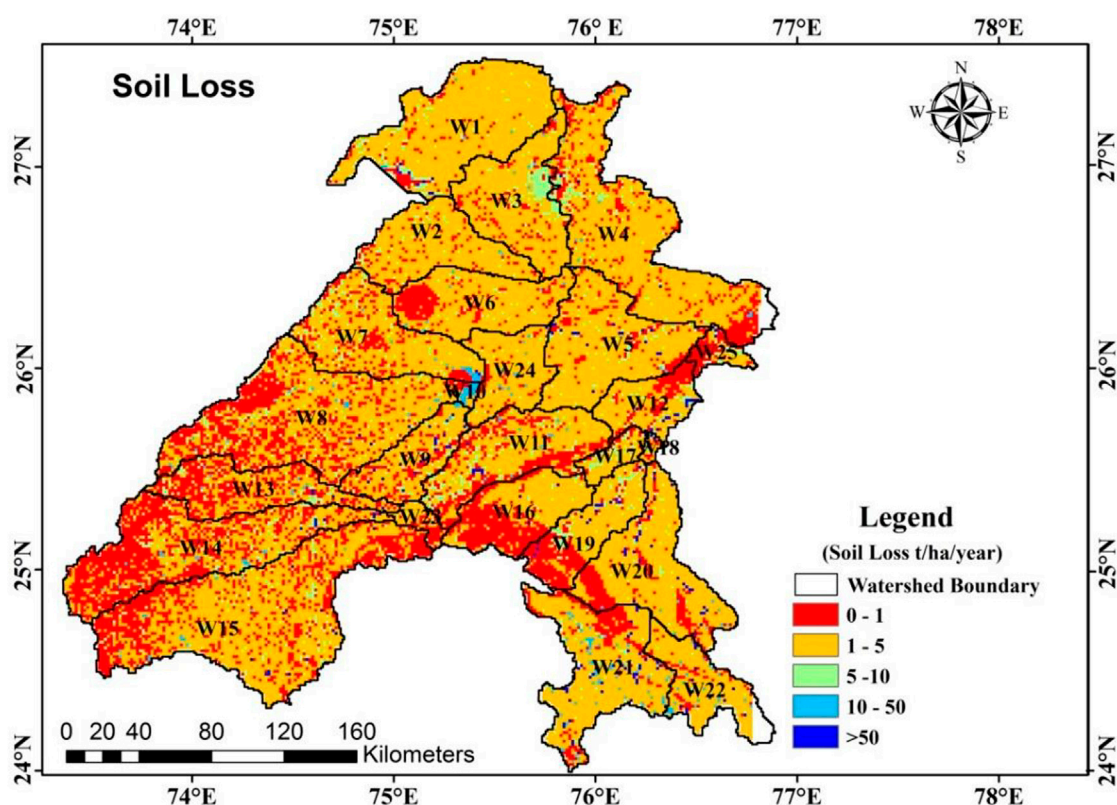
Figure 3 demonstrates the complete methodology adopted for the implementation of the present study.

2.4 Prioritization of watersheds

After the estimation of the soil loss, a priority ranking of all 25 sub-watersheds was done for identifying the highly erosion/soil loss-affected area. The watersheds having the highest and lowest values of average annual soil loss were designated with highest and lowest ranks, respectively for implementation of land and water conservation measures.

TABLE 5 Average annual soil loss under different severity classes in Banas basin.

Soil loss category	Average annual soil loss (t.ha ⁻¹ . year ⁻¹) interval	Area (ha)	Area (%)	Total annual soil loss (t. year ⁻¹)	Average annual soil loss (t.ha ⁻¹ .year ⁻¹)	Total annual soil loss (%)
Very Low	0–1	1653657.3	24.2	1261427.6	0.8	5.8
Low	1–5	4555559.3	66.8	13547258.3	3.0	62.2
Medium	5–10	500610.0	7.3	2993754.3	6.0	13.8
High	10–50	62353.0	0.9	1437416.5	23.1	6.6
Extreme	>50	48602.1	0.7	2526192.2	52.0	11.6
Total		6820781.7	100.0	21766048.8	84.7	100.0

FIGURE 10
Soil loss map of the basin.

3 Results and discussion

3.1 Land use land cover (LULC) of the study area

The study area is mainly occupied by cropland (66.35%), three major crops (wheat, barley, and maize) are grown over this region (Dubey and Sharma, 2018) followed by grassland (17.54%), shrub land (5.43%), barren/sparse vegetation (4.14%), built-up (2.85%), forest (2.34%), water body (1.30%) and wetland (0.05%). The area under cropland varies from 35.69% to 86.64%, being the lowest and highest in WS25 and WS1, respectively. The area under grassland ranges from

0.0% to 35.06%, being the lowest and highest in WS18 and WS16, respectively. The area under shrubland varies from 0.0% to 15.88%, being the lowest and highest shares in WS18 and WS25, respectively. The area under barren/sparse vegetation ranges from 1.56% to 15.01%, being the lowest and highest in WS10 and WS17, respectively. The area under built-up varies from 0.63% to 10.33%, being the lowest and highest in WS25 and WS3, respectively. The area under forest varies from 0.04% to 15.57%, being the lowest and highest in WS1 and WS25, respectively. The area under water bodies varies from 0.09% to 36.62%, being lowest and highest in WS3 and WS10, respectively. The area under wetland varies from 0.0% to 0.78%, being highest in WS25. The area under different LULCs is given in Table 3.

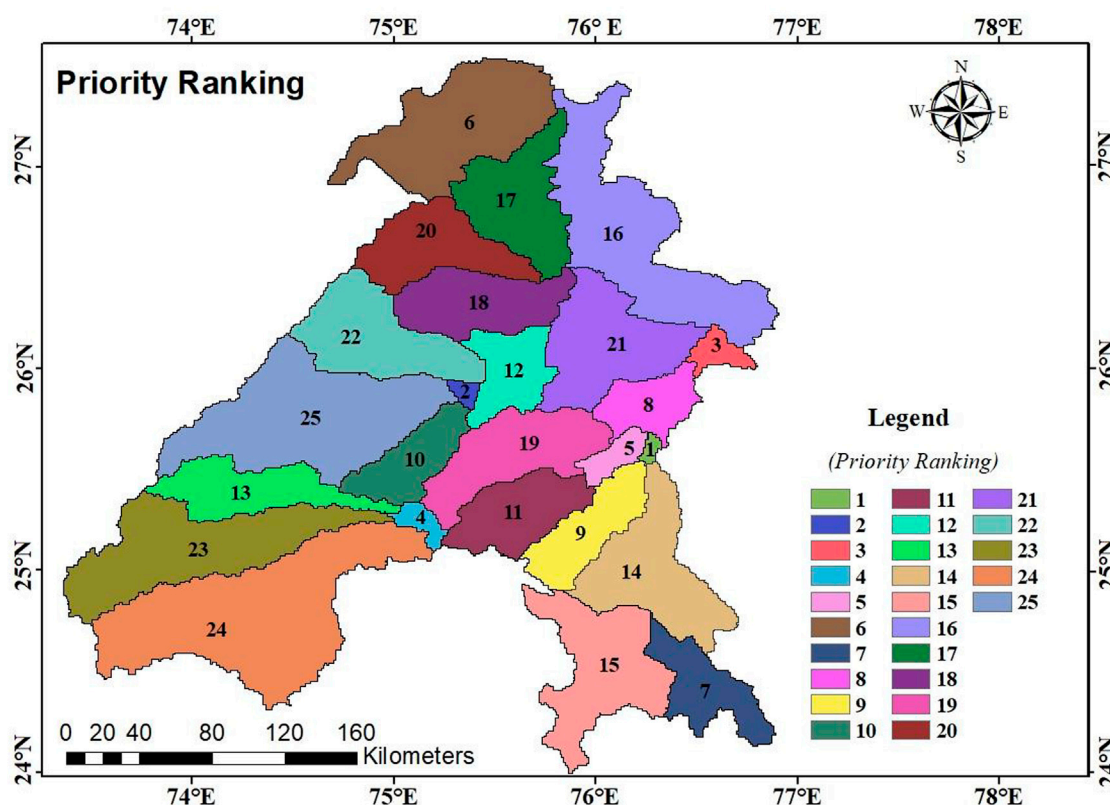


FIGURE 11

Priority ranking of the watershed in relation to the severity of soil loss from their catchments.

3.2 Watershed slope

The slope of the Banas basin varied from <2 to 90% as indicated in Figure 4. The greater slopes of watersheds in this basin make this region highly susceptible to soil loss in relation to the generation of speedy runoff, resulting in severe water erosion with minimum scope for groundwater recharge. The Aravalli axis divides this region into two-halves; therefore, the region exhibits a sharp change from steep land to a flat river plain.

3.3 Parameters of RUSLE

The R-value varied in the range of 147.41–443.85 MJ.mm.ha⁻¹.h⁻¹ year⁻¹ in the Banas basin. Figure 5 shows the map indicating the low to high values of R with different colors. The red and dark blue colors indicate the lowest and highest R values, respectively. The erosivity rate is high in the eastern part than in the western part of the basin due to the high rainfall amount in the eastern part. Studies report that the north-eastern part of the Banas River Basin shows high potential evapotranspiration, therefore erosivity is higher due to less of soil moisture in the soil, while the rest of the area shows low potential evapotranspiration rate indicating less erosivity in the region (Kalyan et al., 2021). The K-factor varied in the range of 0.11–0.15 t.ha.h.MJ⁻¹.mm⁻¹ as indicated in Figure 6. The maximum area of the basin was dominated by K-value in the range of

0.12–0.13 t.ha.h.MJ⁻¹.mm⁻¹, followed by 0.13–0.15 t.ha.h.MJ⁻¹.mm⁻¹ and 0.11–0.12 t.ha.h.MJ⁻¹.mm⁻¹. The LS factor varied from <0.06 to 56.76%. The major part of the basin is dominated by and LS-value of 56.31%–56.76%, followed by 55.87%–56.31%, 54.31%–55.87%, and 0.06%–54.31%. Figure 7 shows the LS-factor map of the basin. LS-factor helps to identify the places with a sudden change in slope, which are more prone to erosion as a result of the accelerated motion of the river channels in this region. Earlier studies have also reported presence of tectonic sub-blocks in the region from hypsometric analysis of this basin showing horst-graben structures (Sinha-Roy, 2002), therefore it is clear that water erosion is active in this region due to unstable slope. The C-factor of the basin varied from 0.001 to 0.629. The basin is dominated by C-value in the range of 0.280–0.629, followed by 0.001–0.003, 0.090–0.280, and 0.003–0.090. Figure 8 shows the C-factor map of the basin. The C-value is directly proportional to the LULC spread over the region. Therefore, the major land cover spread has two distinct ranges of C-factor as 0.280–0.680, which represents the agricultural area, and 0.001 or 0.003 is the area covered by shrub or barren land. The P-factor varied from 0.5 to 1.0, indicating the non-applicability of the conservation strategies in the basin for soil management. The basin is dominated with a *p*-value of 0.5, followed by 0.8–1.0 and 0.5–0.8. The entire arable land falls under *p*-value 0.5 as forest land and built-up, and scrub. Shrubland falls under the *p*-value of 0.8–1.0. The *p*-value ranging from 0.5 to 0.8 is almost insignificant in the region. Figure 9 shows the P-factor map of the basin.

TABLE 6 Soil loss under different severity classes and priority ranking of watersheds in terms of average annual soil loss.

Watershed	Very low (0–1)	Low (1–5)	Medium (5–10)	High (10–50)	Extreme (>50)	Total annual soil loss (t.year ⁻¹)	Total area (ha)	Total soil (t.ha ⁻¹ .year ⁻¹)	Priority rank
	Soil loss (t.year ⁻¹)								
WS1	51468.0	2541100.0	85350.2	112500.0	93645.6	2884063.8	448845.3	6.4	6
WS2	12268.0	333000.0	17450.2	93105.0	48744.6	504567.8	250237.7	2.0	20
WS3	66668.0	399700.0	83150.2	61105.0	42644.6	653267.8	290728.8	2.2	17
WS4	76368.0	1301458.3	129850.2	69405.0	49344.6	1626426.0	577843.4	2.8	16
WS5	54968.0	387500.0	117750.2	49005.0	58844.6	668067.8	352619.8	1.9	21
WS6	12368.0	287800.0	81500.0	68205.0	108944.6	558817.6	256149.1	2.2	18
WS7	40768.0	347100.0	59250.2	14205.0	51444.6	512767.8	316609.3	1.6	22
WS8	35868.0	401200.0	98600.7	69305.0	62844.6	667818.3	614287.1	1.1	25
WS9	28068.0	409300.0	135450.2	46805.0	52544.6	672167.8	167419.9	4.0	10
WS10	50868.0	353300.0	52750.2	78500.0	98244.6	633662.8	16486.0	38.4	2
WS11	25968.0	395600.0	77350.2	45131.5	71744.6	615794.2	301953.2	2.0	19
WS12	32668.0	437800.0	49450.2	58605.0	39744.6	618267.8	138170.3	4.5	8
WS13	20268.0	401200.0	88650.2	99705.0	124920.6	734743.8	230627.7	3.2	13
WS14	35268.0	419700.0	92350.2	20705.0	173244.6	741267.8	480836.9	1.5	23
WS15	51468.0	450000.0	161550.2	63105.0	138244.6	864367.8	762684.1	1.1	24
WS16	23968.0	368300.0	92000.0	93005.0	136244.6	713517.6	217841.3	3.3	11
WS17	95281.8	209400.0	82100.0	14305.0	142544.6	543631.4	52530.7	10.3	5
WS18	27668.0	390700.0	350650.2	9205.0	181244.6	959467.8	11304.2	84.9	1
WS19	28268.0	401900.0	116450.2	62000.0	199044.6	807662.8	193460.0	4.2	9
WS20	75768.0	481100.0	185050.2	60200.0	200044.6	1002162.8	348840.3	2.87	14
WS21	95681.8	525500.0	318450.2	69000.0	35244.5	1043876.5	363713.1	2.87	15
WS22	95768.0	514500.0	287350.2	58900.0	30644.6	987162.8	183529.7	5.4	7
WS23	98268.0	241600.0	114250.2	40200.0	143744.6	638062.8	35565.8	17.9	4
WS24	25668.0	320400.0	26250.2	23105.0	122744.6	518167.8	162523.1	3.2	12
WS25	99768.0	1228100.0	90750.2	58105.0	119544.6	1596267.8	45975.0	34.7	3
Total	1261427.6	13547258.3	2993754.3	1437416.5	2526192.2	21766048.8	6820781.7	244.8	

3.4 Area under different soil loss categories

The areas under different severity classes (very low, low, medium, high, and extreme) of soil loss are reported in Table 4. The area under the very low category of soil loss was recorded in the range of 0.1%–14.4%, being lowest (2,134 ha) and highest (238,743 ha) in WS18 and WS14, respectively. Under the low soil loss category, the area varied from 0.1% to 10.3%, being lowest (4,742 ha) and highest (469,900 ha) in WS10 and WS15, respectively. The area under the medium soil loss category varied in the range of 0.2%–10.3%, being lowest (952 ha) and highest (51,755 ha) in WS23 and WS4, respectively. Under the high soil loss category, the area varied in the range of 0.0%–20.5%, being lowest (0.0 ha) and highest (12,803 ha) in WS12 and WS21, respectively. The

area under the extreme soil loss category varied from 0.0% to 20.0%, being lowest (0.0 ha) and highest (9,720 ha) in WS7 and WS21, respectively. Irrespective of the different soil loss categories, the area under soil loss was recorded in the range of 0.2%–11.2%, being lowest (16,486 ha) and highest (762,684 ha) in WS10 and WS15, respectively.

3.5 Soil loss and priority ranking of watersheds

The total area under very low, low, medium, high, and extreme soil loss categories was recorded as 24.2, 66.8, 7.3, 0.9, and 0.7%, being the lowest and highest under extreme and low soil loss categories,

respectively. The total soil loss was computed as 5.8% (1261427.6 t year⁻¹), 62.2% (13547258.3 t year⁻¹), 13.8% (2993754.3 t year⁻¹), 6.6% (1437416.5 t year⁻¹) and 11.6% (2526192.2 t year⁻¹) under very low, low, medium, high and extreme soil loss categories (Table 5), being lowest and highest under very low and low soil loss categories. The average annual soil loss under five respective defined categories was obtained as 0.8, 3.0, 6.0, 23.1, and 52.0 t ha⁻¹ year⁻¹, being lowest and highest under very low and extreme soil loss categories, respectively. Figure 10 shows the soil loss under different severity categories. The soil loss under the very low soil loss category was recorded in the range of 1.0%–7.9%, being lowest (12,268 t year⁻¹) and highest in WS2 (99,768 t year⁻¹) and WS25, respectively. Under the low category, the soil loss was computed as 1.5%–18.8%, being lowest (209,400 t year⁻¹) and highest (2,541,100 t year⁻¹) in WS17 and WS1, respectively. In the medium category, the soil loss ranged from 0.6% to 11.7%, being lowest (17,450 t year⁻¹) and highest (350,650 t year⁻¹) in WS2 and WS18, respectively. Similarly, under the high category, the soil loss was computed in the range of 0.6%–7.8%, being lowest (9,205 t year⁻¹) and highest (112,500 t year⁻¹) in WS18 and WS1, respectively. Under the extreme category, the soil loss was computed in the range of 1.2%–7.9%, being lowest (30,645 t year⁻¹) and highest (199,045 t year⁻¹) in WS22 and WS19, respectively. Irrespective of the different soil loss categories, the total soil loss varied in the range of 2.4%–13.3%, being lowest (512,768 t year⁻¹) and highest (2,884,064 t year⁻¹) in WS7 and WS1, respectively. The average annual soil loss varied from 0.4% to 34.7%, being lowest (1.1 t ha⁻¹ year⁻¹) and highest (84.9 t ha⁻¹ year⁻¹) in WS8 and WS18, respectively. The average annual soil loss among different watersheds was recorded in the range of 1.1–84.9 t ha⁻¹ year⁻¹. It was recorded to be highest (84.9 t ha⁻¹ year⁻¹), followed by WS10 (38.4 t ha⁻¹ year⁻¹), SW25 (34.7 t ha⁻¹ year⁻¹) and WS23 (17.9 t ha⁻¹ year⁻¹), whereas lowest was recorded in WS8 (1.1 t ha⁻¹ year⁻¹), WS18 obtained the highest/top priority rank in terms of the average annual soil loss (84.9 t ha⁻¹ year⁻¹) to be considered for land and water conservation planning and implementation (Figure 11). Table 4 demonstrates the area under different severity classes of soil loss. The soil loss under different severity classes and priority ranking of watersheds in terms of average annual soil loss is presented in Table 6.

4 Conclusion

Application of the RUSLE model integrated with the GIS environment proved to be the easiest approach for computing soil loss through sheet and rill erosion and predicting erosion risk zones in the Banas basin. The remote sensing and GIS coupled use of the RUSLE model predicted the average annual soil loss of about 0.8, 3.0, 6.0, 23.1, and 52.0 t ha⁻¹ year⁻¹ under the soil loss categories of very low (0–1 t ha⁻¹ year⁻¹), low (1–5 t ha⁻¹ year⁻¹), medium (5–10 t ha⁻¹ year⁻¹), high (10–50 t ha⁻¹ year⁻¹) and extreme (>50 t ha⁻¹ year⁻¹), respectively. The soil loss was recorded to be highest (84.9 t ha⁻¹ year⁻¹) in WS18 (1st rank), because this region is the junction point where the Aravalli hills take a steep slope and divides the flow of Banas river in two major directions towards the East and West, followed by WS10 (38.4 t ha⁻¹ year⁻¹), which is located in the semi-arid part of the basin and prone to high erosion, as it is the fringe area where the climatic and anthropogenic units change

abruptly, SW25 (34.7 t ha⁻¹ year⁻¹) which is a region affected by the high inflow of the Banas river in the Eastern part and WS23 (17.9 t ha⁻¹ year⁻¹), whereas it was lowest (25th rank) for WS8 (1.1 t ha⁻¹ year⁻¹), which is located in a stable region without much interference of the river, climate and anthropogenic activities. The total annual soil loss from the basin was recorded as 21766048.8 tons. About 24.2, 66.8, 7.3, 0.9, and 0.7% area of the Banas basin fall under very low, low, medium, high, and extreme soil loss categories, respectively. This study opens the eyes of researchers working in the domain of land and water management. It is strongly recommended to carry out studies pertaining to the estimation of soil loss through gully erosion using high-resolution datasets to understand micro level impacts because this increases rate of land degradation and also affects dams or reservoirs located on the catchments, which further impacts the socio-economic life of the people in the region. Most erosion-affected watersheds of the basin in relation to priority ranking should be considered for land and water conservation planning and implementation. The output of the present study would be useful to policymakers, land use planners, and decision-makers in planning and implementing land and water conservation measures in the problematic areas/watersheds of the Banas basin for controlling soil loss through water erosion.

Data availability statement

The raw data supporting the conclusion of this article will be made available by the authors, without undue reservation.

Author contributions

Conceptualization, MS and KS; methodology, MS; software, KS; validation, MS, PA and VV; formal analysis, KS; investigation, MS and KS; writing—original draft preparation, MS, KS, NA-A, PA, VV, and AM; writing—review and editing, MS, KS, NA-A, PA, VV, and AM; visualization, MS, KS, NA-A, PA, VV, and AM; supervision, MS, KS, NA-A, PA, VV, and AM; project administration, NA-A; funding acquisition, NA-A All authors have read and agreed to the published version of the manuscript.

Conflict of interest

The authors declare that the research was conducted in the absence of any commercial or financial relationships that could be construed as a potential conflict of interest.

Publisher's note

All claims expressed in this article are solely those of the authors and do not necessarily represent those of their affiliated organizations, or those of the publisher, the editors and the reviewers. Any product that may be evaluated in this article, or claim that may be made by its manufacturer, is not guaranteed or endorsed by the publisher.

References

- Abdelwahab, O. M., Ricci, G. F., DeGirolamo, A. M., and Gentile, F. (2018). Modelling soil erosion in a mediterranean watershed: Comparison between SWAT and ann AGNPS models. *Environ. Res.* 166, 363–376. doi:10.1016/j.envres.2018.06.029
- Ahmad, N. S., Mustafa, F. B., and Didams, G. A. (2020). Systematic review of soil erosion control practices on the agricultural land in Asia. *Int. Soil Water Conserv. Res.* 8, 103–115. doi:10.1016/j.iswcr.2020.04.001
- Amellah, O., and El Morabiti, K. (2021). Assessment of soil erosion risk severity using GIS, remote sensing and RUSLE model in OuedLaou Basin (north Morocco). *Soil Sci. annu.* 72, 1–11. doi:10.37501/soilsa/142530
- Amsalu, T., and Mengaw, A. (2014). GIS based soil loss estimation using RUSLE model: The case of jabi tehinan worda, ANRS, Ethiopia. *Resour* 05, 616–626. doi:10.4236/nr.2014.511054
- Angima, S. D., Stott, D. E., O'Neill, M. K., Ong, C. K., and Weesies, G. A. (2003). Soil erosion prediction using RUSLE for central Kenyan highland conditions. *Agric. Ecosyst. Environ.* 97, 295–308. doi:10.1016/s0167-8809(03)00011-2
- Beasley, D. B., Huggins, L. F., and Monke, A. (1980). Answers: A model for watershed planning. *Trans. ASAE* 23, 0938–0944. doi:10.13031/2013.34692
- Borrelli, P., Robinson, D. A., Panagos, P., Lugato, E., Yang, J. E., Alewell, C., et al. (2020). Land use and climate change impacts on global soil erosion by water (2015–2070). *Proc. Natl. Acad. Sci. U. S. A.* 117, 21994–22001. doi:10.1073/pnas.2001403117
- Boufala, M., ElHmaidf, A., Chadli, K., Essahlaoui, A., ElOuali, A., and Lahjouj, A. (2020). Assessment of the risk of soil erosion using RUSLE method and SWAT model at the M'dez Watershed, Middle Atlas, Morocco. *E3S Web Conf.* 150, 03014. doi:10.1051/e3sconf/202015003014
- Chahar, B. R., and Dhaka, S. K. (2013). "Groundwater modeling of Banas River basin," in *World environmental and water resources congress* (Cincinnati, Ohio: Showcasing the Future), 450–459. doi:10.1061/9780784412947.044
- Chen, Z., Wang, L., Wei, A., Gao, J., Lu, Y., and Zhou, J. (2019). Land-use change from arable lands to orchards reduced soil erosion and increased nutrient loss in a small catchment. *Sci. Total Environ.* 648, 1097–1104. doi:10.1016/j.scitotenv.2018.08.141
- Das, S., Deb, P., Bora, P. K., and Katre, P. (2021). Comparison of RUSLE and MMF soil loss models and evaluation of catchment scale best management practices for a mountainous watershed in India. *Sustainability* 13, 232. doi:10.3390/su13010232
- Du, Q., Li, G., Chen, D., Zhou, Y., Qi, S., Wu, G., et al. (2021). SBAS-InSAR-Based analysis of surface deformation in the eastern tianshan mountains, China. *Front. Earth Sci.* 9, 729454. doi:10.3389/feart.2021.729454
- Dubey, S. K., and Sharma, D. (2018). Assessment of climate change impact on yield of major crops in the Banas River Basin, India. *Total Environ.* 635, 10–19. doi:10.1016/j.scitotenv.2018.03.343
- Dubey, S. K., Sharma, D., and Mundetia, N. (2015). Morphometric analysis of the Banas River Basin using the geographical information system, Rajasthan, India. *J. Hydrol.* 3, 47–54. doi:10.11648/j.hyd.20150305.11
- Eniyew, S., Teshome, M., Sisay, E., and Bezabih, T. (2021). Integrating RUSLE model with remote sensing and GIS for evaluation soil erosion in Telkwon Watershed, Northwestern Ethiopia. *Remote. Sens. Appl. Soc. Environ.* 24, 100623. doi:10.1016/j.rsase.2021.100623
- Everard, M., Sharma, O. P., Vishwakarma, V. K., Khandal, D., Sahu, Y. K., Bhatnagar, R., et al. (2018). Assessing the feasibility of integrating ecosystem-based with engineered water resource governance and management for water security in semi-arid landscapes: A case study in the Banas catchment, Rajasthan, India. *Total Environ.* 612, 1249–1265. doi:10.1016/j.scitotenv.2017.08.308
- Farhan, Y., Zregat, D., and Nawaiseh, S. (2014). Assessing the influence of physical factors on spatial soil erosion risk in. *North. Jordan. Am. J. Sci.* 10 (7), 29–39.
- Fenta, A. A., Yasuda, H., Shimizu, K., Haregeweyn, N., and Negussie, A. (2016). Dynamics of soil erosion as influenced by watershed management practices: A case study of the agula watershed in the semi-arid highlands of northern Ethiopia. *Manage* 58, 889–905. doi:10.1007/s00267-016-0757-4
- Ganasri, B. P., and Ramesh, H. (2016). Assessment of soil erosion by RUSLE model using remote sensing and GIS - a case study of Nethra-vathi Basin. *Geo. Sci. Front.* 7, 953–961. doi:10.1016/j.gsf.2015.10.007
- Gosain, A. K., Mani, A., and Dwidivi, C. (2009). Hydrological modelling-literature review. *Adv. Fluid Mech.* 339, 63–70.
- Jaydhar, A. K., Pal, S. C., Saha, A., Islam, A. R., and Ruidas, D. (2022). Hydrogeochemical evaluation and corresponding health risk from elevated arsenic and fluoride contamination in recurrent coastal multi-aquifers of eastern India. *J. Clean. Prod.* 369, 133150. doi:10.1016/j.jclepro.2022.133150
- Kalyan, S., Sharma, D., and Sharma, A. (2021). Spatio-temporal variation in desert vulnerability using desertification index over the Banas River Basin in Rajasthan, India. *Arab. J. Geosci.* 14, 54. doi:10.1007/s12517-020-06417-0
- Kaur, B., Sur, K., Verma, V. K., and Pateriya, B. (2022). Implications of watershed management programs for sustainable development in rural scenario—a case study from foothills of Punjab state, India. *Water Conserv.* 7, 647–655. doi:10.1007/s41101-022-00170-z
- Kayet, N., Pathak, K., Chakrabarty, A., and Sahoo, S. (2018). Evaluation of soil loss estimation using the RUSLE model and SCS-CN method in hillslope mining areas. *Int. Soil Water Conserv. Res.* 6, 31–42. doi:10.1016/j.iswcr.2017.11.002
- Kumar, R., Deshmukh, B., and Kumar, A. (2022). Using Google earth engine and GIS for basin scale soil erosion risk assessment: A case study of Chambal River Basin, central India. *J. Earth SystSci* 131, 228. doi:10.1007/s12040-022-01977-z
- Lal, R. (2019). "Adaptation and mitigation of climate change by improving agriculture in India," in *Climate change and agriculture in India: Impact and adaptation* (Cham: Springer), 217–227. doi:10.1007/978-3-319-90086-5_17
- Marondedze, A. K., and Schütt, B. (2020). Assessment of soil erosion using the RUSLE model for the Epworth district of the Harare Metropolitan Province, Zimbabwe. *Sustainability* 12, 8531. doi:10.3390/su12208531
- Mondal, A., Khare, D., and Kundu, S. (2016). A comparative study of soil erosion modelling by MMF, USLE and RUSLE. *Geo. Carto. Int.* 33, 89–103. doi:10.1080/10106049.2016.1232313
- Mundetia, N., Sharma, D., and Dubey, S. K. (2018). Morphometric assessment and sub-watershed prioritization of Khari River basin in semi-arid region of Rajasthan, India. *Arab. J. Geo. Sci.* 11, 530. doi:10.1007/s12517-018-3819-5
- Nampak, H., Pradhan, B., Mojaddadi, R. H., and Park, H. J. (2018). Assessment of land cover and land use change impact on soil loss in a tropi-cal catchment by using multi temporal SPOT -5 satellite images and revised universal soilloss equation model. *Land Degrad. Dev.* 29, 3440–3455. doi:10.1002/ldr.3112
- Ouyang, W., Hao, F., Skidmore, A. K., and Toxopeus, A. G. (2010). Soil erosion and sediment yield and their relationships with vegetation cover in upper stream of the Yellow River. *Yellow River. Sci. Total Environ.* 409, 396–403. doi:10.1016/j.scitotenv.2010.10.020
- Pal, S. C., and Chakraborty, R. (2019a). Simulating the impact of climate change on soil erosion in sub-tropical monsoon dominated watershed based on RUSLE, SCS runoff and MIROC5 climatic model. *Adv. Space Res.* 64, 352–377. doi:10.1016/j.asr.2019.04.033
- Pal, S. C., and Chakraborty, R. (2019b). Modeling of water induced surface soil erosion and the potential risk zone prediction in a sub-tropical watershed of Eastern India. *Environ* 5, 369–393. doi:10.1007/s40808-018-0540-z
- Pal, S. C., Chakraborty, R., Roy, P., Chowdhuri, I., Das, B., Saha, A., et al. (2021). Changing climate and land use of 21st century influences soil erosion in India. *Gondwana Res.* 94, 164–185. doi:10.1016/j.gr.2021.02.021
- Panagos, P., Borrelli, P., Meusburger, K., Poesen, J., Alewell, C., vanderZanden, E. H., et al. (2015). Modelling the effect of support practices (P-factor) on the reduction of soil erosion by water at European scale. *Environ. Sci. Policy* 51, 23–34. doi:10.1016/j.envsci.2015.03.012
- Park, S., Oh, C., Jeon, S., Jung, H., and Choi, C. (2011). Soil erosion risk in Korean watersheds, assessed using the revised universal soil loss equation. *J. Hydrol.* 399, 263–273. doi:10.1016/j.jhydrol.2011.01.004
- Pham, T. G., Degener, J., and Kappas, M. (2018). Integrated universal soil loss equation (USLE) and Geographical Information System (GIS) for soil erosion estimation in A Sap basin: Central Vietnam. *Int. Soil Water Conserv. Res.* 6, 99–110. doi:10.1016/j.iswcr.2018.01.001
- Práválie, R. (2021). Exploring the multiple land degradation pathways across the planet. *Earth-Science Rev.* 220, 103689. doi:10.1016/j.earscirev.2021.103689
- Ranzi, R., Le, T. H., and Rulli, M. C. (2012). A RUSLE approach to model suspended sediment load in the Lo River (Vietnam): Effects of reservoirs and land use changes. *J. Hydrol.* 422–423, 17–29. doi:10.1016/j.jhydrol.2011.12.009
- Rao, C. S., Gopinath, K. A., Prasad, J. V. N. S., and Singh, A. K. (2016). Climate resilient villages for sustainable food security in tropical India: Concept, process, technologies, institutions, and impacts. *Adv. Agron.* 140, 101–214. doi:10.1016/b.s.agron.2016.06.003
- Reddy, R. (2003). Land degradation in India: Extent, costs and determinants. *Econ. Polit. Wkly.* 38, 4700–4713.
- Renard, K. G., Foster, G. R., Weesies, G. A., and Porter, J. P. (1991). Rusle: Revised universal soil loss equation. *J. Soil Water Conserv.* 46, 30–33.
- Ruidas, D., Pal, S. C., Islam, A. R. M., and Saha, A. (2021). Characterization of ground-water potential zones in water-scarce hardrock regions using data driven model. *Environ. Earth Sci.* 80, 1–18. doi:10.1007/s12665-021-10116-8
- Ruidas, D., Chandra Pal, S., Saha, A., Chowdhuri, I., and Shit, M. (2022). Hydrogeochemical characterization based water resources vulnerability assessment in India's first Ramsar site of Chilkalake. *Mar. Pollut. Bull.* 184, 114107. doi:10.1016/j.marpolbul.2022.114107
- Ruidas, D., Chakraborty, R., Reza Md Islam, A., Saha, A., and Pal, S. C. (2022). A novel hybrid of meta-optimization approach for flash flood-susceptibility assessment in a monsoon-dominated watershed, Eastern India. *Environ. Earth Sci.* 81, 145–222. doi:10.1007/s12665-022-10269-0

- Ruidas, D., Pal, S. C., Islam, T., Md, A. R., and Saha, A. (2022). Hydrogeochemical evaluation of groundwater aquifers and associated health hazard risk mapping using ensemble data driven model in a water scares plateau region of eastern India. *Expo. Health* 14, 1–19. doi:10.1007/s12403-022-00480-6
- Safwan, M., Alaa, K., Omran, A., Quoc, B. P., Nguyen, T. T. L., Van, N. T., et al. (2021). Predicting soil erosion hazard in Lattakia Governorate (WSyria). *Int. J. Sediment. Res.* 36, 207–220. doi:10.1016/j.ijsrc.2020.06.005
- Sharda, V. N., and Ojasvi, P. R. (2016). A revised soil erosion budget for India: role of reservoir sedimentation and land-use protection measures: A revised soil erosion budget for India. *Earth Surf. Process. Landf.* 41, 2007–2023. doi:10.1002/esp.3965
- Sharma, A. (2010). Integrating terrain and vegetation indices for identifying potential soil erosion risk area. *Geo. Spat. Inf. Sci.* 13, 201–209. doi:10.1007/s11806-010-0342-6
- Sharma, A., Sharma, D., Panda, S. K., Dubey, S. K., and Pradhan, R. K. (2018). Investigation of temperature and its indices under climate change scenarios over different regions of Rajasthan state in India. *Planet. Chang.* 161, 82–96. doi:10.1016/j.gloplacha.2017.12.008
- Sinha-Roy, S. (2002). Hypsometry and landform evolution: A case study in the Banas drainage basin, Rajasthan, with implications for Aravalli uplift. *Journal-Geological Soc. India* 60 (1), 7–26.
- Srinivasan, R., Karthika, K. S., Suputhra, S. A., Chandrakala, M., and Hegde, R. (2021). Mapping of soil erosion and probability zones using remote sensing and GIS in arid part of south Deccan Plateau India. *J. Ind. Soc. Remote Sens.* 2021 (49), 2407–2423. doi:10.1007/s12524-021-01396-5
- Sujatha, E. R., and Sridhar, V. (2021). Landslide susceptibility analysis: A logistic regression model case study in coonoor, India. *India Hydrol.* 8, 41. doi:10.3390/hydrology8010041
- Sujatha, E., and Sridhar, V. (2018). Spatial prediction of erosion risk of a small mountainous watershed using RUSLE: A case-study of the palarsub-watershed in kodaikanal, south India. *Water* 10, 1608. doi:10.3390/w10111608
- Sur, K., and Chauhan, P. (2019). Imaging spectroscopic approach for land degradation studies: A case study from the arid land of India. *Geomatics, Nat. Hazards Risk* 10, 898–911. doi:10.1080/19475705.2018.1552629
- Thapa, P. (2020). Spatial estimation of soil erosion using RUSLE modeling: A case study of dolakha district, Nepal. *Environ. Syst. Res.* 9, 15. doi:10.1186/s40068-020-00177-2
- Tiwari, A. K., Risse, L. M., and Nearing, M. A. (2000). Evaluation of WEPP and its comparison with USLE and RUSLE. *Trans. ASAE* 43, 1129–1135. doi:10.13031/2013.3005
- USDA (1972). “Soil conservation service, national engineering handbook, section 4 chapters,” in *Hydrology* (Washington, D.C., 4–10).
- Wijesundara, N. C., Abeysingha, N. S., and Dissanayake, D. (2018). GIS-Based soil loss estimation using RUSLE model: A case of kirindi oya River Basin, Sri Lanka. *Environ* 4, 251–262. doi:10.1007/s40808-018-0419-z



OPEN ACCESS

EDITED BY

Faisal Mumtaz,
Aerospace Information Research Institute
(CAS), China

REVIEWED BY

Amit Kumar,
Central University of Jharkhand, India
Jamil Hasan Kazmi,
University of Karachi, Pakistan

*CORRESPONDENCE

Nadhir Al Ansari,
✉ nadhir.alansari@ltu.se

SPECIALTY SECTION

This article was submitted to Land Use
Dynamics,
a section of the journal
Frontiers in Environmental Science

RECEIVED 04 December 2022

ACCEPTED 06 March 2023

PUBLISHED 21 March 2023

CITATION

Rahman G, Chandio NH, Moazzam MFU
and Al Ansari N (2023), Urban expansion
impacts on agricultural land and thermal
environment in Larkana, Pakistan.
Front. Environ. Sci. 11:1115553.
doi: 10.3389/fenvs.2023.1115553

COPYRIGHT

© 2023 Rahman, Chandio, Moazzam and
Al Ansari. This is an open-access article
distributed under the terms of the
[Creative Commons Attribution License](#)
(CC BY). The use, distribution or
reproduction in other forums is
permitted, provided the original author(s)
and the copyright owner(s) are credited
and that the original publication in this
journal is cited, in accordance with
accepted academic practice. No use,
distribution or reproduction is permitted
which does not comply with these terms.

Urban expansion impacts on agricultural land and thermal environment in Larkana, Pakistan

Ghani Rahman¹, Noor Hussain Chandio²,
Muhammad Farhan Ul Moazzam³ and Nadhir Al Ansari^{4*}

¹Department of Geography, University of Gujrat, Gujrat, Pakistan, ²Department of Geography, Shah Abdul Latif University, Khairpur, Pakistan, ³Department of Civil Engineering, College of Ocean Science, Jeju National University, Jeju-si, Republic of Korea, ⁴Department of Civil, Environmental and Natural Resources Engineering, Lulea University of Technology, Lulea, Sweden

Urban area expansion and the increase in the built-up area are major threats to agriculture, the natural environment, and ecology throughout the world. The population of the city of Larkana is rapidly increasing due to natural growth and uncontrolled migration from the surrounding areas, which have resulted in a haphazard increase in the built-up area over the fertile agricultural land and affected the city's thermal environment. This research aims to evaluate the impacts of urban area expansion on agricultural land and the thermal environment of the study area by assessing the change in land use/ land cover (LULC) from 1990 to 2020 and land surface temperature (LST). For this purpose, the Random Forest (RF) algorithm was applied, and LST was calculated in Google Earth Engine (GEE) using Landsat imageries for the years 1990, 2000, 2010, and 2020. For the RF classifier algorithm, 3500 reference random points were generated for each year, which were then randomly divided into two datasets, i.e., a training sample consisting of 70% of the points and a validation dataset (30% of the points). After LULC classification, the results were validated for 1990, 2000, 2010, and 2020, and the accuracy was 88.3%, 89%, 90.01%, and 90.8%, respectively. The study results showed that the built-up area increased from 12.31 to 43.83 km² while the barren land in the study region decreased from 56.51 km² to 11.62 km². The agricultural land was 66.66 km² in 1990, expanded to 101.38 km², and then decreased to 79.49 km² in 2020. The results also revealed that most of the urban expansion in the last decade (2010–2020) took place on agricultural land. The urban thermal environment also showed a gradual increase in surface temperature as recorded by the LST results. The LST results revealed that the maximum LST was 33.4°C in 1990, which increased to 36.1°C in 2020, and similarly, the minimum LST was 25.1°C, which also increased to 26.6°C in 2020. This study provides useful results for stakeholders to devise better policies and plans to control further haphazard urban expansion on fertile agricultural land in the study area.

KEYWORDS

urban expansion, land use land cover change, thermal environment, agriculture, Larkana

1 Introduction

Globally, the agriculture sector is facing several threats like water scarcity, rising temperatures, drought, and urban expansion. Urbanization is a major cause of the conversion of agricultural land into the built-up area due to rapid economic growth, new industrial zones, and migration from rural areas toward towns and cities around the world. The global population is continuously increasing, from 2.5 billion people in 1950 (Al-Thawwad, 2008; Chandio and Shirazi, 2022) to 8 billion today, according to United Nations reports. The unprecedented global population growth is the result of improvements in the health sector, including medication, personal hygiene, and nutrition, which resulted in an increase in human life expectancy. Global data on urbanization also show an increase in population, particularly in the last two decades (Chandio and Shirazi, 2022). Asia is home to 4.7 billion (60%) of the world's population. In North America, 82% of the population, in the Caribbean region 81%, in Europe 74% and in Oceania 68% are settled in urban areas due to the availability of basic human facilities (UN-DESA, 2018; Chandio and Shirazi, 2022). Developing countries have been facing rapid population growth and urban sprawl for the past few decades, and the trend is expected to continue in the future, which is also the case in Pakistan (Ashraf et al., 2022). High population growth and a lack of basic amenities in rural areas have caused rural-urban migration and land use/ land cover change (LULC) from one form to another, such as from agricultural to the built-up area (Moazzam et al., 2022; Yousafzai et al., 2022). Globally, it is estimated that by 2030, 60% of people will be living in urbanized localities (Ashraf et al., 2022; Ashraf et al., 2023). Urbanization is not only the increase in population but also the expansion of residential and commercial areas, boosting the demand for basic amenities like transportation, education, water supply, and sanitation, and ultimately converting agricultural land and areas covered by natural vegetation into a built-up area (Aliyu and Amadu, 2017; Yousafzai et al., 2022). The increase in the built-up area results in a number of environmental issues, such as affecting local and regional temperatures and aggravating the problem of food security (Sun et al., 2018; Farid et al., 2022).

Urban expansion triggers the expansion of the built-up area, recreational parks, and public infrastructure, encroaching on the vast agricultural and open areas surrounding a city. The increase in the built-up environment due to these human interruptions raises the urban temperature, decreases soil infiltration due to the increase in impervious areas, and thus leads to water runoff, resulting in disasters like urban heat waves and urban flooding (Rahman et al., 2019; Zou et al., 2021). Surface energy balance and urban flooding have risen because of urbanization, which has led to naturally high permeable surfaces being replaced by artificial, low-permeable surfaces (Rizwan et al., 2008; Wang et al., 2019; Zou et al., 2021). Among other impacts of urban expansion, it has taken over fertile agricultural land and intensified the issue of food security (Khan, 2019). The target of zero hunger in the Sustainable Development Goals has become a challenge to achieve by the year 2030 (Gandharum et al., 2022).

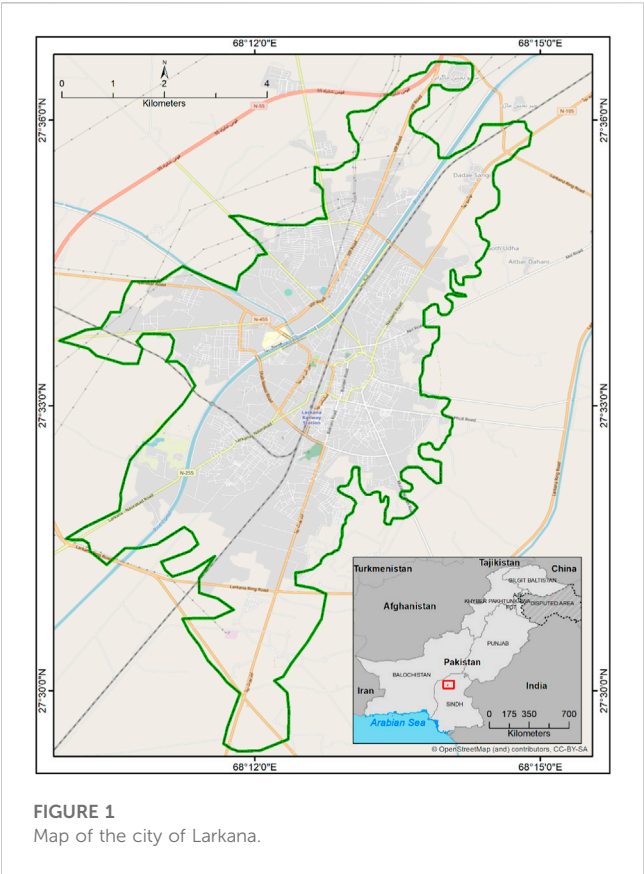
Remote sensing imagery is an important tool for monitoring changes in LULC and urban expansion (Mehdi et al., 2021). In particular, their high temporal resolution helps to monitor the rate of change and identify the possible causative factors (Gul et al., 2022;

Tariq et al., 2022). The long-term temporal availability of Landsat images makes it easier to identify past LULC and detect temporal changes (Butt et al., 2015). No one can deny the role of remote sensing in mapping and monitoring LULC changes over short timescales with greater accuracy at a low or no cost (Gul et al., 2022). Working with the Google Earth Engine (GEE) since 2010, the use of remote sensing images has become more attractive as this online platform provides global scale analysis capabilities and access to multiple catalogs of satellite images, i.e., Landsat, Sentinel, MODIS, and so on (Gandharum et al., 2022). Machine learning algorithms such as the Random Forest algorithm (RF) can be used for the classification of satellite images using GEE, and these algorithms provide high accuracy of more than 90% (Gandharum et al., 2022; E. Nyland et al., 2018; Thanh Noi and Kappas, 2017).

Like other developing countries in the world, Pakistan is also facing the problem of rapid population growth and urban expansion, and it is reported that this trend will continue in the future (Gul et al., 2022). The proportion of the urban population in Pakistan was 17.8% in 1951, which increased to 36% in 2017 (GOP, 2017). This abrupt increase in urban population has led to the expansion of urban areas, which has had negative consequences such as the degradation of drinking water quality, the lowering of groundwater levels, food security issues, poor water supply, and poor sanitation, often creating other related problems such as urban flooding and urban heat island phenomena. Sindh is the most urbanized province as compared to other provinces of Pakistan (Ul Din and Mak, 2021). Due to the high level of urbanization, the land resources of Sindh province have been degraded, including the saline and waterlogged fertile soil, and its freshwater resources depleted, while the infrastructure facilities are in shambles (Panhwar, 2020). Larkana is the fourth most populous city in Sindh province. This study focuses on urban expansion in the city of Larkana and its impact on agricultural land. The impact of urban expansion on the thermal environment of the city is also evaluated. To date, no such study has been conducted in Larkana. This research analyzes the spatial and temporal changes in LULC, linking the changes in LULC with the changes in agricultural land and the urban thermal environment between 1990 and 2020.

2 Study area

Larkana, situated on the right bank of the Indus, is the fourth most populous city in Sindh province after Karachi, Hyderabad, and Sukkur and the fifteenth largest in Pakistan in terms of population. Larkana is one of Pakistan's historic and intermediate cities. In 1951, its population was only 34,000, which increased to 490,508 in 2017 (GOP, 2017). The city extends from 27°48' to 27°61' north latitude and 68°16' to 68°24' east longitude (Figure 1). Geographically, the district has an even topography and is rich in agriculture, and it is known as the "Paris of Pakistan" (Britannica, 2013). During the British era, Larkana was known as the "Garden of Sindh", but lost this status due to rapid urbanization. Larkana's history may be traced back to the Moen-Jo Daro Indus Valley Civilization, which was founded around 2500 BC. Generally, the population has migrated three times from rural areas toward Larkana in the last three decades. First, when Zulfikar Ali Bhutto was Prime Minister and declared the city the Paris of Pakistan, he established the Chandka Medical College



in 1973. Secondly, when Benazir Bhutto was Prime Minister, she redesigned the city, establishing new educational institutions. In 1988, Larkana was given the status of a division and gained more significance as the administrative and service hub of northern Sindh. Thirdly, during the superfloods of 2010, when a large number of people migrated from the different areas of Kamber-Shahdadt, Dadu, and Shikarpur districts to settle near the Larkana city area. On all these three occasions, human migration was attracted, which changed the territorial boundaries of Larkana: significant changes in land use and land cover were observed.

3 Materials and methods

In the current research, the Landsat satellite images from the years 1990, 2000, 2010, and 2020 from the United States Geological Survey (USGS) have been used. The Landsat imageries for the years 1990, 2000, and 2010 were sourced from the Landsat 5 Thematic

Mapper (TM) satellite, whereas the image for 2020 was from the Landsat 8 Operational Land Image (OLI) satellite (Table 1).

3.1 Image classification using a random forest algorithm

The surface reflectance products of Landsat images from each year were used for land use/ land cover classification in Google Earth Engine (GEE). The cloud mask function was applied to get cloud-free pixels. The normalized difference built-up index (NDBI), the normalized difference water index (NDWI), and the normalized difference vegetation index (NDVI) were calculated for each Landsat image. The NDBI was calculated using the NIR and SWIR bands (for Landsat 5, the formula is (Band 5-Band 4) / (Band 5 + Band 4); for Landsat 8, the formula is (Band 6 - Band 5) / (Band 6 + Band 5). Gao (1996) developed the Normalized Difference Water index in order to enhance water bodies. This index uses the NIR and SWIR bands [for Landsat 5, NDWI = (Band 4 - Band 5) / (Band 4 + Band 5), while for Landsat 8 the formula is (Band 5 - Band 6) / (Band 5 + Band 6)]. Similarly, the NDVI uses the NIR and red bands [for Landsat 5, NDVI = (Band 4 - Band 3) / (Band 4 + Band 3), while for Landsat 8 the formula is NDVI = (Band 5 - Band 4) / (Band 5 + Band 4)].

To classify the Landsat images for the years 1990, 2000, 2010, and 2020, the random reference points were generated for four major land use categories, i.e., barren, built-up, water bodies, and agricultural land. Nearly 3500 reference points were generated for each year, of which 70% were used as training samples to create land use maps using the RF algorithm, and the remaining 30% was used for validation purposes. After obtaining LULC maps for each year, an accuracy assessment was performed for each LULC map using validation reference points, and an error matrix was employed to produce overall accuracy for each LULC map.

For the assessment of change in LULC, the classification results were used to observe the trend of land use change in Larkana and analyzed in ArcGIS 10.8. The LULC maps were categorized into four classes: built-up areas, water bodies, agricultural land, and barren land. The built-up area includes residential, commercial, and other urban areas like roads, etc., while the agricultural land includes natural vegetation, cropland, and orchards. The results were then further assessed to calculate the temporal land use change using the following equation:

$$r = 100 \times \frac{A2 - A1}{A1} \times \frac{1}{t2 - t1} \tag{1}$$

where t1 is the initial time, t2 is the final time, A1 is the land use class cover at the initial time, and A2 is the class cover at the final time.

Furthermore, the land surface temperature (LST) for each temporal image was calculated using Google Earth Engine. The

TABLE 1 Satellite data information and color composite band combinations

Year	Satellite sensor	Spatial resolution	Acquisition date	Band combination
1990	Landsat TM 5	30 m × 30 m	1990-02-01	Band 4, Band 3, Band 2
2000	Landsat TM 5	30 m × 30 m	2000-02-13	Band 4, Band 3, Band 2
2010	Landsat TM 5	30 m × 30 m	2010-02-24	Band 4, Band 3, Band 2
2020	Landsat OLI 8	30 m × 30 m	2020-02-20	Band 5, Band 4, Band 3

LST data were then downloaded, and the map was prepared in ArcGIS 10.8. The LST minimum and maximum were acquired from each temporal image for further interpretation. The LST was also analyzed with respect to each land use class in this study. The LST was extracted from the thermal bands of Landsat satellite imagery using the following procedure:

3.1.1 Digital number (DN) to spectral radiance conversion

The data received by thermal sensors were converted to radiance using the following equation:

$$L_{\lambda} = M_L Q_{cal} + A_L \quad (2)$$

where L_{λ} is the TOA spectral radiance (Watts/ (m² * srad * μm); and M_L is the band-specific multiplicative rescaling factor; A_L is the band-specific additive rescaling factor; and Q is the quantized and calibrated standard product pixel values (DN).

3.1.2 Conversion to at-satellite brightness temperature

Band data can then be converted from spectral radiance to top-of-atmosphere brightness temperature using the thermal constants provided in the metadata file by Eq. 3.

$$T_b = K_2 / \ln(K_1 / L_{\lambda} + 1) \quad (3)$$

In the above equation, T or T_b is the top-of-atmosphere brightness temperature (K); L_{λ} is the TOA spectral radiance (Watts/ (m² * srad * μm); K_1 is the band-specific thermal conversion constant available in the metadata; and K_2 is the band-specific thermal conversion constant available in the metadata file.

3.1.3 Land surface temperature

The LST was retrieved using a single-channel algorithm, using a single thermal band of the imagery. For this purpose, band 6 was used for Landsat 5 while band 10 was used for Landsat 8 LST calculations. The annual mean LST has been derived using Google Earth Engine. There is a 15 minutes time lag between Landsat 8 and Landsat 5 satellite equatorial crossing time (Mumtaz et al., 2023) but the mean annual value of LST is not that much affected by this time lag. The emissivity-corrected LST was derived using the Arties and Carnahan (1982) procedure.

$$LST = BT / \left[1 + w * \left(\frac{BT}{p} \right) * \ln(e) \right] \quad (4)$$

In Eq. 4, BT = at satellite temperature, where w is the wavelength of the emitted radiance; $p = h * c / s$ (1.438 * 10⁻² m K); h is the Planck constant (6.626 * 10⁻³⁴ J s); s is the Boltzmann constant; c is the speed of light (2.998 * 10⁸ m/s); e is the emissivity.

LSE, or Land Surface Emissivity, can be defined as the ratio of the energy radiated from the surface of a material to that radiated by a black body at the same temperature and wavelength, under the same viewing conditions. It is calculated based on Eq. 5.

$$LSE = 0.004 * P_v + 0.986 \quad (5)$$

where P_v means vegetation proportion, derived using Eq. 6:

$$P_v = \sqrt{(NDVI - NDVI_{min} / NDVI_{max} - NDVI_{min})} \quad (6)$$

The normalized difference vegetation index (NDVI) in this study was calculated using red and near-infrared bands using the following equation:

$$NDVI = \frac{NIR - RED}{NIR + RED} \quad (7)$$

Conversion of LST from Kelvin to Celsius

The retrieved LST is in Kelvin and was converted to Celsius using Eq. 8.

$$LST - 273.15 \quad (8)$$

All these formulae were set in GEE for both Landsat 5 and Landsat 8 imagery, and the mean annual LST was derived for each study period. The maximum, minimum, and mean LST for each LULC class were calculated using zonal statistics in ArcGIS.

3.2 Validation

The results of LULC maps derived through the RF algorithm in GEE were validated using the 30% sample points. For this purpose, the kappa coefficient technique was used in this study. The 30% validation dataset points were used to compare the original land use type to the classified image. For this purpose, the value of the classified image assigned to each point was extracted using ArcGIS, and then the original image and Google Earth imagery were used as reference data. An error matrix table was generated to quantify and summarize the total accuracy of the classified images. The results showed good performance of the RF algorithm for LULC classification. The overall accuracy in 1990 was 88.3%, 89% in 2000, 90.01% in 2010, and 90.8% in 2020.

4 Results

4.1 Land use/ land cover analysis

The multi-temporal satellite-based LULC mapping for the years 1990, 2000, 2010, and 2020 was categorized into barren land, built-up area, water bodies, and agricultural land. Agricultural land includes orchards and cropland. For each respective year, the Landsat satellite images were converted to color composite with bands 4,3, and 2 RGB for Landsat 5 and 5,4, and 3 for Landsat 8 satellite, using the standard false color composite band combination (Figures 2, 3). The land use for the multi-temporal years was generated from the Landsat 5 and Landsat 8 images using the RF algorithm classification method in GEE. The multi-temporal satellite-based LULC mapping results exhibited a high increase in the built-up area, which was 12.31 km² in 1990 and rose to 19.87 km² in 2000, 23.38 km² in 2010, and 43.83 km² in 2020 (Figures 2, 3, 4). In 1990, the built-up area was only 8.62%, which grew to 13.99% in 2000, 16.68% in 2010, and 30.70% of the total study area in the year 2020 (Figure 5B). During the period 1990-2010, it took two decades to double the built-up area, while during the period 2010-2020, it doubled again in just one decade. This surge in the built-up area was the result of a number of factors, including the special

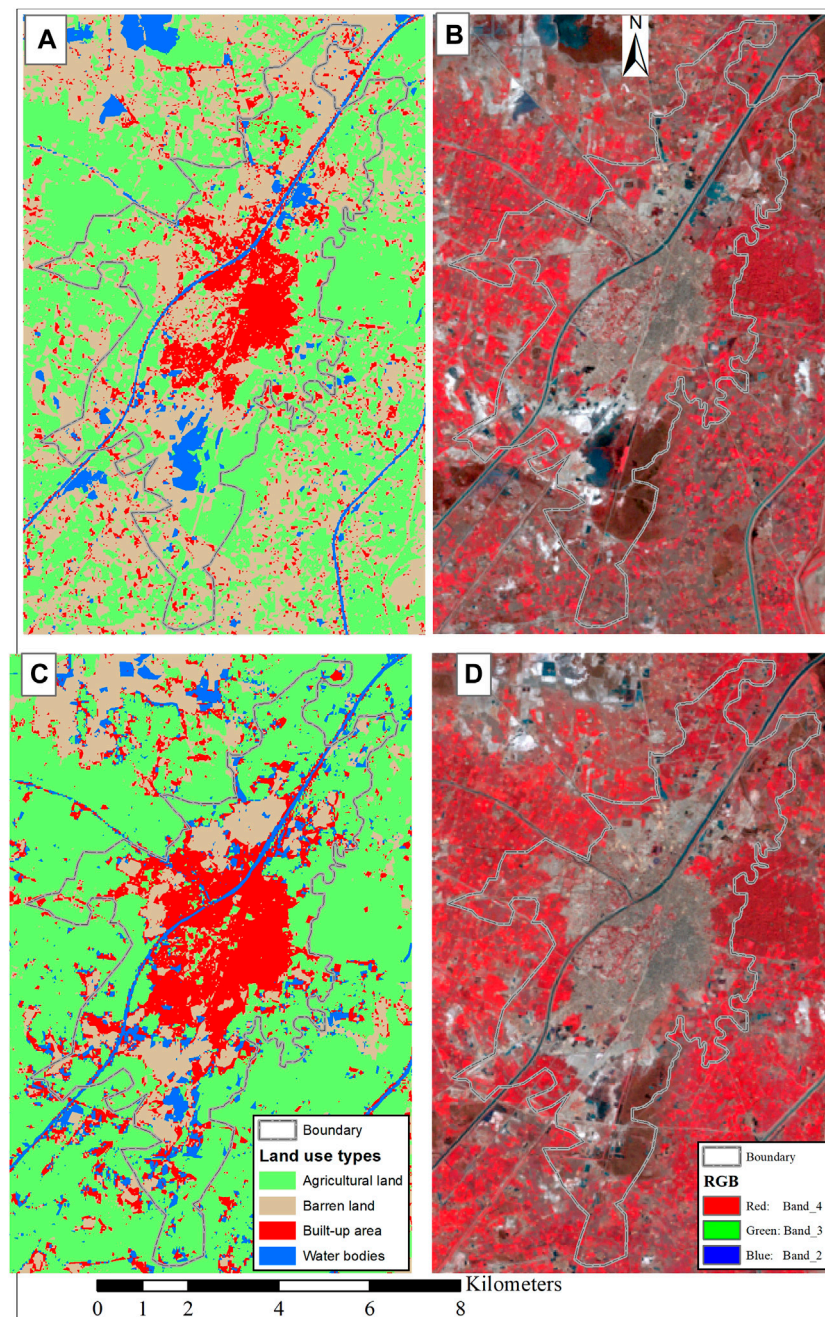


FIGURE 2

LULC maps of Larkana City for the years 1990 and 2000 (A) LULC map for the year 1990 (B) Landsat 5 color composite image for the year 1990 with FCC bands combination (C) LULC for the year 2000 (D) Landsat 5 color composite image for the year 2000 with FCC bands combination.

attention given to the city of Larkana during the People's Party government in 1988-1990, 1993-1996, and 2008-2013. During 1988-1990, Larkana was upgraded to a division, a number of educational and health institutions were built, and housing colonies like OPF and Sindh Green Housing Society were initiated, which boosted the expansion of the city. During the 1993-1996 government, the city was given further attention, and the Board of Intermediate and Secondary Education Larkana was established in 1995. The city continued to grow to the southwest

and northeast with the construction of new roads, a bus terminal, new hospitals, some new educational institutions, planned housing settlements, and small industrial areas. In the LULC map of 1990, most of the barren land is actually the land that has been cleared for different development projects in the city area. The expansion of the built-up area in 1990-2010 was almost all around the city center with a few patches in the surrounding areas, but in 2020 the city expanded along the main canal and to the west. The other factors contributing to the increased built-up

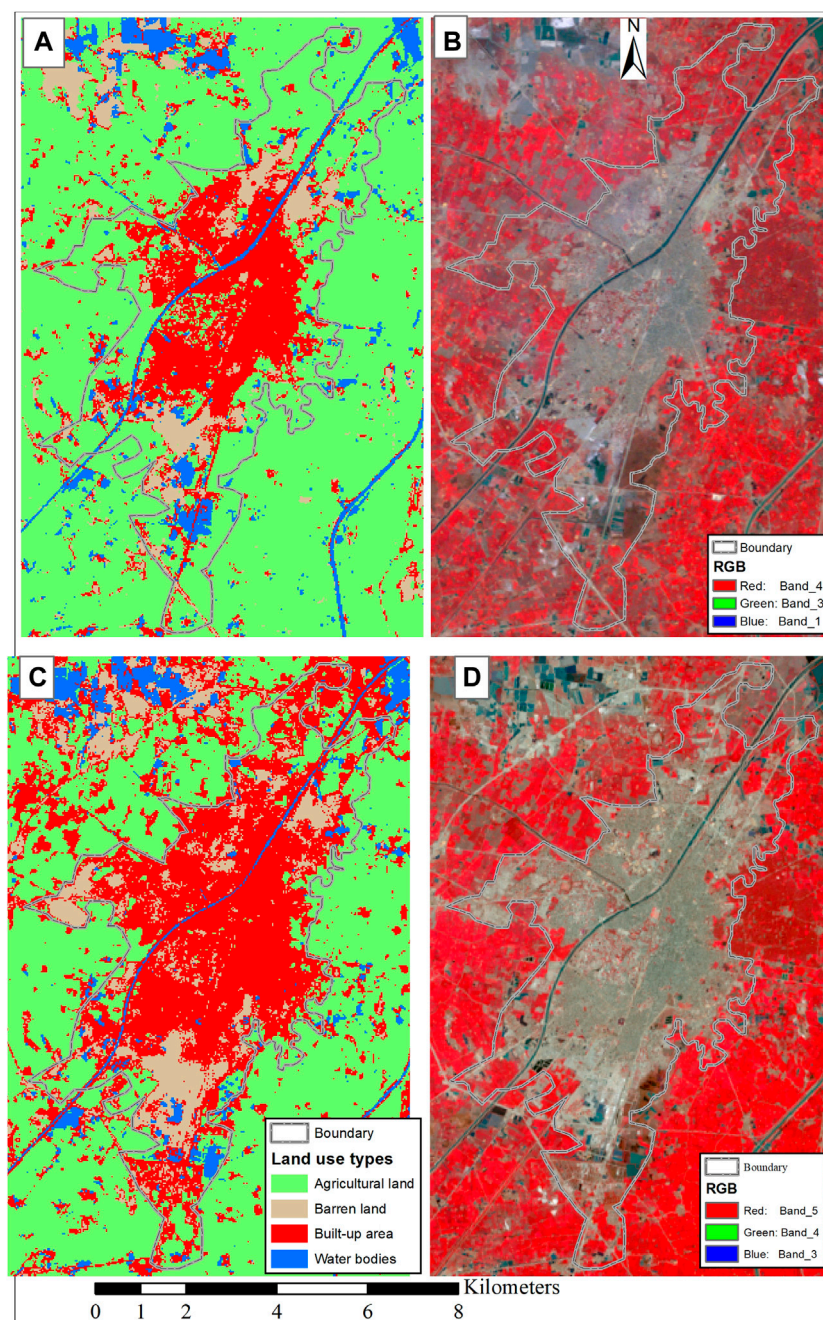


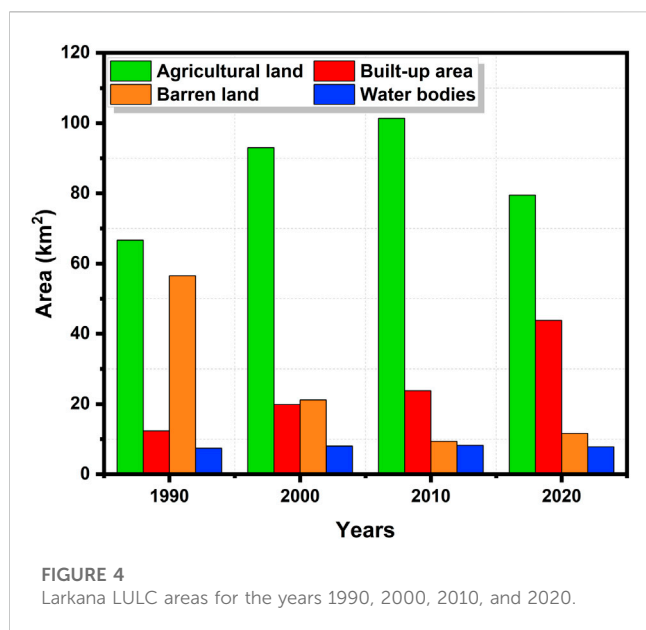
FIGURE 3

LULC maps of Larkana for the years 2010 and 2020 (A) LULC for the year 2010 (B) Landsat 5 color composite image for the year 2010 with FCC bands combination (C) LULC for the year 2020 (D) Landsat 8 color composite image for the year 2020 with FCC bands combination.

area of Larkana include the natural growth of the population and people's migration from the suburbs seeking a safe place and jobs after the massive 2010 floods. The results showed that during 1990–2010, the built-up area and agricultural land expanded over the barren land (Figures 2, 3), and the same was confirmed by the local inhabitants, who said that there was a massive amount of waterlogged and saline land up until 1990, which was later converted to agricultural land. In 1990 and 2000, barren land

was the second largest LULC category, while from 1990 to 2020, agricultural land remained dominant in the study area, which substantially decreased in the last two decades, i.e., between 2010 and 2020 (Figures 4, 5).

Agricultural land accounted for 45.65% of all land in 1990, gradually increasing to 71.02 % by 2010 and decreasing again to 55% by 2020 (Figure 5A). From 1990 to 2010, barren land was the second largest LULC category in terms of area occupied, which



was overtaken by built-up area in 2010, thus becoming the second largest LULC category with 16.68% of the total area in 2010 and 30.70% of the total area in 2020. The built-up area in the study area expanded in all directions during the period 2010–2020, mainly along the major communication routes (Figure 2). A huge change was observed in the built-up area between 2010 and 2020, where it increased from 16.68% in 2010 to 30.70% in 2020 at the expense of agricultural and barren land in the study area. The major reason for this was the mass migration from nearby areas affected by the 2010 floods, especially from Kamber-Shahdaktot, Dadu, and Shikarpur districts and other rural areas. The population spread to the western side after the 2010 floods, mainly because the area is safer from floods than the eastern side. The new expansion on the western side also included government development such as the extension of the industrial area and the building of warehouses for rice sellers. Some new housing projects were also launched and developed on the western side of the city after 2010. The barren land in the study region decreased from 39.55% in 1990 to 8.14% in 2020. This is due to the conversion of the built-up area into agricultural land. The fourth category of LULC is water bodies in Larkana city. From the analysis, an increase in water bodies was observed in the study area. This increase is due to the intensification of inland fish farming (Figure 4D).

The results revealed that the agricultural land in the study area increased from 1990 until 2010 (Figures 4, 5A). In 1990, the total area covered by agricultural land amounted to 46.65% and it increased to 65.48% in 2010, to 71.02% in 2010, and it decreased again to 55.69% in 2020. According to the field observation and discussion with the local elders, the increase in agricultural land in Larkana and its surrounding areas is the result of clearing and converting the waterlogged and saline areas into agricultural land. Most of the surrounding areas in the northern and southern parts of the city neighboring were once waterlogged and saline, and were later converted to agricultural land with support from the local community and the government. After 2010, the agricultural land

decreased and the major reason is the continuous increase in the built-up area; the current study also found that the majority of agricultural land was used to expand the urban area. Therefore, we can observe that the built-up area has an incrementing trend. The relative change in the built-up area between 1990 and 2000 was 5.4%, which increased to 14% between 2010 and 2020 (Figures 4, 5B).

The overall LULC area in 1990 and 2020 and their respective changes in percentage have been shown in Table 2 and Figure 7. The results indicate that agricultural land increased by 19.24% during the study period, while the increase in the built-up area was 256.00%. The barren land in the study area decreased by almost 79.44% during the study period (Figure 7). The increase in the built-up area has grabbed the barren land and agricultural land, in the study area. Most of the changes in the built-up area were observed between 2010 and 2020 and the main reason was a mass migration from the surrounding areas after the 2010 floods. A slight increase in water bodies was observed from the study results, amounting to 5.23% (Table 2). The increase in water bodies is due to an increase in fish farming in the study region.

In this study, the change from one land use category to another was calculated (Figure 8). For this purpose, the post-classification change detection technique was applied to quantify the change in each land use category between 1990 and 2020. The change matrix technique was adopted for this purpose to analyze the LULC changes. The LULC conversion from one category to another is represented by a two-way cross-matrix, and its corresponding value was calculated from 1990 to 2020. The largest LULC change, measuring 28.71 km², went from barren land to agricultural land, followed by barren land to a built-up area (18.13 km²). Similarly, a 12.63 km² area of agricultural land was converted into a built-up area during the last three decades (Figure 8). During the same period, 3.15 km² of agricultural land was converted into barren land.

4.2 LULC and land surface temperature

In this study, we also used the Landsat thermal band to calculate the land surface temperature (LST) of the study area. The LST map was arranged into five different classes (Figure 9A). It can be observed that in 1990, the temperature of the study area was generally under 28°C. There were only a few patches of temperature class $\geq 32.1^\circ\text{C}$ because most of Larkana was covered with agricultural/open land and the built-up area was smaller (Figures 6, 8A). As the agricultural land decreased and the built-up area increased, the surface temperature started to rise and continued to do so until 2020. In the year 2020, more than 80% of the area within the city boundary experienced high surface temperatures because impervious surfaces absorb more heat, which is the main reason for high temperatures in cities (Moazzam et al., 2022). It can be observed that in 2000 and 2010, the patches of high surface temperatures grew, but in 2020, the high surface temperature expanded over the city border zone and the surrounding temperature also remained high (Figure 9A).

The Figure 9B revealed that the research area's mean minimum and mean maximum temperatures grew steadily over the course of the investigation. In 1990, the minimum temperature was 25.1°C,

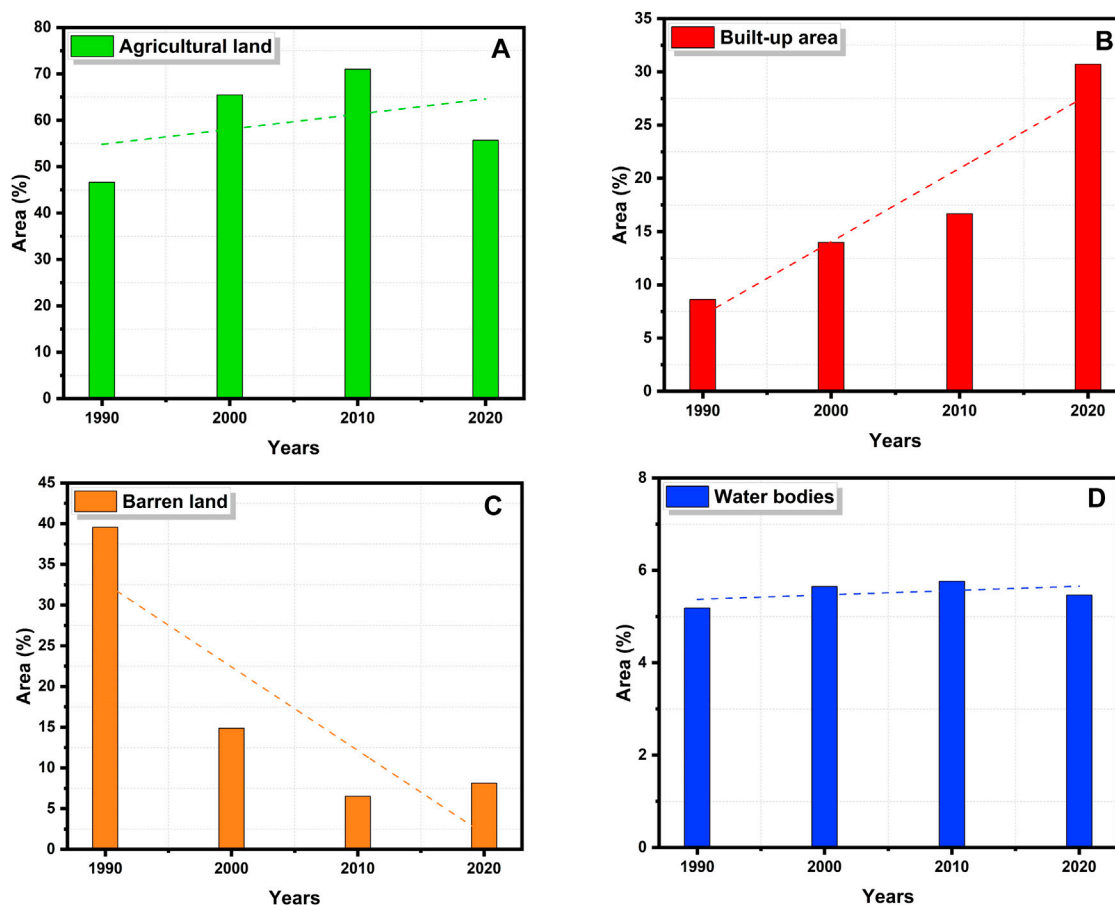


FIGURE 5

Trends in LULC change over the last three decades (A) Agricultural land, (B) Built-up area (C) Barren land (D) Water bodies.

while the maximum temperature was 33.4°C. By 2020, those numbers eventually grew to 26.6°C and 36.1°C, respectively (Figure 9B). Therefore, we further evaluated and compared the built-up area with the mean temperature of the urban area, and we found that as the urban area increased, so did the mean surface temperature of the urban land (Figure 8C). The mean temperature in 1990, when urban land was only 8.62% of the total area, was 29.25°C; however, as the urban area expanded, so did Larkana and the surrounding areas' mean surface temperature, reaching a maximum of 36.1°C, and 31.35°C when the urban area increased to 30.70% in 2020 (Figure 9C).

We have extended our analysis and tried to find out the difference in the mean LST of the built-up area with barren land,

agricultural land, and water bodies. It was observed that barren land has a higher surface temperature than the built-up area (Figure 10). However, the surface temperature of built-up land was higher than that of agricultural land and water bodies, and it increased consistently with time (Figure 10). In Table 3, the minimum, maximum, and mean LST and their respective standard deviations were compared for each LULC category in each year. The results of LST show a continuous rise in minimum, maximum, and mean LST for each LULC category from 1990 to 2020.

The lowest recorded mean average temperature in Larkana was 15°C in January, with a maximum temperature of 22.7°C and a minimum temperature of 7.6°C in the same month (Figure 10).

TABLE 2 Percentage change in land cover from 1990 to 2020.

Land use categories	1990 area in km ²	2020 area in km ²	Percentage change
Agricultural Land	66.66	79.49	19.24 ↑
Built-up Area	12.31	43.83	256.00 ↑
Barren Land	56.51	11.62	-79.44 ↓
Water Bodies	7.41	7.80	5.23 ↑



June, while they started to decrease in July and August. The monsoon rains occur in the study area during July and August, which decrease the temperature to an optimal level. The annual range of mean temperature in the study area is almost 21° C (Figure 11).

Frontiers in Environmental Science

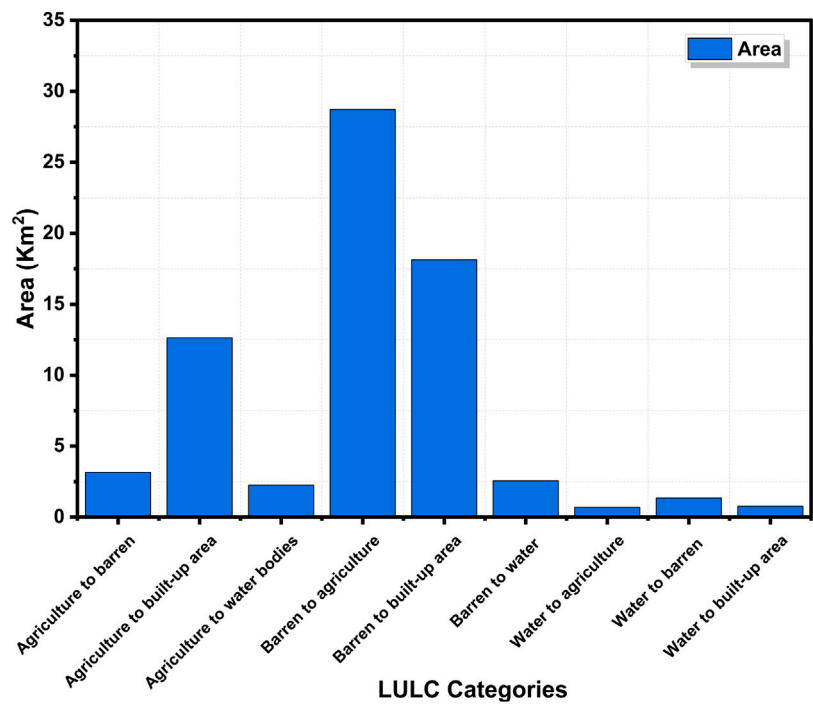


FIGURE 8
LULC category conversion between 1990 and 2020.

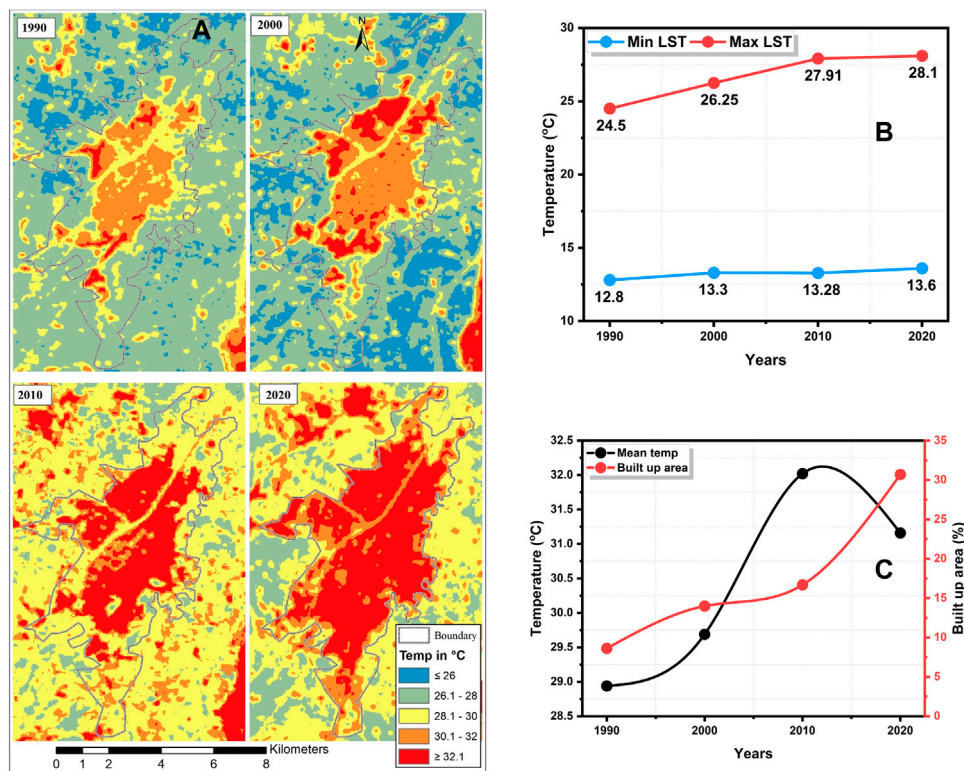
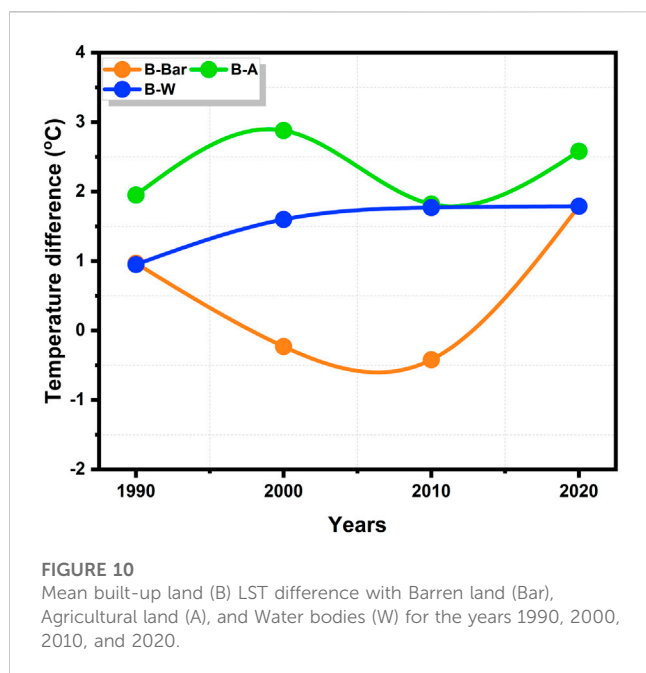


FIGURE 9
(A) LST in Larkana; (B) Minimum and maximum LSTs, and (C) Mean urban LST and urban area in 1990, 2000, 2010, and 2020.



attracted the monsoonal winds and became the cause of massive flooding (Rahman and Khan, 2013). In 2010, the highest temperature ever recorded in South Asia was 53.5 °C on 26 May at Mohenju-Daro, near the city of Larkana (Rahman and Khan, 2013). Agricultural land also showed the highest LST during 2000–2010, indicating that crops were also under high stress during this period. Similar results were observed for water bodies.

The annual mean air temperature obtained from the Larkana meteorological station for each particular year was compared with the annual mean land surface temperature derived from

TABLE 3 Minimum, maximum, mean LST, and standard deviation for different land use classes during 1990, 2000, 2010, and 2020.

Barren land				
Year	Minimum LST	Maximum LST	Mean LST	Std
1990	25.23	33.41	27.97	1.75
2000	24.61	34.93	29.92	2.41
2010	27.25	35.49	32.44	1.53
2020	26.75	35.58	29.37	1.47
Built-up Area				
1990	25.24	32.96	28.94	1.73
2000	25.34	34.15	29.69	1.85
2010	27.65	35.08	32.02	1.12
2020	26.91	35.87	31.16	1.78
Agricultural Land				
1990	25.13	32.96	26.99	1.01
2000	24.60	33.74	26.81	1.17
2010	27.29	35.49	30.20	1.06
2020	26.64	35.14	28.58	1.21
Water Bodies				
1990	25.29	33.30	27.99	1.30
2000	24.60	33.73	28.09	1.39
2010	26.85	35.07	30.25	1.18
2020	26.76	35.58	29.37	1.47

Landsat imagery. Both the annual mean air temperature and the mean annual LST show a gradual increase in temperature in the study area (Figure 12). In 1990, the mean annual air temperature was 26.87°C, which increased to 28.05°C in 2020, while the mean annual LST was 29.25°C in 1990, which rose to 31.35°C in 2020 (Figure 12).

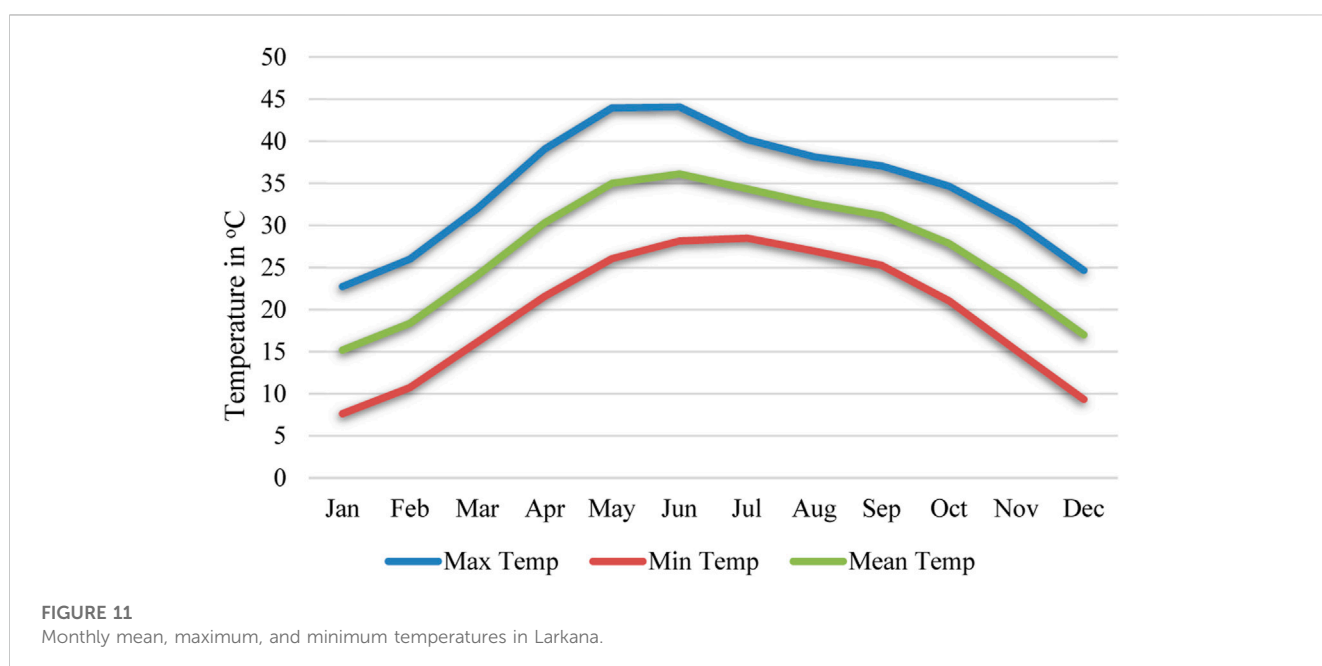


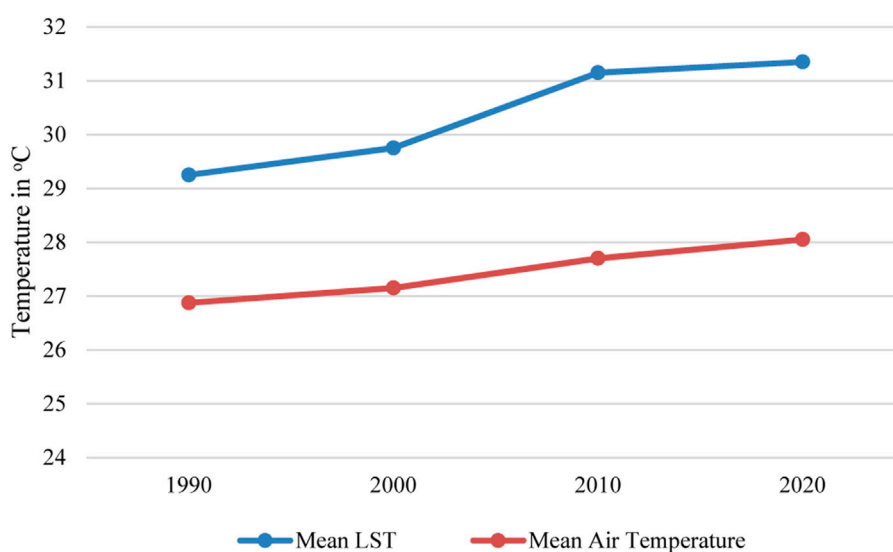
TABLE 4 Change in minimum, maximum, and mean LST of different land use classes during 1990, 2000, 2010, and 2020.

Barren land			
Year	Minimum LST	Maximum LST	Mean LST
1990–2000	−0.62	1.52	1.95
2000–2010	2.64	0.56	2.52
2010–2020	−0.5	0.09	−3.07
1990–2020	1.52	2.17	1.4
Built-up Area			
1990–2000	0.1	1.19	0.75
2000–2010	2.31	0.93	2.33
2010–2020	−0.74	0.79	−0.86
1990–2020	1.67	2.91	2.22
Agricultural Land			
1990–2000	−0.53	0.78	−0.18
2000–2010	2.69	1.75	3.39
2010–2020	−0.65	−0.35	−1.62
1990–2020	1.51	2.18	1.59
Water Bodies			
1990–2000	−0.69	0.43	0.1
2000–2010	2.25	1.34	2.16
2010–2020	−0.09	0.51	−0.88
1990–2020	1.47	2.28	1.38

5 Discussion

The current study analyzed the impacts of urban expansion on agricultural land and the urban thermal environment in Larkana. Larkana is the fourth largest city in Sindh after

Karachi, Hyderabad, and Sukkur. For LULC classification, the Random Forest algorithm was applied in the Google Earth Engine online platform for the years 1990, 2000, 2010, and 2020, while the land surface temperature was also calculated in GEE using a single channel algorithm. In this study, the most pronounced change was the abrupt increase in the built-up area and the drastic decline in the open barren land area, and to some extent, a decrease in agricultural land. In the last three decades, such abrupt changes have been more likely due to population growth in Larkana. According to government records, in 1951, the Larkana city population was merely 34,000 persons, which increased to 490,508 persons as of the 2017 census (GOP, 2017). Such abrupt changes in the built-up area created a number of environmental issues and replaced other LULC categories like agricultural and open spaces (barren land) (Aburas et al., 2021; Yousafzai et al., 2022). No such study has been conducted in Larkana or even other intermediate cities in the Sindh province to date; therefore, the results of this study have been discussed in light of other studies conducted worldwide and in other cities of Pakistan. From the analysis, it was observed that an increase in the built-up area caused a decrease in the proportion of barren land or open areas in addition to agricultural land, and the same results are consistent with other studies conducted in different parts of the world and different cities of Pakistan, such as the Nile delta in Egypt (Radwan et al., 2019), the Tarai region in Nepal (Rimal et al., 2018), Kansas City, USA (Zubair et al., 2019), Torres Vedras, Portugal (Gomes et al., 2019), Kolkata, India (Sahana et al., 2018), Karachi (Arshad et al., 2020), Peshawar (Khan et al., 2019; Yousafzai et al., 2022), Faisalabad (Tariq and Shu, 2020), Islamabad (Sohail et al., 2019), Hyderabad (Peerzado et al., 2019), Quetta (Khan et al., 2020), and Lahore (Fahad et al., 2021). The change in the built-up area was more pronounced between 2010 and 2020, and according to the local community, this abrupt increase in the built-up area is due to large migration after the 2010 floods

**FIGURE 12**

Comparison of mean air temperature and land surface temperature in Larkana.

in the Kamber-Shahdadkot, Dadu, and Shikarpur districts. This migration not only increased the built-up area but also caused a sharp decline in the agricultural land between 2010 and 2020 (Figures 3–5). The increase in urban population and urban expansion in Larkana and its surroundings was further discussed with local elders, as no satisfactory literature was available from which we could determine the possible causes. According to the elders of the area, Larkana is the home of versatile politicians like the late Zulfiqar Ali Bhutto and Benazir Bhutto, and during their time of government they improved the city's infrastructure in many areas, including health, education, and housing. As a result, people from the districts moved in search of better education, health, quality of life, and jobs. This overwhelming migration resulted in an unplanned expansion of the built-up area over agricultural land and encroached on open areas. The inner-city areas became congested due to the low availability of land for new development, resulting in other environmental and social issues. The LST for each category of LULC was also evaluated in this study, and it was observed that barren land and built-up area have the highest LST and similar results have been observed in other six urban centers in Pakistan (Dilawar et al., 2021). The mean, maximum, and minimum LST of all categories of LULC recorded a consistent increase, and a similar increase was also observed in other studies (Ibrahim and Rasul, 2017; Dilawar et al., 2021; Moazzam et al., 2022). The results revealed that between 1990 and 2020, the minimum LST increased by 1.52°C, the maximum LST by 2.17°C and the mean LST increased by 1.4°C in the barren land category, while in the built-up area the minimum LST increase was 1.67°C, the maximum LST was 2.91°C, and the mean LST increase was 2.22°C. Similarly, during the study period, the increase in minimum LST in agricultural land was 1.51°C, in maximum LST it was 2.18°C and in mean LST was 1.59°C. A comparable increase was observed in the land surface temperature of water bodies during the study period. The land surface temperature of the inner city and its surroundings rose due to increase in the impervious surfaces.

6 Conclusion

This study assessed the urban expansion impacts on agricultural land and the urban thermal environment in Larkana by performing a Random Forest algorithm for land use/ land cover classification in Google Earth Engine and calculating land surface temperature using Landsat images. The Random Forest algorithm is a useful and highly accurate technique for assessing temporal LULC change. The results revealed that the urban area expanded over barren land and agricultural land in Larkana. In the last three decades (1990–2020), the built-up area of the city increased from 12.31 km² to 43.83 km², which is more than a threefold increase. This surge in the built-up area took over the surrounding open land, which was either barren land or agricultural land. This haphazard expansion in the urban built environment not only displaced agricultural land but also caused different environmental

hazards like increasing land surface temperature and affecting the urban thermal environment. Barren land in the study area decreased from 56.51 km² to 11.62 km², representing a decrease of 79.44% over three decades. The water bodies increased in the study region due to the increasing importance of inland fish farming. The LULC classification results were validated using 30% sample points data, and for all selected years, the accuracy was close to 90%, which indicates the importance and accuracy of the RF algorithm for temporal LULC classification. The LST maps were prepared for 1990, 2000, 2010, and 2020 using GEE in order to check the status of the urban thermal environment, and the results indicated a gradual increase in surface temperature in all land use categories. The cause of this gradual increase in surface temperature is the increase in built-up area over barren, agricultural land, and open green vegetation. This study's results endorse prior planning and policy implementation to control the haphazard urban expansion over fertile agricultural land.

Data availability statement

The raw data supporting the conclusion of this article will be made available by the authors, without undue reservation.

Author contributions

GR and NC conceptualization, GR acquired the data, data curation, formal analysis, investigation, methodology, GR, MM, and NC validation, visualization, writing original draft, NA acquire funding, supervision, project administration, resources, writing, review, and editing.

Acknowledgments

The authors acknowledge the United States Geological Survey (USGS) and the National Aeronautics and Space Administration (NASA) for providing Landsat data free of charge.

Conflict of interest

The authors declare that the research was conducted in the absence of any commercial or financial relationships that could be construed as a potential conflict of interest.

Publisher's note

All claims expressed in this article are solely those of the authors and do not necessarily represent those of their affiliated organizations, or those of the publisher, the editors and the reviewers. Any product that may be evaluated in this article, or claim that may be made by its manufacturer, is not guaranteed or endorsed by the publisher.

References

- Aburas, M. M., Ho, Y. M., Pradhan, B., Salleh, A. H., and Alazaiza, M. Y. (2021). Spatio-temporal simulation of future urban growth trends using an integrated CA-Markov model. *Arabian J. Geosciences* 14, 131–212. doi:10.1007/s12517-021-06487-8
- Al-Thawwad, R. M. (2008). “Technology transfer and sustainability-Adapting factors: Culture, physical environment, and geographical location,” in *Proceedings of the 2008 IAJC-IJME international conference* (Sheraton Music City, USA: Citeseer).
- Aliyu, A. A., and Amadu, L. (2017). Urbanization, cities, and health: The challenges to Nigeria—a review. *Ann. Afr. Med.* 16, 149–158. doi:10.4103/aam.aam_1_17
- Arshad, A., Ashraf, M., Sundari, R. S., Qamar, H., Wajid, M., and Hasan, M. U. (2020). Vulnerability assessment of urban expansion and modelling green spaces to build heat waves risk resiliency in Karachi. *Int. J. disaster risk Reduct.* 46, 101468. doi:10.1016/j.ijdrr.2019.101468
- Ashraf, H., Mobeen, M., Miandad, M., Khan, M. A., Rahman, G., and Munawar, S. (2022). Assessment of urban sprawl in sargodha city using remotely sense data. *Ecol. Quest.* 33, 1–16. doi:10.12775/eq.2022.030
- Ashraf, H., Rahman, G., Khan, M. A., Moazzam, M. F. U., and Miandad, M. (2023). “Spatio-temporal urban sprawl of sargodha city, Punjab, Pakistan,” in *Urban environment and smart cities in asian countries*. Editor U. C. E. AL (Cham, Switzerland: Springer).
- Britannica (2013). *Larkana*. Chicago, USA: Britannica.
- Butt, A., Shabbir, R., Ahmad, S. S., and Aziz, N. (2015). Land use change mapping and analysis using remote sensing and gis: A case study of simly watershed, Islamabad, Pakistan. *Egypt. J. Remote Sens. Space Sci.* 18, 251–259. doi:10.1016/j.ejrs.2015.07.003
- Chandio, N. H., and Shirazi, S. A. (2022). Implications of urbanization on agricultural land: A case study of khairpur district, Pakistan. *Pak. Soc. Sci. Rev.* 6, 232–240. doi:10.35484/psr.2022(6-ii)21
- Dilawar, A., Chen, B., Trisurat, Y., Tuankrui, V., Arshad, A., Hussain, Y., et al. (2021). Spatiotemporal shifts in thermal climate in responses to urban cover changes: A-Case analysis of major cities in Punjab, Pakistan. *Geomatics, Nat. Hazards Risk* 12, 763–793. doi:10.1080/19475705.2021.1890235
- Fahad, S., Li, W., Lashari, A. H., Islam, A., Khattak, L. H., and Rasool, U. (2021). Evaluation of land use and land cover Spatio-temporal change during rapid Urban sprawl from Lahore, Pakistan. *Urban Clim.* 39, 100931. doi:10.1016/j.uclim.2021.100931
- Farid, N., Moazzam, M., Ahmad, S., Coluzzi, R., and Lanfredi, M. (2022). Monitoring the impact of rapid urbanization on land surface temperature and assessment of surface urban heat island using landsat in megacity (Lahore) of Pakistan. *Front. Remote Sens.* 3, 897397. doi:10.3389/frsen.2022.897397
- Gandharum, L., Hartono, D. M., Karsidi, A., and Ahmad, M. (2022). Monitoring urban expansion and loss of agriculture on the north coast of west java province, Indonesia, using Google Earth engine and intensity analysis. *Sci. World J.* 2022, 1–16. doi:10.1155/2022/3123788
- Gao, B. C. (1996). NDWI—a normalized difference water index for remote sensing of vegetation liquid water from space. *Remote Sens. Environ.* 58, 257–266. doi:10.1016/s0034-4257(96)00067-3
- Gomes, E., Abrantes, P., Banos, A., Rocha, J., and Buxton, M. (2019). Farming under urban pressure: Farmers’ land use and land cover change intentions. *Appl. Geogr.* 102, 58–70. doi:10.1016/j.apgeog.2018.12.009
- GOP (2017). “Larkana district census report-2017,” in *Pakistan bureau of statistics* (Islamabad: Pakistan Bureau of Statistics, Government of Pakistan).
- Gul, S., Bibi, T., Rahim, S., Gul, Y., Niaz, A., Mumtaz, S., et al. (2022). Spatio-temporal change detection of land use and land cover in Malakand Division Khyber Pakhtunkhwa, Pakistan, using remote sensing and geographic information system. *Environ. Sci. Pollut. Res.* 30, 10982–10994. doi:10.1007/s11356-022-22960-7
- Ibrahim, F., and Rasul, G. (2017). Urban land use land cover changes and their effect on land surface temperature: Case study using Dohuk City in the Kurdistan Region of Iraq. *Climate* 5, 1–18. doi:10.3390/cli5010013
- Khan, I., Javed, T., Khan, A., Lei, H., Muhammad, I., Ali, I., et al. (2019). Impact assessment of land use change on surface temperature and agricultural productivity in Peshawar-Pakistan. *Environ. Sci. Pollut. Res.* 26, 33076–33085. doi:10.1007/s11356-019-06448-5
- Khan, S. (2019). The impact of urban expansion on agricultural land use changes in Aligarh, Uttar Pradesh, India. *Int. Archives Photogrammetry, Remote Sens. Spatial Inf. Sci.* 42, 381–384. doi:10.5194/isprs-archives-42-3-w6-381-2019
- Khan, Z., Saeed, A., and Bazai, M. H. (2020). Land use/land cover change detection and prediction using the CA-markov model: A case study of Quetta city, Pakistan. *J. Geogr. Soc. Sci.* 2, 164–182.
- Mehdi, S. S., Miandad, M., Anwar, M., Rahman, G., and Ashraf, H. (2021). Temporal variation in land use and land cover in gujrat (Pakistan) from 1985 to 2015. *Geogr. Nat. Resour.* 42, 151–161. doi:10.15372/gipr20210416
- Moazzam, M. F. U., Doh, Y. H., and Lee, B. G. (2022). Impact of urbanization on land surface temperature and surface urban heat island using optical remote sensing data: A case study of jeju island, republic of Korea. *Build. Environ.* 222, 109368. doi:10.1016/j.buildenv.2022.109368
- Mumtaz, F., Li, J., Liu, Q., Tariq, A., Arshad, A., Dong, Y., et al. (2023). Impacts of green carbon emissions: Comparison under forestation and urbanization reshaping scenarios. *Remote Sens.* 15 (3), 1–24. doi:10.3390/rs15030859
- Nyland, E., Gunn, K. E., Shiklomanov, G. I., Engstrom, N. N., and Streletskiy, A. (2018). Land cover change in the lower Yenisei River using dense stacking of landsat imagery in Google Earth Engine. *Remote Sens.* 10, 1–20. doi:10.3390/rs10081226
- Panhwar, N. A. (2020). *Tackling urbanisation in Sindh*. Karachi, Pakistan: The Express Tribune.
- Peerzado, M. B., Magsi, H., and Sheikh, M. J. (2019). Land use conflicts and urban sprawl: Conversion of agriculture lands into urbanization in Hyderabad, Pakistan. *J. Saudi Soc. Agric. Sci.* 18, 423–428. doi:10.1016/j.jssas.2018.02.002
- Radwan, T. M., Blackburn, G. A., Whyatt, J. D., and Atkinson, P. M. (2019). Dramatic loss of agricultural land due to urban expansion threatens food security in the Nile Delta, Egypt. *Remote Sens.* 11, 332. doi:10.3390/rs11030332
- Rahman, A. U., Khan, A., Haq, N., and Shaw, R. (2019). *Soil sealing and depletion of groundwater in rapidly growing Peshawar City District, Pakistan*. Urban Drought. Pakistan: Springer.
- Rahman, A., and Khan, A. N. (2013). Analysis of 2010-flood causes, nature and magnitude in the Khyber Pakhtunkhwa, Pakistan. *Nat. Hazards* 66, 887–904. doi:10.1007/s11069-012-0528-3
- Rimal, B., Zhang, L., Stork, N., Sloan, S., and Rijal, S. (2018). Urban expansion occurred at the expense of agricultural lands in the Tarai region of Nepal from 1989 to 2016. *Sustainability* 10, 1341–1419. doi:10.3390/su10051341
- Rizwan, A. M., Dennis, L. Y., and Chunho, L. (2008). A review on the generation, determination and mitigation of Urban Heat Island. *J. Environ. Sci.* 20, 120–128. doi:10.1016/s1001-0742(08)60019-4
- Sahana, M., Hong, H., and Sajjad, H. (2018). Analyzing urban spatial patterns and trend of urban growth using urban sprawl matrix: A study on Kolkata urban agglomeration, India. *Sci. Total Environ.* 628, 1557–1566. doi:10.1016/j.scitotenv.2018.02.170
- Sohail, M. T., Mahfooz, Y., Azam, K., Yen, Y., Genfu, L., and Fahad, S. (2019). Impacts of urbanization and land cover dynamics on underground water in Islamabad, Pakistan. *Desalin Water Treat.* 159, 402–411. doi:10.5004/dwt.2019.24156
- Sun, X., Crittenden, J. C., Li, F., Lu, Z., and Dou, X. (2018). Urban expansion simulation and the spatio-temporal changes of ecosystem services, a case study in Atlanta Metropolitan area, USA. *Sci. Total Environ.* 622, 974–987. doi:10.1016/j.scitotenv.2017.12.062
- Tariq, A., Mumtaz, F., Zeng, X., Baloch, M. Y. J., and Moazzam, M. F. U. (2022). “Spatio-temporal variation of seasonal heat islands mapping of Pakistan during 2000–2019, using day-time and night-time land surface temperatures MODIS and meteorological stations data,” in *Remote sensing applications: Society and Environment* 27, 100779. doi:10.1016/j.rsase.2022.100779
- Tariq, A., and Shu, H. (2020). CA-Markov chain analysis of seasonal land surface temperature and land use land cover change using optical multi-temporal satellite data of Faisalabad, Pakistan. *Remote Sens.* 12, 3402. doi:10.3390/rs12203402
- Thanh Noi, P., and Kappas, M. (2017). Comparison of Random forest, k-nearest neighbor, and support vector machine classifiers for land cover classification using Sentinel-2 imagery. *Sensors* 18, 18–20. doi:10.3390/s18010018
- Ul Din, S., and Mak, H. W. L. (2021). Retrieval of land-use/land cover change (LUCC) maps and urban expansion dynamics of Hyderabad, Pakistan via landsat datasets and support vector machine framework. *Remote Sens.* 13, 3337–3425. doi:10.3390/rs13163337
- UN-DESA (2018). *2018 revision of world urbanization prospects*. New York, NY, USA: United Nations Department of Economic and Social.
- Wang, J., Zhou, W., Pickett, S. T., Yu, W., and Li, W. (2019). A multiscale analysis of urbanization effects on ecosystem services supply in an urban megaregion. *Sci. total Environ.* 662, 824–833. doi:10.1016/j.scitotenv.2019.01.260
- Yousafzai, S., Saeed, R., Rahman, G., and Farish, S. (2022). Spatio-temporal assessment of land use dynamics and urbanization: Linking with environmental aspects and DPSIR framework approach. *Environ. Sci. Pollut. Res.* 29, 81337–81350. doi:10.1007/s11356-022-21393-6
- Zou, Z., Yan, C., Yu, L., Jiang, X., Ding, J., Qin, L., et al. (2021). Impacts of land use/land cover types on interactions between urban heat island effects and heat waves. *Build. Environ.* 204, 108138–108211. doi:10.1016/j.buildenv.2021.108138
- Zubair, O. A., Ji, W., and Festus, O. (2019). Urban expansion and the loss of prairie and agricultural lands: A satellite remote-sensing-based analysis at a sub-watershed scale. *Sustainability* 11, 4673–4712. doi:10.3390/su11174673



OPEN ACCESS

EDITED BY

Alban Kuriqi,
University of Lisbon,
Portugal

REVIEWED BY

Xing Gao,
Yangzhou University,
China
Dipankar Bera,
Vidyasagar University,
India

*CORRESPONDENCE

Qin Yaochen
✉ qinyao@henu.edu.cn

[†]These authors have contributed equally to this work

SPECIALTY SECTION

This article was submitted to
Environmental Informatics and Remote
Sensing,
a section of the journal
Frontiers in Ecology and Evolution

RECEIVED 03 December 2022

ACCEPTED 28 February 2023

PUBLISHED 28 March 2023

CITATION

Mehmood MS, Rehman A, Sajjad M, Song J,
Zafar Z, Shiyan Z and Yaochen Q (2023)
Evaluating land use/cover change associations
with urban surface temperature *via* machine
learning and spatial modeling: Past trends and
future simulations in Dera Ghazi Khan, Pakistan.
Front. Ecol. Evol. 11:1115074.
doi: 10.3389/fevo.2023.1115074

COPYRIGHT

© 2023 Mehmood, Rehman, Sajjad, Song,
Zafar, Shiyan and Yaochen. This is an open-
access article distributed under the terms of
the [Creative Commons Attribution License](#)
(CC BY). The use, distribution or reproduction
in other forums is permitted, provided the
original author(s) and the copyright owner(s)
are credited and that the original publication in
this journal is cited, in accordance with
accepted academic practice. No use,
distribution or reproduction is permitted which
does not comply with these terms.

Evaluating land use/cover change associations with urban surface temperature *via* machine learning and spatial modeling: Past trends and future simulations in Dera Ghazi Khan, Pakistan

Muhammad Sajid Mehmood^{1,2,3,4†}, Adnanul Rehman^{5,6†},
Muhammad Sajjad⁷, Jinxi Song^{5,6}, Zeeshan Zafar^{5,6},
Zhai Shiyan^{1,2,4} and Qin Yaochen^{1,2,3*}

¹The College of Geography and Environmental Science, Henan University, Kaifeng, China, ²Key Laboratory of Geospatial Technology for Middle and Lower Yellow River Regions, Ministry of Education, Henan University, Kaifeng, China, ³Key Research Institute of Yellow River Civilization and Sustainable Development, Collaborative Innovation Center on Yellow River Civilization Jointly Built by Henan Province and Ministry of Education, Henan University, Kaifeng, China, ⁴Center for Computational Geography, The College of Geography and Environmental Science, Henan University, Kaifeng, China, ⁵College of Urban and Environmental Sciences, Northwest University, Xi'an, China, ⁶Shaanxi Key Laboratory of Earth Surface System and Environmental Carrying Capacity, Northwest University, Xi'an, China, ⁷Department of Geography, Hong Kong Baptist University, Kowloon, Hong Kong SAR, China

While urbanization puts lots of pressure on green areas, the transition of green-to-grey surfaces under land use land cover change is directly related to increased land surface temperature—compromising livability and comfort in cities due to the heat island effect. In this context, we evaluate historical and future associations between land use land cover changes and land surface temperature in Dera Ghazi Khan—one of the top cities in Pakistan—using multi-temporal Landsat data over two decades (2002–2022). After assessing current land use changes and future predictions, their impact on land surface temperature and urban heat island effect is measured using machine learning *via* Multi-Layer Perceptron-Markov Chain, Artificial Neural Network and Cellular Automata. Significant changes in land use land cover were observed in the last two decades. The built-up area expanded greatly (874ha) while agriculture land (–687ha) and barren land (–253ha) show decreasing trend. The water bodies were found the lowest changes (57ha) and vegetation cover got the largest proportion in all the years. This green-grey conversion in the last two decades (8.7%) and prospect along the main corridors show the gravity of unplanned urban growth at the cost of vegetation and agricultural land (–6.8%). The land surface temperature and urban heat island effect shows a strong positive correlation between urbanization and vegetation removal. The simulation results presented in this study confirm that by 2032, the city will face a 5° C high mean temperature based on historical patterns, which could potentially lead to more challenges associated with urban heat island if no appropriate measures are taken. It is expected that due to land cover changes by 2032, ~60% of urban and peri-urban areas will experience very hot to hot temperatures (> 31.5°C). Our results provide baseline information to urban managers and planners to understand the increasing trends of land surface temperature in response to land cover changes. The study is important for urban resource management, sustainable development policies, and actions to mitigate the heat island effect. It will further asset the broader audience to understand the

impact of land use land cover changes on the land surface temperature and urban heat island effect in the light of historic pattern and machine learning approach.

KEYWORDS

land use land cover, land surface temperature, urban heat island, artificial neural network, Markov chain

1. Introduction

Land use (LU)/land cover (LC) refers to the classification of landscape according to the natural elements and anthropogenic activities. Collectively, the terms are often used as LULC due to their interrelationship (Hussain et al., 2020; Sadiq Khan et al., 2020; Das et al., 2021). In recent decades, urban sprawl caused a tremendous amount of landscape changes that led to land surface temperature (LST) variation from local to global scales. In the 1950s, the urban area contained only 3% of the world's population, which boosted to 51% in 2007, and will reach 70% by 2050 (UN, 2017). The massive population influx in urban areas causes the exploitation of resources and economic development (Castelli, 2018), which results in huge impacts on local LULC changes (Thériault et al., 2020; Aktaş and Dönmez, 2021), LST variation (Kafy et al., 2020; Das et al., 2021; Kafy et al., 2021a), seasonal variability (Bera et al., 2022) and regional to global climate change (Zhou et al., 2019; Lustgarten, 2020). This situation often leads to pollution and unequal distribution of resources and services, creating significant challenges for urban developers and policymakers (Lakshmisha et al., 2019; Gan et al., 2020).

Cities are considered the locomotive of development. Development practices across the world have accelerated urbanization (Wang et al., 2020; Korkmaz and Meşhur, 2021). Unplanned urbanization often results in degraded ecology, biodiversity, and landscapes along with several surface changes (Hassan, 2017; Heikkinen et al., 2019). This situation represents negative consequences (both short and long-term) of economic developments in cities. The short-term consequences that urban dwellers face include degraded natural systems, poor sanitation, waste management, and poor air/water quality (Kadhim et al., 2016; Musse et al., 2018; Luo et al., 2019). The increase in LST in cities is one of the long-term repercussions of changes in LULC (Peng et al., 2018; Akinyemi et al., 2019; Kafy et al., 2021a). These LULC transitions from marshes, vegetation, and agricultural lands into the impervious surface are particularly associated with increased LST into urban roots. According to recent studies (Cai et al., 2018; Peng et al., 2018; Kafy et al., 2021a,b), the average LST in cities is typically 2–4°C higher than in rural areas, which is mostly contributed by the removal of green cover and

installation of gray infrastructure. In addition, the increase in the impervious surface makes societies more vulnerable to flooding due to the higher flow velocity of the water (Rehman et al., 2022).

The high LST concentration is primarily influenced by both horizontal and vertical expansion (Crum and Jenerette, 2017), the space between buildings, building material (Faroughi et al., 2020; Sadiq Khan et al., 2020; Song et al., 2020), landscape composition, and topographic parameters (Peng et al., 2017; Bera et al., 2022) among other factors. Also, the geographical location and seasonal variations play important roles in increasing LST, resulting in the creation of Urban Heat Islands (UHIs) (Khan I. et al., 2019; Guo et al., 2020; Bera et al., 2022; Tariq et al., 2022a; Mehmood et al., 2023). These geographical locations/places near the equator receive more radiation and thus, are more susceptible to the formation of UHIs, which is directly linked to high energy consumption, air pollution, and risks to human health (Shahmohamadi et al., 2011; Heaviside et al., 2017). For better living conditions, public health, and community well-being, systematic adoption of measures to mitigate the consequences of UHI is desirable.

To measure variations in LULC and LST in cities, geo-information technologies such as Geographic Information Systems (GIS) and remote sensing (RS) are flourishing (Ahmed et al., 2013; Alqurashi et al., 2016; Hassan, 2017; Shen et al., 2017; Tariq et al., 2021). GIS and RS applications have gained much attention in studies related to ecosystem change, biodiversity, and changes in climatic conditions (Mengistu and Salami, 2007; Maurya et al., 2021). Monitoring LST through direct site visits to detect changes in LULC is time-consuming, tedious, labor-intensive, and error prone. Furthermore, the coupling of GIS and RS allows for the practical evaluation, monitoring, and simulation of LULC and LST variations (Samie et al., 2017; Kafy et al., 2020, 2021c). Spatial-temporal modeling of LULC and LST dynamics is also necessary to address the difficulties related to land cover change and temperature rise, thanks to developments in statistical methods using remote sensing data (Wang et al., 2019). Several studies have employed thermal infrared sensors with varying spatial resolutions to study LST properties in diverse urban areas (by LULC categories), which reflects the applicability and utilization of remotely sensed data (Zhou et al., 2019; Tariq et al., 2022b). Another example of RS data is the derivative products of Landsat imageries such as the Normalized Difference Vegetation Index (NDVI) and Normalized Difference Built-up Index (NDBI). These spatial indices are used to identify the spatial-temporal LULC trend and LST variation. Based on the historical trends, climate data along with anthropogenic activities information can be used to seek the prediction of LULC changes and LST variations.

Although some previous studies have focused on the historical changes and future LULC scenarios in Pakistan and worldwide (Bokaie et al., 2016; Heaviside et al., 2017; Ullah et al., 2019a; Amir

Abbreviations: LULC, Land Use Land Cover; LST, Land Surface Temperature; TM/OLI, Thematic Mapper/Operational Land Imager; UHI, Urban Heat Island; UN, United Nations; GIS, Geographic Information System; RS, Remote Sensing; NDVI, Normalized Difference Vegetation Index; NDBI, Normalized Difference Built-up Index; DG Khan, Dera Ghazi Khan; FBS, Federal bureau of Statistics; CPEC, China Pakistan Economic Corridor; SUPARCO, Space & Upper Atmosphere Research Commission; FAO, Food and Agricultural Organization; MLP-MC, Multi-layer Perceptron-Markov Chain; CA, Cellular Automata; ANN, Artificial Neural Network.

Siddique et al., 2020; Imran and Mehmood, 2020; Kafy et al., 2020; Sadiq Khan et al., 2020; Tariq and Shu, 2020; Arshad et al., 2022; Bera et al., 2022; Tariq and Mumtaz, 2022; Waleed and Sajjad, 2022; Mehmood et al., 2023; Zafar et al., 2023), research on LULC and LST modeling, particularly under historical and future scenarios, is rare to find. This situation of absence of information on LULC transitions, their association with LST, and future dynamics of both hinder informed planning of urban regions in Pakistan in the face of environmental changes—representing a potential domain of research that requires the attention of researchers. Similarly, the site-specific spatial-temporal insights related to LULC transitions and LST variations are a prerequisite to planning effective measures for livable and comfortable urban designs. It is crucial to examine how urban surface temperature is affected by different spatial patterns of LULC. For urban planners, understanding which kinds of LULC changes exacerbate or mitigate impacts on urban surface temperature can contribute significantly to UHI mitigation strategy. In this context, the present study is focused on *Dera Ghazi Khan* (hereafter D. G. Khan) city in Pakistan, to explore historical changes and predict LULC scenarios along with their influence on urban LST. This study uses multi-source earth observation data to investigate the temporal and spatial trends of LULC and LST changes in the study area over the past two decades (2002–2022). Further this research enlighten the scientific community and urban managers to design better mitigation strategies to cope the growing trend of UHI especially at city scale. The main contributions of this work are to provide a reliable analysis on LST patterns and the UHI effect along with predicting LULC and LST change and investigating relationships between them, if any. Therefore, the objectives of this work are: (1) to examine the LULC changes and their transitions from a spatial-temporal lens; (2) model LST and its association with spatial indices as NDVI and NDBI; (3) simulate future changes in LULC and LST for 2032; and (4) explore the impact of different LULC changes on LST and formation of UHI effect.

1.1. Study area

The study area is situated in the southwestern district in Punjab province at the foothill of the *Koh-e-Suleiman* mountain range (*Suleiman Range*) (Munir and Iqbal, 2016). The city has gone through a population increase of ~110% between 1998 and 2017 (FBS, 2017). To accommodate this population, the city has also gone through an immense urbanization process, resulting in several challenges for city dwellers (Garcia et al., 2019). Geographically, the D. G. Khan district is the third largest district in the Punjab province in terms of area (13,740 km²). The city area lies between 30° to 30° 05' 28" N Latitude and 73° 35' 33" to 73° 41' 41" E Longitude, which covers ~100 km² (10,000 hectares) (Supplementary Figure S1, a separate file containing additional information). In terms of demography, D. G. Khan district is the most populous in the Southern Punjab, with ~3 million people and the city has 0.4 million urban dwellers as per the recent census in 2017 (FBS, 2017). The climate of the study area defines the arid zone with average annual precipitation of about 150 mm mostly in the summer monsoon season July–August. The average temperature range from cold-mild winter and hot summer shows a huge difference from 13 to 50°C (Munir and Iqbal, 2016). The landscape

is characterized by a flat city center and gradually increasing topography towards the west.

The study area received a large population from the surrounding less developed areas in the past two decades mainly due to better quality of life, health care, education, and security reasons. Also, an influx of migrants from rural areas after the destructive flood event in 2010 brought significant changes in the existing LULC pattern (Hashmi et al., 2012). The study area was selected due to its geo-strategic location as it is situated almost in the center of the country and provide access to three provinces (i.e., Punjab, Sindh, and Baluchistan). Due to its significant international economic importance, the city is now a part of the China-Pakistan Economic Corridor (CPEC) under the One Road One Built project. The basic aim is to identify the current LULC transitions along with LST variation to measure the UHI effect. The prospect based on the historical trend analysis at the city scale will allow an understanding of the current situation to implement the right decision and policies for sustainable resource management and urban development.

2. Methodology

2.1. Data Collection and Pre-processing

For this research, the study period is considered as the years 2002, 2012, and 2022. In these two decades, three Multi-spectral Landsat Satellite data (for the years mentioned) are downloaded from the United States Geological Survey's (USGS) Earth Explorer archives to evaluate LULC changes and their association with LST. The Landsat 5 Thematic Mapper (TM) data are used for 2002 and 2012, and the Landsat 8 Operational Land Imager (OLI) data are used for 2022. All the data are retrieved for March to prevent any influences of seasonal variations. Cloud coverage is set to a minimum scale of <10% for all Landsat images. However, it is notable that the cloud cover is nearly 0 % for all the used images of the study area. Additional details (metadata) regarding the images were retrieved from the USGS repository. Detailed information about the images is provided in Table 1.

2.2. Classification of LULC and change detection

The Image Classification tool in ArcGIS 10.5 is used to classify the LULC map due to its straightforward processing approach and simple-to-use nature with higher accuracy in terms of LULC classification. Following other research in this field, we use the supervised classification based on the maximum likelihood technique—one of the most applied techniques for LULC classification. Under the supervised classification, the images are classified using spectral signatures that are provided through training samples. Landsat-5 TM imaging bands 1–5 and band-7 are utilized to classify different land use classes. It is noted that band 6 is rejected since it represents a thermal band. In the case of Landsat-8 OLI imagery, bands 1–7 are employed. To create the LULC maps, all bands are initially stacked in ArcGIS 10.5 software using the Image Analyst Tool. To attain the accurate LULC classification, Landsat surface reflectance-derived spectral indices, such as the Normalized

TABLE 1 Description of earth observation sensors and remote sensing data used in this study.

Acquired Date	Spacecraft ID	Sensor ID	Cloud cover	Spatial resolution	Path/Row	Time (GMT)
09 March 2002	Landsat-5	Thematic Mapper	~ 1	30 × 30 m	151/039	05:22:48.2970940Z
24 March 2012	Landsat-5	Thematic Mapper	~ 0	30 × 30 m	151/039	05:39:10.2300060Z
26 March 2022	Landsat-8	OLI_TIRS	~ 0.86	30 × 30 m	151/039	05:49:12.3399780Z

Difference Vegetation Index (NDVI) and Normalized Difference Built-up Index (NDBI) were utilized (Tariq et al., 2020; Andrade et al., 2021; Das et al., 2021). Later, the Training Sample Manager tool is employed to detect the pixels' signatures. The training samples for the supervised image classification are collected randomly across the entire study area and 150 samples (30 samples per LULC type) were collected for each year. A total number of five LULC types were identified and detail of each LULC type (see Supplementary Table S1) and their associated classes are explained in section 3.1.

2.2.1. Accuracy assessment of classified maps

The confusion matrix, also known as the error matrix, is used to measure the accuracy of the classified maps. The pixel's actual and expected identity information is explained in this matrix as suggested by (Tilahun and Teferie, 2015; Rwanga and Ndambuki, 2017; Rehman et al., 2021). For this purpose, a total of 210 sample locations are selected using the stratified sampling tool in ArcGIS for equal representation of all LULC types. Later, these sample locations act as ground truths to verify the classified maps. These samples are collected using the Google Earth platform coupled with actual ground conditions of LULC via the Global Positioning System (GPS) for the recent year (2022). The 2002 ground truth data were also acquired from the Land Cover Atlas of Pakistan-The Punjab Province series which is prepared by the collaboration of The Space & Upper Atmosphere Research Commission (SUPARCO) and the Food and Agricultural Organization (FAO) due to lower resolution image data of Google Earth before 2005. These samples are cross-examined with the classified maps to estimate the accuracy. The producer's accuracy (PA) is a referenced-based approach in which the accuracy is calculated by analyzing the forecasts provided for a class and expressed as a percentage. Besides PA, there is another type of map-based accuracy measure known as user accuracy (UA). This measure is calculated by analyzing a class's referenced data and expressed as a percentage (Platt and Rapoza, 2008; Shafi et al., 2023). Aside from the approaches mentioned above, another commonly adopted accuracy coefficient is the Kappa coefficient. Due to its wide use in LULC classification, we use the Kappa coefficient in our study to estimate the accuracy of classified maps. The Kappa value varies from 0 to 1, with 0 denoting low agreement and representing 1 nearly perfect agreement between ground truths and the classes obtained through the classification of images (Foody et al., 1992).

2.3. Retrieval of land surface temperature

The LST is calculated by employing the thermal bands of radiometrically and geometrically corrected earth observation data from Landsat satellite during 2002–2022 for the periods 2002, 2012,

and 2022. Thermal data are retrieved from the Landsat sensors and stored as Digital Numbers (DN). Later, these DNs are transformed into LST using a four-step procedure described by (Artis and Carnahan, 1982).

Step 1 involves the conversion of DNs values to radiance utilizing the following Equation (1):

$$L_{\lambda} = LMIN + (LMAX - LMIN) \times DN / 255 \quad (1)$$

where.

L_{λ} represents spectral radiance for both Landsat 5 TM and 8 OLI images;

LMIN for Landsat 5 TM is 1.238 and 0.10033 for both thermal bands (Bands 10 and 11) of Landsat 8 OLI image.

LMAX represents the Landsat 5 TM as 15.30 and 22.00180 for both thermal bands (Bands 10 and 11) of the Landsat 8 OLI image.

Step 2 follows the conversion of the radiance above to satellite brightness temperature (BT) at sensors into degree Celsius as Equation 2:

$$TB = K2 / \ln((K1 / L_{\lambda}) + 1) - 273.15 \quad (2)$$

Here, K1 and K2 reflect calibration constants given as 607.76 and 1260.56 accordingly for Landsat 5 TM. For Landsat 8, OLI images of K1 and K2 (both bands 10 and 11) are given as 774.89, 1321.08, and 480.88, 1201.14, respectively. The information on these constants is available from the USGS through the metadata files of the satellite images.

Step 3 involves the final step to calculate the LST by utilizing the following three Equations 3:

$$LST = TB / [1 + (\lambda \times TB / \rho) \times \ln(\varepsilon)] \quad (3)$$

in which, LST reflects land surface temperature; TB represents satellite brightness temperature; λ represents the wavelength of emitted radiance with a peak discharge of 11.5 μm ; ρ can be calculated by applying the following Equation (4), and ε offers the ground surface emissivity that can be calculated from proportion vegetation (PV) using Equation 5.

$$\rho = h \times c / \sigma \quad (4)$$

where.

h is Planck's constant ($6.626 \times 10^{-34} \text{ J s}$), σ is Boltzmann constant ($1.380649 \times 10^{-23} \text{ J/K}$), and c = velocity of light ($2.998 \times 10^8 \text{ m/s}$).

Further,

$$PV = (NDVI - NDVI_{min} / NDVI_{max} - NDVI_{min})^2 \quad (5)$$

PV represents vegetation proportion calculated from the normalized difference vegetation index (NDVI) for all the respective years (2002, 2012, and 2022). Finally, the surface emissivity (ε) is calculated using Equation 6.

$$\varepsilon = 0.004 \times PV + 0.986 \quad (6)$$

The LST drives from Landsat 8, bands 10, and 11 are then averaged to obtain the cumulative LST composite image using the Cell Statistics Spatial Analyst tool extension in ArcGIS 10.5 software.

2.3.1. Land surface temperature classification in relation to LULC changes

To determine the relationship between LST and land cover changes over the past 20 years, if any, the LST is categorized into six different zones to better understand the temporal and spatial differences. The selection of LST threshold values to visualize clusters/zones, past literature, expert opinion, and study area characteristics were considered. We categorize the LST zones as very cold (<21.1°C), cold (21.1–<23.1°C), chilly (23.1–<25.1°C), cool (25.1–<27.1°C), warmish (27.1–<29.1°C), hot (29.1–<31.1°C), and very hot (> 31.1°C) (Utomo and Kurniawan, 2016). After the classification, each LST zone is overlaid on LULC change maps, and LST variations are calculated using the “Tabulate Area” tool in ArcGIS 10.5.

2.3.2. Land surface temperature in relation to spatial indices

Indices such as the Normalized Difference Vegetation Index (NDVI) and the Normalized Difference Built-up Index (NDBI) have been linked to LST (Guha et al., 2019). The NDVI characterizes vegetation phenology as the difference between near-infrared and red reflectance (Wessels et al., 2011; Mas and Soares de Araújo, 2021). The following procedure (Equation 7) is used to extract the NDVI value (Townshend and Justice, 1986).

$$NDVI = NIR - R / NIR + R \quad (7)$$

where NIR represents the Near-infrared band and R is the Red band of the satellite image. Landsat TM bands 4 and 3 are utilized to derive NDVI, while Landsat OLI bands 5 and 4 are used. The NDVI scale runs between –1 to +1, with a negative value of NDVI indicating water whereas positive NDVI indicates vegetation.

Except for NDVI, LST is significantly influenced by impervious surfaces. Hence, we also consider this parameter and represent it using the well-known NDBI. The following equation (Equation 8) is used to calculate NDBI, as given by (Zha et al., 2003).

$$NDBI = SWIR - NIR / SWIR + NIR \quad (8)$$

where,

SWIR represents the Short-wave Infrared band and NIR is the Near-infrared band of satellite images.

Utilizing the NDBI, we can determine the built-up areas using remotely sensed data. For Landsat TM and Landsat OLI, bands 5 and 6 are utilized for SWIR, respectively. Similarly, bands 4 and 5 are utilized from Landsat TM and Landsat OLI images for NIR, respectively. Similar to NDVI, the NDBI values lie between –1 to +1, with values closer to –1 reflecting lesser built-up and values closer to +1 showing a high density of built-up areas.

The association between LST and spatial indices is initially determined using single and multiple linear regression analysis (Tran et al., 2017; Das et al., 2021). For each point data type, values for NDVI and NDBI are retrieved from each pixel in the study area. The linear regression model is fed with these data points as input. This model depicts the correlation/association between LST and LULC, if any, in broader terms.

2.4. Simulating LULC projections for the year 2032

Given the fact that LULC is spatially dynamic, their simulation necessitates the use of spatial techniques for guaranteeing long-term sustainability and addressing current and future development needs. By combining GIS and RS methodologies, precise spatial models such as the Multi-layer Perceptron-Markov Chain (MLP-MC) have been developed to properly simulate future LULC (Hamad et al., 2018; Kafy et al., 2021b). Based on the MLP-MC, the MOLUSCE tool in QGIS and the cellular automata (CA) model are used to forecast future LULC changes. The CA model, for example, accounts for both aspects (i.e., static and dynamic) of LULC changes, which are essential for detailed insights related to urban planning and design (Ullah et al., 2019a; Kafy et al., 2021c). Another reason to utilize this model is its well-document accuracy to project future land cover patterns (Xu et al., 2016) based on a set of the function of five-parts transition rules on the status of cells to simulate and predict the future LULC changes (Wang et al., 2020).

The projection is made using two sorts of data: dependent variables like the previous LULC changes estimated (transitional matrix) from Landsat images of 2012, and 2022 and independent variables including elevation, slope, distance from activity centers, distance from waterways, and proximity to road networks. The distances to activity centers, waterways, and roads are estimated using the Euclidian distance function in ArcMap software. Furthermore, the ALOS-PALSAR DEM (12.5 × 12.5 meters spatial resolution) is employed in ArcMap software to estimate the elevation and slope of the study area. The up-scaling procedure with mean aggregation rules (resampling function in ArcGIS) was used to homogenize the spatial resolution of DEM and Landsat images. The transition potential matrix is created using the aforementioned variables. A random sampling approach is used to collect the samples of LULC. The maximum iteration (1000) and neighborhood pixel (9 cells) are selected to automatically train the prediction model (Mansour et al., 2020). After modeling the transition potential matrix with the logistic regression, the CA model creates a future LULC map (for 2032 in our case). Validation of the model using current datasets is required to

show that it is trustworthy in projecting LULC change for a specific forecasted year (Ruben et al., 2020; dos Santos et al., 2021). Therefore, before the projection for 2032 is made, the CA model is tested for accuracy *via* simulating LULC for 2022 and then compared to the study area's estimated LULC (based on Landsat data) for the same year. The QGIS-MULUSCE validation module is used to calculate the overall kappa coefficients and percent-correctness of 2022 classified and projected LULC maps. Once a reasonable accuracy is determined, the model is finally used for the 2032 LULC prediction.

2.5. Simulating LST projection for years 2032

Under the global warming situation, increased LST in metropolitan areas is a matter of serious concern for urban planners and decision-makers as it would impact energy demands, compromise livability in cities, and has potential health-related challenges (Li et al., 2017). With the advancement in artificial intelligence and machine learning-based modeling approaches, it has now become possible to spatially simulate climate-related indices such as LST with higher confidence. For instance, a Multi-layer Feed-Forward Back-Propagation Artificial Neural Network approach in TerrSet software (Maduako et al., 2016) is used to model, simulate, and project future LST patterns (Maduako et al., 2016; Ullah et al., 2019a). The Multi-Layer Perceptron (MLP) neural network decides network parameters and how they should be updated to automatically model the networks (Dey et al., 2021). This MLP algorithm is based on the concept of error-corrective learning. When a network gets a pattern, the MLP analyzes it and a potentially less accurate random output is generated. Furthermore, it computes a self-computed error function by subtracting the random output from the intended (goal) output. Using the "Leveraging back-propagation" algorithm, correction weights are estimated between the output and hidden layers as well as between hidden and input layers (Kafy et al., 2021c). This iterative approach is repeated until a reasonable and acceptable error is achieved between the network and the desired output.

In this study, LST simulation is based on the LST data from 2002 to 2022. Using QGIS software, the study area is subdivided into 500 × 500 meters spatial grids (fishnet) to obtain the sample points. The said grid size is set with the minimum spacing range in mind where features of one point can significantly influence LST. The LST and LULC data from previous steps are utilized for the training of a Neural Network in Terrset in order to predict LST (Vinayak et al., 2021). Additionally, we input the information on the latitudes and longitude of the defined samples to improve the model efficiency considering the notion; the more the input parameters, the better the network model's efficiency. The process of LST prediction includes network building → network training → network performance evaluation → and prediction. The confidence of the network is determined through the Mean Square Error (MSE) and the correlation coefficient (R).

The regression analysis offers information on how well the target data set describes the variance in the output results. The closer the value of R is to 1, the perfect correlation between the output and target data is expected. The Graphic User Interface (GUI) is created to test the performance indication before implementing the network. After the network's performance metrics are reasonable, they are retained for prediction. During the evaluation, the values of R and MSE are

reported as 0.8 and 0.5, respectively. Thus, LST for 2032 is simulated using the call-back function. The number of hidden layers is determined by numerous experiments depending on MSE and R values. These hidden layers are significant because they influence the outcomes by allowing the network to display non-linear behavior. Three hidden layers were chosen for the current study (Mallick et al., 2021). We use 0.1 as the starting learning rate and control it using the decay rate. To update the learning rate, the decay rate of 0.9 is used. If the error function between the current and previous iterations increases, the learning rate is upgraded by division. Similarly, it is multiplied when the error function decreases to recede (Kazemzadeh-Zow et al., 2017; Talukdar et al., 2020; Alqadhi et al., 2021).

3. Results

3.1. Spatial-temporal heterogeneities in LULC

Two precise patterns are observed in terms of LULC classification (Figure 1A) and the statistical results are detailed in Table 2. As per the analysis, a constant increase in urban areas and water bodies is observed at the cost of vegetation and bare lands. For instance, ~37% of the land in 2002 was urban, which increased to 40% in 2012, and 45.7% in 2022 (Figure 1B). It is noted that the consistent observed increase in water bodies from 2002 to 2022 (0.7–1.3%) is due to the construction of a new project called the "Kachhi Canal." This project is a part of a government initiative for Baluchistan province to provide water for drinking and agriculture purposes (Yasin and Nabi, 2014; Khan, 2018). The study area is a significant part of this project. The visual interpretation of this project can be observed in Figure 1A (2022 image), where a new canal suddenly appeared parallel to the old, constructed Ghazi Canal. A gradual downfall is observed in vegetation areas as 58.6% of vegetation land cover in 2002 decreased to 56.5% in 2012 and 51.9% in 2022. The amount of bare land was reduced to 1.2% in 2022, almost half of the amount in 2002 (3.7%).

Moving forward, Supplementary Figure S2 shows the graphical representation of the year-to-year land cover transition in relation to positive and negative changes. Two clear patterns are a constant increase in the urban areas as in 2002–2012; almost 3% of the area was transformed into urban areas. Also, 2.1% of vegetation land decreased and transitioned to urban areas and other land use. In the next decade (2012–2022), 5.7% of the land cover transformed into urban areas with a decrease of 4.7% in vegetation land and a 1.1% decrease in bare land. Analyzing the two-decade scenario, 8.7% of the total land was converted to urban areas resulting in a vast increase in built-up areas and a 6.8% decrease in vegetation cover along with a 2.5% decrease in bare soil. As for the water body, a small amount of increase is observed across the overall study period. For 2002–2012, a 0.2% increase in water bodies can be seen, which accelerated to a 0.4% increase in the 2012–2022 period. Overall, a 0.6% increase is estimated in water bodies during 2002–2022—see Table 2 for detailed statistics.

One of the important aspects of LULC classification is its reliability and accuracy. Detailed accuracy assessment is performed by picking 210 ground truth points (GTP) for all years. Multiple sources were used to seek the accuracy assessment and their detail is given in section 2.2.1. Table 3 shows the detailed assessment scenario of the

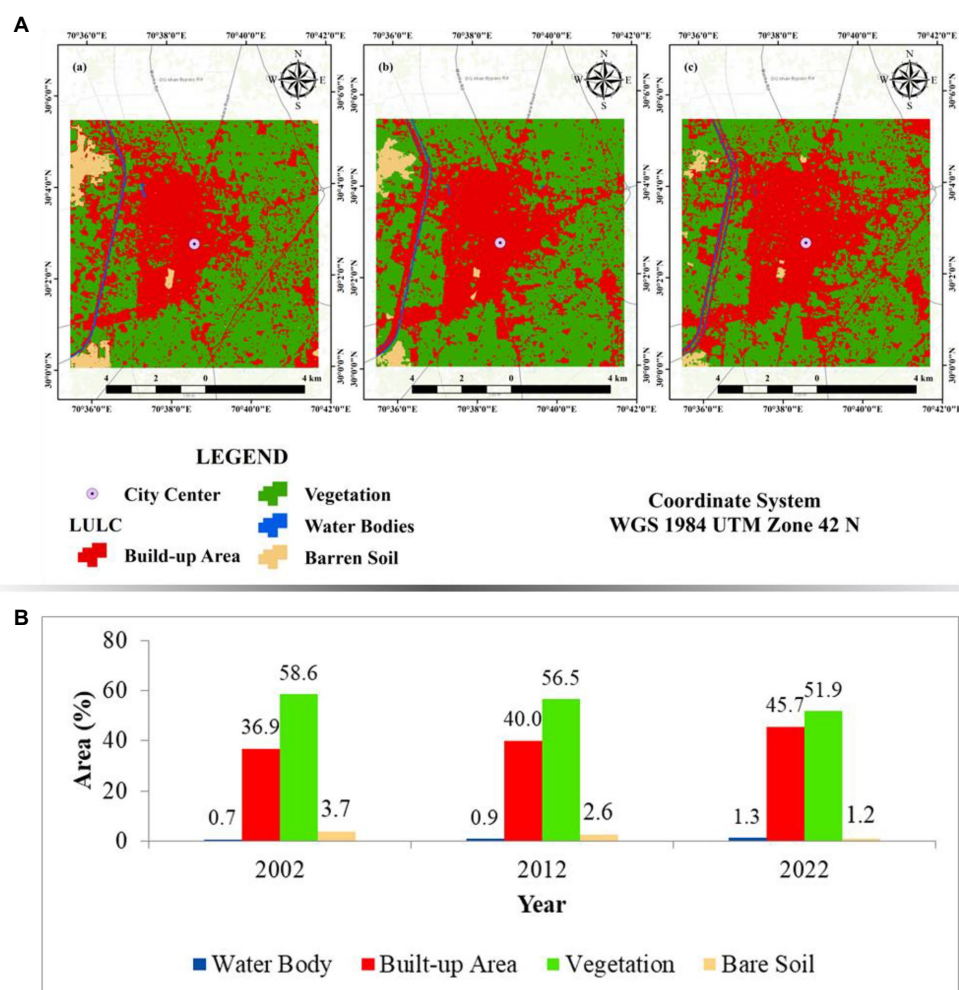


FIGURE 1

(A) Land use land cover (LULC) maps of Dera Ghazi Khan City from 2002 (left), 2012 (center), and 2022 (right). (B) Area percentage of different LULC types from 2002, 2012 and 2022.

TABLE 2 LULC area distribution and change detection from 2002, 2012, and 2022.

LULC	LULC area distribution						Change detection					
	2002		2012		2022		2002–2012		2012–2022		2002–2022	
	Area (ha)	Area (%)	Area (ha)	Area (%)	Area (ha)	Area (%)	Area (ha)	Area (%)	Area (ha)	Area (%)	Area (ha)	Area (%)
Water body	69	0.7	88	0.9	126	1.3	19	0.2	38	0.4	57	0.6
Built-up area	3,693	36.9	3,997	40.0	4,567	45.7	304	3.0	570	5.7	874	8.7
Bare soil	374	3.7	260	2.6	121	1.2	–114	–1.1	–138	–1.4	–253	–2.5
Vegetation	5,864	58.6	5,655	56.5	5,186	51.9	–209	–2.1	–469	–4.7	–678	–6.8
Total	10,000	100										

LULC classification. The estimated Kappa Coefficient is higher than 0.90 for each year. Similarly, the Overall accuracy is also higher than 90% for all the years, whereas it almost reached perfection in 2022. However, the producer's accuracy is low for Bare Soil for 2002 (56.25%). A possible justification for this low producer accuracy is the limited exposure area for sample collection but in the recent decade,

it shows satisfactory results as 81.82% (2012) and 81.30% (2022), accordingly. All other accuracy level is more than 90%. The most corrected classification was recorded for water bodies for almost all the periods, which reached 100% for the producer's accuracy scenario in 2022. This situation shows the reliability of the LULC classification results from this study.

TABLE 3 Detail of all LULC classification accuracy assessments from 2002, 2012, and 2022 Landsat images.

Year	User's accuracy (%)				Producer's accuracy (%)				Overall accuracy (%)	Kappa Coefficient
	Water Body	Built-up Area	Vegetation	Bare Soil	Water Body	Built-up Area	Vegetation	Bare Soil		
2002	90	89.61	92.98	90	100	92	95.5	56.25	91.5	0.913
2012	100	93.75	95.66	90	100	93.75	96.43	81.82	94.8	0.947
2022	100	97.73	97.1	92.9	100	97.73	99	81.3	97.2	0.97
Mean	96.7									

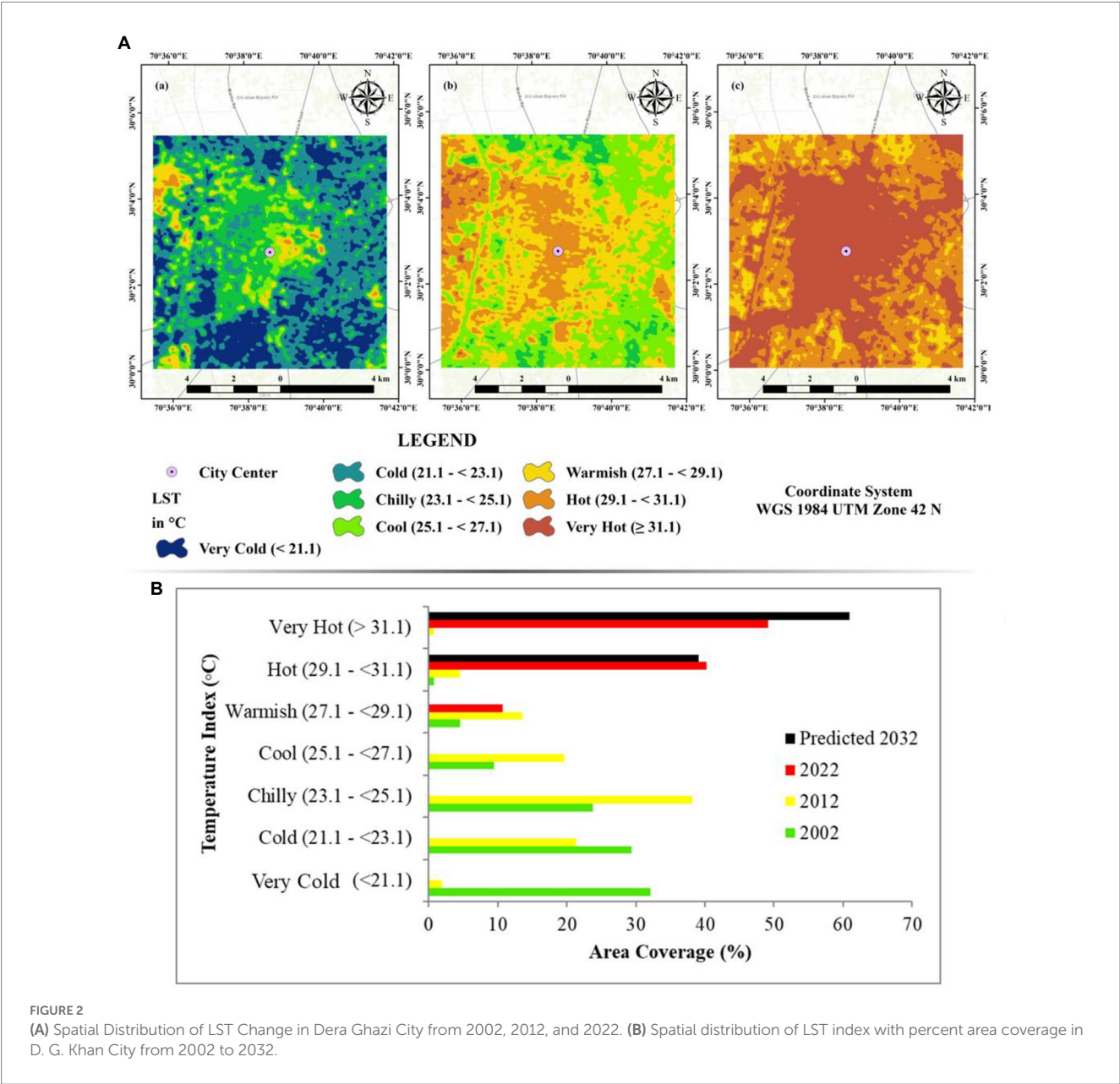


FIGURE 2 (A) Spatial Distribution of LST Change in Dera Ghazi City from 2002, 2012, and 2022. (B) Spatial distribution of LST index with percent area coverage in D. G. Khan City from 2002 to 2032.

3.2. Spatial–temporal heterogeneities in LST (2002–2022)

As the urban areas increased, so did the study area’s temperature in the last two decades (Figure 2A). In 2002, a meager amount of hot

areas is observed in the study area. Major areas are covered in very cold to chilly class (<21.1–<25.1). Around 33% of the area is covered in a very cold region. Nearly 2% of the area lies in the hot region. However, this situation changed in 2012 as the maximum temperature in the study area raised to 33.096 °C from 30.896 °C—approximately

3° C higher than in the year 2002. Similarly, the mean temperature increased by approximately 2° C, but the standard deviation remained the same (Table 4). About 40% of the area falls into the chilly region, and around 20% falls into the cold region. However, in 2012, the very cold regions consisted of only 3% of areas, approximately decreasing from 33% in 2002. Some areas in the 2012 scenario also fall into a very hot region. In 2022, the maximum temperature increased at the same rate. The highest temperature recorded was 36.661°C in 2022, having the same increasing trend as 2002–2012. Despite this, the mean temperature increased at an alarming rate. Almost a 7° C increase is observed in the 2012–2022 LST scenarios. This situation shows no area falling into cool, chilly, cold, and very cold regions. Most areas in 2022 are covered with “very hot” and “hot” regions (85% approximately). Nearly 11% of the area is covered with warmish regions. These results show an overall increase in the mean, minimum, and maximum LST in the study area—which should be a matter of serious concern for the relevant authorities. The rate of average annual LST change for the study area is noted as 0.3° C.

The prediction of LST for 2032 shows that an additional 5° C increase in maximum and a 4° C raise in the mean temperature is expected. Under these circumstances, the study area is expected to consist of very hot and hot regions mostly. By 2032, nearly 60% of areas in the study area are expected to be in the “very hot” class along with 40% of areas in hot regions (Figure 2B).

3.2.1. LULC-wise LST discrepancies

As expected, the lowest temperature in comparison with other land use classes is recorded for water bodies over 2002–2022 and in the predicted scenario for 2032. Where 23°C is the mean temperature in 2002 for water bodies, the value remained almost the same in 2012. In 2022, however, the value jumped to 33°C (Figure 3). The predicted scenario also recorded nearly a similar situation for water bodies in 2032. For the built-up areas, the mean temperature gradually increased throughout the study period. For instance, in 2002, the mean temperature is estimated as 23°C, which increased to ~25°C in 2012. However, in the next decade, the mean temperature increased to more than 30° C, which eventually became nearly 38°C in the predicted scenario of 2032. This situation represents that the temperature for the built-up areas is the highest as compared with other land use types—which is expected due to an increase in impervious surface. On the other hand, the mean temperature for vegetation cover is observed at ~22° C in 2002, which gradually increased to 25°C in 2012, and nearly 30°C in 2022. For the simulated scenario, the mean temperature is predicted as 35°C in 2032 (Figure 3). Lastly, bare soil shows the highest mean temperature in almost all the years, even in a predicted scenario. In both 2002 and 2012, the mean temperature of bare soil land cover is approximately 26° C. In 2022, the temperature reached 33°C, and it is predicted to reach 35°C in 2032. Overall, there has been an increase in the mean temperature for almost all of the LULC types during the study period, and this increasing trend is more likely to remain the same in the future without proper measures.

3.3. Exploring connections among LST, NDBI and NDVI

NDBI is used to identify the human settlements in land cover with few other essential features like roads, dams, canals, etc. (Kafy et al.,

TABLE 4 Detail of LST in Dera Ghazi Khan City from 2002, 2012 and 2022.

Year	Minimum	Maximum	Mean	STD
2002	16.942	30.896	22.632	2.319
2012	19.142	33.096	24.832	2.319
2022	26.984	36.661	31.193	1.692
2032	29.335	41.165	35.71	1.622

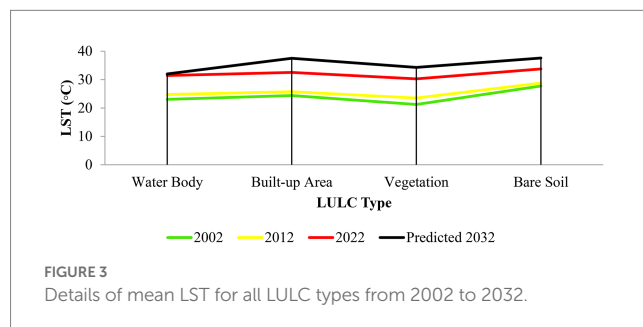


FIGURE 3
Details of mean LST for all LULC types from 2002 to 2032.

2019). A value of NDBI closer to +1 indicates land use covered with man-made features like buildings, roads, etc. Conversely, the values relative to −1 represent natural features like a forest, water body, vegetation, etc. Based on our assessment, an increasing NDBI index is as the value approached gradually +1 in the urban areas (Figure 4A). As for 2002, the maximum value for NDBI was closest to 0.35, which increased to 0.38 in 2012 and reached 0.43 in 2022. The increased value of NDBI in the central region of the study area represents a major urban expansion during the study period.

As for the NDVI, a completely mirrored scenario can be seen. For instance, the variation of NDVI values can be analyzed based on the radiation absorbed by the red spectral area chlorophyll and reflectance near the infrared spectral area of NDVI the more vegetation there will be. However, Figure 4B shows a different scenario as the value is decreasing towards −1. A gradual increase of urban areas at a cost of vegetation removal can be seen in a gradual decrease of NDVI values, as the maximum value for 2012 was reduced to 0.64 from 0.70 for 2002. In the recent decade (2022), the NDVI value decreased to 0.56. A similar pattern is observed for the minimum value too. In the 2002–2012 period, the minimum value of NDVI decreased by about 0.20 percent.

The relation between LST and NDVI for the study area during the last decade shows a disproportionate relation. In 2002, the highest concentration of NDVI values was between the 25 to 30°C range, with a low value of −0.2 to 0.2 (Supplementary Figure S3). In 2012, a different scenario was seen. The value was not concentrated in a specific range but equally distributed in all LST ranges, having the highest value of 0.6 in the 21–25°C LST range. In 2022, higher values of NDVI (0.6–0.3) were seen in the low value of the LST range (27–29°C). The overall scenario shows that the lower the value of NDVI, the higher the value of LST in the study area. The goodness-of-fit for all the linear relationships is well observed by higher values of R^2 (Supplementary Figure S3).

The relation between LST and NDBI shows the corresponding scenario of LST and NDBI. An evaluation of the linear relationship between NDBI and LST shows a positive association between both (Supplementary Figure S3). This implied that the LST is expected to

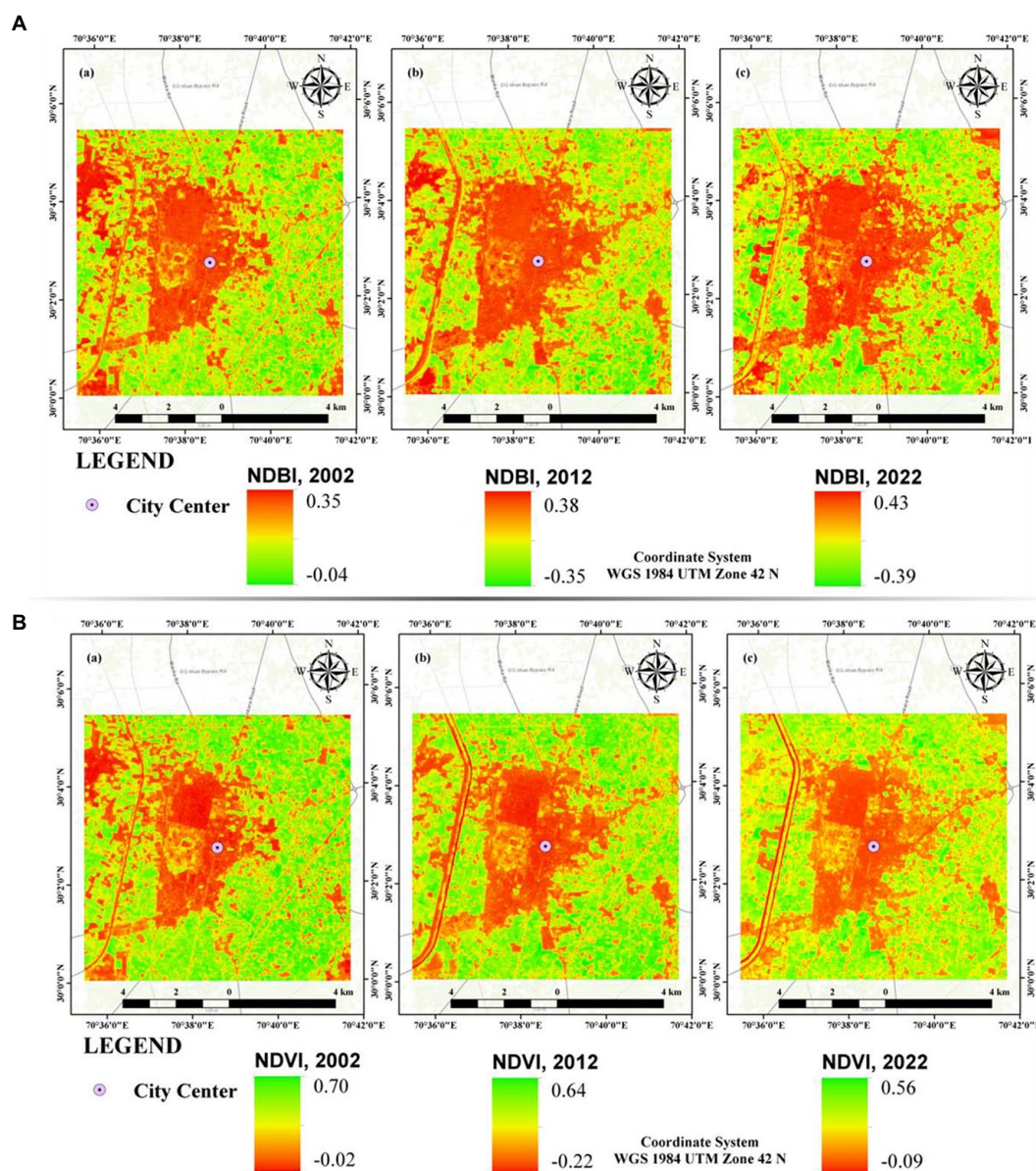


FIGURE 4

(A) Spatial pattern of NDBI in Dera Ghazi Khan City. (B) Spatial pattern of NDVI in Dera Ghazi Khan City. It is noted that the left, center, and right figures in both panels represent 2002, 2012, and 2022, respectively.

rise in the study area with an increase in NDBI. Similar to NDVI, there is high confidence in this association as reflected by higher goodness of fit values for all the periods (0.83, 0.85, and 0.89 for 2002, 2012, and 2022, respectively). In 2002, the NDBI pointed to having a higher value of 0.1 to 0.4 concentrated in the LST region of 25–30°C. The same scenario can be seen in the next decade as the higher valued NDBI points (0.2–0.4) were in the LST range of 27–33°C. In 2022, the scenario remained the same, but the value changed considerably (Supplementary Figure S3).

3.4. Drivers of LULC and LST changes

Five driving forces are selected to predict the LST and LULC changes for the year 2032. As for the elevation (Figure 5A), the highest

peak was seen in the western part of the study area with a maximum of 94 m. The elevation scenario was gradually decreasing value in the eastern region. A maximum of 15° slope was seen in the study area (Figure 5B). Buffer distances for waterways and road distances are essential to simulate the urban areas in the study area. As for the city center, the urban expansion region was determined by anthropogenic activity centers (Figure 5C). Panels d and e (Figure 5) show the buffered distance covered by the waterways and road distance, respectively, where a low value derives that this area will remain unchanged for at least 2032.

The predicted LULC and LST are illustrated in Figures 6A,B, respectively. According to the simulation results, the study area will go through a tremendous amount of changes in the built-up area at the cost of green areas. Similarly, the LST predicted a high amount of temperature in the city center and its peripheries. The

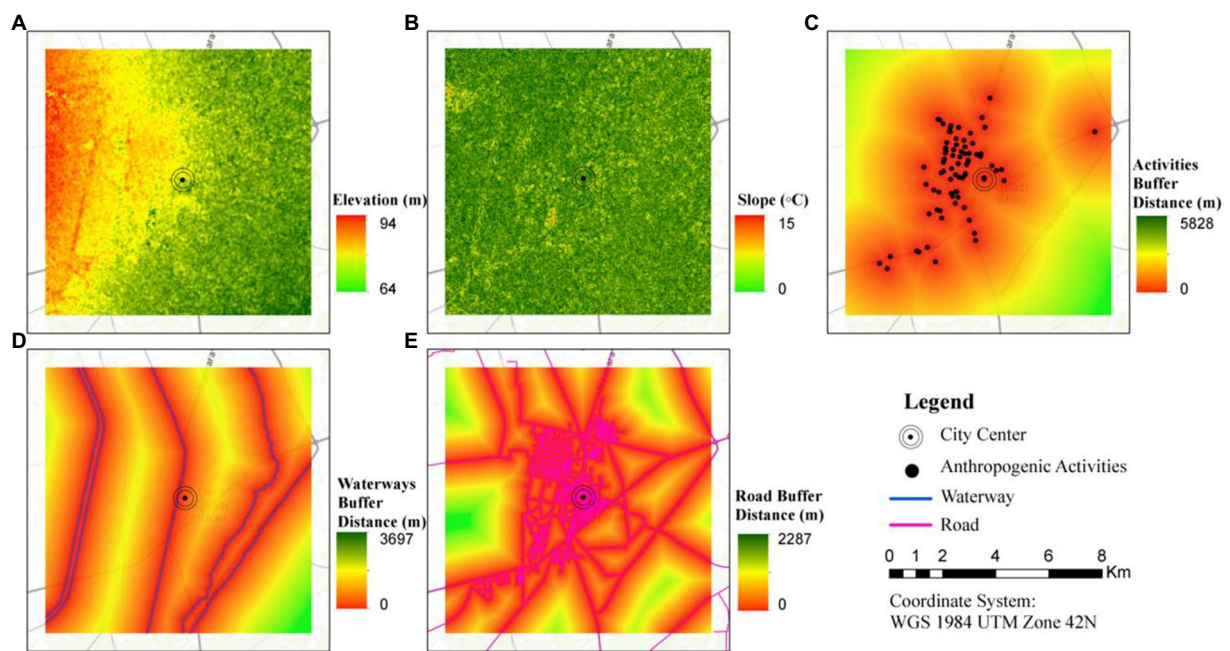


FIGURE 5

All drivers for predicting the LULC and LST change for the year 2032. (A) elevation, (B) slope, (C) anthropogenic activities buffer, (D) waterways buffer, and (E) road buffer.

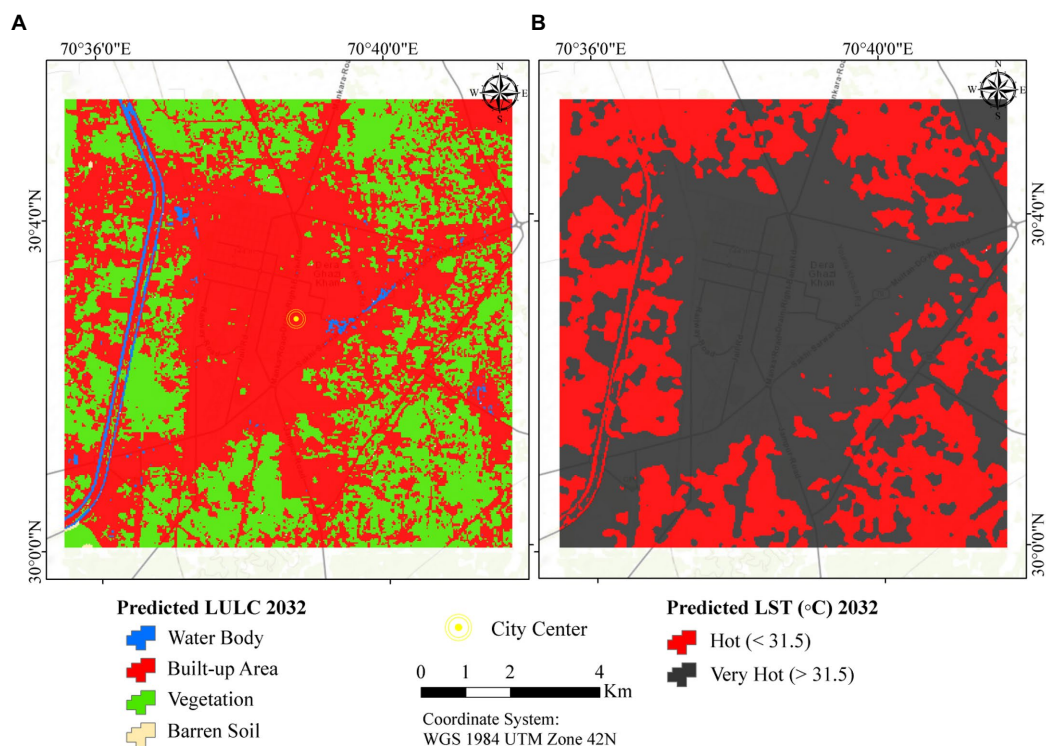


FIGURE 6

(A) Predicted LULC and (B) LST for the year 2032.

uncontrolled urbanization and increasing trends of LST in the study area should be a potential concern for urban managers, city planners, and urban dwellers. The areas where the predicted LST is

comparatively high (i.e., very hot zones represented by black shades in Figure 6B) should be prioritized for measures to mitigate the heat island effect.

4. Discussion

Sustainability in the long-term context requires informed planning and management in the face of environmental changes through space and time. In an anthropogenic activities-based climate change-induced warming world, rapid urbanization-led impervious surface in cities leads to land resource degradation and scorching heat, which creates challenging conditions in terms of health issues and energy use among many others¹. Evaluating drivers of LULC changes, its association with LST, and their simulation for future decision-making is a progressive approach to tackling related climate change impacts. The present study not only effectively explore the historical patterns in LULC and LST, but further goes ahead one step to simulate future expected LULC patterns and LST situation using machine learning, artificial intelligence, and spatial modeling techniques (e.g., Figures 1, 2, 4, 6). The observed changes indicated a constantly increasing trend of built-up area and a consistently decreasing trend of green areas at a pace of 8.7 and 6.8%, accordingly, from 2002 to 2022, which is in line with existing studies in different parts of the world (e.g., Alqurashi et al., 2016; Das et al., 2021; Waleed and Sajjad, 2022). Such findings have particular implications to plan and strategize action plans for sustainable resource use particularly the land resource in cities. While the findings are useful in the elaborated context, similar studies are recommended in other regions beyond the study area in Pakistan to have a broader understanding and provincial and national scale policy on LULC (i.e., no-net-loss of green cover). In terms of LULC classification using the supervised- maximum likelihood classification, the accuracy assessment results (Kappa's Coefficient) found almost perfect agreement as >90% as compared with the Bera et al. (2022) (87%), Das et al. (2021) (88%), Kafy et al. (2021c) (96%) and Hussain et al. (2019) (> 80%).

Notably, the urban fabric in the city area increased by 874 ha with high intensity towards the main corridors in the northeast to the southwest direction (Figure 1A). The haphazard urban expansion and messy development in the study area's center increased LST and spotted the urban heat island effect (Figure 2A). Due to the development planning-related negligence, the city has only one older park and fewer green spaces constructed in recent years, which provided fewer opportunities to lower LST. On the other hand, several large-scale commercial activities and services are distributed in the urban center adding more impervious surfaces to the urban regions of the city. In the future, the introduction of modern integrated gray-green structural development along with initiatives to preserve vegetation cover could potentially compensate for the lack of green areas in the study area leading to lower LST. Except for the central dense urban regions, the peri-urban areas comprised the newly developed housing societies and industrial areas where green spaces are unevenly distributed. The removal of trees and agricultural land, no insertion of new green spaces, and construction are among the critical issues that lead to the rising temperature and, ultimately, the heat island effect (Figure 2). The future scenario depicts the worst scenario if proper planning and mitigation measures are not followed

promptly. Hence, evaluations as such are of high importance to identify priority intervention areas for immediate or gradual actions in the context of climate change adaptations in the study area and beyond.

The historical city of D. G. Khan was the first of its kind gridded planned city in 1911 (Garcia et al., 2019) in the British colonial period where each grid (Block) is interlinked with roads and a community gathering space in the block center with proper green space. The Tehsil Municipal Authority (TMA) autonomously governed the city planning and developmental activities and was responsible for a better quality of life. After the independence on 14th August 1947, district D. G. Khan and its historical city were neglected, and unplanned developmental activities were started due to improper resource allocation and the absence of any effective urban land use policy in Pakistan (Arshad et al., 2022).

In 1970, a flux of labor migration toward the middle east countries (e.g., the United Arab Emirates and Saudi Arabia) (Azhar, 2008), and flood events in 1992, 1998, 2010, 2014 and 2022 (Ahmed et al., 2014; Munir and Iqbal, 2016; Garcia et al., 2018) acted as trigger points that initiated urban migration from rural areas. Such migration, especially from the de-excluded areas, led the high land price and renters, unplanned construction activities, congested road development, improper green space management, and removal of agriculture and scrubland. Similar studies also show the same results in other parts of the country. Arshad et al. (2022), for example, conducted the temporal changes of LULC in association with the surface urban heat island (SUHI) effect. Their study argued that the high demand for housing schemes to a flux of migration from neighboring rural areas in the recent two decades had put lots of pressure on Lahore city (the 2nd largest city in Pakistan). This disorganized urban growth leads to the removal of green spaces and causes 3–4°C higher temperatures and the SUHI effect in the central urban district (CBD) and slum areas. Similar results were found in the capital city of Pakistan (Islamabad) (Waseem and Khayyam, 2019; Aslam et al., 2021). Waseem and Khayyam (2019) discovered the 3–9°C higher LST (0.52°C per year) at the cost of 51% vegetation removal. This green-gray conversion increasing LST and UHI effect also affects the northern mountainous region of Pakistan. Where Ullah et al. (2019b) found that the previous three decades were the most critical that put a lot of pressure on Pakistan's mountainous cities and LULC changes had a stronger relationship to raising the LST in the lower Himalayan region, which further shows our findings' consistency with the literature. In the same year, Ullah et al., (2019a,b) discovered that the flux of migrants from neighboring villages due to insecurity and to seek better living standards causes deforestation and consequently, the removal of urban forest (4.42%) and agriculture land areas (2.74%) led to the rising LST (greater than 27°C) and UHI effect will increased to 42 and 60% in the upcoming years (2032 and 2047). This situation further stresses the need for informed planning of land resources along with preserving the vegetation through no-net-loss policies via empirical references such as those presented in this study.

A clear trend of decreasing NDVI and increasing NDBI (Figure 4) in the study area further confirms the consequences of lack of management, ill-informed construction, and unplanned resource allocation that affect the LST and UHI hotspots. D. G. Khan city is the center point of Pakistan that connects all the adjacent provinces. Being divisional capital, it is the hub of commercial and economic activities. Economic growth results in the LULC change and causes

¹ <https://www.worldweatherattribution.org/climate-change-made-devastating-early-heat-in-india-and-pakistan-30-times-more-likely/>

socio-environmental problems. The simulation results presented in this study confirm that by 2032, the city will face a 5° C high mean temperature based on the historical patterns, which could potentially lead to more challenges associated with UHI (Figures 4, 6 and Table 4) if no appropriate measures are taken. These findings are similar to (Tariq et al., 2023).

Recently, the government developed several land-use policies and rehabilitation programs at the federal and provincial levels. Still, lack of political interest and insufficient urban governance are the main barriers to implementing these initiatives. In recent years, the government has launched a Billion Trees Tsunami program all over Pakistan to tackle green cover degradation in the country, which has important implications for urban climatic conditions (Sajjad, 2020). For instance, this program was initially introduced in Khyber Pakhtunkhwa province and recent research shows positive outcomes regarding land surface temperature reduction (Mumtaz et al., 2020), air surface temperature reduction (Mahmood, 2020), better ecosystem quality (Khan N. et al., 2019), and air pollution control measures (Kharl and Xie, 2017). Taking such programs to the city level particularly to zones of higher LST, as identified in this study, could be a useful approach to mitigate the UHI effect in cities.

Our results have shown that green spaces are insufficient to overcome the large urban footprint. Hence, the green cover should be introduced and preserved on large patches to overcome the impact of impervious surfaces. The city and divisional government should introduce strict policies to implement green space initiatives at a larger scale to overcome the LST effect. The predicted results of 2032 also indicated the tremendous increase of 4–5° C LST and UHI, which represents an alarming situation for urban dwellers and should be a matter of the highest concern for relevant authorities. Estoque et al. (2017) and Arshad et al. (2022) investigated that the temperature of green spaces is ~3° C lower than urban fabric temperature and strongly suggested that the urban green space is one of the most optimal solutions to overcome the LST and mitigate the UHI effect. Hence, we recommend prioritization of the areas with higher LST, particularly in the 2032 prediction map, to initiate efforts for green spaces in the context of mitigating the impacts, especially the health issues, which the country has witnessed recently due to heat wave.

5. Conclusions and recommendations

This study leverages multi-temporal remote sensing data to track historical and predict future patterns of land use/cover changes, LST, and the association between them in a mid-country city that is a part of the China-Pakistan Economic Corridor (CPEC) under the One Road One Built project. The overarching goal of the study is to determine how changes in land use classes affected LST. The methods used in this study are quite effective in accomplishing the research objectives. The study area is divided into four LULC categories, such as water bodies, built-up land, bare land, and vegetation. Due to political and socio-economic considerations, the land cover classification revealed that built-up areas and water bodies increased by 8.7 and 0.6%, respectively, over the study period (2002–2022). In contrast, bare land and vegetation dropped by 2.5 and 6.8%, respectively.

Furthermore, the study determines a negative association of vegetation area (NDVI) and water bodies with LST. The LULC

significantly influences the LST and is extremely sensitive to vegetation and soil moisture; vegetation is the most important element in this connection. Although there is a positive association between NDBI and LST, higher LST is reported in areas with less vegetated (barren land) and vice versa. We conclude that without proper measures, a tremendous increase in the impervious surface is expected at the cost of green areas, which could potentially compromise the livability and comfortability of cities in the wake of global warming. This situation would very well lead to the UHI effect influencing millions of people in terms of increased energy demands and health-related challenges.

In order to cope with this increasing LST situation, green urban design and infrastructure planning and development must be prioritized. Similarly, enhancing water features like lakes, canals, waterfalls, and public fountains along with significantly increasing green areas like artificial parks, green walls, gardens, and linear plantings, particularly woody plants could positively drive the UHI mitigation efforts. In addition, to achieve the intended ecological development in terms of environmental resource planning and management, LULC alteration activities should be minimized, and environmental education should be reawakened. The findings of this study have important implications for urban landscape planning, particularly when it comes to landscape connectivity between green and impervious surfaces and their impact on LST. All of these would result in science-based information having important implications for urban planning and land resource management along with providing opportunities to design appropriate action plans to mitigate the UHI effect.

6. Limitations and future works

The present study provides important and useful information for the study area to design proper adaptation and mitigation policies and action plans. Such actions at local levels would progressively contribute to regional sustainability from a bottom-up perspective. From a short-to-medium-term impact perspective, predicting future changes in LULC and how it will influence the LST under environmental changes provides key references for planning and management of the land resource in a more sustainable way along with providing opportunities for adaptation and mitigating climate change through local actions. Future urban studies could concentrate on the topic of rapid urbanization's impact on public health and infrastructure along with the influence of predicted LST on health-related issues in urban societies—left for upcoming studies. Future research should address the following limitations. Higher-resolution images for LULC categorization may improve LULC composition-LST correlation explanation and urban planner usability. Urban morphology is needed to better understand the nonlinear association between LULC and LST in urban areas. For more conclusive LST prediction findings, other nonlinear regression approaches may need to be investigated. This study used temperature indices to analyze LST; multi-season analysis will provide more information. Although LULC is a primary influence in LST variation, other characteristics affecting LST, most likely topography and elevation, are equally essential. In commercial/industrial locations, surface morphology also effects surface temperature retrieval. More precise spatial distribution information

regarding urban land shape is required for more accurate characterization of patterns and changes of the urban heat island effect.

Landsat data can detect LULC and LST effects, but projecting future changes is challenging. MC, CA, and ANN models are most often employed to predict LULC change. We used MC model based on the LULC conversion is known but spatial dependency and dissemination are unavailable. Future studies will focus on the CA and ANN models. CA is employed in utility and resource research since its greatest advantage depends on the initial configuration of variables like distance to road and rail network, slope, and elevation. To forecast LST, ANN can be used in conjunction with associated LULC indices like as NDVI, NDBI, NDBSI, and NDWI to successfully estimate future changes. ANN technique is an LST predictor because it employs LULC indices to anticipate future scenarios and reflects past patterns. As a result, ANN is often recognized as the best tool for forecasting the effects of LST.

Data availability statement

The original contributions presented in the study are included in the article/[Supplementary material](#), further inquiries can be directed to the corresponding author.

Author contributions

MM and AR acquired data. MM, AR, and ZZ performed data analysis. MM, AR, ZZ, and MS wrote the first draft of the manuscript. QY and ZS supervised and did the final proofreading of the article. All authors substantially contributed to the study's conception and design, feedback and input during the write-up,

analysis, data validation, and proofreading of the present research work.

Funding

This research was funded by the National Natural Science Foundation of China (42171295), and the Major Project of Collaborative Innovation Center on Yellow River Civilization jointly built by Henan Province and the Ministry of Education (2020M19).

Conflict of interest

The authors declare that the research was conducted in the absence of any commercial or financial relationships that could be construed as a potential conflict of interest.

Publisher's note

All claims expressed in this article are solely those of the authors and do not necessarily represent those of their affiliated organizations, or those of the publisher, the editors and the reviewers. Any product that may be evaluated in this article, or claim that may be made by its manufacturer, is not guaranteed or endorsed by the publisher.

Supplementary material

The Supplementary material for this article can be found online at: <https://www.frontiersin.org/articles/10.3389/fevo.2023.1115074/full#supplementary-material>

References

- Ahmed, B., Kamruzzaman, M., Zhu, X., Rahman, M., and Choi, K. (2013). Simulating land cover changes and their impacts on land surface temperature in Dhaka, Bangladesh. *Remote Sens.* 5, 5969–5998. doi: 10.3390/rs5115969
- Ahmed, B., Wei, S., Fu, Y. G., Shabbir, M., and Nabi, G. (2014). Effects of floods policy in Pakistan and management issues: (case of district Dera-ghazi Khan). *Int. J. Adv. Res.* 2, 967–974.
- Akinyemi, F. O., Ikanyeng, M., and Muro, J. (2019). Land cover change effects on land surface temperature trends in an African urbanizing dryland region. *City Environ. Interact.* 4:100029. doi: 10.1016/j.cacint.2020.100029
- Aktaş, N. K., and Dönmez, N. Y. (2021). "An urban paradox: urban resilience or human needs" in *Design of Cities and Buildings: Sustainability and Resilience in the Built Environment*. ed. M. E. Samad (London: IntechOpen), 173.
- Alqadhi, S., Mallick, J., Balha, A., Bindajam, A., Singh, C. K., and Hoa, P. V. (2021). Spatial and decadal prediction of land use/land cover using multi-layer perceptron-neural network (Mlp-Nn) algorithm for a semi-arid region of Asir, Saudi Arabia. *Earth Sci. Inf.* 14, 1547–1562. doi: 10.1007/s12145-021-00633-2
- Alqurashi, A., Kumar, L., and Sinha, P. (2016). Urban land cover change modelling using time-series satellite images: a case study of urban growth in five cities of Saudi Arabia. *Remote Sens.* 8:838. doi: 10.3390/rs8100838
- Amir Siddique, M., Dongyun, L., Li, P., Rasool, U., Ullah Khan, T., Javaid Aini Farooqi, T., et al. (2020). Assessment and simulation of land use and land cover change impacts on the land surface temperature of Chaoyang District in Beijing, China. *PeerJ* 8:e9115. doi: 10.7717/peerj.9115
- Andrade, J., Cunha, J., Silva, J., Rufino, I., and Galvão, C. (2021). Evaluating single and multi-date landsat classifications of land-cover in a seasonally dry tropical forest. *Remote Sens. Appl.* 2021:100515. doi: 10.1016/j.rsase.2021.100515
- Arshad, S., Ahmad, S. R., Abbas, S., Asharf, A., Siddiqui, N. A., and Islam, Z. (2022). Quantifying the contribution of diminishing green spaces and urban sprawl to urban heat island effect in a rapidly urbanizing metropolitan city of Pakistan. *Land Use Policy* 113:105874. doi: 10.1016/j.landusepol.2021.105874
- Artis, D. A., and Carnahan, W. H. (1982). Survey of emissivity variability in thermography of urban areas. *Remote Sens. Environ.* 12, 313–329. doi: 10.1016/0034-4257(82)90043-8
- Aslam, A., Rana, I. A., and Bhatti, S. S. (2021). The spatiotemporal dynamics of urbanisation and local climate: a case study of Islamabad, Pakistan. *Environ. Impact Assess. Rev.* 91:106666. doi: 10.1016/j.eiar.2021.106666
- Azhar, I. A. K. (2008). *Overseas Migration and its Socio-economic Impacts on the Families Left Behind in Pakistan: A Case Study in the Province*. Punjab, Pakistan, Kassel University Press GmbH.
- Bera, D., Das Chatterjee, N., Mumtaz, F., Dinda, S., Ghosh, S., Zhao, N., et al. (2022). Integrated influencing mechanism of potential drivers on seasonal variability of Lst in Kolkata municipal corporation, India. *Land* 11:1461. doi: 10.3390/land11091461
- Bokaie, M., Zarkesh, M. K., Arasteh, P. D., and Hosseini, A. (2016). Assessment of urban Heat Island based on the relationship between land surface temperature and land use/ land cover in Tehran. *Sustain. Cities Soc.* 23, 94–104. doi: 10.1016/j.scs.2016.03.009
- Cai, M., Ren, C., Xu, Y., Lau, K. K.-L., and Wang, R. (2018). Investigating the relationship between local climate zone and land surface temperature using an improved Wudapt methodology—a case study of Yangtze River Delta, China. *Urban Clim.* 24, 485–502. doi: 10.1016/j.uclim.2017.05.010
- Castelli, F. (2018). Drivers of migration: why do people move? *J. Travel Med.* 25:tay040. doi: 10.1093/jtm/tay040
- Crum, S. M., and Jenerette, G. D. (2017). Microclimate variation among urban land covers: the importance of vertical and horizontal structure in air and land surface temperature relationships. *J. Appl. Meteorol. Climatol.* 56, 2531–2543. doi: 10.1175/JAMC-D-17-0054.1

- Das, N., Mondal, P., Sutradhar, S., and Ghosh, R. (2021). Assessment of variation of land use/land cover and its impact on land surface temperature of Asansol subdivision. *Egypt. J. Remote Sens. Space Sci.* 24, 131–149. doi: 10.1016/j.ejrs.2020.05.001
- Dey, N. N., Al Rakib, A., Kafy, A.-A., and Raikwar, V. (2021). Geospatial modelling of changes in land use/land cover dynamics using multi-layer perception Markov chain model in Rajshahi City, Bangladesh. *Environ. Chall.* 4:100148. doi: 10.1016/j.envc.2021.100148
- Dos Santos, J. Y. G., Montenegro, S. M. G. L., Da Silva, R. M., Santos, C. A. G., Quinn, N. W., Dantas, A. P. X., et al. (2021). Modeling the impacts of future Lulc and climate change on runoff and sediment yield in a strategic basin in the Caatinga/Atlantic forest ecotone of Brazil. *Catena* 203:105308. doi: 10.1016/j.catena.2021.105308
- Estoque, R. C., Murayama, Y., and Myint, S. W. (2017). Effects of landscape composition and pattern on land surface temperature: an urban heat island study in the megacities of Southeast Asia. *Sci. Total Environ.* 577, 349–359. doi: 10.1016/j.scitotenv.2016.10.195
- Faroughi, M., Karimimoshaver, M., Aram, F., Solgi, E., Mosavi, A., Nabipour, N., et al. (2020). Computational modeling of land surface temperature using remote sensing data to investigate the spatial arrangement of buildings and energy consumption relationship. *Eng. Appl. Comput. Fluid Mech.* 14, 254–270. doi: 10.1080/19942060.2019.1707711
- FBS. (2017). *Federal Bureau of Statistics: Provisional Summary Results of 6th Population and Housing Census*. Islamabad: Pakistan Bureau Of Statistics, Ministry of Statistics, Islamabad, Islamic Republic of Pakistan.
- Footy, G. M., Campbell, N., Trodd, N., and Wood, T. (1992). Derivation and applications of probabilistic measures of class membership from the maximum-likelihood classification. *Photogramm. Eng. Remote. Sens.* 58, 1335–1341.
- Gan, T., Liang, W., Yang, H., and Liao, X. (2020). The effect of economic development on haze pollution (Pm2. 5) based on a spatial perspective: urbanization as a mediating variable. *J. Clean. Prod.* 266:121880. doi: 10.1016/j.jclepro.2020.121880
- Garcia, A., Orengo, H. A., Conesa, F. C., Green, A. S., and Petrie, C. A. (2018). Remote sensing and historical morphodynamics of alluvial plains. The 1909 Indus flood and the city of Dera Ghazi Khan (province of Punjab, Pakistan). *Geosciences* 9:21. doi: 10.3390/geosciences9010021
- Garcia, A., Orengo, H., Conesa, F., Green, A., and Petrie, C. (2019). Remote sensing and historical morphodynamics of alluvial plains. The 1909 Indus flood and the city of Dera Ghazi Khan (province of Punjab, Pakistan). *Geosciences* 9:21. doi: 10.3390/geosciences9010021
- Guha, S., Govil, H., and Diwan, P. (2019). Analytical study of seasonal variability in land surface temperature with normalized difference vegetation index, normalized difference water index, normalized difference built-up index, and normalized multiband drought index. *J. Appl. Remote. Sens.* 13:024518. doi: 10.1117/1.JRS.13.024518
- Guo, A., Yang, J., Xiao, X., Xia, J., Jin, C., and Li, X. (2020). Influences of urban spatial form on urban heat island effects at the community level in China. *Sustain. Cities Soc.* 53:101972. doi: 10.1016/j.scs.2019.101972
- Hamad, R., Balzter, H., and Kolo, K. (2018). Predicting land use/land cover changes using a ca-Markov model under two different scenarios. *Sustainability* 10:3421. doi: 10.3390/su10103421
- Hashmi, H. N., Siddiqui, Q. T. M., Ghumman, A. R., and Kamal, M. A. (2012). A critical analysis of 2010 floods in Pakistan. *Afr. J. Agric. Res.* 7, 1054–1067. doi: 10.5897/AJARX11.036
- Hassan, M. M. (2017). Monitoring land use/land cover change, urban growth dynamics and landscape pattern analysis in five fastest urbanized cities in Bangladesh. *Remote Sens. Appl.* 7, 69–83. doi: 10.1016/j.rsase.2017.07.001
- Heaviside, C., Macintyre, H., and Vardoulakis, S. (2017). The urban heat island: implications for health in a changing environment. *Curr. Environ. Health Rep.* 4, 296–305. doi: 10.1007/s40572-017-0150-3
- Heikkinen, A., Mäkelä, H., Kujala, J., Nieminen, J., Jokinen, A., and Rekola, H. (2019). *Urban Ecosystem Services and Stakeholders: Towards a Sustainable Capability Approach*. Strongly Sustainable Societies. Taylor & Francis.
- Hussain, S., Mubeen, M., Ahmad, A., Akram, W., Hammad, H. M., Ali, M., et al. (2020). Using Gis tools to detect the land use/land cover changes during forty years in Lodhran District of Pakistan. *Environ. Sci. Pollut. Res. Int.* 27, 39676–39692. doi: 10.1007/s11356-019-06072-3
- Hussain, S., Mubeen, M., Akram, W., Ahmad, A., Habib-Ur-Rahman, M., Ghaffar, A., et al. (2019). Study of land cover/land use changes using Rs and Gis: a case study of Multan district, Pakistan. *Environ. Monit. Assess.* 192:2. doi: 10.1007/s10661-019-7959-1
- Imran, M., and Mehmood, A. (2020). Analysis and mapping of present and future drivers of local urban climate using remote sensing: a case of Lahore, Pakistan. *Arab. J. Geosci.* 13, 1–14. doi: 10.1007/s12517-020-5214-2
- Kadhim, N., Mourshed, M., and Bray, M. (2016). Advances in remote sensing applications for urban sustainability. *EuroMediter. J. Environ. Integr.* 1, 1–22. doi: 10.1007/s41207-016-0007-4
- Kafy, A.-A., Al Rakib, A., Akter, K. S., Rahaman, Z. A., Faisal, A.-A., Mallik, S., et al. (2021a). Monitoring the effects of vegetation cover losses on land surface temperature dynamics using geospatial approach in Rajshahi City, Bangladesh. *Environ. Chall.* 4:100187. doi: 10.1016/j.envc.2021.100187
- Kafy, A.-A., Faisal, A.-A., Sikdar, M. S., Hasan, M. M., and Ahmmed, R. (2019). *Using Geographic Information System and Remote Sensing Techniques in Environmental Management: A Case Study in Cumilla City Corporation*. 1st International Conference on Urban & Regional Planning. Dhaka, Bangladesh: Bangladesh Institute of Planners (Bip).
- Kafy, A. A., Rahman, M. S., Faisal, A.-A., Hasan, M. M., and Islam, M. (2020). Modelling future land use land cover changes and their impacts on land surface temperatures in Rajshahi, Bangladesh. *Remote Sens. Appl.* 18:100314. doi: 10.1016/j.rsase.2020.100314
- Kafy, A.-A., Rahman, M. S., Islam, M., Al Rakib, A., Islam, M. A., Khan, M. H. H., et al. (2021b). Prediction of seasonal urban thermal field variance index using machine learning algorithms in Cumilla, Bangladesh. *Sustain. Cities Soc.* 64:102542. doi: 10.1016/j.scs.2020.102542
- Kafy, A.-A., Shuvo, R. M., Naim, M. N. H., Sikdar, M. S., Chowdhury, R. R., Islam, M. A., et al. (2021c). Remote sensing approach to simulate the land use/land cover and seasonal land surface temperature change using machine learning algorithms in a fastest-growing megacity of Bangladesh. *Remote Sens. Appl.* 21:100463. doi: 10.1016/j.rsase.2020.100463
- Kazemzadeh-Zow, A., Zanganeh Shahraki, S., Salvati, L., and Samani, N. N. (2017). A spatial zoning approach to calibrate and validate urban growth models. *Int. J. Geogr. Inf. Sci.* 31, 763–782. doi: 10.1080/13658816.2016.1236927
- Khan, I. (2018). *Cpec will be Reviewed for Balochistan Promises*. Karachi: Fortnightly Engineering Review.
- Khan, I., Javed, T., Khan, A., Lei, H., Muhammad, I., Ali, I., et al. (2019). Impact assessment of land use change on surface temperature and agricultural productivity in Peshawar-Pakistan. *Environ. Sci. Pollut. Res.* 26, 33076–33085. doi: 10.1007/s11356-019-06448-5
- Khan, N., Shah, S. J., Rauf, T., Zada, M., Yukun, C., and Harbi, J. (2019). Socioeconomic impacts of the billion trees afforestation program in Khyber Pakhtunkhwa Province (kpk). *Pakistan. Forests* 10:703. doi: 10.3390/f10080703
- Kharl, S., and Xie, X. (2017). Green growth initiative will lead toward sustainable development of natural resources in Pakistan: an Investigation of “billion tree tsunami afforestation project”. *Sci Int* 29, 841–843.
- Korkmaz, C., and Meşhur, H. F. A. (2021). Neo-liberal urbanism and sustainability in Turkey: commodification of nature in gated community marketing. *J. Housing Built Environ.* 3, 1–34. doi: 10.1007/s10901-020-09800-1
- Lakshmisha, A., Agarwal, P., and Nikam, M. (2019). Assessing the Double Injustice of Climate Change and Urbanization on Water Security in Peri-urban Areas: Creating Citizen-Centric Scenarios. *Water Insecur. Sanit. Asia* 1:301.
- Li, W., Cao, Q., Lang, K., and Wu, J. (2017). Linking potential heat source and sink to urban heat island: heterogeneous effects of landscape pattern on land surface temperature. *Sci. Total Environ.* 586, 457–465. doi: 10.1016/j.scitotenv.2017.01.191
- Luo, P., Kang, S., Zhou, M., Lyu, J., Aisyah, S., Binaya, M., et al. (2019). Water quality trend assessment in Jakarta: a rapidly growing Asian megacity. *PLoS One* 14:e0219009. doi: 10.1371/journal.pone.0219009
- Lustgarten, A. (2020). *The Great Climate Migration*. New York, New York: Times Magazine.
- Maduako, I., Yun, Z., and Patrick, B. (2016). Simulation and prediction of land surface temperature (Lst) dynamics within Ikom City in Nigeria using artificial neural network (Ann). *J. Remote Sens. Gis* 5, 1–7. doi: 10.4172/2469-4134.1000158
- Mahmood, F. (2020). Politics for environment: youth perception on campaign for billion tree tsunami to combat climate change situation in Pakistan. *J. Med. Stud.* 35, 41–61.
- Mallick, J., Singh, V. P., Almesfer, M. K., Talukdar, S., Alsubhi, M., Ahmed, M., et al. (2021). Spatio-temporal analysis and simulation of land cover changes and their impacts on land surface temperature in urban agglomeration of Bisha watershed, Saudi Arabia. *Geocarto Int.* 37, 1–27. doi: 10.1080/10106049.2021.1980616
- Mansour, S., Al-Belushi, M., and Al-Awadhi, T. (2020). Monitoring land use and land cover changes in the mountainous cities of Oman using Gis and ca-Markov modelling techniques. *Land Use Policy* 91:104414. doi: 10.1016/j.landusepol.2019.104414
- Mas, J.-F., and Soares De Araújo, F. (2021). Assessing Landsat images availability and its effects on Phenological metrics. *Forests* 12:574. doi: 10.3390/f12050574
- Maurya, P., Das, A. K., and Kumari, R. (2021). Managing the blue carbon ecosystem: a remote sensing and Gis approach. *Adv. Remote Sens. Nat. Resour. Monit.*, 247–268. doi: 10.1002/9781119616016.ch13
- Mehmood, M. S., Zafar, Z., Sajjad, M., Hussain, S., Zhai, S., and Qin, Y. (2023). Time series analyses and forecasting of surface urban Heat Island intensity using Arima model in Punjab, Pakistan. *Land* 12:142. doi: 10.3390/land12010142
- Mengistu, D. A., and Salami, A. T. (2007). Application of remote sensing and Gis inland use/land cover mapping and change detection in a part of South Western Nigeria. *Afr. J. Environ. Sci. Technol.* 1, 99–109.
- Mumtaz, F., Tao, Y., De Leeuw, G., Zhao, L., Fan, C., Elnashar, A., et al. (2020). Modeling spatio-temporal land transformation and its associated impacts on land surface temperature (Lst). *Remote Sens.* 12:2987. doi: 10.3390/rs12182987
- Munir, B. A., and Iqbal, J. (2016). Flash flood water management practices in Dera Ghazi Khan City (Pakistan): a remote sensing and Gis prospective. *Nat. Hazards* 81, 1303–1321. doi: 10.1007/s11069-015-2136-5

- Musse, M. A., Barona, D. A., and Rodriguez, L. M. S. (2018). Urban environmental quality assessment using remote sensing and census data. *Int. J. Appl. Earth Obs. Geoinf.* 71, 95–108. doi: 10.1016/j.jag.2018.05.010
- Peng, J., Jia, J., Liu, Y., Li, H., and Wu, J. (2018). Seasonal contrast of the dominant factors for spatial distribution of land surface temperature in urban areas. *Remote Sens. Environ.* 215, 255–267. doi: 10.1016/j.rse.2018.06.010
- Peng, W., Zhou, J., Wen, L., Xue, S., and Dong, L. (2017). Land surface temperature and its impact factors in Western Sichuan plateau, China. *Geocarto Int.* 32, 919–934. doi: 10.1080/10106049.2016.1188167
- Platt, R. V., and Rapozo, L. (2008). An evaluation of an object-oriented paradigm for land use/land cover classification. *Prof. Geogr.* 60, 87–100. doi: 10.1080/00330120701724152
- Rehman, A., Song, J., Haq, F., Ahamad, M. I., Sajid, M., and Zahid, Z. (2021). Geophysical hazards microzonation and suitable site selection through multicriteria analysis using geographical information system. *Appl. Geogr.* 135:102550. doi: 10.1016/j.apgeog.2021.102550
- Rehman, A., Song, J., Haq, F., Mahmood, S., Ahamad, M. I., Basharat, M., et al. (2022). Multi-Hazard susceptibility assessment using the analytical hierarchy process and frequency ratio techniques in the Northwest Himalayas, Pakistan. *Remote Sens.* 14:554. doi: 10.3390/rs14030554
- Ruben, G. B., Zhang, K., Dong, Z., and Xia, J. (2020). Analysis and projection of land-use/land-cover dynamics through scenario-based simulations using the ca-Markov model: a case study in guanting reservoir basin, China. *Sustainability* 12:3747. doi: 10.3390/su12093747
- Rwanga, S. S., and Ndambuki, J. M. (2017). Accuracy assessment of land use/land cover classification using remote sensing and Gis. *Int. J. Geosci.* 8:611. doi: 10.4236/ijg.2017.84033
- Sadiq Khan, M., Ullah, S., Sun, T., Rehman, A. U. R., and Chen, L. (2020). Land-use/land-cover changes and its contribution to urban Heat Island: a case study of Islamabad, Pakistan. *Sustainability* 12:3861. doi: 10.3390/su12093861
- Sajjad, M. (2020). Impacts, Drivers, and Future Adaptation Opportunities for a Warming Pakistan: Learnings from an Industrialized City. *Handbook of Climate Change Management: Research, Leadership, Transformation*, 1–22.
- Samie, A., Deng, X., Jia, S., and Chen, D. (2017). Scenario-based simulation on dynamics of land-use-land-cover change in Punjab Province, Pakistan. *Sustainability* 9:1285. doi: 10.3390/su9081285
- Shafi, A., Chen, S., Waleed, M., and Sajjad, M. (2023). Leveraging machine learning and remote sensing to monitor long-term spatial-temporal wetland changes: towards a national Ramsar inventory in Pakistan. *Appl. Geogr.* 151:102868. doi: 10.1016/j.apgeog.2022.102868
- Shahmohamadi, P., Che-Ani, A., Etesam, I., Maulud, K., and Tawil, N. (2011). Healthy environment: the need to mitigate urban heat island effects on human health. *Proc. Eng.* 20, 61–70. doi: 10.1016/j.proeng.2011.11.139
- Shen, X., Liu, B., and Lu, X. (2017). Effects of land use/land cover on diurnal temperature range in the temperate grassland region of China. *Sci. Total Environ.* 575, 1211–1218. doi: 10.1016/j.scitotenv.2016.09.187
- Song, J., Chen, W., Zhang, J., Huang, K., Hou, B., and Prishchepov, A. V. (2020). Effects of building density on land surface temperature in China: spatial patterns and determinants. *Landsc. Urban Plan.* 198:103794. doi: 10.1016/j.landurbplan.2020.103794
- Talukdar, S., Singha, P., Mahato, S., Pal, S., Liou, Y.-A., and Rahman, A. (2020). Land-use land-cover classification by machine learning classifiers for satellite observations—a review. *Remote Sens.* 12:1135. doi: 10.3390/rs12071135
- Tariq, A., and Mumtaz, F. (2022). Modeling spatio-temporal assessment of land use land cover of Lahore and its impact on land surface temperature using multi-spectral remote sensing data. *Environ. Sci. Pollut. Res.* 30, 23908–23924. doi: 10.1007/s11356-022-23928-3
- Tariq, A., Mumtaz, F., Majeed, M., and Zeng, X. (2023). Spatio-temporal assessment of land use land cover based on trajectories and cellular automata Markov modelling and its impact on land surface temperature of Lahore district Pakistan. *Environ. Monit. Assess.* 195:114. doi: 10.1007/s10661-022-10738-w
- Tariq, A., Mumtaz, F., Zeng, X., Baloch, M. Y. J., and Moazzam, M. F. U. (2022b). Spatio-temporal variation of seasonal heat islands mapping of Pakistan during 2000–2019, using day-time and night-time land surface temperatures Modis and meteorological stations data. *Remote Sens. Appl.* 27:100779. doi: 10.1016/j.rsase.2022.100779
- Tariq, A., Riaz, I., Ahmad, Z., Yang, B., Amin, M., Kausar, R., et al. (2020). Land surface temperature relation with normalized satellite indices for the estimation of spatio-temporal trends in temperature among various land use land cover classes of an arid Potohar region using Landsat data. *Environ. Earth Sci.* 79, 1–15. doi: 10.1007/s12665-019-8766-2
- Tariq, A., and Shu, H. (2020). Ca-Markov chain analysis of seasonal land surface temperature and land use land cover change using optical multi-temporal satellite data of Faisalabad, Pakistan. *Remote Sens.* 12:3402. doi: 10.3390/rs12203402
- Tariq, A., Shu, H., Siddiqui, S., Imran, M., and Farhan, M. (2021). Monitoring land use and land cover changes using geospatial techniques, a case study of Fateh Jang, Attock, Pakistan. *Geogr. Environ. Sustain.* 14, 41–52. doi: 10.24057/2071-9388-2020-117
- Tariq, A., Yan, J., and Mumtaz, F. (2022a). Land change modeler and ca-Markov chain analysis for land use land cover change using satellite data of Peshawar, Pakistan. *Phys. Chem. Earth Parts A/B/C* 128:103286. doi: 10.1016/j.pce.2022.103286
- Thériault, M., Le Berre, I., Dubé, J., Maulpoix, A., and Vandersmissen, M.-H. (2020). The effects of land use planning on housing spread: a case study in the region of Brest, France. *Land Use Policy* 92:104428. doi: 10.1016/j.landusepol.2019.104428
- Tilahun, A., and Teferie, B. (2015). Accuracy assessment of land use land cover classification using Google earth. *Am. J. Environ. Prot.* 4, 193–198. doi: 10.11648/j.ajep.20150404.14
- Townshend, J. R., and Justice, C. (1986). Analysis of the dynamics of African vegetation using the normalized difference vegetation index. *Int. J. Remote Sens.* 7, 1435–1445. doi: 10.1080/01431168608948946
- Tran, D. X., Pla, F., Latorre-Carmona, P., Myint, S. W., Caetano, M., and Kieu, H. V. (2017). Characterizing the relationship between land use land cover change and land surface temperature. *ISPRS J. Photogramm. Remote Sens.* 124, 119–132. doi: 10.1016/j.isprsjprs.2017.01.001
- Ullah, S., Ahmad, K., Sajjad, R. U., Abbasi, A. M., Nazeer, A., and Tahir, A. A. (2019a). Analysis and simulation of land cover changes and their impacts on land surface temperature in a lower Himalayan region. *J. Environ. Manag.* 245, 348–357. doi: 10.1016/j.jenvman.2019.05.063
- Ullah, S., Tahir, A. A., Akbar, T. A., Hassan, Q. K., Dewan, A., Khan, A. J., et al. (2019b). Remote sensing-based quantification of the relationships between land use land cover changes and surface temperature over the lower Himalayan region. *Sustainability* 11:5492. doi: 10.3390/su11195492
- UN. (2017). *World Population Prospects: The 2015 Revision: Key Findings and Advance Tables*. Available at: https://esa.un.org/unpd/wpp/publications/Files/Wpp2017_KeyFindings.pdf. Un.
- Utomo, D. H., and Kurniawan, B. R. (2016). Spatio temporal analysis trend of land use and land cover change against temperature based on remote sensing data in Malang City. *Procedia Soc. Behav. Sci.* 227, 232–238. doi: 10.1016/j.sbspro.2016.06.066
- Vinayak, B., Lee, H. S., and Gedem, S. (2021). Prediction of land use and land cover changes in Mumbai City, India, using remote sensing data and a multilayer perceptron neural network-based markov chain model. *Sustainability* 13:471. doi: 10.3390/su13020471
- Waleed, M., and Sajjad, M. (2022). Leveraging cloud-based computing and spatial modeling approaches for land surface temperature disparities in response to land cover change: evidence from Pakistan. *Remote Sens. Appl.* 25:100665. doi: 10.1016/j.rsase.2021.100665
- Wang, R., Cai, M., Ren, C., Bechtel, B., Xu, Y., and Ng, E. (2019). Detecting multi-temporal land cover change and land surface temperature in Pearl River Delta by adopting local climate zone. *Urban Clim.* 28:100455. doi: 10.1016/j.uclim.2019.100455
- Wang, Z., Xu, X., Wang, H., and Meng, S. (2020). Does land reserve system improve quality of urbanization? Evidence from China. *Habitat Int.* 106:102291. doi: 10.1016/j.habitatint.2020.102291
- Waseem, S., and Khayyam, U. (2019). Loss of vegetative cover and increased land surface temperature: a case study of Islamabad, Pakistan. *J. Clean. Prod.* 234, 972–983. doi: 10.1016/j.jclepro.2019.06.228
- Wessels, K., Steenkamp, K., Von Maltitz, G., and Archibald, S. (2011). Remotely sensed vegetation phenology for describing and predicting the biomes of South Africa. *Appl. Veg. Sci.* 14, 49–66. doi: 10.1111/j.1654-109X.2010.01100.x
- Xu, X., Du, Z., and Zhang, H. (2016). Integrating the system dynamic and cellular automata models to predict land use and land cover change. *Int. J. Appl. Earth Obs. Geoinf.* 52, 568–579. doi: 10.1016/j.jag.2016.07.022
- Yasin, Z., and Nabi, G. (2014). Alternative management plan for flash floods/flows of Mithawan Hill torrents in Pakistan. *Int. J. Sci. Eng. Res.* 5:95518
- Zafar, Z., Mehmood, M. S., Shiyan, Z., Zubair, M., Sajjad, M., and Yaochen, Q. (2023). Fostering deep learning approaches to evaluate the impact of urbanization on vegetation and future prospects. *Ecol. Indic.* 146:109788. doi: 10.1016/j.ecolind.2022.109788
- Zha, Y., Gao, J., and Ni, S. (2003). Use of normalized difference built-up index in automatically mapping urban areas from tm imagery. *Int. J. Remote Sens.* 24, 583–594. doi: 10.1080/01431160304987
- Zhou, Q., Leng, G., Su, J., and Ren, Y. (2019). Comparison of urbanization and climate change impacts on urban flood volumes: importance of urban planning and drainage adaptation. *Sci. Total Environ.* 658, 24–33. doi: 10.1016/j.scitotenv.2018.12.184



OPEN ACCESS

EDITED BY

Pedzisai Kowe,
Midlands State University, Zimbabwe

REVIEWED BY

Voltaire Alvarado Peterson,
University of Concepcion, Chile
Tatenda Musasa,
Midlands State University, Zimbabwe

*CORRESPONDENCE

Mingxue Wang,
✉ wang_mingxue@outlook.com

RECEIVED 20 December 2022

ACCEPTED 17 April 2023

PUBLISHED 05 May 2023

CITATION

Wan T and Wang M (2023), Large-scale measurement of urban streets' space health based on the spatial disorder theory—A case study on the old urban area of Daoli District of Harbin City. *Front. Environ. Sci.* 11:1127910. doi: 10.3389/fenvs.2023.1127910

COPYRIGHT

© 2023 Wan and Wang. This is an open-access article distributed under the terms of the [Creative Commons Attribution License \(CC BY\)](https://creativecommons.org/licenses/by/4.0/). The use, distribution or reproduction in other forums is permitted, provided the original author(s) and the copyright owner(s) are credited and that the original publication in this journal is cited, in accordance with accepted academic practice. No use, distribution or reproduction is permitted which does not comply with these terms.

Large-scale measurement of urban streets' space health based on the spatial disorder theory—A case study on the old urban area of Daoli District of Harbin City

Ting Wan and Mingxue Wang*

School of Landscape Architecture, Northeast Forestry University, Harbin, China

As an essential part of urban public space, the basic framework of urban pattern, and the human landscape of the city and street space is of great significance to urban development. From the perspective of urban living safety, the demand for urban space for health has been considered in depth again. Therefore, with emerging new issues in the post-urbanization period such as the development of public health and slow traffic transportation, street space becomes disordered, and the health of street space has drawn great attention. This paper takes the old urban area of Daoli District of Harbin City as an example. The degree of spatial disorder of different streets in the old urban area of Daoli District of Harbin City is derived by using the off-site built environment audit method and mean square weight analysis and other technical methods with multi-source data such as Baidu map API. In this paper, the spatial health measurement of streets with different properties of land usage in the old urban area of Daoli District of Harbin City is classified, and the classification strategies are proposed based on the calculation results. Based on the theory of spatial disorder, a large-scale measurement of street space health provides insights and references for practical urban management in the future. In terms of theoretical research, this paper attempts to fill the gap in urban geospatial disorder research in China.

KEYWORDS

street space, space health, spatial disorder, quantitative measurements, property of land usage, evaluation

1 Introduction

Chinese cities are experiencing an unprecedented process of rapid development. With a large number of incremental development and stock renewal, urban functions are becoming more and more perfect, and urban appearance is changing with each passing day. Due to the rapid development of the city, the street space design in the old city is backward and cannot keep up with the speed of urban development. A large number of out-of-order street spaces have appeared, and there is a lack of factors conducive to people's health. Consequently, this paper will assess the street space, compile a summary of the disordered issues in the old city area of Daoli District in Harbin City, and explore the urban planning strategies to address these disordered issues.

The old city of Daoli in Harbin, as a built-up area with a relatively long history, is experiencing a development process of numerous contradictions and slow progress.



The phenomena of environmental quality decline and spatial disorder in urban space are scattered in the city in different degrees and ranges. Public health is closely related to the urban environment. Urban planning and design should not only pay attention to the social economy but also need to return to people and the environment. As an important component of urban public space, streets should be re-examined to improve the health of urban street space. In some areas of Harbin, the street space is chaotic, the public space is damaged, and the dilapidated buildings have seriously affected the health of the street space in Harbin. This phenomenon of poor spatial quality and chaotic spatial order is defined as an urban spatial disorder in sociology. This phenomenon has attracted wide attention from researchers in the field of public health and public security. At present, a large number of foreign studies focus on the negative externalities of spatial disorder and summarize and plan urban renewal for the out-of-order space abroad, so as to combine the study of spatial disorder into the research planning of urban health. The research on the urban spatial disorder in China is still preliminary. At present, scholars' research on spatial disorder stays in the use of street view image data to measure the spatial quality and spatial environment of urban space and then summarize the quantitative measurement methods of urban spatial quality.

Therefore, this paper will analyze the street space of old urban areas in China, summarize the current street space disorder problem in Daoli old urban area in Harbin, and analyze the guiding role of the disorder problem in urban planning. The research aims to gain a deeper understanding of the link between human health and spatial disorder problems. In view of the spatial disorder phenomenon, countermeasures and means of spatial intervention in urban design, which is conducive to urban managers and researchers to enrich the

systematic understanding of the characteristics and rules of street optimization, are proposed, so as to provide a decision-making basis for planning management and design countermeasures and improve urban practice and management strategies.

2 Materials and methods

2.1 Description of the study area

In recent years, the main urban area of Harbin City has expanded rapidly. The streetscape of Songbei District and Qunli New District in the outer ring is very different from that of the center of Daoli District. Qunli New District is connected to the old urban area of Daoli District, which makes the street landscape in Daoli District of Harbin City more complex.

Therefore, this research takes the streets in the old urban area of Daoli District of Harbin City as the research target. With a total area of approximately 984.44 hectares, the research target covers the area from Youyi Road Street, Hugu Street to Qianjin Street, south to Qianjin Road, southeast to Tieshun Street and Dagong Street, and north to Yimian Street (Figure 1). The administrative division in Harbin covers a very large area with all kinds of streets (including Harbin commercial streets, green squares in the first ring road, and ordinary residential areas). In addition, the research target is featured by high population density, more employment opportunities, cultural activities, and entertainment activities. Based on the comparative research, the urban area of the old urban area of Daoli District in Harbin is selected.

The research area is divided into four parts based on the landscape of main roads in Daoli District so that it is much easier to make the subsequent analysis and summarize the

calculation results. The land area is divided into four districts, namely, A, B, C, and D, by Jingwei Street, Shanghai Street, Anfa Street, and Tongda Street. Since District B and District C cover large areas with complex situations, District B and District C are further divided for more accurate analysis. District B and District C are further divided into B1, B2, B3, B4, B5, C1, C2, C3, C4, C5, and C6 along Hayao Road, Anlong Street, Anning Street, Jianguo Street, and Fushun Street, respectively (Figure 1). Generally speaking, the whole land area is divided into four major districts, including 11 small districts. The research is analyzed based on these districts.

2.2 Data

In order to make a spatial evaluation and accurately locate the disordered spatial sites, this study adopts the street view image of Baidu Maps for the built environment audit. Baidu Maps (<https://map.baidu.com/>) can provide the latest street view images covering most of the urban roads in the first ring road of Harbin (May 2019), with the maximum resolution (width \times height) of 1024×512 (Chen et al., 2020). Based on the data from Baidu Map, this paper selects streets as the basic units of research. In this paper, based on Baidu Street View images, more than 200 streets within the old city area of Daoli District of Harbin City are used as the original data for the study. Considering the huge workload of downloading all street view images in the research area, the paper uses ArcGIS to obtain points of street view images from 4-dimensional maps at equal intervals (Ye et al., 2019). By manually comparing the homogeneity of urban landscape features in the street view images intercepted at different distances, the homogeneity of landscape types covered by the images intercepted at less than 100 m is very high and some landscape features are even overlapped. The homogeneity of the images intercepted at more than 100 m is very low, so it is easy to omit some street view features. Finally, the sampling distance is set as 100 m. This research finally takes 1,047 points with street view images in the study area (each point can provide a 360° scene) and then captures four street view images, which are parallel to the road (front and back) and perpendicular to the road direction (left and right) at each observation point by the Baidu Map API (Tang et al., 2016). This acquisition form fully covers the environment around the viewpoints and collects a total of 4,188 street-view images.

In addition, the basic GIS data of Harbin City, road network data, and social network data, including microblogs and public comments, are considered in a holistic manner so as to discuss the relationship between urban spatial disorder and public health from a micro perspective at the street level.

2.3 Research methods

In order to facilitate data acquisition and calculation, this paper adopts the following four types of calculation technologies: 1) Data crawling. Through the Python programming language, Baidu Maps is used to obtain the street view image data, multi-source open data, street view, coordinates, angles, and other information of each sample point to support the indicator calculation. 2) Statistical

analysis. Through SPSS 24.0, the obtained indicator data are analyzed mathematically and physically to prove results (Long and Zhou, 2016). 3) Off-site built environment audit. In view of the impact of weather and season on the pictures, factors including weather, season, and traffic conditions are excluded during the audit. 4) Street evaluation. The spatial disorder indicators and spatial health are taken as the dimensions to evaluate street health. In the meantime, cluster analysis is carried out and solutions for the spatial situation and transformation potential of various streets are proposed (Shi, 2021).

In this paper, the off-site environmental audit method is adopted to measure the health of the street view space displayed in the street view images of the old urban area of Daoli District of Harbin City. The existing literature has proved that the audit results of the scoring team with a professional background are more effective than those of laymen. Therefore, in this paper, four auditors with professional backgrounds in architecture or urban planning were selected to conduct the audit.

The research process includes the following four main steps: 1) We used ArcGIS to select observation points and obtain four hundred-degree street view data of each street scenic spot; 2) The obtained street view data was sorted out by SPSS, and the data was handed over to the professional auditor of urban and rural planning for spatial disorder score; 3) The score data was imported into ArcGIS to calculate the spatial disorder score, and the spatial disorder measure map was obtained; 4) The street spatial disorder in Daoli Old town of Harbin was evaluated and analyzed according to the spatial disorder measure map. Finally, we put forward the classification improvement strategy.

In order to minimize the statistical errors caused by the auditors' cognitive backgrounds, the auditors identified the street scene images in four directions of each street scenic spot based on a unified scoring system and scored the spatial disorder elements in the image using a dichotomous approach, that is, the existing disorder elements are counted as one, while the non-existent elements are counted as zero (Chen and Long, 2015; Yu et al., 2021). Finally, various scores are combined to form the evaluation results of the spatial quality.

2.4 Construction of spatial disorder measures

2.4.1 Selection of spatial disorder indicators




















First of all, priority is given to the evaluation indicator system of urban public space quality, which is mainly based on the Beijing City Laboratory (BCL) (Chen et al., 2020), as the evaluation indicator of street space quality. Based on the street landscape and building facade information provided by the street view image, the indicator system selects representative elements for analysis, specifically including five types of first-class evaluation indicators-architecture, commercial activities on the streets, environmental greening, roads, and infrastructure, as well as 19 secondary indicators that are further subdivided (Table 1).

On the other hand, as an important part of the old city of Harbin, the street space in the old urban area of Daoli District is featured by the alternation of old and new. Many old streets are

TABLE 1 Selection of evaluation indicators for space quality.

First-class indicators	Second-class indicators
Building	1. Building removal; 2. Incomplete building facade; 3. Damaged building facade; 4. Old building facades; 5. Graffiti on the facade; 6. Unauthorized construction/temporary buildings
Commerce along the street	1. Old/chaotic signs; 2. Old/dirty shop fronts; 3. Operation of disorderly road occupation; 4. Vacancy and sale of shops
Environment greening	1. Disordered vegetation; 2. Garbage stacking/discarding; 3. Abandoned vehicles; 4. Unremoved construction fence
Roads	1. Unhardened roads; 2. Damaged roads; 3. Road encroachment
Infrastructure	1. Damaged infrastructure; 2. Damaged public interface

TABLE 2 Extraction of reference samples of spatial disorder elements in daoli district of harbin city.

Out-of-order elements reference sample						
Building						
	Building removal	Incomplete building facade	Damaged building facade	Old building facade	Graffiti on the facade	Unauthorized construction/temporary buildings
Commerce along the street						
	Old/chaotic signs	Old/dirty shop fronts	Operation of disorderly road occupation	Vacancy and sale of shops		
Environment greening						
	Disordered vegetation	Garbage stacking/discarding	Abandoned vehicles	Unremoved construction fence		
Roads						
	Unhardened roads	Damaged roads	Road encroachment			
Infrastructure						
	Damaged infrastructure	Damaged public interface				

narrow, relatively close, and messy. Therefore, in terms of space quality, the space quality evaluation indicators also represent the public health problems of street space to a certain extent (Table 2).

2.4.2 Indicator calculation

According to the results measured based on the evaluation system and the formula, the disorder of street space can be calculated, which can more objectively show spatial degradation (Ye et al., 2019; Chen et al., 2020). The specific formula is as follows:

$$D = \frac{n}{N}$$

(1)

In Formula (1), D is the degree of overall spatial disorder, n is the number of street scenes with disordered elements, and street scenes with disordered elements refer to the spatial disorder of street scenes as long as any unordered elements are recognized in images in any direction of street scenes (Naik et al., 2017); N means the total number of street scenes with a total of 1,047 points (Table 2).

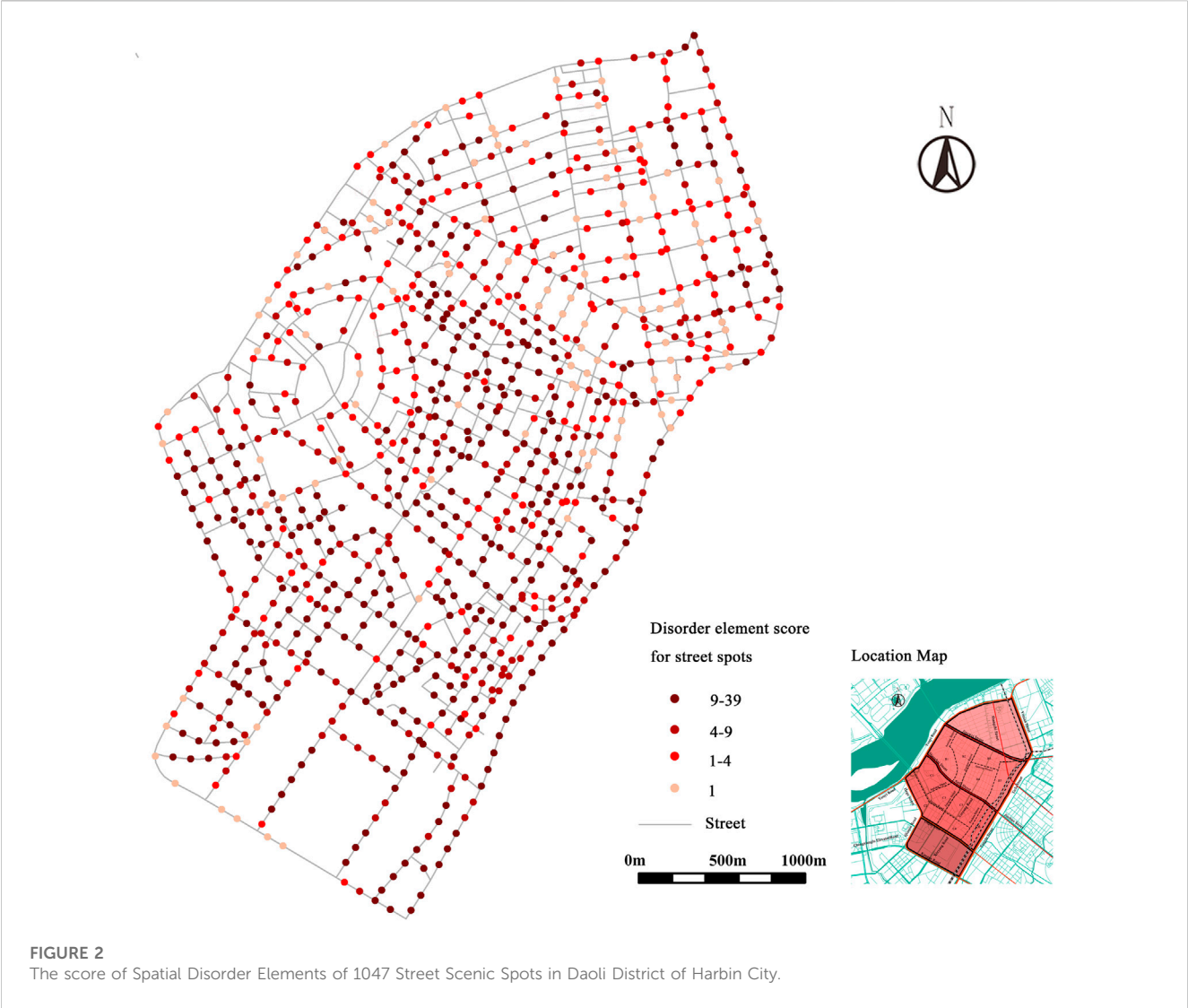


TABLE 3 Number and degree of disorder street scenes in daoli district of harbin city.

First-class indicator	The sum of the number of street scenes with disorder elements	Degree of disorder (%)
Buildings	824	78.70
Commerce along the street	761	72.68
Environmental greening	539	51.48
Roads	651	62.12
Infrastructures	183	17.48

3 Results and discussion

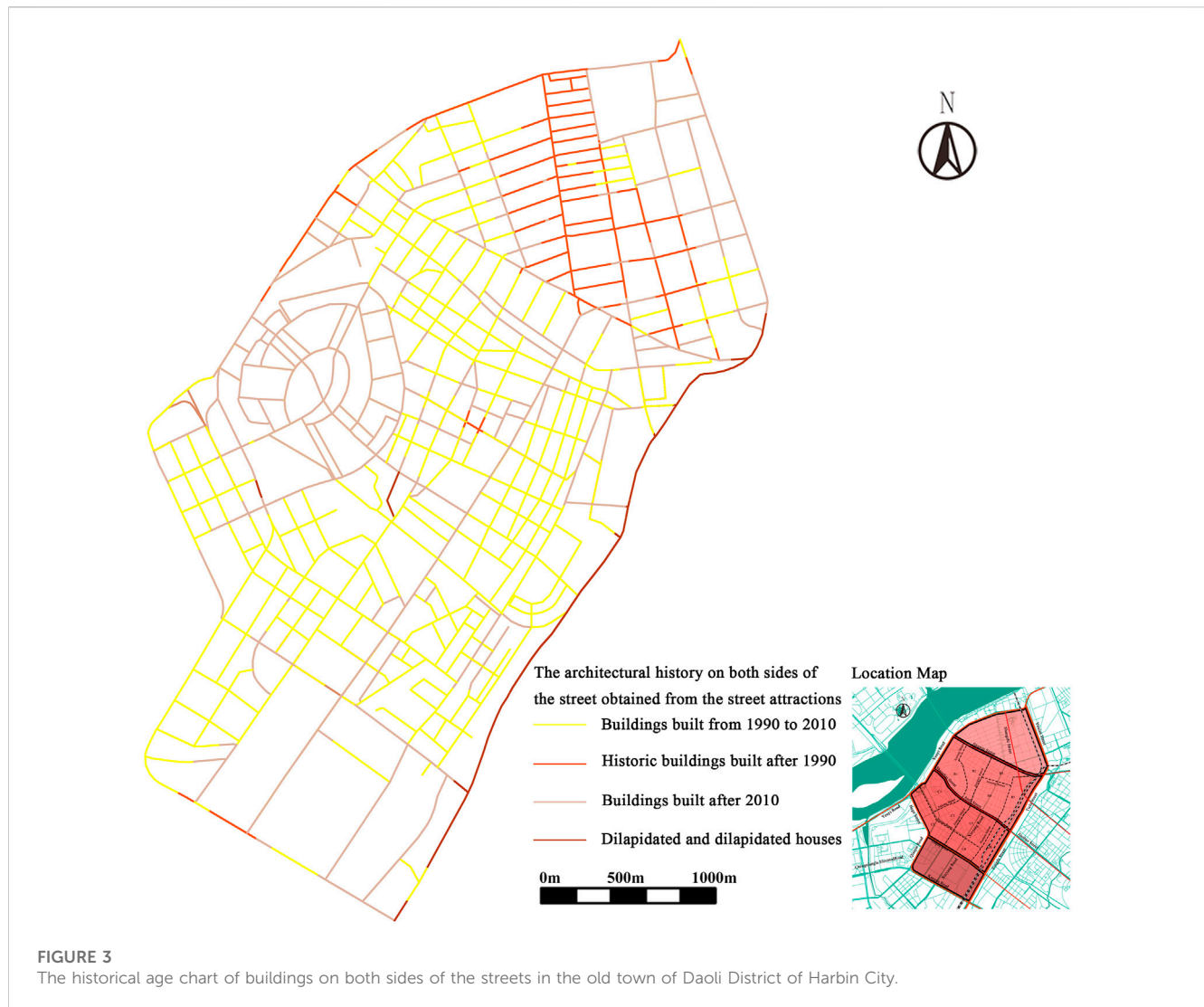
3.1 Status cluster analysis

3.1.1 Overall disorder degree measurement and distribution characteristics

Based on the results of the virtual audit, this paper calculates the total score of the disorder elements of the street view image in four

directions for each street view observation point, and the score of each street viewpoint ranges from 0 to 76 points (Sun and Wang, 2021). Among them, 0 point indicates that there is no disorder element in the four directions of a street scene, and 76 points mean that all disorder elements (19 elements in total) are identified in the four directions of a street scene (Long and Zhou, 2016).

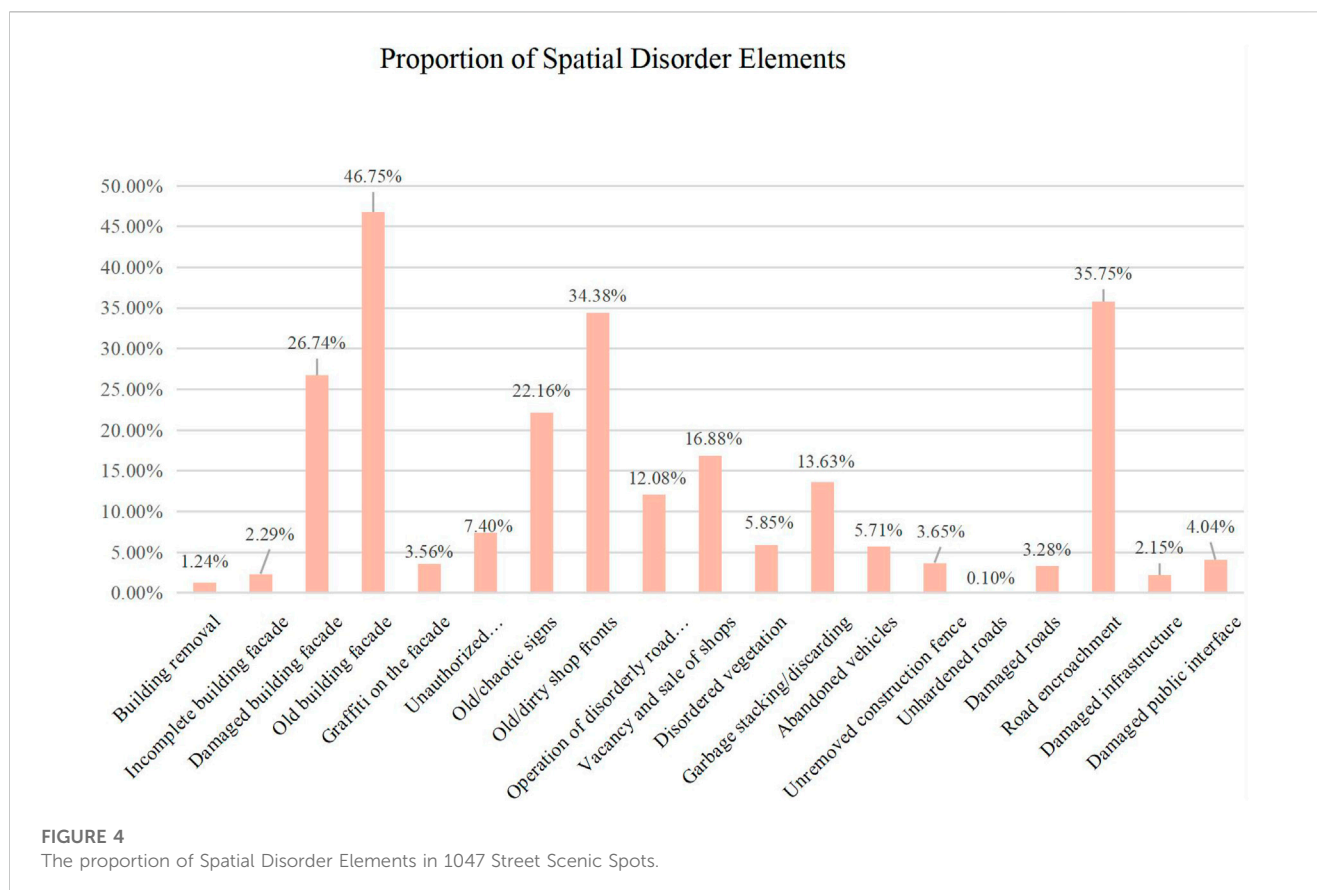
Subsequently, the spatial location and visual expression are carried out through ArcGIS. It shows the total score of disorder



elements identified for the street scenic spots, as shown in Figure 2, and the score is divided into four fractions by quartile, namely, 1, 1–4, 4–9, and 9–39 (Zhang et al., 2019; Chen et al., 2020). Some street scenic spots with a disorder score of zero will not be displayed. The darker the color in the figure, the worse the spatial health of the observation point.

Based on the calculation formula of the degree of spatial disorder (Figure 2), the urban spatial disorder in the old urban area of Daoli District of Harbin City is 87.36%. The building elements have the highest score (78.70%), followed by street commerce (72.68%), and the spatial disorder of infrastructure has the lowest score (17.48%) (Table 3). According to the spatial disorder map of the overall street scenic spot elements, the spatial disorder is more obvious in B2, B3, B4, C3, C4, C5, and D districts. The sequence of the old urban area of the Anzi section in Daoli District composed of B2, B3, B4, C3, C4, and C5 is the most serious. In Aijian, District C1, District B1, and the central street of District A have better space health. The overall dilapidation is serious, showing the characteristics of large-scale tiling in districts B and C.

At the same time, we investigated the building years and building history of the Daocheng Old Town of Harbin City (Figure 3) and found that the Central Street area located in Zone A has long building years, historical significance, is relatively well preserved, and has perfect maintenance and repair program, leading to the central Street and has become a famous scenic spot in Harbin and one of the sources of tourism, which boosts the economy of Harbin. On the other hand, the old urban area of Daoli District, composed of B2, B3, B4, C3, C4, and C5, has a long history but most of the buildings are residential buildings with poor building maintenance, making them the slowest economic development area in the main urban area of Daoli. Aijian area composed of B1 and C1 is a fast-developing area in the central area of Daoli with a new construction period and late economic development. At present, it belongs to the newer area of Daoli Old City. It can be seen that the spatial disorder of the whole of Daoli Old Town is closely related to the development history and economic situation of Harbin. As the central street with a long history in Harbin, the economy is



leading and the architecture has historical characteristics, so the spatial disorder is relatively light. Anzi District has backward economic development and old buildings, so the overall spatial disorder is more serious.

3.1.2 Characteristics and distribution of spatial disorder elements

According to the evaluation results, from the perspective of five categories of first-class indicators, buildings in the elements of spatial disorder in the old urban area of Daoli District of Harbin City account for the largest proportion, indicating that the dilapidated commerce along the street in this area is the most serious (Figure 4). From the subdivided 19 secondary indicators, building facades, encroached roads, and old and dirty road surfaces become the top three most frequent elements of spatial disorder. The primary concerns in the process of improving and upgrading the space quality of the old urban area of Daoli District of Harbin City reflect the urgent need to carry out maintenance, repair, and organic renewal of the dilapidated, damaged, and chaotic buildings of the old urban area of Daoli District of Harbin City. However, in the evaluation of space health in the old urban area of Daoli District of Harbin City, the two disorder elements, namely, the damage to building facades and the old and chaotic signs, happen in a certain frequency, resulting in the urban landscape of dilapidated building planes in the old urban area of Daoli District of Harbin City.

In terms of distribution characteristics, generally speaking, the areas with high degrees of various disorder elements are B2, B3, B4, C3, C4, C5, and D; that is, the old urban center and southwest of Anzi District. However, based on the data from the observation points located in old building facades with road encroachment or defilement, disorder elements are basically all over the whole area of the second-ring road, such as the old building facades and road encroachment; other elements are mainly distributed in B2, B3, B4, C3, C4, and C5; the closer they are to the old city center, the more dilapidated the B4 and C5 districts are. Disorder elements, such as disorder plants and garbage stacking and discarding, reflect that the overall urban landscape of the old urban area of Daoli District in Harbin is old and dilapidated to varying degrees. With the continuous and large-scale extension of urban space, Districts A, B1, C1, and the side close to the Songhua River show a gradually improving trend. In general, the old urban area is relatively underdeveloped in terms of facilities, fragile ecological environment, and inefficient land use (Figure 5).

Compared with the fact that the space disorder of Anzi is more serious, the building disorder of B1 and C1 in the Aijian District is improved. As Aijian District is a relatively new area in Daoli district and its economic situation is relatively good, the building division of the whole Aijian District is zero, the building appearance and the facade of commercial pavement are relatively complete, and the roads and infrastructure are relatively perfect. Zone A is the main tourist attraction of Harbin and tourism is also an industry strongly supported by the Harbin government.

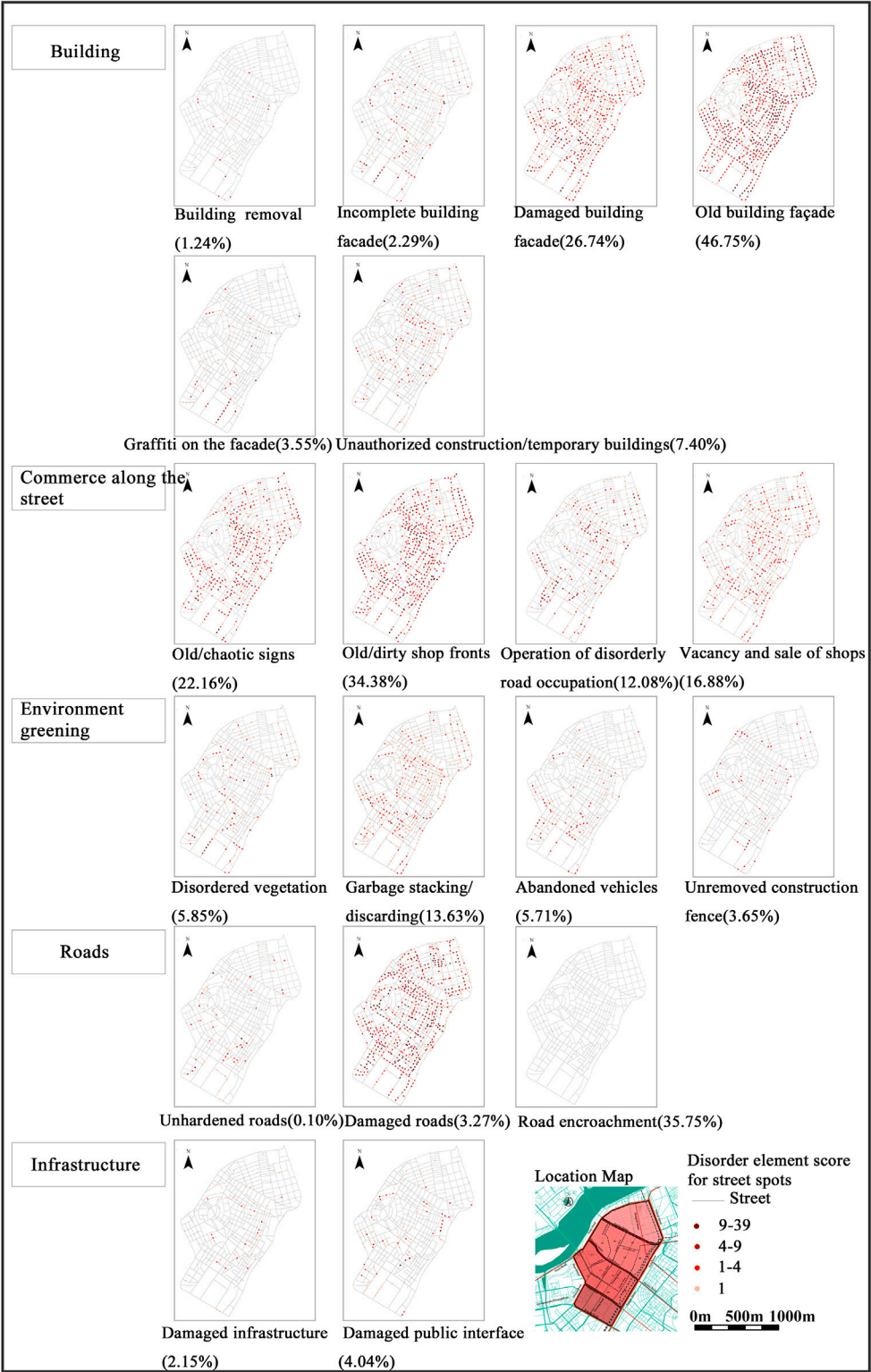


FIGURE 5
The score of Disorder Elements of Scenic Spots in Second-class Indicator Street of Spatial Disorder.

The maintenance measures for the buildings and roads of Central Street are relatively complete, and the maintenance funds are relatively in place. Therefore, there are no problems such as road

encroachment and building unpacking in the whole Central Street area, and only some buildings with a long history have the problem of facade damage.

3.2 Classification improvement strategy

3.2.1 Countermeasures for building space disorder

The evaluation results show that the building space disorder in the old urban area of Daoli District of Harbin City is the most serious, and it is as high as 78.7%. The aging and damage of building facades caused by the lack of maintenance and poor management of building facades are more obvious (Rundle et al., 2011). The degree of aging and disorder of building facades is the highest, reaching 46.75%, followed by the degree of damage of building facades, which is approximately 26.47%. Therefore, to solve the problem of building space disorder, this paper proposes to strengthen the quality control of building facades and informal building management to ensure the integrity of the street profile. As one of the districts with the longest building life in Harbin, the old urban area of Daoli District should improve the local buildings from the following aspects:

- 1) For residential land roads. It is necessary to strengthen the post-repair and management of old buildings, renovate and update buildings and building facade components that affect the street beauty and pedestrian traffic, and dismantle the illegal or temporary buildings (Li and Long, 2019). With the longest building life and the most serious aging problem, the “An” and “Guang” sections need to go through a unified renovation, and a renovation strategy for the residential area should be carried out. “Old and dilapidated” building facades should be renovated forcefully. The building facades and the urban landscape should be preserved by using exterior painting, landscape blocking, and other methods. The improvement of building façade quality and aesthetics have the following advantages: i) it meets the residents’ desire for a better urban living environment, ii) it alleviates the anxiety and other negative emotions caused by disorder phenomena, such as abandoned buildings and lack of maintenance, and iii) it creates a positive psychological perception among local residents.
- 2) In view of disorder problems, such as incomplete building facades and building roads in residential areas without authorization, the government should uniformly manage them, dismantle the illegal and privately built buildings, improve the street appearance, and ensure the safety of residents. For roads on commercial land (Shi, 2021), details and diversity should be provided for the overall segmentation and rhythm of the interface in the architectural design and reconstruction plan of incomplete facades, such as facade materials, structures, and details. Therefore, the visual experience is diversified, especially for the places near the ground, street corners, key sections, and visual nodes.
- 3) For housing demolition, it is necessary to focus on confirming the ownership of land and carry out targeted “urban renovation” for dilapidated or vacant houses.
- 4) Priority should be given to improving construction quality in economically backward areas, attracting residents to move in, enhancing street space vitality, and improving economic conditions in backward areas, thus forming a good cycle of disorder improvement and economic improvement.

3.2.2 Countermeasures for commercial space disorder along the street

The disorder of commercial space mainly is defined as the old, dirty, and chaotic shops and signs along the street, and the improper use of the front of the commercial area along the street, which leads to a disorderly operation on the road.

It can be strengthened from the following aspects: 1) For the “dilapidated and narrow” commercial space at the bottom of the road in the old urban area of the Daoli District residential land, the façade should be repaired and renovated (Yu et al., 2021). When the lower floors are used for commercial and retail uses, the methods, such as materials and rhythm, are used to create a positive business interface, and guide the owners to maintain and update it regularly; 2) For areas with severe road occupation (roads with mixed land use), the overall relationship between the ground floor buildings and the street space should be considered, the building exits should be reasonably controlled and used, and the unqualified outdoor commercial facilities should be strictly managed. For the “morning market” and “night market” in some areas (Gong and Bai, 2021), a reasonable area should be allocated to the “morning market” and “night market” within a time limit, and these two markets should be managed uniformly. For example, according to Shanghai guidelines, “temporary facilities” can be designed in combination with commercial swings, outdoor seats, landscape facilities, etc. (Tang et al., 2016). However, problems such as non-standard temporary commercial facilities and turbulences to pedestrian traffic should be avoided; 3) For the roads on the commercial land in the Central Street Business District and Aijian Business District, coordination between the overall style and features of the ground floor business and the city should be made first, including the design of street signboards, building facade materials, building colors, and night lighting. Creating a commercial atmosphere and compliance management can effectively increase the activity of urban street space. A reasonable outer space can increase the possibility of social interaction and provide more options for residents’ outdoor activities, thus promoting public health.

3.2.3 Countermeasures for space disorder of environmental greening

The disorder of environmental greening in the old urban area of Daoli District mainly focuses on two aspects: garbage piles and vegetation, and abandoned vehicles placed in a disorderly manner. Due to the lack of management and maintenance of greening facilities in the old urban area, greening is chaotic; at the same time, garbage recycling of old streets is poorly managed, so the corner of the street can easily become a waste corner, and no one can handle it. It can be improved from the following aspects: 1) The standardized management of municipal sanitation and engineering construction should be strengthened, and attention should be given to garbage cleaning, greening maintenance, and the overall environmental management of back streets and alleys and urban fringe areas; 2) Attention should be given to the overall ecological and landscape design; tree ponds, rain gardens, and other sponge facilities should be arranged according to local conditions, and the integration of planting and maintenance should be considered. Adequate and well-

TABLE 4 Street health guidance strategy based on the first-class indicator of spatial disorder.

First-class indicators of spatial disorder	Elements of spatial disorder	Guidance methods for improving health
Buildings	Building removal	The land ownership should be clarified and replanned
	Incomplete building facade	The incomplete facade should be beautified by combining the overall facade decoration, and the negative interface should be artistically treated, such as light projection (Ge et al., 2020)
		The physical fence should be reduced by using a hollow fence or three-dimensional greening
	Damaged building facade	The “old, dilapidated, and small” building should be uniformly planned and configured, and regularly repaired, and the later maintenance should be strengthened
	Old building facade	The facade color, size, material, and style should be enriched;
	Facade graffiti	The graffiti should be reasonable and in harmony with the overall style and features of the street (Sun and Wang, 2021)
		The inappropriate graffiti and small advertisement pasting should be timely managed
	Unauthorized construction	The reasonable construction of public space areas should be standardized, and those that affect the beauty of buildings, and the normal use of street space should be rectified and demolished
Commerce along the street	Old/chaotic signs	The pavement signboards and overall coordination of signboard style, scale, material, and street space should be uniformly rectified and repaired
	Old/dirty shop fronts	The ground floor interface and the whole interface should be designed in an integrated way, focusing on management and plot and avoiding negative interfaces
	Operation of disorderly road occupation	Open buildings should be detached to provide temporary activity space; street space and street furniture should be reasonably arranged, and the need to keep the space compact should be advocated.
		According to the needs of the elderly for the “morning market” and “night market”, the activity space should be flexibly arranged and uniformly managed within a limited time
	Vacancy/sale of shops	
Environmental greening	Disordered vegetation	The landscape greening shall be arranged reasonably to form the second interface of the orderly street. The landscape vegetation shall be arranged based on the activity space to form the node space
	Garbage stacking	The garbage cans should be arranged reasonably and compactly and daily management should be strengthened
	Abandoned vehicles	
	Unremoved construction fence	The person in charge of construction should be responsible for repair management to ensure continuity with other bottom commercial interfaces.
		Attention should be given to management and cleaning to avoid a negative interface
Roads	Unhardened roads	The principle of durability, anti-skid, and sustainability for the pavement of damaged and unhardened roads should be adhered to
	Damaged roads	
	Road encroachment	The parking lot should be planned based on restricted vacant land
		The temporary parking area in different periods in combination with street functions should be flexibly set up
		Parking spaces for non-motor vehicles should be set up and shared bicycles should be placed orderly.
Infrastructure	Damaged infrastructure	The layout of municipal facilities and transportation facilities should be intensive with one pole for multiple purposes
	Damaged public interface	Themed and characteristic treatment should be carried out to reflect the street style and features, continuous blank and monotonous interfaces should be avoided, and continuity with other bottom commercial interfaces should be ensured

maintained street greening can improve the visual environment in the landscape; the greening environment can be leveraged to improve people’s mental health, promote residents’ willingness

to participate in outdoor activities, and enhance people’s perception of outdoor space, so as to relieve pressure and improve mental health in a holistic manner.

3.2.4 Countermeasures for road space disorder

The road space disorder in the old urban area is mainly manifested in road pavement damage and item accumulation encroaching on the road space. The disorder rate of road encroachment in the old urban area of Daoli District of Harbin City is as high as 35.75%, ranking third among all the reasons. As a main problem affecting the health of street space, it is mainly managed based on the “vehicle-oriented” transportation concept for a long time and little attention has been paid to the pavement of the pedestrian space and the layout and maintenance of walking and cycling facilities. At the same time, inadequate parking planning in the old urban area has led to the contradiction of more cars and fewer parking spaces in the old urban area (Vich et al., 2019), resulting in a serious parking problem on the road. The disorder of residential land roads can be improved from the following aspects:

- 1) Based on the vacant land around the streets of the old urban area, special parking lots and underground parking lots should be planned in an orderly manner to reduce the contradiction of more cars and less space and to reduce the problem of a slow traffic system.
- 2) As most guidelines propose, great attention should be given to the impact of pavement and sturdiness on the urban landscape and impression. Beautiful, durable, anti-skid, and targeted pavement materials should be used and urban management and maintenance should be strengthened (Franzini et al., 2007).
- 3) Encouraging slow and friendly walks. For example, in commercial streets, residential areas, and other roads, pedestrian and cycling pathways should be arranged during the pavement design. Attention should be paid to the connection with surrounding landscape belts and rest nodes (Kouis et al., 2019), and the traffic of vehicles should be limited to ensure the comfort and safety of the walking environment. In the long run, appropriate pavements also provide a guarantee for road management and maintenance, and more efforts should be made to reduce the deterioration of pavement damage caused by road occupation, crossing, and illegal parking.

3.2.5 Countermeasures for infrastructure space disorder

Due to the long service life and immature planning, the old urban area suffers from insufficient public facilities, a disordered layout, outdated style, and disrepair. Therefore, the transformation of the old city should emphasize the coordination, functionality, and intensification of the infrastructure layout. Specific improvement strategies are as follows: 1) To ensure smooth walking pathways, the negative impact of unreasonably arranged street lights, street trees, garbage cans, and ground walking signs needs to be reduced (Long & Zhou, 2016); 2) Renovating the existing infrastructure based on the interaction between facilities and people and improving the service efficiency of urban public facilities will help increase residents' use of outdoor public space, and improve people's willingness to travel in the city, commute, and communicate in the urban public space (Table 4).

4 Conclusion

Research on urban space health is the top priority in China because China has already entered a certain development level and is transforming from “quantity” to “quality” development (Chen et al., 2020). In order to build a living environment conducive to public health and meet the demands of public health for urban space, the local decision-makers need to decide on the built environment that can guide and respond to how to improve the rate of street health and solve the problem of spatial disorder (Zhou et al., 2022).

Based on the virtual audit and machine learning methods of the built environment of street view images, the paper obtains the preliminary measurement and evaluation results of the street space health in the old urban area of Daoli District of Harbin City. It systematically sorts out the insufficient local street space health in the context of the old urban area. Based on practical experience at home and abroad, it proposes urban design strategies based on five categories of spatial disorder and 19 specific elements. On the one hand, it is beneficial for urban managers and researchers to enrich their systematic understanding of spatial quality characteristics and laws, so as to provide sights for the decision-makers on planning management and design response, and to improve urban practice and management strategies by proposing urban design strategies and spatial intervention measures for the phenomenon of spatial disorder. The historical age chart of buildings on both sides of the streets in Daoli Old Town of Harbin City also shows how the old city, as a historic section, can achieve a virtuous cycle of improving disorder by maintaining the history and improving economic development. On the other hand, the health improvement of humanistic street space discussed in the paper is conducive to improving the quality of urban residents' living environment. From the perspective of urban design and management maintenance, the paper discusses the strategies and methods for the maintenance, renovation, and organic renewal of the built environment to promote public health. Also, more targeted and more suitable strategies for public health are proposed to further provide refined urban management and improve the quality and efficiency of the human living environment.

Data availability statement

The original contributions presented in the study are included in the article/Supplementary Material, further inquiries can be directed to the corresponding author.

Author contributions

TW wrote the draft of the manuscript. TW and MW contributed to data curation, analysis. MW contributed to manuscript revision. All authors approved the submitted version.

Conflict of interest

The authors declare that the research was conducted in the absence of any commercial or financial relationships that could be construed as a potential conflict of interest.

Publisher's note

All claims expressed in this article are solely those of the authors and do not necessarily represent those of their affiliated

organizations, or those of the publisher, the editors and the reviewers. Any product that may be evaluated in this article, or claim that may be made by its manufacturer, is not guaranteed or endorsed by the publisher.

References

- Chen, C., Chen, J. J., Jia, Z. M., Zheng, Z., Ma, S., Long, Y., et al. (2020). Limb ischemic preconditioning ameliorates renal microcirculation through activation of PI3K/Akt/eNOS signaling pathway after acute kidney injury. *South. Constr.* 25 (02), 10–18. doi:10.1186/s40001-020-00407-4
- Chen, J. J., and Long, Y. (2015). Identification, measurement, externality and intervention of elements of disorder in urban public space. *Time Archit.* (01), 44–50.
- Franzini, L., O'Brien Caughy, M., Nettles, S. M., and O'Campo, P. (2007). Perceptions of disorder: Contributions of neighborhood characteristics to subjective perceptions of disorder. *J. Environ. Psychol.* 28 (1), 83–93. doi:10.1016/j.jenvp.2007.08.003
- Ge, Y., Shen, X., and Cai, C. T. (2020). Theory, methodology and practice of healthy street design. *Shanghai Urban Plan.* (02), 49–56.
- Gong, W. J., and Bai, X. P. (2021). Study on the shared design of living street space in settlements from a health perspective. *Archit. Creat.* (06), 179–190.
- Kouis, P., Kakkoura, M., Ziogas, K., Paschalidou, A. K., and Papatheodorou, S. I. (2019). The effect of ambient air temperature on cardiovascular and respiratory mortality in Thessaloniki, Greece. *Sci. Total Environ.* 647, 1351–1358. doi:10.1016/j.scitotenv.2018.08.106
- Li, Z., and Long, Y. (2019). Analysis of spatial quality changes of shrinking urban streets based on dynamic street view image recognition - taking Qiqihar as an example. *Urban Archit.* 6, 21–25.
- Long, Y., and Zhou, Y. (2016). Quantitative evaluation of street vitality and analysis of influencing factors - chengdu as an example. *New Constr.* 1, 52–57.
- Naik, N., Kominers, S. D., Raskar, R., Glaeser, E. L., and Hidalgo, C. A. (2017). Computer vision uncovers predictors of physical urban change. *Proc. Natl. Acad. Sci.* 114 (29), 7571–7576. doi:10.1073/pnas.1619003114
- Rundle, A. G., Bader, M. D. M., Richards, C. A., Neckerman, K. M., and Teitler, J. O. (2011). Using Google street view to audit neighborhood environments. *Am. J. Prev. Med.* 40 (1), 94–100. doi:10.1016/j.amepre.2010.09.034
- Shi, J. Q. (2021). *Commerc Sial renewal design for marketplace-type communities based on spatial disorder theory*. Shanghai, China: Shanghai Normal University.
- Sun, R. F., and Wang, Y. Y. (2021). Research on the construction of urban street space quality evaluation system. *Anhui Archit.* 28 (03), 16–17.
- Tang, J. X., Long, Y., Zhai, Y., and Ma, Y. T. (2016). Measurements of spatial quality of streets, evaluation of changes and identification of influencing factors--analysis based on large-scale multi-temporal streetscape images. *New Constr.* 22(05), 110–115.
- Vich, G., Marquet, O., and Miralles-Guasch, C. (2019). Green streetscape and walking: Exploring active mobility patterns in dense and compact cities. *J. Transp. Health* 12, 50–59. doi:10.1016/j.jth.2018.11.003
- Ye, Y., Zhang, Z. X., Zhang, X. H., and Zeng, W. (2019). Human-scale quality on streets: A large-scale and efficient analytical approach based on street view images and new urban analytical tools. *Int. Urban Plan.* 34 (01), 18–27. doi:10.22217/upi.2018.490
- Yu, Y., Jiang, Y. Q., and Zhang, Q. Y. (2021). Study of urban street health impact pathways and spatial elements. *Scen. Gard.* 28 (02), 55–61.
- Zhang, L. Y., Pei, T., Chen, Y. J., Song, C., and Liu, X. Q. (2019). A review of urban environment evaluation research based on street view images. *J. Geoinformation Sci.* 21 (01), 46–58.
- Zhou, L. L., An, J., Yu, Y., and Shen, Z. M. (2022). Spatial quality measurement and feature identification of urban streets based on multi-source data--Guangzhou City as an example. *Traffic Transp.* 35, 7–13.



OPEN ACCESS

EDITED BY

Pedzisai Kowe,
Midlands State University, Zimbabwe

REVIEWED BY

Andreea Nita,
University of Bucharest, Romania
Liang Yuan,
China Three Gorges University, China
Trylee Nyasha Matongera,
University of KwaZulu-Natal, South Africa

*CORRESPONDENCE

Bin Xu
✉ 20010051@zafu.edu.cn

†These authors have contributed equally to this work and share first authorship

RECEIVED 11 March 2023

ACCEPTED 17 April 2023

PUBLISHED 11 May 2023

CITATION

Cheng X, Zhang Y, Yang G, Nie W, Wang Y, Wang J and Xu B (2023) Landscape ecological risk assessment and influencing factor analysis of basins in suburban areas of large cities – A case study of the Fuchunjiang River Basin, China.
Front. Ecol. Evol. 11:1184273.
doi: 10.3389/fevo.2023.1184273

COPYRIGHT

© 2023 Cheng, Zhang, Yang, Nie, Wang, Wang and Xu. This is an open-access article distributed under the terms of the [Creative Commons Attribution License \(CC BY\)](#). The use, distribution or reproduction in other forums is permitted, provided the original author(s) and the copyright owner(s) are credited and that the original publication in this journal is cited, in accordance with accepted academic practice. No use, distribution or reproduction is permitted which does not comply with these terms.

Landscape ecological risk assessment and influencing factor analysis of basins in suburban areas of large cities – A case study of the Fuchunjiang River Basin, China

Xiaomeng Cheng^{1†}, Yaping Zhang^{1†}, Guofu Yang², Wenbin Nie¹, Yinyi Wang¹, Jing Wang¹ and Bin Xu^{1*}

¹School of Landscape Architecture, Zhejiang A&F University, Hangzhou, China, ²School of Art and Archaeology, Zhejiang University City College, Hangzhou, China

Landscape ecological risk reflects the impact of human activities or natural hazards on landscape patterns, functions, and processes in a region. The scientific assessment of its evolutionary trends can play an essential role in maintaining and improving regional human wellbeing. This study focused on the Fuchunjiang River Basin in the suburbs of Hangzhou, a large city in China with a high degree of landscape heterogeneity and rapid economic growth. Based on land use data from 1990 to 2020, an ecological risk assessment model and geodetector tools were combined to study the spatiotemporal variation characteristics and influencing factors of landscape ecological risk in the basin. The results showed the following: (1) from 1990 to 2020, the landscape pattern of various land use types showed a general trend of an increasing degree of agglomeration and decreasing loss index; (2) the spatial distribution pattern of landscape ecological risk was “high in the northwest and low in the southeast.” From basin to township scales, landscape ecological risk showed a decreasing trend on long time scales, although the changes were relatively drastic in short time periods; (3) GDP, human interference, area of urban and rural residential land, area of arable land transferred in, and area of arable land transferred out were the dominant influencing factors of landscape ecological risk; (4) the coupling between landscape ecological risk and GDP in 2020 exhibited an inverted “U” shaped relationship, indicating that the environmental Kuznets curve (EKC) may have the same applicability in the ecological risk management; (5) according to the main functions of different risk agglomerations, targeted ecological risk management strategies were proposed. In short, this study carried out the landscape ecological risk assessment at the township scale for the first time, quantitatively analyzed the relationship between economic development and

ecological risk, and proposed targeted risk prevention strategies, which are instructive for other basin areas that are experiencing rapid urbanization in the world.

KEYWORDS

landscape ecological risk, LUCC, landscape pattern, spatiotemporal evolution, influencing factor, environmental Kuznets curve, risk management, landscape sustainability

1. Introduction

Landscape sustainability is an integrated representation of the capacity of ecosystems to provide services and goods that are critical to maintaining and improving human wellbeing on a global scale (Riggs et al., 2021; Wu, 2022). In the past decades, the dramatic increase in human disturbance has posed various threats to natural ecosystems, such as habitat fragmentation, biodiversity loss, disruption of energy and material flow, and reduction of service provisioning capacity, which hinder the development of landscape sustainability globally (Baffoe and Matsuda, 2018; Bhattachan et al., 2018; Bryan et al., 2018; Frazier et al., 2019; Cui H. et al., 2022). For this, many efforts have been made in many countries worldwide. For example, Europe proposed the “European Landscape Convention” as early as 2000 to promote the conservation, management and planning of landscapes in the form of legislation, and to organize countries to cooperate on landscape issues, thus promoting the development of landscape sustainability and landscape governance (Pătru-Stupariu and Nita, 2022). However, there are still many regions in the world that are undergoing or about to undergo rapid urbanization, and they urgently need to promote economic development transformation through intensive exploitation of land resources (Bamrungkhul and Tanaka, 2022; Benti et al., 2022), which will continuously exacerbate the evolution of landscape patterns and the increase of various ecological risks in the region (Bryan et al., 2018; Xie et al., 2020). It is foreseeable that the conflict between human living space and ecological protection will become more intense. Therefore, it is imperative to select suitable indicators to quantitatively identify the current environment quality in rapidly urbanizing areas and propose targeted control measures.

Ecological risk refers to the potential damage to ecosystem structure and function when an area is subjected to external stress (Wang et al., 2021; Ran et al., 2022). As a vital indicator of characterizing environmental change, ecological risk assessment plays an important role in indicating the sustainable supply capacity, health status and management level of ecosystem services and is widely used in assessing ecosystem security and predicting future benefits (Levine et al., 2019; Nepal et al., 2020; Zhang D. et al., 2022), thus providing a comprehensive characterization of regional landscape sustainability (Xu et al., 2021). The origins of ecological risk assessment can be traced back to the 1970s (Barnthouse et al., 1987; Xie et al., 2021). Traditional ecological risk assessment focused on assessing the potential adverse impacts of microscopic factors, such as chemical contaminants, on the ecosystem and human health in a small geographic area (Diggle, 1995; Landis, 2003; Raitano et al., 2018). With climate change and the expansion of human activities, many regional crises and

challenges have arisen (Lal et al., 2021), making the scope of ecological risk sources expand and gradually shifting from a single chemical pollution factor to multiple factors, such as climate, biology, natural disasters, and anthropogenic stresses (Peng et al., 2015), and the traditional risk assessment framework is no longer applicable. Therefore, to reasonably address multi-scale and multi-source compound ecological risks (Hunsaker et al., 1990; Wang et al., 2020), the concept of landscape ecological risk was proposed. It was defined as a comprehensive reflection of the possible adverse effects of human activities or natural disasters on the landscape's compositions, structures, functions, and processes based on the perspective of landscape patterns (Mo et al., 2017; Jin et al., 2019; Hou et al., 2020; Zhang et al., 2020).

Landscape ecological risk assessment includes two evaluation methods based on risk source-sink and landscape patterns (Jin et al., 2019; Hou et al., 2020). The rapid development of remote sensing technology has led to the widespread application of landscape pattern-based evaluation methods in current research (Hou et al., 2020). With the advantages of multi-scale, high resolution, dynamic monitoring, and wide observation range (Peng et al., 2022), remote sensing data can rapidly and accurately characterize regional landscape patterns, thus revealing the dynamic response of landscape patterns to comprehensive risks (Jin et al., 2019). Thus, this method can achieve comprehensive characterization and spatiotemporal differentiated expression of multisource risks without relying on large amounts of actual measurement data (Peng et al., 2015). Currently, many scholars have used this method to conduct numerous studies on landscape ecological risk at multiple scales, mainly including countries (Zhang X. et al., 2022), urban agglomerations (Li Z. et al., 2020), plateaus (Hou et al., 2020), basins (Lin et al., 2020), lakes (Xie et al., 2021), and other administrative and geographical units. Among them, basins are the most fundamental ecosystem management unit with unique geographic and socioeconomic characteristics (Bai et al., 2016) and are an important object for landscape ecological risk research. Research on landscape ecological risk in basins has mainly focused on urban agglomerations and special terrain areas, such as deserts and plateaus (Xue et al., 2019; Cui B. et al., 2022). Fewer studies have focused on the suburban areas of large cities, which are geographically special; this type of area is characterized by active urbanization, rapid changes in land use structure, and the significant evolution from a suburban agricultural landscape into a combined urban and suburban landscape (Tokarczyk-Dorociak et al., 2018). Also, suburban areas are located within the ecological buffer zone of large cities and have crucial ecological barrier functions. Therefore, it is essential to explore the evolution of landscape ecological risk in the basins of suburban areas of large cities for the development of landscape sustainability.

The Fuchunjiang River Basin is found in Hangzhou City, Zhejiang Province, one of the most developed cities in China, and has experienced rapid economic development since 2000, with a clear decreasing gradient distribution of economic levels within the basin from northeast to southwest. The region covers a wide variety of topographical features, with high landscape heterogeneity and the coexistence of urban and rural landscapes. It exhibits typical suburban regional characteristics, making it an ideal subject of study. After years of industrial development and unsustainable land use, a series of water problems (Kong et al., 2021; Yuan et al., 2023), such as high consumption, low use efficiency, and pollution have emerged in the basin, thus triggering the deterioration of the ecological environment and leading to frequent ecological problems, such as the reduction of biodiversity, shrinkage of wetland areas, and increase of landscape fragmentation, which seriously threaten the ecological security of the Fuchunjiang River Basin. As an essential ecological conservation corridor in the upstream waters of Hangzhou city, the Fuchunjiang River provides ecosystem services such as water cleanup and soil and water conservation for the downstream areas. Therefore, the conflict between urban development and ecological protection is particularly prominent in this area.

In summary, the theoretical framework and research methods of landscape ecological risk assessment have become increasingly mature, and fruitful research results have been achieved for comprehensive regional risk assessment on large-scale areas. Although previous large-scale risk assessments supported the formulation of risk management policies in theory, it was often challenging to apply the theoretical results in practice due to the lack of specific policy operation units. Therefore, this research aims to construct an ecological risk assessment model based on landscape patterns, selects the smallest administrative unit in China's three-level administrative divisions (townships) as the research unit, and considers the Fuchunjiang River Basin as a case study to implement landscape ecological risk assessment and the influencing factor analysis of the basin in the suburban areas of large cities, with the intention of answering the following three questions: (1) How are the various types of land use in the Fuchunjiang River Basin changing as the economy develops? What is the impact on landscape patterns? (2) Does the comprehensive ecological risk in the Fuchunjiang River Basin increase or decrease over time? What are the characteristics of spatial distribution? (3) What are the dominant influencing factors on landscape ecological risk? How will these factors affect changes in landscape ecological risk? Investigating the above issues can not only be an inspiration for ecological assessment and policy-making in other regions that are experiencing rapid urbanization in the world, but also provide a model case for exploring the quantitative relationship between economic development and ecological conservation in regions that are in the late stage of development.

2. Materials and methods

2.1. Study area

The Fuchunjiang River is in the Yangtze River Delta of China—Hangzhou city, Zhejiang province, flowing from southwest to

northeast through Jiande, Tonglu, Fuyang, Xiaoshan, and other districts and counties. The river section is 110 km long and is the main channel of the Qiantang River (Figure 1). The Fuchunjiang River Basin is located between 29.4°–30.2°N and 119.4°–120.3°E, with a basin area of 4,524 km²; it involves many townships in Hangzhou. The topography of the basin is complex and dominated by mountains and hills, which account for approximately 68% of the total area. The hills and mountains in the southwest are undulating, while the terrain in the northeast is low-lying, forming a general topography surrounded by plains and mountains with the Fuchunjiang River as the axis. The land type is dominated by forest land, which accounts for about 70% of the total area of the study area and is mainly distributed in the southeastern part of the basin with high elevation, followed by arable land and urban and rural residential land, accounting for about 20 and 5% of the total area and distributing along the river. The main climate type is subtropical monsoon climate, with an annual average temperature of approximately 16.5°C and annual total precipitation of approximately 1,550 mm. In 2020, the GDP and total population of the Fuchunjiang River Basin were US\$48.88 billion and 1.84 million, respectively. With the increasing economic radiation effect of the Hangzhou Bay Area, the Fuchunjiang River Basin has shown remarkable economic vitality and population clustering effects.

2.2. Data sources and processing

The data used in this study included three main categories: land-use data, geographic data, and influencing factor data.

The land-use data were obtained from the Resource and Environment Science and Data Center of Chinese Academy of Sciences,¹ including the spatial distribution data of land use/cover remote sensing monitoring in China in 1990, 2000, 2010, and 2020 with a spatial resolution of 30 m. The dataset was based on Landsat images, with an overall accuracy above 92%. According to the “China Remote Sensing Monitoring Land Use/Cover Classification System” and the actual situation of the study area, land use in the study area was classified into seven types: arable land, forestland, grassland, waters, urban and rural residential land, other construction lands, and unused land. The specific spatial distribution is shown in Figure 2.

The geographic data mainly included administrative boundaries² and river data.³

The influencing factor dataset contained four main categories: topography data, climate data, accessibility data, and socioeconomic data, which were used to analyze the dominant driving factors and changing trends in landscape ecological risk for 2000, 2010, and 2020. Details and sources of the dataset are shown in Table 1. Among them, the DEM and township government location data slightly differed in year correspondence because of small changes and little data information. Only the years in Table 1 were selected for analysis.

1 <https://www.resdc.cn/>

2 <https://ditu.zjzfw.gov.cn/>

3 <https://www.openstreetmap.org/>

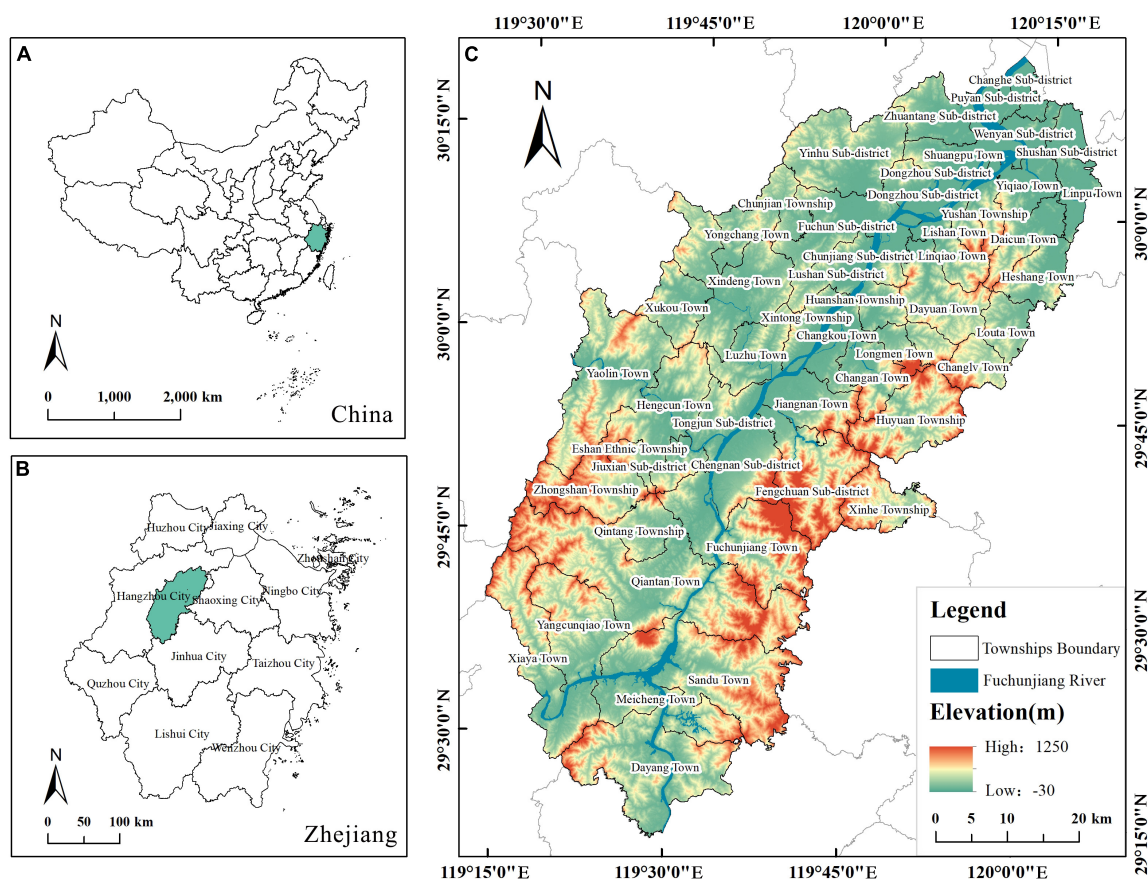


FIGURE 1

Location of the study area. Note: (A) Administrative division of China. (B) Administrative division of Zhejiang. (C) Elevation and township boundary of the Fuchunjiang River Basin.

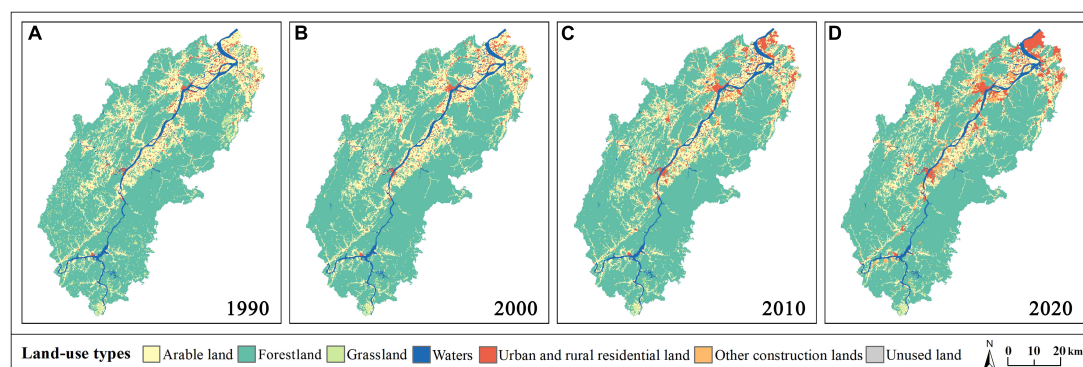


FIGURE 2

Classification map of land use in the Fuchunjiang River Basin for (A) 1990, (B) 2000, (C) 2010, and (D) 2020.

2.3. Methods

As an intuitive feedback of human disturbance on regional ecosystems, LUCC has been demonstrated to be closely related to the spatiotemporal evolution of landscape ecological risk (Chen C. et al., 2019; Jiang et al., 2020). Therefore, this article establishes the relationship between LUCC and ecological risk using landscape patterns as a medium, and the spatiotemporal dynamic evaluation

system of landscape ecological risk is proposed as follows: firstly, based on land use data, spatial analysis and landscape pattern index method are used to identify the overall characteristics of dynamic changes of regional land use and landscape pattern; secondly, taking townships as the minimum assessment unit, a landscape ecological risk evaluation model is constructed based on the obtained landscape pattern index values to evaluate the spatial differences, temporal changes, transfer characteristics and

TABLE 1 Influencing factor dataset details and sources.

Dataset	Details	Year	Resolution	Sources
Topography raster data	Digital elevation model (DEM) ^a	2008	12.5 m	The Earth Science Data Systems (ESDS) (https://search.asf.alaska.edu/#/)
	Normalized difference vegetation index (NDVI) maximum data	2000 2010 2020	30 m	Chinese Academy of Sciences Discipline Data Center for Ecosystem (http://www.nesdc.org.cn/)
Climate data	Annual average temperature data of each meteorological station in Hangzhou	2000 2010 2020	Point data	China Meteorological Data Service Centre (http://data.cma.cn)
	Annual total precipitation data of each meteorological station in Hangzhou	2000 2010 2020	Point data	China Meteorological Data Service Centre (http://data.cma.cn)
Accessibility data ^b	Longitude and latitude of township government location	2020	Point data	AMAP open platform (https://lbs.amap.com/)
	Longitude and latitude of Hangzhou city government location	2000 2010 2020	Point data	AMAP open platform (https://lbs.amap.com/)
Socioeconomic raster data	GDP data	2000 2010 2020	1 km	Resource and Environment Science and Data Center, Chinese Academy of Sciences (http://www.resdc.cn)
	Population density data	2000 2010 2020	100 m	WorldPop data platform (https://www.worldpop.org/)

^aThe DEM data is resampled and the resolution is adjusted to 30 m to make it consistent with the resolution of the land use data.

^bThe accessibility data include the longitude and latitude of township government location and longitude and latitude of Hangzhou city government location, which are mainly used to calculate two accessibility influencing factors: the distance of each township from the Fuchunjiang River and the distance of each township from Hangzhou city.

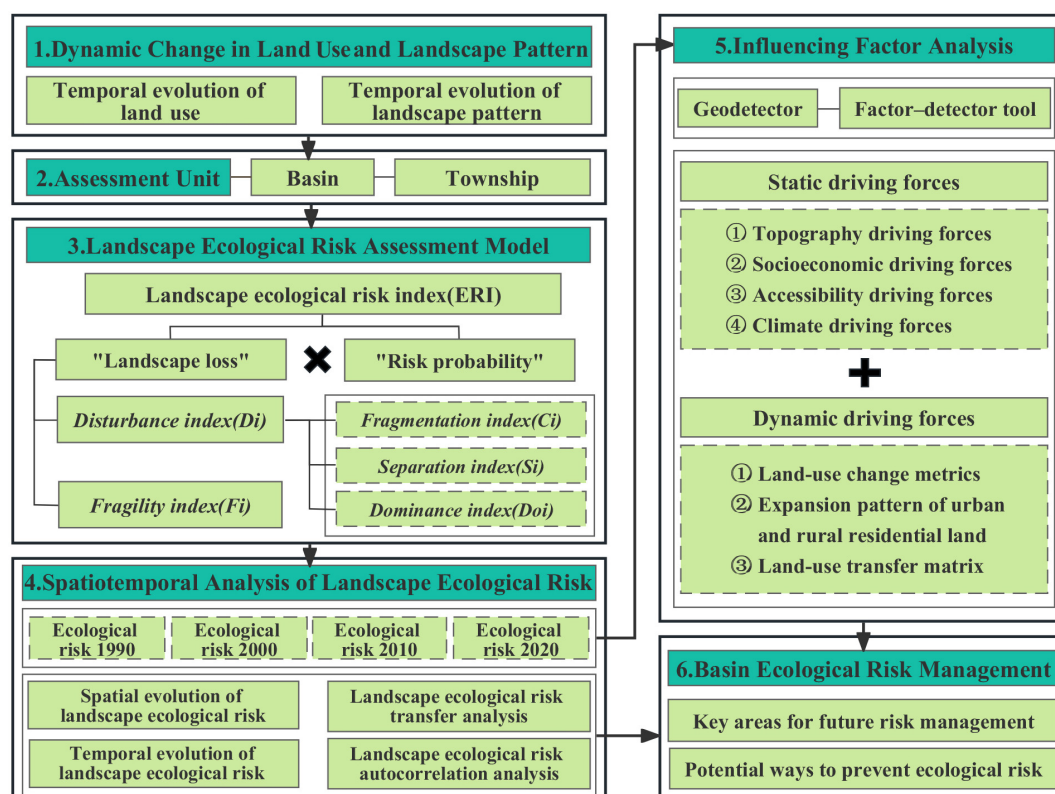


FIGURE 3
Research framework.

TABLE 2 Formula for the landscape ecological risk index and its ecological significance.

Index	Calculation formula	Ecological significance and parameter explanation
Landscape fragmentation index	$C_i = \frac{n_i}{A_i}$	To describe the degree of patches fragmentation for a certain landscape type (Lin et al., 2019). n_i , patch number of landscape type i ; A_i , total area of landscape type i .
Landscape separation index	$S_i = \frac{l_i}{P_i}$ $l_i = \frac{1}{2} \sqrt{\frac{n_i}{A_i}}$, $P_i = \frac{A_i}{A}$	To describe the degree of patches separation for a certain landscape type (Lin et al., 2019). l_i , distance index of landscape type i ; P_i , area index of landscape type i ; A , total area of the entire landscape.
Landscape dominance index	$D_{oi} = \frac{Q_i + M_i}{4} + \frac{L_i}{2}$ $Q_i = \frac{B_i}{B}$, $M_i = \frac{n_i}{N}$, $L_i = \frac{A_i}{A}$	To describe the degree of patches importance for a certain landscape type (Lin et al., 2019). Q_i , the frequency of landscape type i ; M_i , the density of landscape type i ; L_i , the ratio of landscape type i ; B_i , number of samples appearing landscape type i ; B , total sample number; N , total number of all types of patches.
Landscape disturbance index	$D_i = aC_i + bS_i + cD_{oi}$	To quantify the intensity of a landscape subjected to external interference (Lin et al., 2019). a , b , and c are weights of indexes C_i , S_i , and D_{oi} , according to the previous research results, $a = 0.5$, $b = 0.3$, and $c = 0.2$ (Xue et al., 2019).
Landscape fragility index	F_i , obtained by experts assignment and normalization	To indicate the sensitivity and vulnerability of different landscape types to external disturbances (Ran et al., 2022). The landscape fragility index is classified into six grades: unused land = 6, waters = 5, arable land = 4, grassland = 3, forestland = 2, urban and rural residential land = 1, other construction lands = 1 (Wang et al., 2019).
Landscape loss index	$R_i = D_i \times F_i$	To indicate the loss of natural properties of ecosystems of different landscape types caused by external disturbances. The landscape loss index is characterized by a combination of landscape disturbance index (D_i) and landscape fragility index (F_i).
Landscape ecological risk index	$ERI_k = \sum_{i=1}^n \frac{A_{ki}}{A_k} \times R_i$	The landscape ecological risk index is constructed by combining the area weight of landscape components and the landscape loss index. A_{ki} , the area of landscape type i in township k ; A_k , the total area of the township k ; n , the number of landscape types; ERI_k , landscape ecological risk index of the township k .

change rate situation of landscape ecological risk in the study area, and combined with spatial autocorrelation model to analyze the spatial clustering characteristics of landscape ecological risk; finally, based on the influencing factors dataset, the dominant influencing factors of dynamic changes in landscape ecological risk are analyzed from both static and dynamic levels with the help of Geodetector model. The general framework of the study is shown in Figure 3.

2.3.1. Landscape ecological risk assessment

Based on previous research results, in this article, landscape fragmentation, separation, and dominance indexes were selected to build the landscape disturbance index and were then combined with the fragility index normalized by expert assignment to characterize the landscape loss index (Lin et al., 2019; Xue et al., 2019). The “loss and probability multiplication” model was constructed to calculate each township’s landscape ecological risk index (ERI) in the Fuchunjiang River Basin. The specific calculation formula and ecological significance are shown in Table 2.

According to the calculation formula of the landscape ecological risk, the landscape ERI of each township was obtained and divided into five classes according to equal intervals (Xu et al., 2021): low ecological risk area ($ERI < 0.007$), sub-low ecological risk area ($0.007 \leq ERI < 0.009$), medium ecological risk area ($0.009 \leq ERI < 0.011$), sub-high ecological risk area ($0.011 \leq ERI < 0.013$), and high ecological risk area ($ERI \geq 0.013$).

2.3.2. Spatial autocorrelation analysis

2.3.2.1. Global spatial autocorrelation

Exploratory spatial data were used to analyze the spatial distribution pattern of landscape ecological risk in the Fuchunjiang River Basin (Zhao et al., 2018). The *Global Moran’s I* index was used to determine whether there were clustering or dispersion

characteristics of landscape ecological risk. The calculation formulas are as follows:

$$Global\ Moran's\ I = \frac{\left[\sum_{i=1}^n \sum_{j=1}^n W_{ij} (X_i - \bar{X}) (X_j - \bar{X}) \right]}{\left(S^2 \sum_{i=1}^n \sum_{j=1}^n W_{ij} \right)} \quad (1)$$

$$S^2 = \frac{1}{n} \sum_{i=1}^n (X_i - \bar{X})^2, \bar{X} = \frac{1}{n} \sum_{i=1}^n X_i \quad (2)$$

where X_i and X_j are the attribute values of spatial units i and j , W_{ij} is the spatial weight matrix, which indicates the proximity of each spatial unit, and n is the number of risk units. The *Global Moran’s I* index is between $[-1, 1]$. An index greater than 0 indicates a positive spatial correlation, and the risk values show clustering characteristics; an index less than 0 indicates a negative spatial correlation, and the risk values show dispersal characteristics; an index equal to 0 indicates no spatial correlation, and the risk values are randomly distributed.

2.3.2.2. Local spatial autocorrelation

For the specific spatial distribution of high-value or low-value clusters, global spatial autocorrelation cannot be used for further analysis, so the Hot Spot Analysis tool (*Getis-Ord Gi**) was chosen to identify spatial clusters with statistically significant high values (hot spots) and low values (cold spots). The results can generate maps of hot spot and cold spot distribution to show the spatial correlation and distribution.

2.3.3. Geodetector

The geodetector is a set of statistical methods for detecting spatial differentiation and revealing the driving forces behind it (Wang and Xu, 2017). Referring to previous research results, combined with the actual situation of the Fuchunjiang River Basin, 12 static influencing factors were selected from four

categories of topography, socioeconomic, accessibility, and climate: elevation, slope, aspect, NDVI maximum, GDP, population density, area of urban and rural residential land, human interference, the distance of each township from the Fuchunjiang River, the distance of each township from Hangzhou city, annual average temperature, and annual total precipitation. Thirteen dynamic influencing factors were selected from three categories of land-use change metrics, expansion pattern of urban and rural residential land and land-use transfer matrix: dynamic attitude of urban and rural residential land area, patch number of in-fill expansion mode, patch number of marginal expansion mode, patch number of enclave expansion mode, patch area of in-fill expansion mode, patch area of marginal expansion mode, patch area of enclave expansion mode, area of arable land transferred out, area of arable land transferred in, area of urban and rural residential land transferred out, area of urban and rural residential land transferred in, area of other construction lands transferred out, and area of other construction lands transferred in. These 25 influencing factors were input as variable X , and the landscape ecological risk value and its dynamic attitude were used as attribute Y of the static and dynamic influencing factors, respectively, to explore the dominant driving factors of landscape ecological risk changes. The specific formula is as follows:

$$q = 1 - \frac{\sum_{h=1}^L N_h \sigma_h^2}{N \sigma^2} \quad (3)$$

where q is the detection value of the ecological risk influencing factors, σ_h^2 denotes the discrete variance of Y , h is the number of variable X , N_h denotes the township unit, N is the total number of township units, and σ^2 is the total regional variance. q is between $[0, 1]$, and the larger the value of q is, the stronger the explanatory power of the independent variable X on attribute Y . The value of q indicates the proportion of landscape ecological risk explained by the influencing factors.

2.3.4. Land-use change metrics

The concept of land-use dynamic attitude was introduced to study the dynamic impact of the magnitude of changes in urban and rural residential land on the landscape ecological risk, and its expression is as follows (Zhou, 2022):

$$K = \frac{U_b - U_a}{U_a} \times \frac{1}{T} \times 100\% \quad (4)$$

where K is the area dynamic attitude of urban and rural residential land in the study period, U_a and U_b are the areas of the urban and rural residential land at the beginning and end of the study period, respectively, and T is the difference between the years of the study period.

2.3.5. Expansion pattern of urban and rural residential land

The concept of the multi-order adjacency index was introduced to investigate the dynamic influence of the number and area of patches of various expansion patterns of urban and rural residential land on the landscape ecological risk (Liu et al., 2018). This index was used to describe the expansion of urban and rural residential

land by defining the degree of adjacency of the spatial relationship between old and new patches, setting the buffer distance, and quantifying the patch expansion characteristics using the multi-order buffer method. Its calculation formula is as follows:

$$MAI = N - A_i/A_0 \quad (5)$$

where MAI is the multi-order adjacency index of the new patches; N is the number of buffers made for the new patches; A_0 is the area of the N -th buffer (the outermost buffer); and A_i is the area of the part of the N -th buffer intersecting with the original patch. When the value of MAI is between $[0, 0.5)$, the expansion mode of urban and rural residential land is in-fill expansion; when the value is between $[0.5, 1)$, it is marginal expansion; when the value is greater than 1, it is enclave expansion.

2.3.6. Land-use transfer matrix

The land-use transfer matrix model was introduced to investigate the dynamic influence of the area transferred in and out of a certain land-use type on the landscape ecological risk and to characterize the dynamic process of the interconversion between the area of each land type at the beginning and the end of a period in a certain region (Zhou, 2022). Its mathematical form is as follows:

$$S_{ij} = \begin{bmatrix} S_{11} & S_{12} & \dots & S_{1n} \\ S_{21} & S_{22} & \dots & S_{2n} \\ \dots & \dots & \dots & \dots \\ S_{n1} & S_{n2} & \dots & S_{nn} \end{bmatrix} \quad (6)$$

where S represents the area; n is the number of land use types; and i and j are the land use types at the beginning and end of the study, respectively. Each row in the matrix represents the transferred-out information of a certain land type, and each column represents the transferred-in information of a certain land type. In this article, ArcGIS10.6 software was used to cross-analyze data of land use types in different periods and establish each period's land-use transfer matrix.

3. Results

3.1. Land use and landscape pattern changes

The land use types in the Fuchunjiang River Basin that changed from 1990 to 2020 accounted for 12.64% of the total area (Table 3). During the period, the area of arable land decreased by 216.18 km², and the grassland area decreased by 69.66 km². The area of these two land types decreased by 21.83 and 49.55%, respectively. The area of urban and rural residential land increased by 89.11%, while the number of patches showed a slight decrease, indicating that as the urban and rural settlement clusters expanded, the area of patches increased, and the edges gradually merged. The growth of other construction lands was as high as 1,415.59%, and the number of patches also increased by 526%, especially between 2000 and 2010. The area and number of patches increased by 845.29 and 462.79%, respectively, which was mainly related to the "Industrial

TABLE 3 Landscape pattern indexes of various land use types in the Fuchunjiang River Basin from 1990 to 2020.

Type	Year	Patch number	Patch area/km ²	F_i	C_i	S_i	D_{oi}	D_i	R_i
Waters	1990	161	155.02	0.2392	0.0104	0.2753	0.2792	0.1436	0.0344
	2000	166	155.96	0.2392	0.0106	0.2778	0.2837	0.1454	0.0348
	2010	174	161.13	0.2392	0.0108	0.2753	0.2844	0.1449	0.0347
	2020	174	159.94	0.2392	0.0109	0.2774	0.2838	0.1454	0.0348
Arable land	1990	833	990.42	0.1573	0.0084	0.0980	0.4217	0.1180	0.0186
	2000	543	945.05	0.1573	0.0057	0.0829	0.4084	0.1094	0.0172
	2010	476	855.71	0.1573	0.0056	0.0857	0.3900	0.1065	0.0168
	2020	551	774.25	0.1573	0.0071	0.1020	0.3866	0.1115	0.0175
Forestland	1990	448	3,104.40	0.0650	0.0014	0.0229	0.6266	0.1329	0.0086
	2000	394	3,209.02	0.0650	0.0012	0.0208	0.6438	0.1356	0.0088
	2010	401	3,187.75	0.0650	0.0013	0.0211	0.6406	0.1351	0.0088
	2020	404	3,168.06	0.0650	0.0013	0.0213	0.6376	0.1346	0.0087
Grassland	1990	855	140.56	0.1017	0.0608	0.6996	0.3295	0.3062	0.0311
	2000	386	67.55	0.1017	0.0571	0.9781	0.2958	0.3812	0.0388
	2010	389	71.66	0.1017	0.0543	0.9256	0.2951	0.3638	0.0370
	2020	401	70.91	0.1017	0.0566	0.9497	0.2950	0.3722	0.0379
Urban and rural residential land	1990	985	124.08	0.0413	0.0794	0.8506	0.3374	0.3624	0.0150
	2000	975	137.58	0.0413	0.0709	0.7633	0.3621	0.3368	0.0139
	2010	927	180.04	0.0413	0.0515	0.5687	0.3585	0.2681	0.0111
	2020	847	234.65	0.0413	0.0361	0.4171	0.3544	0.2141	0.0088
Other construction lands	1990	50	7.55	0.0413	0.0663	3.1515	0.2546	1.0295	0.0425
	2000	43	6.97	0.0413	0.0617	3.1637	0.2550	1.0310	0.0426
	2010	242	65.89	0.0413	0.0367	0.7940	0.2804	0.3126	0.0129
	2020	313	114.36	0.0413	0.0274	0.5203	0.2916	0.2281	0.0094
Unused land	1990	12	1.83	0.3543	0.0656	6.3733	0.2511	1.9950	0.7068
	2000	8	1.76	0.3543	0.0454	5.3923	0.2510	1.6906	0.5990
	2010	8	1.77	0.3543	0.0452	5.3759	0.2510	1.6856	0.5972
	2020	8	1.78	0.3543	0.0450	5.3487	0.2509	1.6773	0.5943

Development” strategy proposed by Hangzhou in 2000. During this period, the rapid development and dominance of industrial manufacturing in the townships led to a dramatic expansion in the area and the number of patches. Forestland was the dominant landscape in the study area and has remained relatively stable over the past 30 years, and waters and unused land also remained unchanged.

The changes in land-use structure and function caused significant changes in the landscape pattern of the Fuchunjiang River Basin. Overall, the dynamic responses of landscape pattern indexes in various land types to land-use changes during the study period showed strong consistency. The fragmentation, separation, and dominance indexes of urban and rural residential land patches gradually declined, and the loss index also maintained the same decreasing trend, from 0.015 to 0.009, with a total decrease of 40.92%. The fragmentation and separation index of other construction lands exhibited a decreasing trend, and the dominance index increased slightly, among which the separation index dropped sharply from 3.16 to 0.79 between

2000 and 2010, with a drop of 74.90%, which directly led to a significant decrease in the disturbance and loss index, decreasing from 1.03 to 0.31 and 0.04 to 0.01, respectively. The changing trend of the landscape pattern in grassland was the same as that of arable land patches, with the fragmentation and dominance index decreasing and the separation index increasing, reflecting the decrease in arable land patches and the increase in grassland patches in terms of the loss index. The landscape pattern indexes of unused land showed a slight downward trend, while the landscape pattern indexes of waters and forestland patches remained stable. In general, the fragmentation and separation index of multiple types of land patches had an obvious downward trend, and the degree of agglomeration increased. The loss degree from highest to lowest was as follows: unused land > grassland > waters > other construction lands > arable land > urban and rural residential land > forestland. The results indicated that the loss of unused land was the greatest and forestland was the most stable when subjected to human disturbance.

3.2. Spatiotemporal variation characteristics of landscape ecological risk

3.2.1. Spatial differences in landscape ecological risk

The spatial distribution of landscape ecological risk in the Fuchunjiang River Basin varied greatly, showing a spatial pattern of “high in the northwest and low in the southeast” (Figure 4). High-risk townships were mainly concentrated in the downstream areas of the Fuchunjiang River Basin, including Wenyan Subdistrict, Changhe Subdistrict, and Shuangpu Town, where the landscape was dominated by construction lands such as settlements and industrial gathering areas, with dense cities, a vibrant economy, and high land-use intensity. The sub-high ecological risk areas were distributed along the periphery of the high-risk areas and the middle reaches of the Fuchunjiang River, including subdistricts such as Shushan, Zhuantang, and Puyan and towns such as Yiqiao, Linpu, and Hengcun, with the landscape type still dominated by construction land. The low ecological risk areas were mainly distributed in the eastern part of the study area bordering Shaoxing city, including Changlv Town, Huyuan Township, Xinhe Township, Dayuan Township, and other townships, where there were many mountains with forestland and grassland as the main landscape types, and the degree of human interference was low. The sub-low ecological risk areas were mainly distributed in the southern part of the study area, adjacent to the Jiande and Chun'an areas. The medium-risk townships were concentrated in the northwest block of Fuyang and Tonglu, where the terrain was relatively flat, and the arable land area was large and wide-ranging.

3.2.2. Temporal changes in landscape ecological risk

From 1990 to 2020, the landscape ecological risk in the Fuchunjiang River Basin generally showed a downward trend. The 4-year landscape ecological risk values were 0.0129, 0.0124, 0.0120, and 0.0119, with an overall decrease of 7.75%. At the same time, the annual maximum and average values of the landscape ERI of the 51 townships also gradually decreased (Figure 4). As seen in Figure 5, the area proportion of regions with landscape ecological risk levels from low to high was approximately 10, 59, 21, 7, and 3% during the study period, and the sub-low and medium ecological risk areas were always dominant. Except for 1990, when the area of the medium ecological risk areas accounted for the highest percentage (39.44%), the rest of the years were dominated by the sub-low ecological risk areas, which accounted for more than 55% of the total area, and the number of townships was the largest, increasing from 16 to 25; the area and number of townships in sub-high and high ecological risk areas gradually decreased, and the area proportion stabilized below 10%. A comparison of three periods revealed that the area of ecological risk areas at all levels changed significantly during the period from 1990 to 2000, except for the high ecological risk areas. The area of low and sub-low ecological risk areas increased by 62.24 and 45.01%, respectively, while the area of medium and sub-high ecological risk areas decreased by 45.66 and 51.04%. Overall, due to the changes in landscape pattern, the area of low and sub-low ecological risk areas continued to increase, which led to a significant decrease in regional landscape

ecological risk and a gradual improvement in habitat quality and ecological safety.

3.2.3. Landscape ecological risk transfer analysis

From 1990 to 2020, the ecological risk level of each township in the Fuchunjiang River Basin mainly shifted from high-risk to low-risk levels, with a total shift of 2,039.29 km², accounting for 83.72% of the total transferred area (Figure 6A). Divided into three stages, from 1990 to 2000, the ecological risk level of 14 townships changed, and the landscape ecological risk level decreased in all of them. The number of townships that shifted ecological risk levels from sub-high to medium, medium to sub-low, medium to low, and sub-low to low was 4, 7, 2, and 1, respectively, with a total shift of 1,460.45 km². From 2000 to 2010, there were 6 townships with elevated ecological risk levels, among which 2, 1, and 3 townships shifted ecological risk levels from medium to sub-high, sub-low to medium, and low to sub-low, respectively, with a total shift of 359.44 km². There were 2 townships with decreased risk levels; Changhe Subdistrict changed from high to sub-high risk, and Linpu Town changed from sub-high to medium risk. From 2010 to 2020, there was only one township (Yushan Township) with elevated ecological risk levels, changing from low to sub-low risk. There were 6 townships with decreased risk levels; two changed from sub-high to medium, two changed from medium to sub-low, and two changed from sub-low to low risk, with a total shift of 522.95 km². In terms of spatial distribution (Figure 6B), from 1990 to 2020, the areas with frequent changes in ecological risk levels were mainly distributed in the townships along the Fuchunjiang River and close to the center of Hangzhou, primarily shifting from the high-risk level to the low-risk level. It is indicated that the comprehensive ecological risk in the Fuchunjiang River Basin was alleviated, and the pressure on the ecological environment caused by human activities gradually improved.

3.2.4. Change rate of landscape ecological risk

After analyzing the comprehensive transfer of ecological risk across townships over a 30-year period, the magnitude of change in landscape ecological risk was further explored over three time intervals (Figure 7). From 1990 to 2000, the change rate of risk in the study area was between 0 and −28.09%, with only two townships having a slightly elevated risk, both with growth rates below 1%. From 2000 to 2010, the number of townships with rising ecological risk increased significantly, mainly concentrated on the south bank of the Fuchunjiang River, and the risk grew at a faster rate, with the highest growth rate of 15.05%. From 2010 to 2020, the block with elevated risk shifted southward, forming two clusters in the north and south, but the growth rate decreased compared to the previous period, and the decline in risk became greater. In general, the growth rate of landscape ecological risk in the three stages showed a trend of increasing and then decreasing. The groups with high growth rates gradually moved south from the north, and the number of townships gradually increased.

3.3. Spatial autocorrelation analysis of landscape ecological risk

Based on the spatial distribution of the landscape ERI in each township, the *Global Moran's I* of landscape ecological

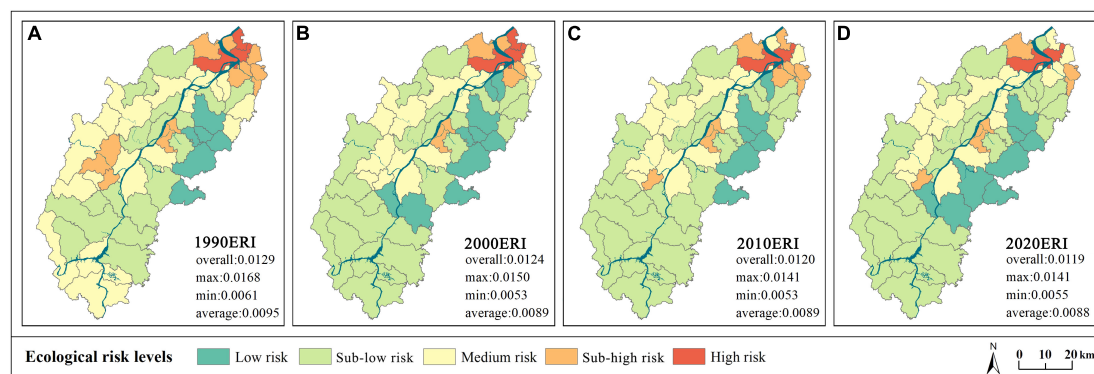


FIGURE 4

Spatiotemporal variation characteristics of landscape ecological risk in the Fuchunjiang River Basin for (A) 1990, (B) 2000, (C) 2010, and (D) 2020. Note: ERI is the abbreviation of the landscape ecological risk index (1990ERI means the landscape ecological risk value in 1990); *overall* represents the overall landscape ecological risk value of the Fuchunjiang River Basin; *max* represents the maximum value of landscape ecological risk among 51 townships; *min* represents the minimum value of landscape ecological risk among 51 townships; *average* is the average value of landscape ecological risk among 51 townships.

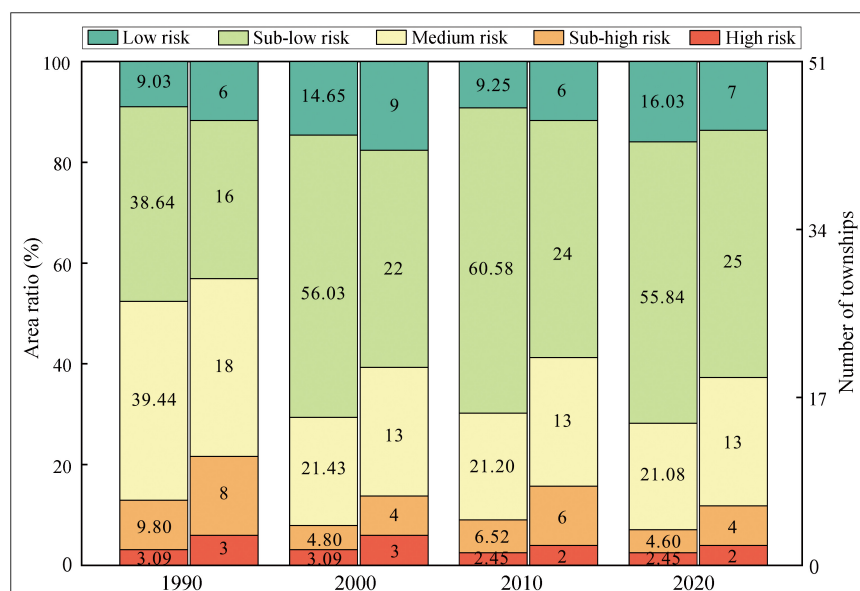


FIGURE 5

The area ratio and the number of townships in various levels of landscape ecological risk areas in the Fuchunjiang River Basin from 1990 to 2020. The data in the left column of each year are the area ratio in various levels of landscape ecological risk areas, and the data in the right column of each year are the number of townships in various levels of landscape ecological risk areas.

risk in the Fuchunjiang River Basin from 1990 to 2020 was 0.5542, 0.5033, 0.4672, and 0.3561, respectively, and the *Z* scores were all greater than 1.96. During the study period, the landscape ERI in the Fuchunjiang River Basin showed significant spatial autocorrelation, i.e., townships with high or low landscape ecological risk values were clustered.

The Hot Spot Analysis (*Getis-Ord Gi**) tool was used to further analyze the landscape ecological risk aggregation characteristics of the study area, which were divided into four categories according to the *Z* score: cold spot (Z score < -1.96), sub-cold spot: ($-1.96 \leq Z$ score < 0), sub-hot spot: ($0 < Z$ score ≤ 1.96), and hot spot: (Z score > 1.96). Overall, the Fuchunjiang River was used as a dividing line to separate the cold and hot spot areas. The northern area

of the Fuchunjiang River was dominated by hot spots and sub-hot spots, while the southern bank of the river was dominated by cold spots and sub-cold spots, which exhibited strong consistency with the spatial pattern of risk levels (Figure 8). The hot spot areas were mainly found in the more populous and economically developed northern area, with towns and subdistricts such as Wenyan, Zhuantang, and Shuangpu as the core to form a group. The sub-hot spot areas were mainly distributed in the northwest, located in the territory of Fuyang and Tonglu. The cold spot areas were distributed in the eastern area with high altitude and mainly forestland, with Shangguan, Huyuan, Changlv, and other townships as the core; the sub-cold spot areas were mainly located in the southern part within the Jiande area.

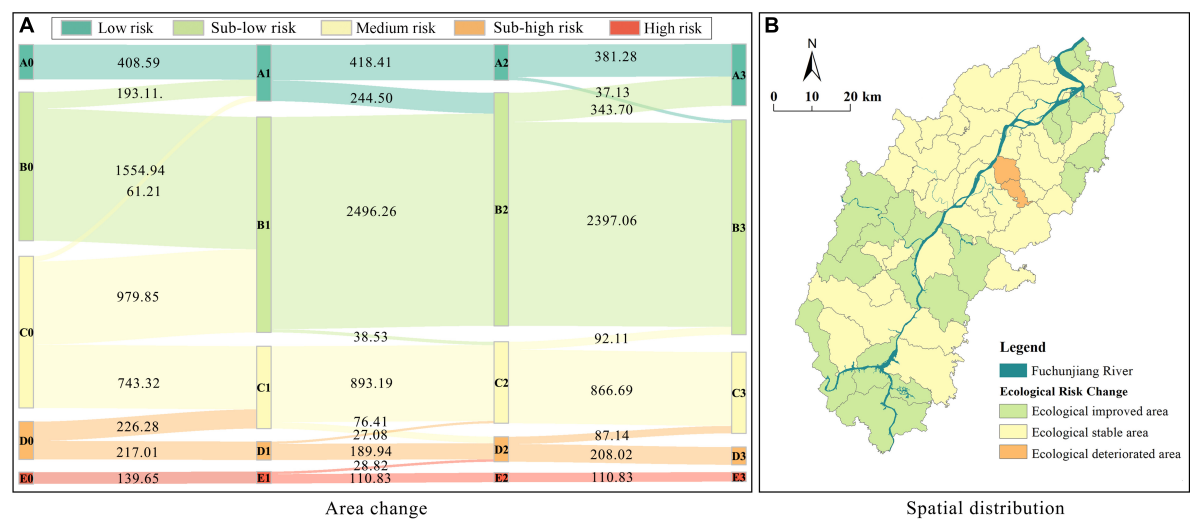


FIGURE 6
Area change and spatial distribution of landscape ecological risk shift areas in the Fuchunjiang River Basin from 1990 to 2020. **(A)** Area change. **(B)** Spatial distribution. A, B, C, D, and E represent low risk area, sub-low risk area, medium risk area, sub-high risk area, and high risk area, respectively. 0, 1, 2, and 3 represent 1990, 2000, 2010, and 2020, respectively, and the area unit in the figure is km².

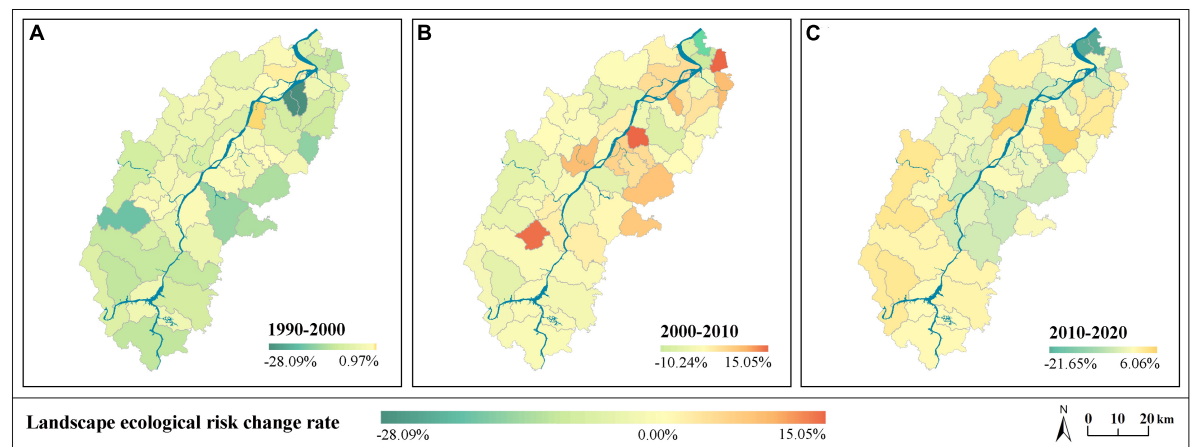


FIGURE 7
Change rate and spatial distribution of landscape ecological risk in the Fuchunjiang River Basin for **(A)** 1990–2000, **(B)** 2000–2010, and **(C)** 2010–2020.

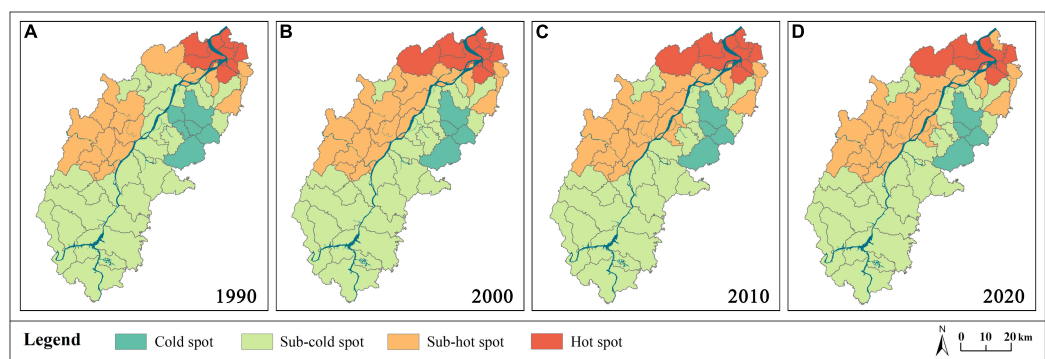


FIGURE 8
Spatial distribution of hot spots and cold spots in landscape ecological risk in the Fuchunjiang River Basin for **(A)** 1990, **(B)** 2000, **(C)** 2010, and **(D)** 2020.

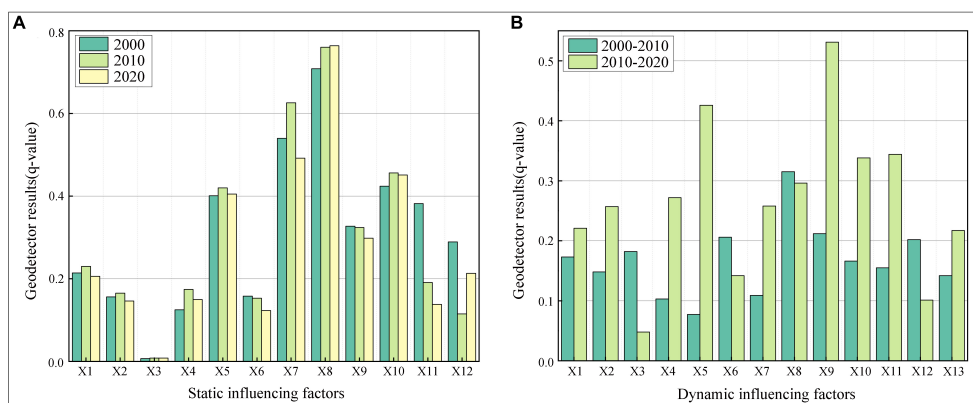


FIGURE 9

Geodetector results of static and dynamic influencing factors of landscape ecological risk in the Fuchunjiang River Basin from 2000 to 2020.

(A) X1 elevation; X2, slope; X3, aspect; X4, NDVI maximum; X5, GDP; X6, population density; X7, area of urban and rural residential land; X8, human interference; X9, the distance of each township from the Fuchunjiang River; X10, the distance of each township from Hangzhou city; X11, annual average temperature; X12, annual total precipitation. **(B)** X1, dynamic attitude of urban and rural residential land area; X2, patch number of in-fill expansion mode; X3, patch number of marginal expansion mode; X4, patch number of enclave expansion mode; X5, patch area of in-fill expansion mode; X6, patch area of marginal expansion mode; X7, patch area of enclave expansion mode; X8, area of arable land transferred out; X9, area of arable land transferred in; X10, area of urban and rural residential land transferred out; X11, area of urban and rural residential land transferred in; X12, area of other construction lands transferred out; X13, area of other construction lands transferred in.

3.4. Landscape ecological risk influencing factor analysis

3.4.1. Analysis of the static influencing factors

Based on the results of previous studies and the field situation of the Fuchunjiang River Basin, a total of 12 static indicators in four categories of topography, socioeconomic, accessibility, and climate were selected to explore the main influencing factors of landscape ecological risk in 3 years, 2000, 2010, and 2020. The factor-detector tool of the geodetector was used to obtain the detection power (q -value) corresponding to each factor. The results showed that the explanatory power of each static influencing factor was from high to low: $X8 > X7 > X10 > X5 > X9 > X11 > X1 > X12 > X2 > X4 > X6 > X3$ (Figure 9A). The q -values of the human interference factor and the area of urban and rural residential land factor were both above 0.5, with average q -values of 0.74 and 0.55, respectively, which had a significant influence. Overall, the explanatory power of socioeconomic and accessibility factors was significantly higher than that of topography and climate factors. Among all the influencing factors, the explanatory power of human interference increased year by year. Except for the four factors of aspect, NDVI maximum, GDP, and the distance of each township from Hangzhou city, whose influence fluctuated upward with the year, all the other factors showed a decreasing trend. The explanatory power of the annual average temperature and total precipitation factors declined the fastest, decreasing by 63.89 and 26.43%, respectively, indicating that climate factors were becoming less influential on the landscape ecological risk.

3.4.2. Analysis of the dynamic influencing factors

From the situation of urban and rural residential land expansion and land use transfer, a total of 13 dynamic indicators in three categories of land-use change metrics, expansion pattern

of urban and rural residential land, and land-use transfer matrix were selected. The dynamic attitude of landscape ecological risk was considered the dependent variable, and two periods (from 2000 to 2010 and from 2010 to 2020) were defined for factor influence detection to obtain the corresponding q values. The results showed that the explanatory power of each dynamic influencing factor was in descending order: $X9 > X8 > X10 > X5 > X11 > X2 > X1 > X4 > X7 > X13 > X6 > X12 > X3$ (Figure 9B). The two factors of the area of arable land transferred out and the area of arable land transferred in were dominant, and the average explanatory power was above 0.3. Except for the factors of patch number of marginal expansion mode of urban and rural residential land, patch area of marginal expansion mode of urban and rural residential land, and the area of other construction lands transferred out which showed a decreasing trend, the explanatory power of all the other factors increased. The patch area of in-fill expansion mode of urban and rural residential land grew the fastest with a growth rate of 457.05%. In general, the influence of the land-use transfer matrix factors was generally more significant than that of the expansion pattern of urban and rural residential land and the land-use change metrics factors.

4. Discussion

4.1. Spatial heterogeneity of landscape ecological risk

Shifts in landscape structure and function are often caused by LUCC, and landscape ecological risk is mainly generated based on the evolution of landscape patterns (Jiang et al., 2021). Therefore, this article constructs a close correlation between LUCC and landscape ecological risk using landscape pattern as a medium, and provides a theoretical approach for ecological risk assessment. It

can be seen that the heterogeneity of land use largely determines the spatial heterogeneity of landscape ecological risk (Chen C. et al., 2019; Jiang et al., 2020).

The spatial distribution of landscape ecological risk in the Fuchunjiang River Basin from 1990 to 2020 showed significant heterogeneity, forming a spatial pattern of “high in the northwest and low in the southeast.” The townships with high risk were mainly concentrated in the northwestern part of the study area, which was the downstream region of the Fuchunjiang River Basin, while the townships with low risk were distributed in the southeastern region (Figure 4). The spatial differences in landscape ecological risk between the northwest and southeast were mainly related to the economic development, policy guidance, and natural attributes of the suburban areas of Hangzhou city (Karimian et al., 2022). Compared with the southeast, the northwest part, which was closer to the central area of Hangzhou, was an area of concentrated population and developed economy, where high-intensity industrial activities and accelerating urbanization put great pressure on the regional ecosystems and increased the local ecological risk (Karimian et al., 2022). This result was generally consistent with the previous study’s results (Zhou et al., 2022). In contrast, the southeastern part of the study area had significantly less human disturbance to the environment due to the overall high elevation (Figure 1). There were several national forest parks in and around the area, such as Qiandao Lake, Dachishan, and the Fuchunjiang River, with high vegetation coverage (Figure 2). These factors were conducive to maintaining the natural landscape and ecological vitality (Lu et al., 2020), and thus, the ecological risk in the region was generally low. The spatial autocorrelation analysis results of ecological risk also showed the same distribution characteristics: The Fuchunjiang River was a dividing line to separate the cold and hot spot areas. The northern area of the Fuchunjiang River was dominated by hot spots and sub-hot spots, while the southern bank of the river was dominated by cold spots and sub-cold spots (Figure 8). This suggested that the distribution of regional geographical elements would affect the spatial heterogeneity of ecological risks (Lin et al., 2019); for example, the Fuchunjiang River as a natural geographical barrier objectively limited the spread of ecological risks from the north to the south bank. In conclusion, the spatial heterogeneity characteristics of landscape ecological risk in the Fuchunjiang River Basin were also corroborated by many previous studies on the ecological environment assessment in the Hangzhou area (Li et al., 2021; Zhang et al., 2023). It is the spatial heterogeneity of landscape ecological risk in the study area that requires decision makers to develop targeted management strategies for different blocks (Lu et al., 2020) to reduce risks in the area or prevent new risks from arising.

4.2. Temporal evolution of landscape ecological risk

From 1990 to 2020, the evolution of ecological risk in the Fuchunjiang River Basin over time showed a trend of “changes dramatically in short time scales and declines in long time scales” at both the basin and township scales. At the basin level, with the reduction in medium, sub-high and high risk areas (from 52.33

to 28.14%, Figure 5), the overall landscape ecological risk of the Fuchunjiang River Basin showed a downward trend during the study period, with an overall decrease of 7.75%. By stage, the magnitude of the decrease in the overall ecological risk became progressively smaller in the three time intervals, especially between 2010 and 2020, in which it remained almost constant (only 0.83%). This time-scale feature was consistent with the study of Guo et al. (2022). Combined with studies of Zhou et al. (2022) and Fu et al. (2022) on environmental optimization and policy protection in the Hangzhou area, it can be seen that this phenomenon was mainly attributed to the fact that after 2000, under the interaction of the urbanization process and ecological protection policies in Hangzhou, the disturbance and restoration of the ecosystems tended to balance and gradually reached a stable state (Ma et al., 2019). From the township perspective, the landscape ecological risk maintained a decreasing trend generally during the study period. There were 17 townships with declining ecological risk levels, accounting for 37.88% of the total area of the study area, while there were only 2 townships whose ecological risk levels increased, accounting for 1.46% of the total area of the study area (Figure 6). On this basis, further analysis of the change rate in landscape ecological risk in each township during the three time periods (Figure 7) revealed that more than 40% of the townships had increasing ecological risk in two time periods from 2000 to 2010 and 2010 to 2020, with a maximum growth rate of 15.05%. This result was in agreement with the study of Shen et al. (2023) on the plateau scale. It is likely that the averaging effect at long-time scales (DeFries et al., 2010) made changes in landscape ecological risk at short-time scales appear relatively drastic. Overall, there was a decreasing trend in landscape ecological risk at both the basin and township levels over long time scales. This finding was inextricably linked to the “three rivers and two banks” ecological landscape protection and construction project implemented by the Hangzhou Government (Wang, 2014): Since 2010, the Hangzhou Government has invested approximately US\$445 million in this project, completing 58 km² of forest-nurturing projects and 204 km of forest ecological landscape green belts, as well as a series of water pollution remediation and greenway construction projects, which have contributed significantly to the environmental improvement of the Fuchunjiang River Basin. However, studies on ecological risk in areas of plateau and opencast coal mine have shown a rising trend in landscape ecological risk with economic development (Xu et al., 2021; Li et al., 2022), differing significantly from the results of this study, which might be more related to economic inputs. The improvement of ecological risks requires significant government investment. Thus, in the process of ecological risk control, many regions face a trade-off between improving ecological risks and economic investment.

4.3. Dominant influencing factors of landscape ecological risk

Among the static impact factors, socioeconomic factors were considered the dominant influencing factors on the landscape ecological risk in the Fuchunjiang River Basin (Figure 9A), especially the human interference and GDP factors, with strong explanatory power. This result has been corroborated by a large

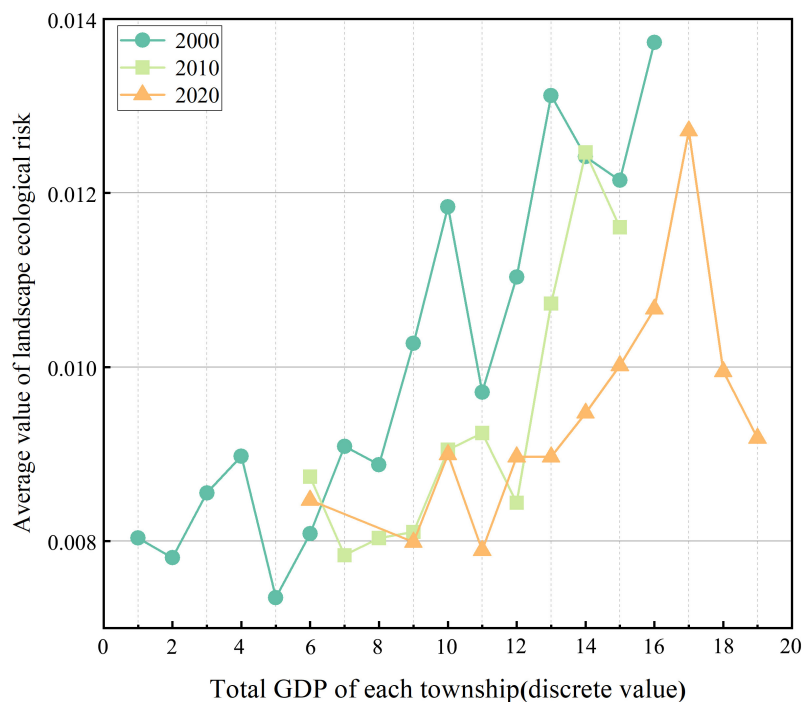


FIGURE 10

Coupling relationship between the average value of landscape ecological risk and the GDP of townships.

number of studies (Ai et al., 2022; Karimian et al., 2022; Shi et al., 2022). However, this study found that natural factors such as topography and climate had less influence on ecological risks in the study area and exhibited a decreasing trend, which was quite different from the results of some studies for particular topographic areas (Hou et al., 2020; Wang et al., 2021). A primary reason was that in rapidly urbanizing areas, the active socioeconomic factors had a greater impact on landscape ecological risk than natural factors. It can be seen that the dominant driving factors of landscape ecological risk could change significantly with changes in the study area's location, social environment, and other factors. Among the dynamic impact factors, the influence of land use transfer factors was generally greater than that of other factors (Figure 9B). The transfer intensity of arable land and urban and rural residential land, as areas with frequent human activities, had the greatest impact on landscape ecological risk, which further confirmed the findings of Zhang S. et al. (2022) and Li W. et al. (2020). Accurate identification of the dominant influencing factors of landscape ecological risk was the basis for carrying out targeted risk management, making it possible to prevent and control ecological risks.

To explore the association between economic development and ecological risk, the representative socioeconomic factor GDP was selected for coupling analysis with landscape ecological risk (Figure 10). The average value of landscape ecological risk in 2000 and 2010 fluctuated upward with the increase in the GDP of townships, indicating that the ecological environment was damaged to a deeper extent with socioeconomic development. The average value of landscape ecological risk in 2020 showed an inverted U-shaped relationship with the GDP of townships. The landscape ecological risk gradually increased with the increase

of GDP at the beginning; after the discrete value of GDP reached 17 (US\$29.2 million–122.7 million/km²), the increase of GDP led to a decrease of ecological risk, which confirmed that the environmental Kuznets curve (EKC) might have the same applicability in ecological risk management. However, the GDP of townships in 2000 and 2010 had not yet reached the tipping point, so their landscape ecological risks were still in a state of fluctuating increase. The figure shows that the landscape ecological risk corresponding to the same discrete value of GDP decreased as the year increased, and the area enclosed by the inverted “U” curve also decreased, which was similar to the results of empirical studies of the Kuznets curve between environmental pollution and economic development at the micro level (Chen X. et al., 2019; Yu et al., 2022). This could be due to the rapid development of the social economy promoting the change in urban industrial structure, and the unit output of the service and high-tech industries had less impact on the environment (Hamann et al., 2015). At the same time, comparing the study of the “economy-ecology” relationship by Leal and Marques (2022) and Yuan et al. (2022), it can be seen that the early experience of environmental problems management, the development of new technology, and the role of government policy guidance will also make environmental restoration costs lower and time shorter in the context of rapid economic development.

4.4. Potential ways to prevent ecological risks

Many processes and functions of ecosystems are scale dependent, and in this study, landscape ecological risk was also found to be scale-dependent at the spatial level. During the period

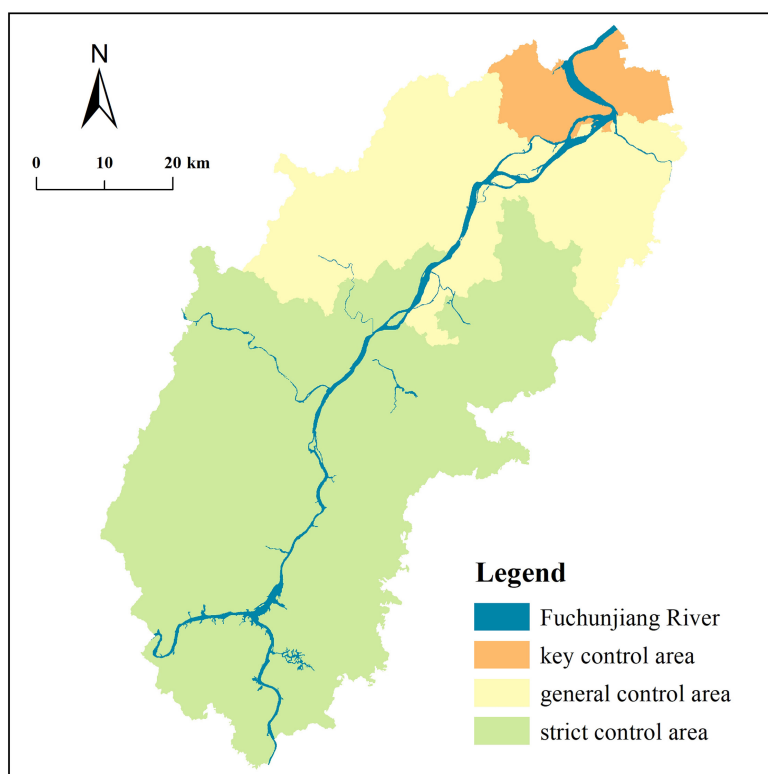


FIGURE 11
Zoning control map of landscape ecological risk in the Fuchunjiang River Basin.

from 2000 to 2020, some townships experienced a significant increase in landscape ecological risk (Figure 7), but the overall ecological risk of the basin remained on a downward trend (Figure 4). This means that the increase in ecological risk in local small-scale areas did not definitely lead to the reduction in overall large-scale regional ecological safety. Similar results have been verified in studies on ecosystem services. Ecosystem services for which trade-offs exist at small scales behave synergistically on larger spatial scales (Yang et al., 2015).

In this context, while designating the overall management and control scheme of the basin, it is also indispensable to implement differentiated ecological risk management according to the main functions of different agglomerations. Therefore, to scientifically maintain the ecological security in the suburban areas of Hangzhou city, the Fuchunjiang River Basin was divided into key control area, strict control area, and general control area of landscape ecological risk (Figure 11) based on the findings of this study. The following control strategies are proposed according to the divided blocks:

4.4.1. Key control area

This area mainly contains sub-high and high ecological risk areas, which is in the downstream areas of the Fuchunjiang River Basin with a dense economy and population and undertakes a crucial regional development function. If conventional control methods such as strict land use restrictions are still used to reduce regional ecological risks (Liang et al., 2022), it will inevitably reduce the living space for human beings. Therefore, compared to the studies of Ran et al. (2022) and Lu et al. (2020), such regions

should adopt economic tools such as promoting benign iterations of industrial structure and increasing ecological compensation investment for ecological restoration, while land control should still be aimed at ensuring the living space necessary for the growing population, optimizing the land use structure, increasing infrastructure development, and significantly improving human welfare.

4.4.2. Strict control area

This area is mainly located in the southeastern part of the study area and contains sub-low and low ecological risk areas, with an excellent natural substrate and low human disturbance. Wang et al. (2021) pointed out that such areas were key areas for controlling ecological security and stability. Therefore, such regions need managers to change the development mindset, incorporate risk prevention and control into regional development planning, and play a vital role in safeguarding the overall stability of landscape ecological risk in the Fuchunjiang River Basin by reasonably delineating ecological protection red lines, strictly limiting human activities in ecological conservation areas (Melnykovich et al., 2018), and regulating regional development and construction (Karimian et al., 2022).

4.4.3. General control area

This area mainly contains the medium ecological risk areas in the middle reaches of the basin, which is strongly radiated by Hangzhou's economy and has frequent risk transitions (Cui et al., 2018). Appropriate policy guidance and financial support

(Zhang et al., 2020) can be provided to strengthen the optimization and integration of construction land, restore the damaged ecological environment, improve ecosystem stability, and avoid the transformation from medium risk to high risk.

4.5. Limitations and future prospects

The spatial and temporal evolutionary characteristics and the dominant influencing factors of landscape ecological risk in the Fuchunjiang River Basin on long time scales were explored in this study. The results can not only be an inspiration for ecological assessment and policy-making in other regions that are experiencing rapid urbanization in the world, but also provide a model case for exploring the quantitative relationship between economic development and ecological conservation in regions that are in the late-stage of development. However, limited by the methodology and data availability, this study still had some limitations.

First, due to the difficulty of obtaining the early data of impact factors, only data after 2000 were included for analysis, and the correspondence between the year of data and the year of study needs to be further improved.

Second, the scale of this study is relatively singular. At the temporal level, only 4 years were selected for analysis, with a long time span; at the spatial level, the township was considered as the smallest assessment unit, and no multi-scale spatial validation was performed. It cannot be assumed that the results would remain stable after cross-scale deduction. Therefore, follow-up should continue to strengthen comprehensive multi-scale research to enhance the scientific validity of the results (Li W. et al., 2020).

Third, there is less research on EKC based on ecological risk. This article only makes a preliminary exploration of EKC between landscape ecological risk and GDP, and further theoretical or practical verification should be strengthened in the future to explore the applicability of EKC in the field of ecological risk.

Fourth, a detailed analysis of landscape ecological risk for the period from 1990 to 2020 was explored in this study. However, to better apply the assessment results to decision-making and local management, land use simulations can also be conducted by combining FLUS, PLUS, and CLUE-S models to carry out landscape ecological risk prediction studies in the future (Gao et al., 2022).

Fifth, although landscape ecological risk assessment methods based on landscape patterns have been widely used, their evaluation endpoints are still unclear (Gong et al., 2021), creating a challenge for implementing the assessment results at the specific decision-making level. Therefore, using an analytical approach that overlays ecosystem service with landscape ecological risk, introducing ecosystem services as an evaluation endpoint into ecological risk assessment will be the focus of subsequent research (Munns et al., 2016), which can provide effective interactive spatial information for adaptive landscape management, thus providing a more solid theoretical and methodological basis for improving human wellbeing.

5. Conclusion

Based on the land use data of the Fuchunjiang River Basin for four periods from 1990 to 2020, a study on the spatiotemporal

variation pattern of landscape ecological risk and its influencing factors of the basin in the suburban area of large cities was carried out, with the following conclusions:

- (1) During the study period, the area of various land use types changed considerably and the landscape pattern showed a general trend of increasing agglomeration degree and decreasing loss index.
- (2) The landscape ecological risk in the Fuchunjiang River Basin showed a spatial pattern of “high in the northwest and low in the southeast,” with high and low values clustering on the north and south sides of the Fuchunjiang River, respectively. During the study period, the overall landscape ecological risk of the basin declined continuously, but the magnitude of the decrease became smaller in three time intervals; the ecological risk level of townships mainly shifted from high-risk to low-risk levels, but more than 40% of townships were of increased risk during 2000–2020. It can be seen that rapid economic development has contributed to the reduction of landscape ecological risk in the basin, and the ecological environment has been restored with economic inputs to some extent. Thus, in the process of ecological risk control, many regions face a trade-off between improving ecological risks and economic investment.
- (3) Among all the influencing factors, socioeconomic and land use transfer category factors had the strongest explanatory power on landscape ecological risk and its changes. GDP, human interference, area of urban and rural residential land, area of arable land transferred in, and area of arable land transferred out were the dominant influencing factors. Accurate identification of the dominant influencing factors of landscape ecological risk is the basis for carrying out targeted risk management, making it possible to prevent and control ecological risks.
- (4) Coupling landscape ecological risk with GDP, it can be found that the relationship between landscape ecological risk and GDP in 2020 presented as an inverted U-shaped curve. The landscape ecological risk gradually increased with the increase in GDP at the beginning, and after reaching a tipping point, increases in GDP led to decreases in ecological risk. This result suggests that the EKC might have the same applicability in ecological risk management. Therefore, it is theoretically possible to manage ecological risks within the safety boundary through appropriate management policies.
- (5) According to the main functions of different ecological risk gathering areas, the Fuchunjiang River Basin was divided into key control area, strict control area and general control area, and targeted risk control strategies were proposed in each area. This can be connected with the subsequent territorial spatial planning and help to clarify the development direction and the core focus of ecological management in the Fuchunjiang River Basin in the future.

Data availability statement

The raw data supporting the conclusions of this article will be made available by the authors, without undue reservation.

Author contributions

XC and YZ contributed to the conceptualization, methodology, and writing—original draft. GY and WN processed and analyzed the data. YW and JW conducted the investigation and preliminary analysis. BX edited and revised the manuscript, and provided project management support. All authors contributed to manuscript revision, read, and approved the submitted version.

Funding

This research was financially supported by the Zhejiang Province Key Research and Development Project under Grant No. 2019C02023.

References

- Ai, J., Yu, K., Zeng, Z., Yang, L., Liu, Y., and Liu, J. (2022). Assessing the dynamic landscape ecological risk and its driving forces in an island city based on optimal spatial scales: Haitan Island, China. *Ecol. Indic.* 137:108771. doi: 10.1016/j.ecolind.2022.108771
- Baffoe, G., and Matsuda, H. (2018). A perception based estimation of the ecological impacts of livelihood activities: The case of rural Ghana. *Ecol. Indic.* 93, 424–433. doi: 10.1016/j.ecolind.2018.04.074
- Bai, Y., Jiang, B., Alatalo, J. M., Zhuang, C., Wang, X., Cui, L., et al. (2016). Impacts of land management on ecosystem service delivery in the Baiyangdian river basin. *Environ. Earth Sci.* 75:258. doi: 10.1007/s12665-015-4831-7
- Bamrungkhul, S., and Tanaka, T. (2022). The assessment of land suitability for urban development in the anticipated rapid urbanization area from the Belt and Road Initiative: A case study of Nong Khai City, Thailand. *Sustain. Cities Soc.* 83:103988. doi: 10.1016/j.scs.2022.103988
- Barnhouse, L. W., Suter II, G. W., Rosen, A. E., and Beauchamp, J. J. (1987). Estimating responses of fish populations to toxic contaminants. *Environ. Toxicol. Chem.* 6, 811–824. doi: 10.1002/etc.5620061010
- Benti, S., Terefe, H., and Callo-Concha, D. (2022). Implications of overlooked drivers in Ethiopia's urbanization: Curbing the curse of spontaneous urban development for future emerging towns. *Heliyon* 8:e10997. doi: 10.1016/j.heliyon.2022.e10997
- Bhattachan, A., Emanuel, R. E., Ardón, M., Bernhardt, E. S., Anderson, S. M., Stillwagon, M. G., et al. (2018). Evaluating the effects of land-use change and future climate change on vulnerability of coastal landscapes to saltwater intrusion. *Elementa* 6:62. doi: 10.1525/elementa.316
- Bryan, B. A., Gao, L., Ye, Y., Sun, X., Connor, J. D., Crossman, N. D., et al. (2018). China's response to a national land-system sustainability emergency. *Nature* 559, 193–204. doi: 10.1038/s41586-018-0280-2
- Chen, C., Park, T., Wang, X., Piao, S., Xu, B., Chaturvedi, R. K., et al. (2019). China and India lead in greening of the world through land-use management. *Nat. Sustain.* 2, 122–129. doi: 10.1038/s41893-019-0220-7
- Chen, X., Huang, B., and Lin, C. T. (2019). Environmental awareness and environmental Kuznets curve. *Econ. Model.* 77, 2–11. doi: 10.1016/j.econmod.2019.02.003
- Cui, B., Zhang, Y., Wang, Z., Gu, C., Liu, L., Wei, B., et al. (2022). Ecological risk assessment of transboundary region based on land-cover change: A case study of Gandaki River Basin, Himalayas. *Land* 11:638. doi: 10.3390/land11050638
- Cui, H., Wagg, C., Wang, X., Liu, Z., Liu, K., Chen, S., et al. (2022). The loss of above- and belowground biodiversity in degraded grasslands drives the decline of ecosystem multifunctionality. *Appl. Soil Ecol.* 172:104370. doi: 10.1016/j.apsoil.2021.104370
- Cui, L., Zhao, Y., Liu, J., Han, L., Ao, Y., and Yin, S. (2018). Landscape ecological risk assessment in Qinling Mountain. *Geol. J.* 53, 342–351. doi: 10.1002/gj.3115
- DeFries, R., Rovero, F., Wright, P., Ahumada, J., Andelman, S., Brandon, K., et al. (2010). From plot to landscape scale: Linking tropical biodiversity measurements across spatial scales. *Front. Ecol. Environ.* 8:153–160. doi: 10.1890/080104
- Diggle, G. (1995). Science and judgement in risk assessment. *Occup. Environ. Med.* 52, 784–784. doi: 10.1136/oem.52.11.784-a
- Feng, L., You, Y., Liao, W., Pang, J., Hu, R., and Feng, L. (2022). Multi-scale change monitoring of water environment using cloud computing in optimal resolution remote sensing images. *Energy Rep.* 8, 13610–13620. doi: 10.1016/j.egyr.2022.09.134
- Frazier, A. E., Bryan, B. A., Buyantuev, A., Chen, L., Echeverria, C., Jia, P., et al. (2019). Ecological civilization: Perspectives from landscape ecology and landscape sustainability science. *Landscape Ecol.* 34, 1–8. doi: 10.1007/s10980-019-00772-4
- Fu, L., Ren, Y., Lu, L., and Chen, H. (2022). Relationship between ecosystem services and rural residential well-being in the Xin'an river Basin, China. *Ecol. Indic.* 140:108997. doi: 10.1016/j.ecolind.2022.108997
- Gao, L., Tao, F., Liu, R., Wang, Z., Leng, H., and Zhou, T. (2022). Multi-scenario simulation and ecological risk analysis of land use based on the PLUS model: A case study of Nanjing. *Sustain. Cities Soc.* 85:104055. doi: 10.1016/j.scs.2022.104055
- Gong, J., Cao, E., Xie, Y., Xu, C., Li, H., and Yan, L. (2021). Integrating ecosystem services and landscape ecological risk into adaptive management: Insights from a western mountain-basin area China. *J. Environ. Manag.* 281:111817. doi: 10.1016/j.jenvman.2020.111817
- Guo, H., Cai, Y., Li, B., Tang, Y., Qi, Z., Huang, Y., et al. (2022). An integrated modeling approach for ecological risks assessment under multiple scenarios in Guangzhou, China. *Ecol. Indic.* 142:109270. doi: 10.1016/j.ecolind.2022.109270
- Hamann, M., Biggs, R., and Reyers, B. (2015). Mapping social-ecological systems: Identifying 'green-loop' and 'red-loop' dynamics based on characteristic bundles of ecosystem service use. *Glob. Environ. Change* 34, 218–226. doi: 10.1016/j.gloenvcha.2015.07.008
- Hou, M., Ge, J., Gao, J., Meng, B., Li, Y., Yin, J., et al. (2020). Ecological risk assessment and impact factor analysis of alpine wetland ecosystem based on LUCC and boosted regression tree on the Zoige Plateau, China. *Remote Sens.* 12:368. doi: 10.3390/rs12030368
- Hunsaker, C. T., Graham, R. L., Suter, G. W., O'Neill, R. V., Barnhouse, L. W., and Gardner, R. H. (1990). Assessing ecological risk on a regional scale. *Environ. Manag.* 14, 325–332. doi: 10.1007/BF02394200
- Jiang, S., Meng, J., and Zhu, L. (2020). Spatial and temporal analyses of potential land use conflict under the constraints of water resources in the middle reaches of the Heihe River. *Land Use Policy* 97:104773. doi: 10.1016/j.landusepol.2020.104773
- Jiang, S., Meng, J., Zhu, L., and Cheng, H. (2021). Spatial-temporal pattern of land use conflict in China and its multilevel driving mechanisms. *Sci. Total Environ.* 801:149697. doi: 10.1016/j.scitotenv.2021.149697
- Jin, X., Jin, Y., and Mao, X. (2019). Ecological risk assessment of cities on the Tibetan Plateau based on land use/land cover changes – Case study of Delingha City. *Ecol. Indic.* 101, 185–191. doi: 10.1016/j.ecolind.2018.12.050
- Karimian, H., Zou, W., Chen, Y., Xia, J., and Wang, Z. (2022). Landscape ecological risk assessment and driving factor analysis in Dongjiang river watershed. *Chemosphere* 307:135835. doi: 10.1016/j.chemosphere.2022.135835
- Kong, Y., He, W., Yuan, L., Zhang, Z., Gao, X., Zhao, Y., et al. (2021). Decoupling economic growth from water consumption in the Yangtze River Economic Belt, China. *Ecol. Indic.* 123:107344. doi: 10.1016/j.ecolind.2021.107344
- Lal, P., Shekhar, A., and Kumar, A. (2021). Quantifying temperature and precipitation change caused by land cover change: A case study of India using the WRF model. *Front. Environ. Sci.* 9:766328. doi: 10.3389/fevns.2021.766328
- Landis, W. G. (2003). Twenty years before and hence: Ecological risk assessment at multiple scales with multiple stressors and multiple endpoints. *Hum. Ecol. Risk Assess.* 9, 1317–1326. doi: 10.1080/10807030390248500
- Leal, P. H., and Marques, A. C. (2022). The evolution of the environmental Kuznets curve hypothesis assessment: A literature review under a

critical analysis perspective. *Heliyon* 8:e11521. doi: 10.1016/j.heliyon.2022.e11521

Levine, S. L., Giddings, J., Valenti, T., Cobb, G. P., Carley, D. S., and McConnell, L. L. (2019). Overcoming challenges of incorporating higher tier data in ecological risk assessments and risk management of pesticides in the United States: Findings and recommendations from the 2017 workshop on regulation and innovation in agriculture. *Integr. Environ. Assess. Manag.* 15, 714–725. doi: 10.1002/ieam.4173

Li, C., Zhang, J., Philbin, S. P., Yang, X., Dong, Z., Hong, J., et al. (2022). Evaluating the impact of highway construction projects on landscape ecological risks in high altitude plateaus. *Sci. Rep.* 12:5170. doi: 10.1038/s41598-022-08788-8

Li, W., Wang, Y., Xie, S., Sun, R., and Cheng, X. (2020). Impacts of landscape multifunctionality change on landscape ecological risk in a megacity, China: A case study of Beijing. *Ecol. Indic.* 117:106681. doi: 10.1016/j.ecolind.2020.106681

Li, Z., Jiang, W., Wang, W., Chen, Z., Ling, Z., and Lv, J. (2020). Ecological risk assessment of the wetlands in Beijing-Tianjin-Hebei urban agglomeration. *Ecol. Indic.* 117:106677. doi: 10.1016/j.ecolind.2020.106677

Li, X., Guo, J., and Qi, S. (2021). Forestland landscape change induced spatiotemporal dynamics of subtropical urban forest ecosystem services value in forested region of China: A case of Hangzhou city. *Environ. Res.* 193:110618. doi: 10.1016/j.envres.2020.110618

Liang, T., Yang, F., Huang, D., Luo, Y., Wu, Y., and Wen, C. (2022). Land-use transformation and landscape ecological risk assessment in the three gorges reservoir region based on the “production–living–ecological space” perspective. *Land* 11:1234. doi: 10.3390/land11081234

Lin, Y., Hu, X., Zheng, X., Hou, X., Zhang, Z., Zhou, X., et al. (2019). Spatial variations in the relationships between road network and landscape ecological risks in the highest forest coverage region of China. *Ecol. Indic.* 96, 392–403. doi: 10.1016/j.ecolind.2018.09.016

Lin, Z., Peng, S., Pu, S., Ma, X., and Zhou, Y. (2020). Landscape ecological risk assessment of Dianchi Lake basin based on land use change. *IOP Conf. Ser.* 730:012033. doi: 10.1088/1757-899x/730/1/012033

Liu, J., Jiao, L., Dong, T., Xu, G., Zhang, B., and Yang, L. (2018). A novel measure approach of expansion process of urban landscape: Multi-order adjacency index. *Sci. Geogr. Sin.* 38, 1741–1749. doi: 10.13249/j.cnki.sgs.2018.11.001

Lu, S., Tang, X., Guan, X., Qin, F., Liu, X., and Zhang, D. (2020). The assessment of forest ecological security and its determining indicators: A case study of the Yangtze River Economic Belt in China. *J. Environ. Manag.* 258:110048. doi: 10.1016/j.jenvman.2019.110048

Ma, L., Bo, J., Li, X., Fang, F., and Cheng, W. (2019). Identifying key landscape pattern indices influencing the ecological security of inland river basin: The middle and lower reaches of Shule River Basin as an example. *Sci. Total Environ.* 674, 424–438. doi: 10.1016/j.scitotenv.2019.04.107

Melnykovich, M., Nijnik, M., Soloviy, I., Nijnik, A., Sarkki, S., and Bihun, Y. (2018). Social-ecological innovation in forest mountain areas: Adaptive responses of forest-dependent communities to the challenges of a changing world. *Sci. Total Environ.* 613–614, 894–906. doi: 10.1016/j.scitotenv.2017.07.065

Mo, W., Wang, Y., Zhang, Y., and Zhuang, D. (2017). Impacts of road network expansion on landscape ecological risk in a megacity, China: A case study of Beijing. *Sci. Total Environ.* 574, 1000–1011. doi: 10.1016/j.scitotenv.2016.09.048

Munns, W. R., Rea, A. W., Suter, I. J., G. W., Martin, L., Blake-Hedges, L., Crk, T., et al. (2016). Ecosystem services as assessment endpoints for ecological risk assessment. *Integr. Environ. Assess. Manag.* 12, 522–528. doi: 10.1002/ieam.1707

Nepal, P., Khanal, N. R., Zhang, Y., Paudel, B., and Liu, L. (2020). Land use policies in Nepal: An overview. *Land Degrad. Dev.* 31, 2203–2212. doi: 10.1002/ldr.3621

Pătru-Stupariu, I., and Nita, A. (2022). Impacts of the European landscape convention on interdisciplinary and transdisciplinary research. *Landsc. Ecol.* 37, 1211–1225. doi: 10.1007/s10980-021-01390-9

Peng, J., Dang, W., Liu, Y., Zong, M., and Hu, X. (2015). Review on landscape ecological risk assessment. *Acta Geogr. Sin.* 70, 664–677. doi: 10.11821/DLXB201504013

Raitano, G., Goi, D., Pieri, V., Passoni, A., Mattiussi, M., Lutman, A., et al. (2018). (Eco)toxicological maps: A new risk assessment method integrating traditional and in silico tools and its application in the Ledra River (Italy). *Environ. Int.* 119, 275–286. doi: 10.1016/j.envint.2018.06.035

Ran, P., Hu, S., Frazier, A. E., Qu, S., Yu, D., and Tong, L. (2022). Exploring changes in landscape ecological risk in the Yangtze River Economic Belt from a spatiotemporal perspective. *Ecol. Indic.* 137:108744. doi: 10.1016/j.ecolind.2022.108744

Riggs, R. A., Achdiawan, R., Adiwinata, A., Boedhihartono, A. K., Kastanya, A., Langston, J. D., et al. (2021). Governing the landscape: Potential and challenges of integrated approaches to landscape sustainability in Indonesia. *Landsc. Ecol.* 36, 2409–2426. doi: 10.1007/s10980-021-01255-1

Shen, W., Zhang, J., Wang, K., and Zhang, Z. (2023). Identifying the spatio-temporal dynamics of regional ecological risk based on Google Earth Engine: A case study from Loess Plateau, China. *Sci. Total Environ.* 873:162346. doi: 10.1016/j.scitotenv.2023.162346

Shi, Y., Feng, C. C., Yu, Q., Han, R., and Guo, L. (2022). Contradiction or coordination? The spatiotemporal relationship between landscape ecological risks and urbanization from coupling perspectives in China. *J. Clean. Prod.* 363:132557. doi: 10.1016/j.jclepro.2022.132557

Tokarczyk-Dorociak, K., Kazak, J., and Szwedrański, S. (2018). The impact of a large city on land use in suburban area – the case of Wrocław (Poland). *J. Ecol. Eng.* 19, 89–98. doi: 10.12911/22998993/81783

Wang, B., Ding, M., Li, S., Liu, L., and Ai, J. (2020). Assessment of landscape ecological risk for a cross-border basin: A case study of the Koshi River Basin, central Himalayas. *Ecol. Indic.* 117:106621. doi: 10.1016/j.ecolind.2020.106621

Wang, F., Ye, C., Hua, J., and Li, X. (2019). Coupling relationship between urban spatial expansion and landscape ecological risk in Nanchang City. *Acta Ecol. Sin.* 39, 1248–1262. doi: 10.5846/stxb201811082426

Wang, H., Liu, X., Zhao, C., Chang, Y., Liu, Y., and Zang, F. (2021). Spatial-temporal pattern analysis of landscape ecological risk assessment based on land use/land cover change in baishuijiang national nature reserve in Gansu Province, China. *Ecol. Indic.* 124:107454. doi: 10.1016/j.ecolind.2021.107454

Wang, J., and Xu, C. (2017). Geodetector: Principle and prospective. *Acta Geogr. Sin.* 72, 116–134.

Wang, X. (2014). *Promote the resonance of ecological economy and ecological environment at the same frequency*. Hangzhou: Zhejiang Today.

Wu, J. (2022). A new frontier for landscape ecology and sustainability: Introducing the world's first atlas of urban agglomerations. *Landsc. Ecol.* 37, 1721–1728. doi: 10.1007/s10980-022-01475-z

Xie, H., He, Y., Choi, Y., Chen, Q., and Cheng, H. (2020). Warning of negative effects of land-use changes on ecological security based on GIS. *Sci. Total Environ.* 704:135427. doi: 10.1016/j.scitotenv.2019.135427

Xie, H., Wen, J., Chen, Q., and Wu, Q. (2021). Evaluating the landscape ecological risk based on GIS: A case-study in the Poyang Lake region of China. *Land Degrad. Dev.* 32, 2762–2774. doi: 10.1002/ldr.3951

Xu, W., Wang, J., Zhang, M., and Li, S. (2021). Construction of landscape ecological network based on landscape ecological risk assessment in a large-scale opencast coal mine area. *J. Clean. Prod.* 286:11. doi: 10.1016/j.jclepro.2020.125523

Xue, L., Zhu, B., Wu, Y., Wei, G., Liao, S., Yang, C., et al. (2019). Dynamic projection of ecological risk in the Manas River basin based on terrain gradients. *Sci. Total Environ.* 653, 283–293. doi: 10.1016/j.scitotenv.2018.10.382

Yang, G., Ge, Y., Xue, H., Yang, W., Shi, Y., Peng, C., et al. (2015). Using ecosystem service bundles to detect trade-offs and synergies across urban–rural complexes. *Landsc. Urban Plann.* 136, 110–121. doi: 10.1016/j.landurbplan.2014.12.006

Yu, Y., Duan, C., Li, S., Peng, C., Yang, J., Yan, K., et al. (2022). Relationship between environmental pollution and economic development in late-developing regions shows an inverted V. *Sci. Total Environ.* 838:156295. doi: 10.1016/j.scitotenv.2022.156295

Yuan, L., Li, R., He, W., Wu, X., Kong, Y., Degefu, D. M., et al. (2022). Coordination of the industrial-ecological economy in the Yangtze River Economic Belt, China. *Front. Environ. Sci.* 10:882221. doi: 10.3389/fenvs.2022.882221

Yuan, L., Yang, D., Wu, X., He, W., Kong, Y., Ramsey, T. S., et al. (2023). Development of multidimensional water poverty in the Yangtze River Economic Belt, China. *J. Environ. Manag.* 325:116608. doi: 10.1016/j.jenvman.2022.116608

Zhang, D., Jing, P., Sun, P., Ren, H., and Ai, Z. (2022). The non-significant correlation between landscape ecological risk and ecosystem services in Xi'an Metropolitan Area, China. *Ecol. Ind.* 141:109118. doi: 10.1016/j.ecolind.2022.109118

Zhang, S., Zhong, Q., Cheng, D., Xu, C., Chang, Y., Lin, Y., et al. (2022). Landscape ecological risk projection based on the PLUS model under the localized shared socioeconomic pathways in the Fujian Delta region. *Ecol. Indic.* 136:108642. doi: 10.1016/j.ecolind.2022.108642

Zhang, X., Yao, L., Luo, J., and Liang, W. (2022). Exploring changes in land use and landscape ecological risk in key regions of the Belt and Road Initiative Countries. *Land* 11:940. doi: 10.3390/land11060940

Zhang, H., Liu, Y., Li, X., Feng, R., Gong, Y., Jiang, Y., et al. (2023). Combining remote sensing information entropy and machine learning for ecological environment assessment of Hefei-Nanjing-Hangzhou region, China. *J. Environ. Manag.* 325:116533. doi: 10.1016/j.jenvman.2022.116533

Zhang, W., Chang, W. J., Zhu, Z. C., and Hui, Z. (2020). Landscape ecological risk assessment of Chinese coastal cities based on land use change. *Appl. Geogr.* 117:102174. doi: 10.1016/j.apgeog.2020.102174

Zhao, X., Wang, W., and Wan, W. (2018). Regional differences in the health status of Chinese residents: 2003–2013. *J. Geogr. Sci.* 28, 741–758. doi: 10.1007/s11442-018-1502-0

Zhou, K. (2022). Study on wetland landscape pattern evolution in the Dongping Lake. *Appl. Water Sci.* 12:200. doi: 10.1007/s13201-022-01721-4

Zhou, Y., Wu, T., and Wang, Y. (2022). Urban expansion simulation and development-oriented zoning of rapidly urbanising areas: A case study of Hangzhou. *Sci. Total Environ.* 807:150813. doi: 10.1016/j.scitotenv.2021.150813



OPEN ACCESS

EDITED BY

Cletah Shoko,
University of the Witwatersrand, South
Africa

REVIEWED BY

Andrea Augusto Sfriso,
University of Ferrara, Italy
Muhsan Ehsan,
Bahria University, Pakistan

*CORRESPONDENCE

Sheng Ye

✉ yscxz@outlook.com

Desheng Pei

✉ peids@cqmu.edu.cn

RECEIVED 08 April 2023

ACCEPTED 05 June 2023

PUBLISHED 15 June 2023

CITATION

Ye S and Pei D (2023) Relationships
between microplastic pollution and land
use in the Chongqing section of the
Yangtze River.

Front. Ecol. Evol. 11:1202562.

doi: 10.3389/fevo.2023.1202562

COPYRIGHT

© 2023 Ye and Pei. This is an open-access
article distributed under the terms of the
[Creative Commons Attribution License](#)
(CC BY). The use, distribution or
reproduction in other forums is permitted,
provided the original author(s) and the
copyright owner(s) are credited and that
the original publication in this journal is
cited, in accordance with accepted
academic practice. No use, distribution or
reproduction is permitted which does not
comply with these terms.

Relationships between microplastic pollution and land use in the Chongqing section of the Yangtze River

Sheng Ye^{1,2,3,4*} and Desheng Pei^{5*}

¹Chongqing University, Chongqing, China, ²Chongqing Institute of Green and Intelligent Technology, Chinese Academy of Sciences, Chongqing School, University of Chinese Academy of Sciences, Chongqing, China, ³Chongqing Geomatics and Remote Sensing Center, Chongqing, China, ⁴Key Laboratory of Monitoring, Evaluation and Early Warning of Territorial Spatial Planning Implementation, Ministry of Natural Resources, Chongqing, China, ⁵School of Public Health, Chongqing Medical University, Chongqing, China

Microplastic (MP) pollution is an emerging environmental issue. While it is evident that human activities are the primary source of MP pollution, the relationship between land use and MP pollution in rivers requires further study. Using data from 26 MP monitoring sites in the Chongqing section of the Yangtze River, we analyzed MP data along with land use and construction data. We improved the model for the Land Use Intensity Composite Index (LUI) to obtain correlations between land use and MP pollution. We found: 1) The concentration of microplastics in surface water (MPsw) in the Chongqing section of the Yangtze River gradually declined from upstream (central urban section of Chongqing) to downstream (northeastern section of Chongqing). 2) From 2016 to 2020, MPsw in the Chongqing section of the Yangtze River decreased by about 7.5-fold. 3) MPsw in the Chongqing section of the Yangtze River was positively correlated with the amount of surrounding urban and garden land. When the buffer radius was 1 km, the correlation coefficient was 0.53 ($p < 0.05$). With increasing buffer radius, the correlation between land use and gradually weakened. 4) The LUI was also strongly correlated with MPsw. The correlation was strongest when the buffer radius was 1 km, with a correlation coefficient of 0.59 ($p < 0.05$). At all buffer scales, microplastics in sediments (MPss) was positively correlated with village land and arable land. Unlike MPsw, as the buffer radius increased, the strength of the correlations between land use types and MPss gradually increased. The LUI was strongly correlated with MPsw. As the buffer radius increases, the correlation between the two gradually weakens. These results provide information useful for remediation and reduction of MP in river systems.

KEYWORDS

microplastics, land use, correlation analysis, redundancy analysis, buffer scale

Highlights

- Microplastics are declining in the Chongqing section of the Yangtze River.
- There are spatial differences in microplastics in the Chongqing section of the Yangtze River.
- The correlation between land use and microplastics is affected by buffer scale.
- Microplastics were positively correlated with urban and garden areas.

1 Introduction

Water resources cover about 71% of the surface of the earth and are the main source of water for human life, agriculture, and development (Bhuvanesh et al., 2022). Due to anthropogenic influences, surface water resources have become polluted, posing a threat to human health and aquatic ecosystems (Anas et al., 2019). Thus, surface water pollution is one of the main global crises faced by humans. In addition to sulfur dioxide, nitrogen oxides, fine particles, chemical oxygen demand, ammonia nitrogen, and other conventional pollutants, new pollutants such as microplastics have recently been found in surface water resources (Mao R. et al., 2020; Issaka et al., 2023). Microplastics (MP) are a new type of persistent organic pollutant with a particle size of <5 mm (Agarwal, 2020; Lozano and Rillig, 2020; Rillig and Lehmann, 2020). MP are becoming an increasing focus of research in environmental science and ecology because of their differences in degradation and complex interactions with environmental media and other pollutants, which can directly or indirectly affect aquatic and terrestrial communities (Bank and Hansson, 2019; Baho et al., 2021; Hoellein and Rochman, 2021). Microplastics are globally distributed, and have been documented in the Arctic, Antarctic, Mariana Trench, Mount Everest, Rhine River, Yangtze River, Seine River, Columbia River, the Great Lakes of the United States, Qinghai Tibet Plateau lakes, Qinghai Lake, and many other areas (Browne et al., 2011; Auta et al., 2017; Ajith et al., 2020; Yuan et al., 2022). Most research on MP globally has focused on marine environments (Bakir et al., 2020; Fang et al., 2021; Liu M. et al., 2021), with research on MP in freshwater environments being relatively scarce. In fact, the concentration of microplastics in some inland rivers is much higher than that in the ocean (Luo et al., 2018). Compared to the marine environment, the inland freshwater environment is more closely linked to human activities. Existing research on MP in freshwater environments has mainly focused on regions such as the middle and lower reaches of the Yangtze River (Li et al., 2020), and the Pearl River in China (Yan et al., 2019), while there has been relatively little research on river MP in more remote areas such as the upper reaches of the Yangtze River.

Land is a bridge between humans and natural ecosystems, and changes in land use can affect ecosystems such as the aquatic

environment, leading to changes in the structure and function of these ecosystems (Luan and Liu, 2022; Katusiime et al., 2023). Human activities are the main source of MP production and therefore, land use changes will inevitably have an impact on MP pollution (Chen et al., 2021; Wei et al., 2022). Recent studies have begun to analyze the relationship between land use and MP (Klein et al., 2015; Barrows et al., 2018). For example, Zhang et al. (2022) studied the effects of land use on the distribution of soil MP in the Qinghai-Tibet Plateau. Hao et al. (2022) studied the effects of land use on the abundance of MP in the Loess Plateau. Guo et al. (2020) and Bläsing and Amelung (2018) conducted studies on the origins of MP in soil. Research on factors influencing MP pollution currently focuses on aspects such as the impact of land use methods on soil MP; there have been relatively few preliminary studies of factors influencing river MP. For example, Fan et al. (2022) and others have conducted preliminary analysis and research on the factors influencing MP in surface water of the Xishui River Basin. Research on the relationship between river MP and land use is also limited. In particular, research on the relationship between land use intensity and river MP has not yet been conducted. Here we present research on the relationship between land use and MP in the aquatic environment at multiple scales. The results of this research can inform policy recommendations and future research prospects for better prevention and remediation of MP pollution in river systems.

1.1 Study area

The Yangtze River is the third longest river in the world, with a total length of 6,300 km. Previous studies have suggested that the Yangtze River is the largest source of MP to the ocean (Lebreton et al., 2017; Mai et al., 2020), but controversy remains (Meijer et al., 2021). The Chongqing section of the Yangtze River flows through mountainous and hilly areas at the southern border of the Sichuan Basin and the Eqian Mountains. The Chongqing section of the Yangtze River runs from Yangshi Town in Jiangjin District to Peishi Township in Wushan County, with a total length of about 691 km. The Yangtze River traverses the territory of Chongqing from west to east, and flows through 18 districts and counties, including Jiangjin, Yongchuan, Banan, and Dadukou, with a drainage area of 82,000 km². With a large population and rapid economic development, Chongqing is the economic center of the upper reaches of the Yangtze River, with an urbanization rate of over 70%. These variations in land use provide a suitable area for this study. The scope of the study area is shown in Figure 1.

1.2 Data sources

We used three main types of data for this study: ① MP concentrations in surface water and sediments of the Chongqing section of the Yangtze River collected in 2016 and 2020 were obtained from Wuhan Botanical Garden, Chinese Academy of Sciences (Di, 2019; Yuan et al., 2022); ② current land use data for Chongqing in 2020 were obtained from remote sensing

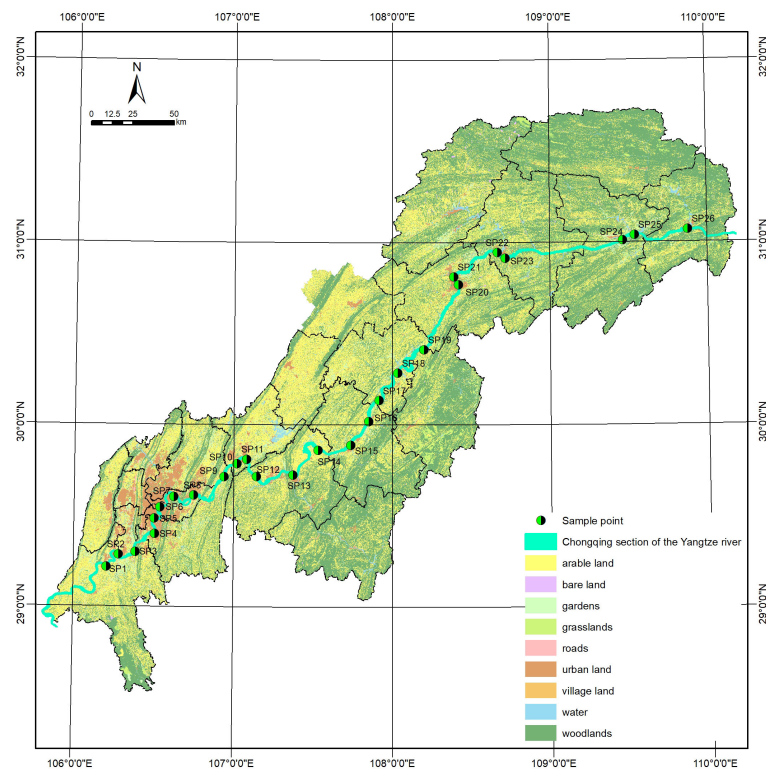


FIGURE 1
Study area map.

interpretation; and ③ building data in 2020 were obtained from a 1:2000 topographic map.

1.3 Methods

1.3.1 Sampling and analysis of river MP samples

Twenty-six sampling sites were selected that were evenly distributed in the Chongqing section of the Yangtze River, including urban, suburban, and rural areas. The coordinates of the sampling points were recorded with a GPS locator. Twenty-five liters of surface water were collected from each sampling point at a sampling depth of 1 m, filtered through a 48- μ m stainless steel sieve, and the residue on the filter was rinsed with deionized water into a 50-mL wide-mouth glass bottle. Samples were fixed in 5% formalin at 4°C prior to laboratory analysis. At the same location, sediment was collected using a grab sampler, placed in a 1-L glass wide-mouth bottle, and stored at 4°C. Replicate sample numbers were established for each sampling point for water and sediment samples. During the sampling process, all sampling tools and solvents were isolated from contact with plastic materials at all times to prevent contamination. All sampling tools were cleaned before each sample collection (Di, 2019). Water samples were treated with 30% H₂O₂ for 12 h to dissolve natural organic matter in the water (Liebezeit and Dubaish, 2012). Each sample was diluted with an appropriate amount of deionized water and then vacuum-filtered. The filter membrane was 0.45- μ m glass fiber filter paper (GF/F, diameter 47 mm, Whatman). The filter paper was placed in a glass Petri dish,

dried in a 50°C oven, and the material on the film was observed with a stereoscopic microscope.

Extraction of MP in sediments was conducted using the two-step density separation method of Nuelle et al. (Nuelle et al., 2014), with a slight modification. First, 500 g of sediment were placed in a 2-L glass beaker, 1 L of saturated NaCl solution was added, the mixture was stirred for 2 min and allowed to settle for 10 min. The supernatant was passed through a 48- μ m stainless steel sieve, the MP on the sieve were washed into a beaker, and the beaker was covered with tinfoil. Each sample was extracted three times and the filtered NaCl solution was recovered. After the first extraction step, the remaining sediment was collected and transferred to a 500-mL triangular flask; 60% NaI solution was added to about 3/4 of the volume of the flask. The mixture was then shaken on a shaker at 200 rpm for 2 min and allowed to settle for 10 min. After stratification, the supernatant was treated as in the first step. The shaking and extraction process was repeated 3 times for each sample and the NaI solution was also recovered. Finally, the suspension obtained from these two steps was combined and 30% H₂O₂ was added to digest natural organic matter. The subsequent vacuum filtration and drying steps were the same as for the water samples.

Finally, a digital camera (M165FC, Leica, Germany) was used to visually inspect the material on the filter paper under a dissecting microscope. To avoid misidentification and underestimation of microplastics it is necessary to standardize the plastic particle selection, following certain criteria to guarantee proper identification. We visually distinguished plastics according to the following criteria: no cellular or organic structures are visible, fibers

should be equally thick throughout their entire length, particles must present clear and homogeneous colors, and if they are transparent or white, they must be examined under high magnification and a fluorescence microscope (Hidalgo-Ruz et al., 2012). During observation of the MP, the concentration of MP in each sample was recorded. The MP concentration for surface water samples was calculated as the number of MP per m³ (n/m³). The concentration of MP in sediments was calculated as the number of MP per kg (n/kg wet weight).

1.3.2 Redundancy analysis

Redundancy analysis (RDA) models were used to study the ability to explain the MP concentrations based on land use. The RDA models were tested using the Monte Carlo method (500 random samples) along with the significance of the RDA analysis results. In gradient sorting calculations, RDA and canonical correspondence analysis (CCA) can be used for linear or single peaks, respectively. Generally, de-trend correspondence analysis (DCA) is used to determine the maximum values of the gradients along four axes before gradient sorting. If the gradient is short (≤ 3), linear fitting is better; i.e., the RDA linear model method is more suitable for sorting. If the gradient is long (≥ 4), the single-peak model fits better and the CCA single-peak model is more suitable. If the gradient is between 3 and 4, both methods are applicable (Jan and Petr, 2003). The general RDA calculation formula is:

$$R_d(X; W_k) = \frac{1}{p} \sum_{j=1}^p r^2(X_j, W_k) (k = 1, 2, \dots, r)$$

$$R_d(Y; V_z) = \frac{1}{q} \sum_{j=1}^q r^2(Y_j, V_z) (z = 1, 2, \dots, r)$$

where $(X; W_k)$ and $(Y; V_z)$ are two sets of standardized variables for X- and Y-extracted components, respectively. The ecological analysis software Canoco (v.5) was used to analyze the relationship between MP concentration and land use in the Chongqing section of the Yangtze River. The correlation between the two in the sorting chart of the RDA analysis is represented by the cosine of the angle between the arrows. The larger the cosine value, the greater the correlation between the two. A longer arrow line indicates that that type of land use has a greater influence on the abundance of MP than shorter arrow lines.

1.3.3 Improved comprehensive index model of land use intensity

Land-use intensity composite index models are used to measure the extent to which human activities affect land use patterns. Based on relevant research (Zhuang and Liu, 1997; Brown and Vivas, 2005; Chen and Lin, 2013; Chen et al., 2015; Ge and Yue, 2016), the standard method was improved to support the study environment and goals. Using the previous method, land use intensity was divided into four levels according to land use type: other land (corresponding to bare land); woodlands, grass, and water (corresponding to woodlands, grasslands, and water); agricultural

land (corresponding to arable lands, gardens); and developed land (corresponding to towns, villages, industrial mines, and transportation infrastructure) with intensity classification indices of 1, 2, 3, and 4, respectively. Considering that the intensity of developed land varies greatly, this level should be further broken down to provide greater objectivity and reflect realistic conditions. Therefore, in this study, developed land was further refined into three grades based on the actual proportion of developed land. For a volume ratio ≤ 1 , the intensity classification index was set to 4; for $1 < \text{volume ratio} \leq 3$, the intensity classification index was set to 5; and when the volume ratio was > 3 , the intensity classification index was set to 6. Therefore, in this study, the land use intensity classification index was established as 1, 2, 3, 4, 5, and 6 in increasing order. Since there may be a variety of land use patterns in each region, the comprehensive index of land use intensity (LUI) was used to reflect the intensity of land use, with the following formula:

$$LUI = \sum_{i=1}^n A_i \cdot \frac{S_i}{S}$$

where LUI is the comprehensive index of land use intensity for the sampling area, A_i is the grade i land use intensity classification index for the sampling area, S_i is the area of grade i land use in the sampling area, S is the total area in the sampling area, and n is the number of land use intensity grades.

2 Results

2.1 MP concentrations in the Chongqing section of the Yangtze River

The average concentration of microplastics in surface water (MPsw) in the Chongqing section of the Yangtze River was $4807 \pm 2706 \text{ n/m}^3$, gradually decreasing from upstream (Chongqing central city section) to downstream (northeast section of Chongqing). The average MPsw in the central urban section of Chongqing was $6811 \pm 3101 \text{ n/m}^3$, in the northeast section of Chongqing was $3564 \pm 1640 \text{ n/m}^3$, and in the central urban area was about twice that of the northeastern section of Chongqing. The highest MPsw was located at the SP7 sampling site in Nan'an District, while other relatively high concentrations were present at the Changshou SP10 sampling site and the Fuling SP13 sampling site. There was a clear turning point at the SP14 sampling site in eastern Fuling, where the MPsw changed from high to low (Figure 2).

The average concentration of microplastics in sediments (MPss) in the Chongqing section of the Yangtze River was $84.9 \pm 61 \text{ n/kg}$, gradually increasing from upstream (central urban section of Chongqing) to downstream (northeastern section of Chongqing). The average MPss in the central urban area of Chongqing was $45.4 \pm 28 \text{ n/kg}$, in the northeastern section of Chongqing was $89.6 \pm 69 \text{ n/kg}$, and the northeastern section of Chongqing was about twice that of the central urban section of Chongqing (Figure 2).

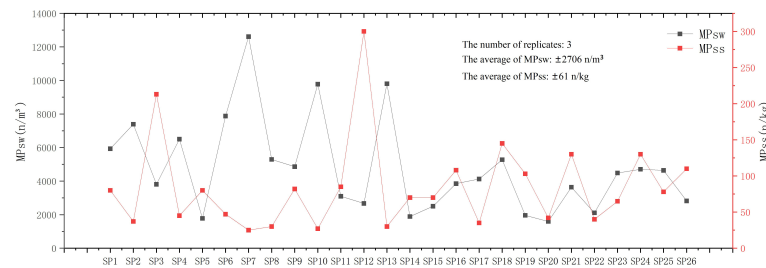


FIGURE 2
MP concentrations in the Chongqing section of the Yangtze River.

2.2 Trends in MP concentration in the Chongqing section of the Yangtze River

In recent years, levels of MPsw pollution in the Chongqing section of the Yangtze River have been improving. From 2016 to 2020, the MPsw of the Chongqing section of the Yangtze River decreased by about 7.5 times. In 2016, the average MPsw in the Chongqing section of the Yangtze River was 4700 ± 2605 n/m³ and had declined to 623 ± 265 n/m³ by 2020. Subregionally, MPsw in the central urban section of Chongqing improved more than the northeast section of Chongqing. From 2016 to 2020, MPsw in the central urban section of Chongqing fell from 6227 ± 2889 n/m³ to 589 ± 243 n/m³, a decrease of about 10.6 times. From 2016 to 2020, MPsw in the northeast section of Chongqing fell from 4016 ± 1876 n/m³ to 705 ± 271 n/m³, a decrease of about 5.7 times. Judging from this data comparison, the central urban section of Chongqing has received better treatment or source control of MP.

2.3 Composition of land use types at different scales

Previous studies have shown that the land use from 100 to 2000 m from the shoreline is significantly correlated with the water quality of the river (Duan et al., 2017; Xu et al., 2017; Xiang et al., 2018). Combined with the width of the Yangtze River, buffer radii of 1 km, 1.5 km, and 2 km from the sampling points were selected for this study. ArcGIS 10.3 software was used to plot circles with buffer radii of 1 km, 1.5 km, and 2 km around each sampling point. The three buffer ranges were superimposed on the land use maps and land use data within the three buffer ranges around each sample were obtained. The field fusion tool was used to combine the land use data for different sampling points to ensure that there was only one record for each land type within the buffer range of each sampling point. Finally, the attribute sheet records for the sampling points were exported to Excel and Origin for sorting and statistical analysis.

When the buffer radius was 1 km, the proportion of towns, villages, roads, and arable land was small, and that of woodland, grassland, bare land, and garden land was large. When the buffer radius was 2 km, the proportion of towns, villages, roads, and arable land was large, and that of woodland, grassland, bare land, and garden land was small.

When the buffer radius was 1 km, water area accounted for 62.9% of the total, followed by urban land at 21.8%. Sampling points SP4, SP5, SP6, and SP7 were located in the central urban section of Chongqing in the main stream of the Yangtze River, so the proportion of urban land use was relatively high. In addition, SP10 and SP20 were located in the Changshou urban section and the Wanzhou urban section of the Yangtze River, respectively (Figure 3).

When the buffer radius was expanded to 1.5 km, the proportions of all types of land uses other than water areas increased. Among these, the proportions of urban land and arable land increased significantly, by 7.25% and 4.13% respectively, and the proportion of water areas decreased by 17.5% (Figure 4).

When the buffer radius was expanded to 2 km, the proportions of all types of land use except water areas continued to increase, but the increase was small, on average about 1%, indicating that the proportions of all types of land uses were stabilizing (Figure 5).

2.4 Composite index of land use intensity at different scales

The land use type takes into account both the land type and the spatial structure of the land, while the LUI is a measure of the degree of land transformation. The focus of the two are not the same. To calculate the optimized comprehensive index model of LUI, the

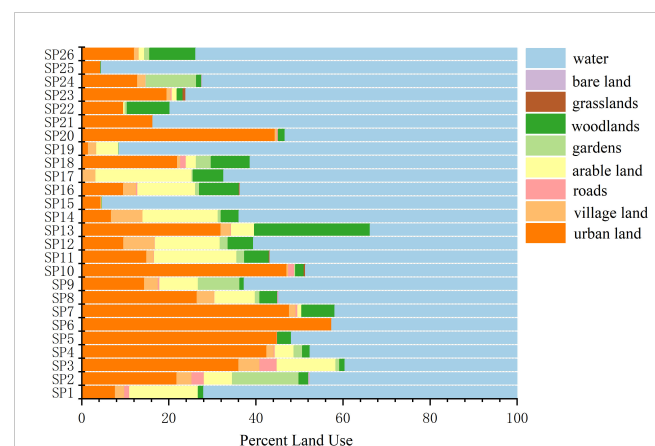
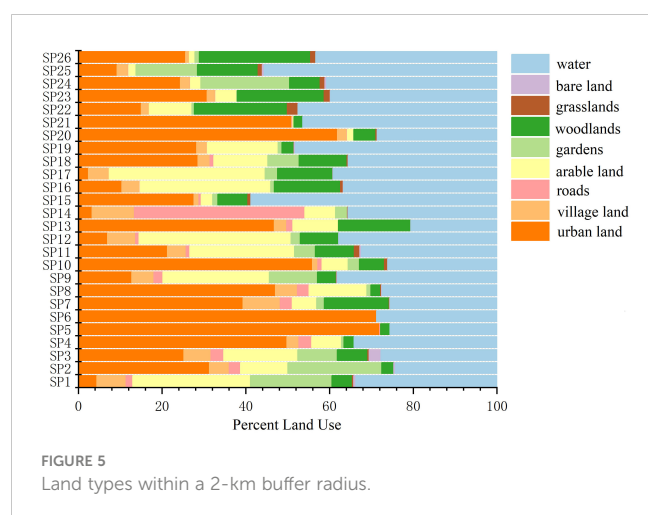
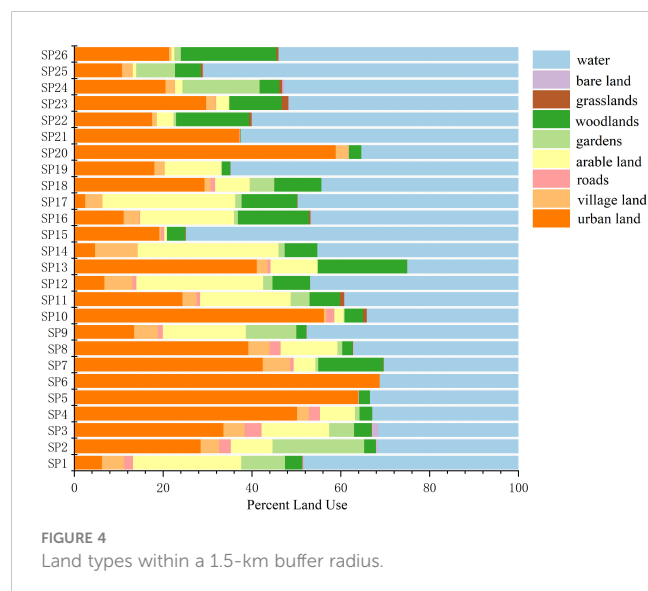


FIGURE 3
Land types within a 1-km buffer radius.



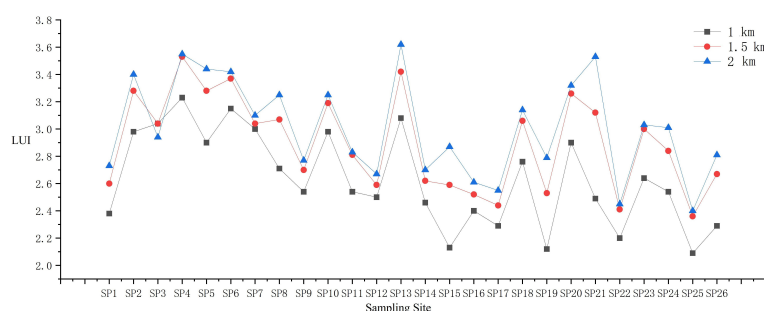
same three buffer scales were used (Figure 6). We found that with expansion of the buffer radius, the LUI also gradually increases. This is because as the buffer radius expands, the proportion of developed land use gradually increases. Overall, from the upper reaches of the Yangtze River (central urban section of Chongqing) to the lower reaches (northeast section of Chongqing), the LUI gradually declined. The LUI was highest near the SP4 sampling site located in Longzhou Bay, in the central city of Chongqing. The LUIs for SP4 within buffer radii of 1 km, 1.5 km, and 2 km were 3.23, 3.53, and 3.55, respectively. The LUI was lowest near the SP25 sampling site in Fengjie. The LUIs for SP25 within the buffer radii of 1 km, 1.5 km, and 2 km were 2.09, 2.36, and 2.4, respectively.

2.5 Correlation between land types and MP concentrations

At all buffer scales, MPss was positively correlated with village land and arable land. With increasing buffer radius, the strength of the correlation between land use types and MPss gradually increased (Figure 7). When the buffer radius was 1 km, MPsw was positively correlated with urban land, roads, gardens, woodlands, and bare land. When the buffer radius was 1.5 km, MPsw was positively correlated with urban land, roads, gardens, and woodlands (Figure 8). When the buffer radius was expanded to 2 km, MPsw had a weak positive correlation with urban land, village land, and gardens (Figure 9).

Redundancy analysis showed that as the radius of the buffer zone increased, the difference in interpretation rates among different land types gradually decreased. When the buffer zone radius was 1 km, the difference in the interpretation rate of land type on MP concentration was up to 17%. When the buffer radius was 1.5 km, the difference was 11.2%, and when the buffer radius was 2 km, the difference was 7.2% (Figures 10–12).

When the buffer radius was 1 km, the correlation between the LUI and MPsw was strongest at 0.59 ($p < 0.05$). At all buffer scales, there was no significant correlation between the LUI and MPss (Figure 13). When the buffer radius was 1 km, the LUI



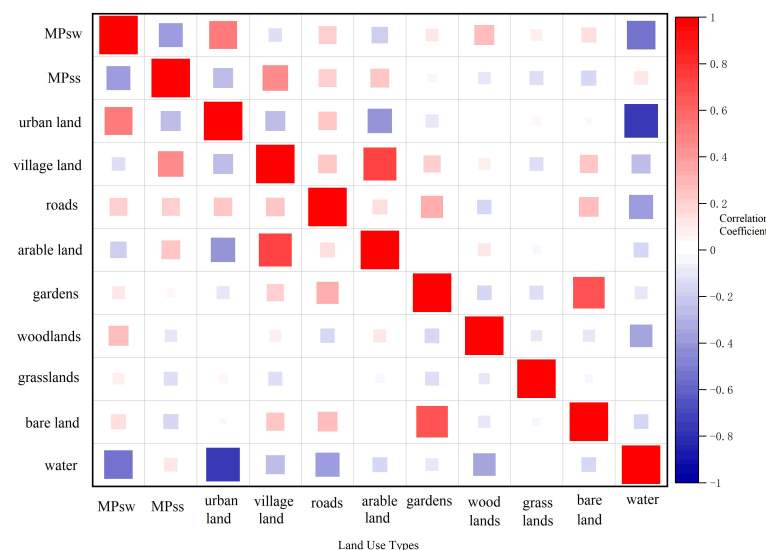


FIGURE 7
Correlation analysis of land types and MP concentrations within a 1-km buffer radius.

interpretation rate for the MP concentration was highest, at 18.9% (Figure 14).

3 Discussion

3.1 Characteristics and origin of MP concentrations in the Chongqing section of the Yangtze River

The MPsw in the Chongqing section of the Yangtze River gradually decreased from upstream (central urban section of Chongqing) to downstream (northeast section of Chongqing). There was a clear transition at the SP14 sampling site in eastern Fuling (Figure 2), where MPsw changed from high to low. These

results are largely consistent with those of Zhang et al. (2022). The reason for this phenomenon may be that the SP1–SP13 sampling sites were generally located in the central urban areas of Changshou, Fuling, etc. These regions have relatively developed economies and are densely populated, and plastic products are used relatively often. The SP15–SP26 sampling sites were mainly located in the northeastern region of Chongqing. The level of social and economic development there is relatively low and the use of plastic products is relatively low. We found that there is a clear negative correlation between MPss and MPsw for sampling sites SP1–SP13 (central urban area, Changshou, Fuling section). The data for MPss and MPsw for sampling sites SP14–SP26 (northeastern section of Chongqing) had a weaker negative correlation. Moreover, MPss at the SP1–SP13 sampling sites (central urban area, Changshou, Fuling section) was generally lower than at the SP14–SP26 sampling sites (northeastern Chongqing section). The SP1–SP13 sampling sites (central urban area, Changshou, Fuling section) were located in the upper reaches of the Yangtze River; the MP discharged into the surface water of this area of the Yangtze River may be carried by surface flow downstream to areas such as the SP14–SP26 section (northeastern section of Chongqing). MPsw sink during downstream transport when combined with other minerals and organic matter and MP that are ingested by aquatic biota also sink when excreted. Previous studies have found that more than half of MPsw sinks to the riverbed (Choy et al., 2019; Kane et al., 2020; Pohl et al., 2020). In addition, MP in the river will also migrate into the sediments through Brownian diffusion and gravity sedimentation (Li et al., 2019; Wong et al., 2020). As a result, MPsw originating upstream may become MPss downstream, consistent with the studies cited above. Therefore, MPsw in the SP1–SP13 section (central urban area, Changshou, Fuling section) was high, while MPss was low. Conversely, MPsw was low in the SP14–SP26 section (northeast section of Chongqing), while MPss was relatively high.

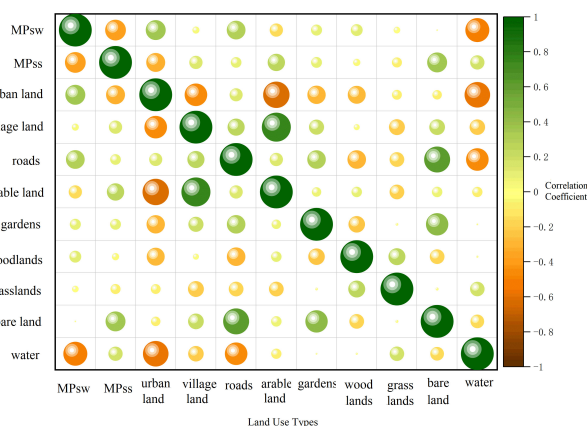
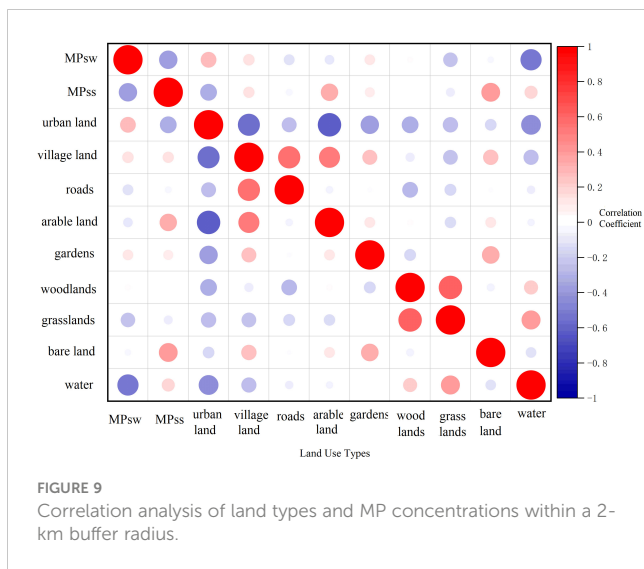
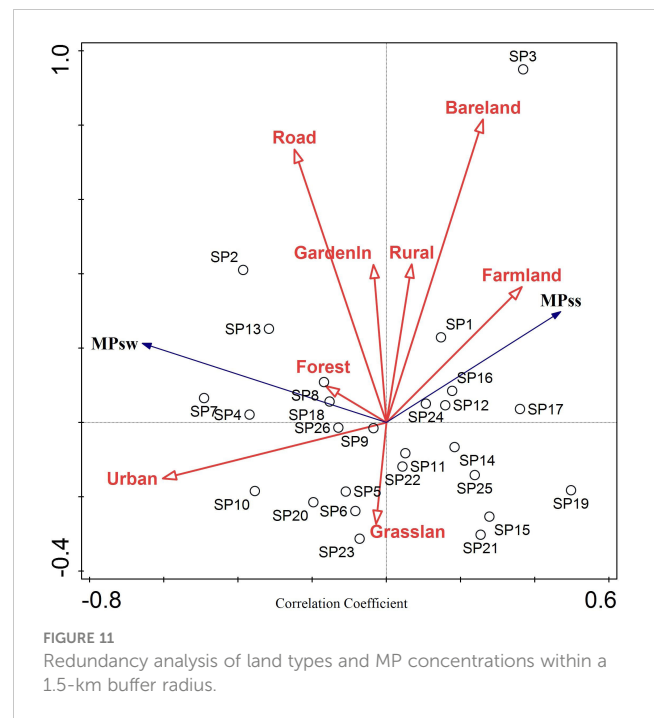
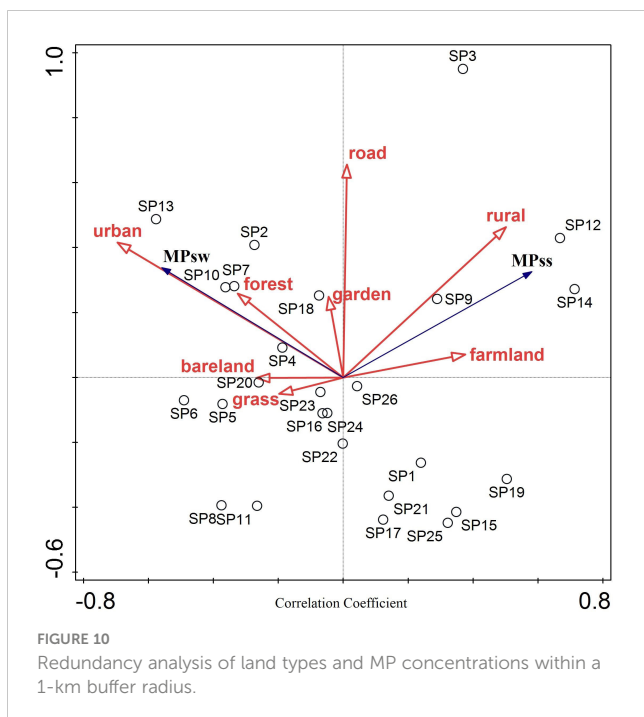


FIGURE 8
Correlation analysis of land types and MP concentrations within a 1.5-km buffer radius.



3.2 Effects of land use types on the concentration of MP in the river at different scales

Origin (v. 2022) software was used to analyze correlations between land use types and MP concentrations at various buffer ranges and scales. At all buffer scales, MPsw was positively correlated with urban and garden land, and negatively correlated with arable land. Urban land with intensive human activity increases the concentration of MP, consistent with previous studies (McCormick et al., 2014; Mao R. et al., 2020; Nguyen et al., 2021). Townsend et al. (2019) also found that the concentration of MP is positively correlated with the level of urbanization in watersheds. As the buffer radius increases, the strength of the correlation between land use and MPsw gradually

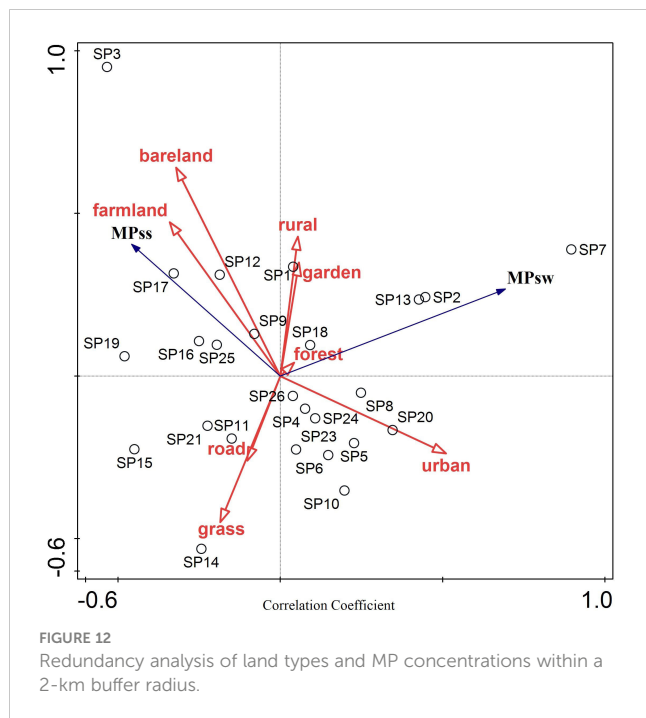


decreases and the number of land use types that are directly correlated with it also gradually decreases (Gu et al., 2019). In the present study, five types of land use were directly correlated with MPsw with a 1-km buffer radius, four types with a 1.5-km buffer radius, and three types with a 2-km buffer radius.

At all buffer scales, MPss was positively correlated with village land and arable land (Li et al., 2022). Unlike MPsw, as the buffer radius increased, the strength of the correlations between land use types and MPss gradually increased (Figure 7).

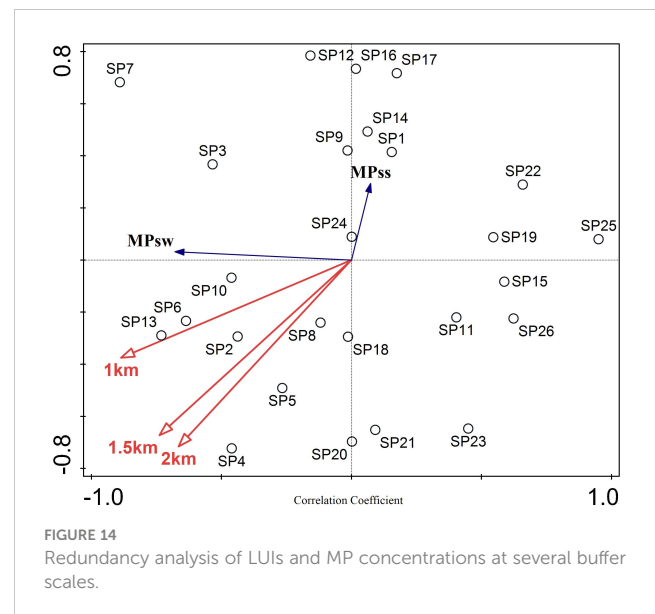
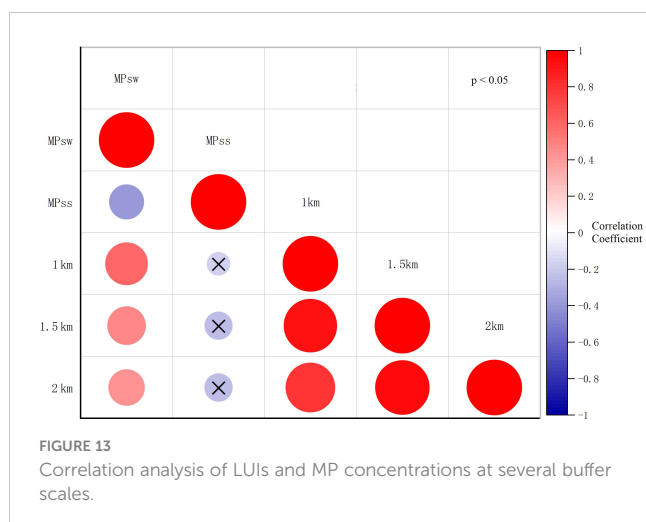
When the buffer radius was 1 km, MPsw was positively correlated with urban land, roads, gardens, woodland, and bare land, consistent with (Mao Y. et al., 2020). The correlation coefficient for urban land was strongly positive (0.53, $p < 0.05$), while the remaining land types had weak positive correlations (Figure 7). Village land and arable land had weak negative correlations with MPsw. There was no obvious correlation between MPsw and grasslands. The results of this study are similar to those of Hong et al. (2016), who found that water pollution was positively correlated with urban land and arable land and negatively correlated with grasslands. MPss was positively correlated with village land, roads, and arable land. The correlation with village land was moderately positive (0.44, $p < 0.05$). MPss had weak negative correlations with urban land (-0.27 , $p < 0.05$), woodland (-0.1 , $p < 0.05$), grasslands (-0.13 , $p < 0.05$), and bare land (-0.16 , $p < 0.05$). There was no significant correlation between MPss and gardens.

When the buffer radius was 1.5 km, MPsw was positively correlated with urban land, roads, gardens, and woodland, consistent with (Townsend et al., 2019). Among these, MPsw had moderate positive correlations with urban land (0.4, $p < 0.05$) and roads (0.32, $p < 0.05$), while the other land types had weak positive correlations (Figure 8). There was a weak negative correlation between arable land and MPsw and no obvious correlations between MPsw and village land, grasslands, or bare land. MPss



was positively correlated with village land, roads, arable land, gardens, and bare land. The correlation was moderately positive for bare land (0.37, $p < 0.05$) and arable land (0.3, $p < 0.05$). MPss was negatively correlated with urban land (-0.33 , $p < 0.05$). There were no significant correlations between MPss and woodlands or grasslands.

When the buffer radius was expanded to 2 km, MPsw had weak positive correlations with urban land (0.29, $p < 0.05$), village land (0.15, $p < 0.05$), and gardens (0.13, $p < 0.05$). MPsw had weak negative correlations with roads (-0.14 , $p < 0.05$), arable land (-0.11 , $p < 0.05$), and grasslands (-0.25 , $p < 0.05$), consistent with (Hong et al., 2016). No significant correlations between MPsw and woodland or bare land were found (Figure 9). MPss was positively correlated with village land, arable land, gardens, and bare land; correlations were moderately strong for bare land (0.41, $p < 0.05$) and arable land (0.35, $p < 0.05$). MPss was negatively correlated with



urban land (-0.33 , $p < 0.05$), which may be due to effects such as sediment migration, gravity settlement, and adhesion settlement as MP migrate from urban to rural areas of the river (Li et al., 2019; Wong et al., 2020). There were no significant correlations between MPss and roads, woodland, or grasslands.

Based on the correlation analysis, redundant analysis methods were further used to explain and analyze the concentration of MP with multi-scale land use types (Figures 10–12). When the buffer radius was 2 km, the land use type best explains the concentration of MP, with an explanation rate of 46.4%. When the buffer radius was 2 km, the proportion of each land use type was relatively balanced, which can comprehensively explain changes in the concentration of MP by land use type (Liu C. J. et al., 2021). With increasing buffer radius, differences in the interpretation rates of the various land use types gradually decreased. When the buffer radius was 1 km, land use types had interpretation rates for MP concentration that differed by as much as 17%. When the buffer radius was 1.5 km, the difference was 11.2%, and when the buffer radius was 2 km, the difference was 7.2%. For all buffer radii, urban land had the highest explanation rate for MP concentrations, consistent with the conclusions of the correlation analysis. Urban populations intensively produce and use the most plastic products, so more MP are released. Village land and bare land also had high explanation rates for MP concentrations. Village populations are also relatively active and produce a fair amount of plastic products. The high explanation rate for MP concentrations by bare ground is because it is generally used to store garbage containing large amounts of plastic waste, which is a major source of MP.

3.3 Effects of land use intensity on fluvial MP concentrations at different scales

At all buffer scales, the LUI was strongly correlated with MPsw (Figure 13). As the buffer radius increases, the correlation between the two gradually weakens (Zeng et al., 2022). In this analysis,

when the buffer radius was 1 km, the correlation between the two was strongest at 0.59 ($p < 0.05$). When the buffer radius was 1.5 km, the correlation coefficient was 0.48 ($p < 0.05$) and when the buffer radius was 2 km, the correlation coefficient was 0.43 ($p < 0.05$). There was no significant correlation between the LUI and MPss at any buffer scale. Thus, the LUI had a greater impact on MPsw than on MPss.

Further using the redundancy analysis method, a multi-scale LUI interpretive analysis of MP concentrations was conducted (Figure 14). When the buffer radius was 1 km, the LUI interpretation rate for the MP concentration was highest at 18.9%. When the buffer radii were 1.5 and 2 km, the LUI interpretation rates for the MP concentration were low, 4% and 4.7%, respectively. Thus, the LUI within a buffer radius of 1 km of the sampling site has the strongest impact on MP concentrations.

4 Conclusions

Using the Chongqing section of the Yangtze River as an example, we explored relationships between land use and MP concentrations in water and sediments, with the following conclusions. 1) MPsw gradually decreased from upstream (central urban section) to downstream (northeastern section of Chongqing). 2) From 2016 to 2020, MPsw decreased by about 7.5 times overall. 3) MPsw was positively correlated with the proportion of surrounding urban and garden lands. When the buffer radius was 1 km, the MPsw was most strongly correlated with urban land (0.53, $p < 0.05$). As the buffer radius increased, the correlation between land use and MPsw gradually weakened. 4) The LUI was also strongly correlated with MPsw, particularly at a buffer radius of 1 km (0.59, $p < 0.05$).

We also identified an interesting phenomenon. During migration downstream, MPsw can sink when it binds to other minerals and organic matter, as well as with the waste of aquatic organisms that ingest them. MPsw was higher in the upper reaches of the Yangtze River (central urban section of Chongqing) than in the lower reaches (northeast section of Chongqing), while the MPss was lower in the upper reaches than in the lower reaches. The discovery of this phenomenon suggests how MP may move through river systems. In future studies, we will explore whether this phenomenon also occurs in other rivers.

To our knowledge, this is the first study of the relationship between the LUI and river MP concentrations, and the first exploration of the relationship between MP concentrations and land use in the upper reaches of the Yangtze River. These results enrich our understanding of the sources and transport of MP in freshwater environments and provide information useful for remediation and reduction of MP in river systems.

Data availability statement

The original contributions presented in the study are included in the article/supplementary material. Further inquiries can be directed to the corresponding authors.

Author contributions

SY: data curation, writing the original draft, and software analysis. DP: conceptualization, funding acquisition, project administration, writing, and editing. All authors contributed to the article and approved the submitted version.

Funding

High-level Talents Project of Chongqing Medical University (No. R4014), CAS Team Project of the Belt and Road (to DP), Research Program of Chongqing Science and Technology Commission (No. cstc2019jcyj-zdxmX0035 and CSTCCXLJRC201714), National Natural Science Foundation of China (No.42001269), China–Sri Lanka Joint Center for Education and Research of the Chinese Academy of Sciences (CAS), International Partnership Program of CAS (No.121311kysb20190071), and Program of China–Sri Lanka Joint Center for WaterTechnology Research and Demonstration of the Chinese Academy of Sciences (CAS). Special Project for Performance Incentive and Guidance of Research Institutions in Chongqing (No.DLYG2022JXL004).

Acknowledgments

The authors are grateful for the Wuhan Botanical Garden, Chinese Academy of Sciences for providing data on microplastics.

Conflict of interest

The authors declare that the research was conducted in the absence of any commercial or financial relationships that could be construed as a potential conflict of interest.

Publisher's note

All claims expressed in this article are solely those of the authors and do not necessarily represent those of their affiliated organizations, or those of the publisher, the editors and the reviewers. Any product that may be evaluated in this article, or claim that may be made by its manufacturer, is not guaranteed or endorsed by the publisher.

References

- Agarwal, S. (2020). Biodegradable polymers: present opportunities and challenges in providing a microplastic-free environment. *Macromol. Chem. Phys.* 221 (6), 2000017. doi: 10.1002/macp.202000017
- Ajith, N., Arumugam, S., Parthasarathy, S., Manupoori, S., and Janakiraman, S. (2020). Global distribution of microplastics and its impact on marine environment-a review. *Environ. Sci. Pollut. Res.* 27 (21), 25970–25986. doi: 10.1007/s11356-020-09015-5
- Anas, N. A. A., Fen, Y. W., Omar, N. A. S., Daniyal, W. M. E. M. M., Ramdzan, N. S. M., and Saleviter, S. (2019). Development of graphene quantum dots-based optical sensor for toxic metal ion detection. *Sensors* 19 (18), 3850. doi: 10.3390/s19183850
- Auta, H. S., Emenike, C. U., and Fauziah, S. H. (2017). Distribution and importance of microplastics in the marine environment: a review of the sources, fate, effects, and potential solutions. *Environ. Int.* 102, 165–176. doi: 10.1016/j.envint.2017.02.013
- Baho, D. L., Bundschuh, M., and Futter, M. N. (2021). Microplastics in terrestrial ecosystems: moving beyond the state of the art to minimize the risk of ecological surprise. *Glob. Chang. Biol.* 27 (17), 3969–3986. doi: 10.1111/gcb.15724
- Bakir, A., Desender, M., Wilkinson, T., Van Hoytema, N., Amos, R., Airahui, S., et al. (2020). Occurrence and abundance of meso and microplastics in sediment, surface waters, and marine biota from the south pacific region. *Mar. Pollut. Bull.* 160, 111572. doi: 10.1016/j.marpolbul.2020.111572
- Bank, M. S., and Hansson, S. V. (2019). The plastic cycle: a novel and holistic paradigm for the anthropocene. *Environ. Sci. Technol.* 53 (13), 7177–7179. doi: 10.1021/acs.est.9b02942
- Barrows, A. P. W., Christiansen, K. S., Bode, E. T., and Hoellein, T. J. (2018). A watershed-scale, citizen science approach to quantifying microplastic concentration in a mixed land-use river. *Water Res.* 147, 382–392. doi: 10.1016/j.watres.2018.10.013
- Bhuvanes, N., Kumaresan, G., Renuka, K., Mukeshu, R., Mohammed, H., and Harish, V. N. N. (2022). Investigation on development and performance analysis of water trash collector. *Mater. Today: Proc.* 66 (P3), 1216–1220. doi: 10.1016/J.MATPR.2022.05.014
- Bläsing, M., and Amelung, W. (2018) Plastics in soil: Analytical methods and possible sources. *Sci. Total Environ.* 612, 422–435. doi: 10.1016/j.scitotenv.2017.08.086
- Brown, M. T., and Vivas, M. B. (2005). Landscape development intensity index. *Environ. Monit. Assess.* 101 (1–3), 289–309. doi: 10.1007/s10661-005-0296-6
- Browne, M. A., Crump, P., Niven, S. J., Teuten, E., Tonkin, A., Galloway, T., et al. (2011). Accumulation of microplastic on shorelines worldwide: sources and sinks. *Environ. Sci. Technol.* 45 (21), 9175–9179. doi: 10.1021/es201811s
- Chen, G., Li, Y., and Wang, J. (2021). Occurrence and ecological impact of microplastics in aquaculture ecosystems. *Chemosphere* 274, 129989. doi: 10.1016/j.chemosphere.2021.129989
- Chen, T.-S., and Lin, H.-J. (2013). Development of a framework for landscape assessment of Taiwanese wetlands. *Ecol. Indic.* 25, 121–132. doi: 10.1016/j.ecolind.2012.09.012
- Chen, Q., Zhu, H. M., HE, R., A.Dahlgren, R., Zhang, M. H., and Mei, K. (2015). Evaluating the impacts of land use on surface water quality using geographically weighted regression. *Acta Scientiae Circumstantiae* 35 (05), 1571–1580. doi: 10.13671/j.hjkxb.2015.0013
- Choy, C. A., Robison, B. H., Gagne, T. O., Erwin, B., Firl, E., Halden, R. U., et al. (2019). The vertical distribution and biological transport of marine microplastics across the epipelagic and mesopelagic water column. *Sci. Rep.* 9 (1), 7843. doi: 10.1038/s41598-019-44117-2
- Di, M. X. (2019). *A study on microplastic pollution in river-style reservoirs of the Yangtze river basin and adsorption behavior of estradiol onto microplastics* (Wuhan Botanical Garden, Chinese Academy of Sciences).
- Duan, S. Q., An, Y. L., Su, X. L., Wu, Q. X., Jin, T., Hou, Y. L., et al. (2017). Effects of multi-scale land use on water quality in sancha river. *Environ. Pollut. Control* 39 (05), 525–529 + 533. doi: 10.15985/j.cnki.1001-3865.2017.05.013
- Fan, M.Y., Huang, Y.M., Zhang, H.X., Li, H.H., and Huang, Q.(2022). Distribution, risk, and influencing factors of microplastics in surface water of Huangshui River Basin. *Environ. Sci.* 43 (10), 4430–4439. doi: 10.13227/j.hjks.202201087
- Fang, L., Qz, B., Jia, X. A., Yl, B., Yc, B., Km, D., et al. (2021). Microplastics in biota and surface seawater from tropical aquaculture area from hainan, China. *Gondwana Res.* 108), 41–48. doi: 10.1016/j.gr.2021.11.008
- Ge, S., and Yue, W. (2016). Spatial and temporal distribution of land use pattern change in songnen high plain. *Trans. Chin. Soc. Agric. Eng.* 32 (18), 225–233. doi: 10.11975/j.issn.1002-6819.2016.18.031
- Gu, Q., Hu, H., Ma, L., Sheng, L., Yang, S., Zhang, X., et al. (2019). Characterizing the spatial variations of the relationship between land use and surface water quality using self-organizing map approach. *Ecol. Indic.* 102, 633–643. doi: 10.1016/j.ecolind.2019.03.017
- Guo, J.-J., Huang, X.-P., Xiang, L., Wang, Y.-Z., Li, Y.-W., et al. (2020). Source, migration and toxicology of microplastics in soil. *Environ. Int.* 137, 105263. doi: 10.1016/j.envint.2019.105263
- Hao, Y.L., Hu, Y.X., Bai, X.X., and Guo, S.L. (2022). Abundances and morphology patterns of microplastics under different land use types on the loess plateau. *Environ. Sci.* 43 (09), 4748–4755. doi: 10.13227/j.hjks.202112199
- Hidalgo-Ruz, V., Gutow, L., Thompson, R. C., and Thiel, M. (2012). Microplastics in the marine environment: a review of the methods used for identification and quantification. *Environ. Sci. Technol.* 46 (6), 3060–3075. doi: 10.1021/es2031505
- Hoellein, T. J., and Rochman, C. M. (2021). The “plastic cycle”: a watershed-scale model of plastic pools and fluxes. *Front. Ecol. Environ.* 19 (3), 176–183. doi: 10.1002/fee.2294
- Hong, C., Xiaode, Z., Mengjing, G., and Wu, W. (2016). Land use change and its effects on water quality in typical inland lake of arid area in China. *J. Environ. Biol.* 37 (4), 603–609. doi: 10.1360/972010-1322
- Issaka, E., Yakubu, S., Sulemana, H., Kerkula, A., and Nyame-do, A. O. (2023). Current status of the direct detection of microplastics in environments and implications for toxicological effects. *Chem. Eng. J. Adv.* 14 (01), 432–443. doi: 10.1016/J.CEJA.2023.100449
- Jan, L., and Petr, S. (2003). *Multivariate analysis of ecological data using CANOCO* (Cambridge University Press).
- Kane, I. A., Clare, M. A., Miramontes, E., Wogelius, R., Rothwell, J. J., Garreau, P., et al. (2020). Seafloor microplastic hotspots controlled by deep-sea circulation. *Science* 368 (6495), 1140–1145. doi: 10.1126/science.aba5899
- Katusiime, J., Schütt, B., and Mutai, N. (2023). The relationship of land tenure, land use and land cover changes in lake Victoria basin. *Land Use Policy* 126 (02), 231–245. doi: 10.1016/J.LANDUSEPOL.2023.106542
- Klein, S., Worch, E., and Knepper, T. P. (2015). Occurrence and spatial distribution of microplastics in river shore sediments of the Rhine-main area in Germany. *Environ. Sci. Technol.* 49 (10), 6070–6076. doi: 10.1021/acs.est.5b00492
- Lebreton, L. C. M., van der Zwet, J., Damsteeg, J. W., Slat, B., Andrady, A., and Reisser, J. (2017). River plastic emissions to the world’s oceans. *Nat. Commun.* 8, 15611. doi: 10.1038/ncomms15611
- Li, W.-H., Jian, M.-F., Liu, S.-L., Jiang, Y.-M., Deng, Y.-B., and Zhu, L. (2020). Occurrence Relationship between microplastics and heavy metals pollutants in the estuarine sediments of poyang lake and the Yangtze river. *Environ. Sci.* 41 (1), 242–252. doi: 10.13227/j.hjks.201907169
- Li, W. G., Jian, M. F., Nie, J. M., and Wu, X. E. (2022). Spatiotemporal distribution and multi-source characteristics of microplastics in the soil and water environment of poyang lake Wetland, China. *Chin. J. Appl. Ecol.* 33 (10), 2862–2870. doi: 10.13287/j.1001-9332.2022.10.034
- Li, Y., Wang, X., Fu, W., Xia, X., Liu, C., Min, J., et al. (2019). Interactions between nano/micro plastics and suspended sediment in water: implications on aggregation and settling. *Water Res.* 161, 486–495. doi: 10.1016/j.watres.2019.06.018
- Liebezeit, G., and Dubaish, F. (2012). Microplastics in beaches of the East Frisian islands spiekeroog and kachelotplate. *Bull. Environ. Contam. Toxicol.* 89 (1), 213–217. doi: 10.1007/s00128-012-0642-7
- Liu, M., Ding, Y., Huang, P., Zheng, H., Wang, W., Ke, H., et al. (2021). Microplastics in the western pacific and south China Sea: spatial variations reveal the impact of kuroshio intrusion. *Environ. Pollut.* 288, 117745. doi: 10.1016/j.envpol.2021.117745
- Liu, C. J., Xia, J., Song, J. X., Zhang, Y., and Cheng, B. F. (2021). Spatial and temporal characteristics of water quality and Response identification of land use patterns in middle and downstream of hanjiang river. *Res. Environ. Sci.* 34 (4), 910–919. doi: 10.13198/j.issn.1001-6929.2020.08.15
- Lozano, Y. M., and Rillig, M. C. (2020). Effects of microplastic fibers and drought on plant communities. *Environ. Sci. Technol.* 54 (10), 6166–6173. doi: 10.1021/acs.est.0c01051
- Luan, C. X., and Liu, R. Z. (2022). A comparative study of various land use and land cover change models to predict ecosystem service value. *Int. J. Environ. Res. Public Health* 19 (24), 16484. doi: 10.3390/IJERPH192416484
- Luo, W., Su, L., Craig, N. J., Du, F., Wu, C., and Shi, H. (2018). Comparison of microplastic pollution in different water bodies from urban creeks to coastal waters. *Environ. Pollut.* 246, 174–182. doi: 10.1016/j.envpol.2018.11.081
- Mai, L., Sun, X. F., Xia, L. L., Bao, L. J., Liu, L. Y., and Zeng, E. Y. (2020). Global riverine plastic outflows. *Environ. Sci. Technol.* 54 (16), 10049–10056. doi: 10.1021/acs.est.0c02273
- Mao, R., Hu, Y., Zhang, S., Wu, R., and Guo, X. (2020). Microplastics in the surface water of wuliangsuhai lake, northern China. *Sci. Total Environ.* 723, 137820. doi: 10.1016/j.scitotenv.2020.137820
- Mao, Y., Li, H., Gu, W., Yang, G., Liu, Y., and He, Q. (2020). Distribution and characteristics of microplastics in the yulin river, China: role of environmental and spatial factors. *Environ. Pollut.* 265 (Pt A), 115033. doi: 10.1016/j.envpol.2020.115033
- McCormick, A., Hoellein, T. J., Mason, S. A., Schluep, J., and Kelly, J. J. (2014). Microplastic is an abundant and distinct microbial habitat in an urban river. *Environ. Sci. Technol.* 48 (20), 11863–11871. doi: 10.1021/es503610r
- Meijer, L. J. J., van Emmerik, T., van der Ent, R., Schmidt, C., and Lebreton, L. (2021). More than 1000 rivers account for 80% of global riverine plastic emissions into the ocean. *Sci. Adv.* 7 (18), eaaz5803. doi: 10.1126/sciadv.aaz5803

- Nguyen, N. B., Kim, M. K., Le, Q. T., Ngo, D. N., Zoh, K. D., and Joo, S. W. (2021). Spectroscopic analysis of microplastic contaminants in an urban wastewater treatment plant from Seoul, south Korea. *Chemosphere* 263, 127812. doi: 10.1016/j.chemosphere.2020.127812
- Nuelle, M. T., Dekiff, J. H., Remy, D., and Fries, E. (2014). A new analytical approach for monitoring microplastics in marine sediments. *Environ. pollut.* 184, 161–169. doi: 10.1016/j.envpol.2013.07.027
- Pohl, F., Eggenhuisen, J. T., Kane, I. A., and Clare, M. A. (2020). Transport and burial of microplastics in deep-marine sediments by turbidity currents. *Environ. Sci. Technol.* 54 (7), 4180–4189. doi: 10.1021/acs.est.9b07527
- Rillig, M. C., and Lehmann, A. (2020). Microplastic in terrestrial ecosystems. *Science* 368 (6498), 1430–1431. doi: 10.1126/science.abb5979
- Townsend, K. R., Lu, H. C., Sharley, D. J., and Pettigrove, V. (2019). Associations between microplastic pollution and land use in urban wetland sediments. *Environ. Sci. Pollut. Res.* 26 (22), 22551–22561. doi: 10.1007/s11356-019-04885-w
- Wei, Y. F., Ma, W. G., Xu, Q., Sun, C. Y., Wang, X. Y., and Gao, F. (2022). Microplastic distribution and influence factor analysis of seawater and surface sediments in a typical bay with diverse functional areas: a case study in xincun lagoon, China. *Front. Environ. Sci.* 10. doi: 10.3389/FENV.S.2022.829942
- Wong, J. K. H., Lee, K. K., Tang, K. H. D., and Yap, P. S. (2020). Microplastics in the freshwater and terrestrial environments: prevalence, fates, impacts and sustainable solutions. *Sci. Total Environ.* 719, 137512. doi: 10.1016/j.scitotenv.2020.137512
- Xiang, S., Pang, Y., Dou, J. S., Lu, X. Z., Xue, L. Q., and Chu, Z. S. (2018). Impact of land use on the water quality of inflow river to erhai lake at different temporal and spatial scales. *Acta Ecologica Sin.* 38 (03), 876–885. doi: 10.5846/stxb201612192610
- Xu, N., Gao, J. Q., and Wang, Q. (2017). Simulation of non-point source pollution in the state river basin based on SWAT model. *Haihe Water Resour.* 05, 53–56. doi: 10.3969/j.issn.1004-7328.2017.05.018
- Yan, M., Nie, H., Xu, K., He, Y., Hu, Y., Huang, Y., et al. (2019). Microplastic abundance, distribution and composition in the pearl river along guangzhou city and pearl river estuary, China. *Chemosphere* 217, 879–886. doi: 10.1016/j.chemosphere.2018.11.093
- Yuan, W., Christie-Oleza, J. A., Xu, E. G., Li, J., Zhang, H., Wang, W., et al. (2022). Environmental fate of microplastics in the world's third-largest river: basin-wide investigation and microplastic community analysis. *Water Res.* 210, 118002. doi: 10.1016/j.watres.2021.118002
- Zeng, Z. W. Y. H., Ning, Q. M., and Tang, H. (2022). Temporal and spatial evolution of land use intensity and its impact on ecosystem services in dongting lake zone. *Economic Geogr.* 42 (9), 176–185. doi: 10.15957/j.cnki.jjdl.2022.09.020
- Zhang, X. Q., Peng, M., Wang, Y., Li, L. J., Chai, Y., Shen, Z. W., et al. (2022). Composition and distribution characteristics of microplastics insurface water of chongqing section of the three gorges reservoir. *Freshw. Fisheries* 52 (01), 90–95. doi: 10.13721/j.cnki.dsyy.20211125.001
- Zhuang, D. F., and Liu, J. Y. (1997). Study on the model of regional differentiation of land use degree in china. *J. Natural Resour.* 12 (02), 10–16. doi: 10.11849/zrzyxb.1997.02.002



OPEN ACCESS

EDITED BY

Cletah Shoko,
University of the Witwatersrand, South
Africa

REVIEWED BY

I. Gusti Bagus Rai Utama,
Dhyana Pura University, Indonesia
Weili Duan,
Chinese Academy of Sciences (CAS),
China

*CORRESPONDENCE

Jingyi Xiao,
✉ xiaojingyi@qhnu.edu.cn
Yanxia Yang,
✉ 202147331019@stu.qhnu.edu.cn

RECEIVED 16 April 2023

ACCEPTED 07 July 2023

PUBLISHED 28 July 2023

CITATION

Shu R, Xiao J, Yang Y and Kong X (2023),
The evolution of spatiotemporal patterns
and influencing factors of high-level
tourist attractions in the Yellow
River Basin.
Front. Earth Sci. 11:1206716.
doi: 10.3389/feart.2023.1206716

COPYRIGHT

© 2023 Shu, Xiao, Yang and Kong. This is
an open-access article distributed under
the terms of the [Creative Commons
Attribution License \(CC BY\)](https://creativecommons.org/licenses/by/4.0/). The use,
distribution or reproduction in other
forums is permitted, provided the original
author(s) and the copyright owner(s) are
credited and that the original publication
in this journal is cited, in accordance with
accepted academic practice. No use,
distribution or reproduction is permitted
which does not comply with these terms.

The evolution of spatiotemporal patterns and influencing factors of high-level tourist attractions in the Yellow River Basin

Rentian Shu^{1,2}, Jingyi Xiao^{1,2*}, Yanxia Yang^{1,2*} and Xiangdan Kong³

¹Qinghai Normal University, School of Geographical Sciences, Xining, Qinghai, China, ²Key Laboratory of Natural Geography and Environmental Processes of Qinghai Province, Xining, Qinghai, China, ³Qinghai Normal University, School of History, Xining, Qinghai, China

Introduction: High-level tourist attractions (HLTAs) are essential components of high-quality tourism development in the Yellow River Basin. In the context of holistic tourism and mass tourism, it is necessary to re-examine the spatial pattern of HLTAs.

Methods: Selecting the Qing–Gan–Ning region of the Yellow River Basin as a case study site, based on the data on 590 high-level tourist attractions in 2009, 2015, and 2021, and with the help of ArcGIS10.8 spatial analysis tools, the nearest neighbor index, kernel density analysis, and standard deviation ellipse methods, such as ellipse and ESDA spatial exploratory analysis, were used to analyze the spatiotemporal pattern of the spatial distribution of high-level tourist attractions in the study area from the aspects of type, density, and spatial autocorrelation. Overlay analysis, buffer analysis, and other methods were used to select the influencing factors, and finally, the influencing factors were verified with the help of GeoDetector.

Conclusions: The conclusions are as follows: the NNI values for the Qing–Gan–Ning area of the Yellow River Basin are 0.699, 0.7, and 0.618, and the spatial structure type was clustered. The distribution density showed an evolutionary trend of point-like agglomeration and linear expansion, with the provincial capital as the core and the Yellow River as the axis. The distribution density of high-level tourist attractions is 27, 44, and 74 per 10,000 km². In terms of the dynamic distribution direction of the center of mass, there was little interannual variation, showing a northeast–southwest direction, which is consistent with the flow direction of the Yellow River in the region. Furthermore, the analysis of Moran's I index showed clear spatial autocorrelation at the county scale. HLTAs exhibited clustering and wider distribution in H–H and L–L zones, while the L–H and H–L zones displayed a more dispersed and narrower distribution. The order of factors affecting the spatial distribution of HLTAs was economic factors (0.5257) > social factors (0.5235) > natural factors (0.491), and interactive detection showed that there were two-factor enhancements and nonlinear enhancements in the factors.

Dicussions: This study contributes to the conservation development and sustainable development of ecotourism resources in the Yellow River Basin.

KEYWORDS

Yellow River Basin, high-level tourist attractions, spatiotemporal pattern, influencing factors, GeoDetector, Qing–Gan–Ning region

1 Introduction

1.1 Research background and literature review

As an important ecological function zone and economic zone in China, the Yellow River Basin is an important focal point for economic and social development, and ecological construction in the new era. It is also a key area for establishing a modern economic system, in which people and nature coexist harmoniously (Yang et al., 2021). In 2019, ecological conservation and high-quality development in the Yellow River Basin (YB conservation and development) were identified as important national strategies. The development of the tourism industry in the basin is of great significance to the transformation of the development mode, economic structure optimization, and sustainable development of the Yellow River Basin. It is also an effective way to realize ecological protection and high-quality development of the basin, and plays an important role in the green ecological corridor of the Yellow River and the construction of an ecological civilization.

A-level tourist attractions are a comprehensive assessment method for the quality of tourist attractions in China (Wu et al., 2009), classifying them as 1A–5A. Attractions of 3A and above are of high standards in terms of infrastructure, resource attractiveness, management, and reception capacity, and are tourist destinations with high visitor arrival rates. The development status of level 3A and above is a barometer of tourism development in a region and has become an important reference for tourists' choice of tourist destinations and the government's integration planning of tourism resources. Zhang et al. (2018), Wang et al. (2020), Liao and Zhang (2021), and Qiu et al. (2021) define tourist attractions of 3A and above as high-level tourist attractions (MA XF, 2019; Li et al., 2020), whose number and spatial distribution largely determine the spatial pattern of tourism in the region.

Overseas research on high-level tourist attractions (HLTAs) has mostly been conducted in the case of national parks (Weber and Sultana, 2013) and World Heritage Sites (Jaafar et al., 2015), especially covering accessibility (Weber and Sultana, 2013), recreational behavior (Grayson and Martinec, 2004), demand forecasting (Samitas et al., 2018), and visitor perception (Fyall et al., 2017). Chinese scholars have mainly researched scenic planning and development (Zhan and Zhu, 2019), management models and economic benefits (Yuan et al., 2015; Cheng and Niu, 2016), spatial structure and distribution characteristics (Wu and Chen, 2022), economic value assessment (Zha and Qiu, 2015), and scenic capacity (ZHANG and WANG, 2007). In terms of the research timeframe, scholars mostly use single-year cross-sectional data to explore the spatial differentiation patterns and characteristics of scenic spots from a static perspective (Wu et al., 2017; Li et al., 2020); research methods are mostly qualitative analysis (Lin et al., 2014), AHP (Gu et al., 2015), and location entropy (Li et al., 2013). In recent years, mathematical and spatial analysis has become the mainstream method for exploring spatial distribution patterns (Yao et al., 2019) and correlation analysis (Wu et al., 2013; Wu et al., 2017). The geographical linkage rate (Xinyue and Juanjuan, 2016) and the GWR model (Zhu et al.,

2017) have been used to study the influencing factors. Case studies cover countries (Zhu and Chen, 2008; Guedes and Jiménez, 2015; Kang et al., 2018), regions (Ma et al., 2013; Tang et al., 2019; Yang et al., 2019; Zhu et al., 2022), provinces (Wu et al., 2013; Xinyue and Juanjuan, 2016; Qiu et al., 2021; Bao et al., 2023), and municipalities (Liu et al., 2014); they include the Yangtze River Economic Belt (Zhang et al., 2018), Pearl River Delta (Chen et al., 2011), and Poyang Lake Ecological Economic Zone (Guo et al., 2012).

Existing studies in related fields have made advancements; however, there are still some shortcomings. First, in terms of research time frame, few scholars have studied the spatiotemporal evolution characteristics of the spatial distribution of HLTAs under long time series based on panel data. Second, in terms of research methods, mathematical models and spatial analysis are not linked closely enough, and there is a lack of spatial econometric analysis based on GIS visualization. Third, GeoDetectors are not adequately used in the study of influencing factors, and most of the use of GeoDetectors usage is focused on single-factor detection (Tang et al., 2019; Yao et al., 2019). Multifactor interaction detection is lacking. Finally, there are few basin-based studies (Li et al., 2019; Zhang et al., 2021) and even fewer results for the Yellow River Basin (Zhang C. et al., 2020; Li et al., 2020). In summary, there is a lack of quantitative analysis of spatial patterns and their influencing factors at long timescales based on panel data, spatial visualization analysis, and GeoDetector interaction detection for HLTAs in the Yellow River Basin regions.

The Qing–Gan–Ning region of the Yellow River Basin is located at the intersection of the Upper Yellow River Economic Belt and the Silk Road Economic Belt, with connected geography and humanities, and close social, economic, and cultural ties (Xiaoxiao et al., 2018). This area is also an important ecological barrier and a typical zone for high-quality development in the Upper Yellow River area. Based on this finding, this study uses spatial analysis, mathematical statistics, and other methods to analyze the basic features and evolutionary laws of spatial pattern changes in HLTAs, and uses GIS spatial analysis and GeoDetectors to determine the influencing factors. This approach helps identify the spatial structure of tourism resources with a view of providing a decision basis for the optimal layout and business mode enhancement of cross-regional high-level tourist attractions, which has theoretical and practical significance for the coordinated, high-quality, and sustainable development of the cultural tourism belt in the Yellow River Basin.

1.2 Study area overview

The Qing–Gan–Ning region in the Yellow River Basin refers to the basin area of the Yellow River from Maduo in Qinghai to Huinong in Ningxia. It is in the upper reaches of the Yellow River. The geographical range is 95°57'–108°46'E and 32°55'–39°18'N, with a basin area of 359,300 km², covering 22 cities and autonomous prefectures in three provinces of Qinghai, Gansu, and Ningxia. The terrain is dominated by plateaus, and the overall presentation is high in the west and low in the east. It mainly flows through the Qinghai–Tibet Plateau, Loess Plateau,

loop plain, and other geomorphic units. The complex geographical environment has bred rich natural and cultural tourism resources. It belongs to the transition zone of the Qinghai–Tibet alpine region and the eastern monsoon region, and is an important water connotation and recharge area of the Yellow River Basin, as well as an important ecological barrier in the northwest (Figure 1).

The Yellow River Basin Qing–Gan–Ning region (hereinafter referred to as “the region”) has a long history and culture, where multiple ethnic cultures are intertwined, the mountains and waters are connected, and the cultures are close to each other and connected. Natural and humanistic environments are similar and exhibit regional cultural characteristics. In 2009, the three regions of Qing, Gan, and Ning received 0.483 billion tourist trips and 28,035 billion yuan in tourism revenue. In 2021, 352 million people received a tourism revenue of 247,868 billion yuan, and the tourism revenue accounted for a GDP increase from 4.83% to 13.69%. The tourism industry has become a strong engine of economic growth in this region. As of November 2021, there are 475 high-level tourist attractions ranked 3A and above in the Qing–Gan–Ning region, including 14 5A-, 160 4A-, and 301 3A-level tourist attractions.

2 Data sources and research methods

2.1 Data sources

Since high-level tourist attractions are stable and may not change significantly in adjacent years (Gan and Wang, 2021), 594 high-level tourist attractions in 3 years (i.e., 2009, 2015, and 2021) were selected for this study over a span of 6 years. In terms of geographic base data, the tourist attractions' catalogs were obtained from the lists of 2009, 2015, and 2021 A-class tourism scenic spots published on the official websites of the Department of Culture and Tourism of Qinghai, Gansu, and Ningxia provinces (autonomous regions); the coordinate data on the scenic spots were obtained from the Baidu Map API, and the coordinates were picked up one by one to build the database by year. The vector data (e.g., elevation DEM, river data, road data, etc.) were obtained from the Institute of Geography and Environment, Chinese Academy of Sciences (<https://www.resdc.cn/>). Socio-economic data such as population data, GDP data, *per capita* disposable income data, and fiscal expenditure data were obtained from 2009 to 2021 provincial and regional statistical yearbooks, statistical bulletins, government work reports, and China's economic and social big data platform (<https://data.cnki.net/>).

2.2 Research methodology

2.2.1 Clustering analysis method for spatial distribution

The nearest neighbor index (NNI) is the ratio of the observed nearest neighbor distance to the theoretical nearest neighbor distance. It is used to express the type of distribution of point-like elements in geospatial space.

$$R_1 = \frac{\sum_{i=1}^n d_i}{n}, R_E = \frac{1}{2\sqrt{\frac{\pi}{A}}}, R = \frac{R_1}{R_E}. \quad (1)$$

Here, R denotes the nearest neighbor index, R_1 denotes the observed distance, R_E denotes the theoretical distance, n denotes the number of points, A is the total area of the region, and d_i is the distance from point i to its nearest neighbor. When the value of R is close to 1, the point elements are randomly distributed; when $R > 1$, the distribution is discrete; and when $R < 1$, the distribution is coalescent.

2.2.2 Morphological analysis method of spatial distribution

2.2.2.1 Kernel density

Kernel density was used to estimate the spatial distribution of the geographic elements and visualize the spatial agglomeration state. The higher the kernel density value is, the higher the probability of event occurrence and the denser the points.

$$\hat{f}(x) = \frac{1}{nh^d} \sum_{i=1}^n K\left(\frac{x - x_i}{h}\right). \quad (2)$$

Here, \hat{f} is the kernel density estimate of high-level tourist attractions, and a larger $\hat{f}(x)$ indicates a denser distribution. h is the search radius, K is the kernel function, n is the number of tourist attractions, $(x - x_i)$ denotes the distance from the valuation point x to the sample, and d is the dimensionality.

2.2.2.2 Standard deviation ellipse

The standard deviation ellipse (SDE) quantitatively explains the characteristics of aggregation, spreading, direction, and spatial patterns of the spatial distribution of geographical elements from the perspective of global space. The parameters include the position of the center of the ellipse and the distance between the long and short axes. The change in the position of the center of the ellipse intuitively reflects the spatial change in the center of gravity of tourist attractions.

2.2.3 ESDA exploratory space analysis

The ESDA spatial exploratory analysis method integrates various techniques. Global autocorrelation uses global Moran's I to describe the overall trend and variability of spatial correlation of the geographic element attribute values across the region, and the local spatial autocorrelation uses the local Moran's I index to further reveal the heterogeneity of elements at the spatial scale. All of the aforementioned steps can be calculated using the spatial autocorrelation tool in the ArcGIS spatial statistics module.

2.2.4 GeoDetector

GeoDetector was used to detect spatial heterogeneity, explain the degree of the differential driving forces behind its influencing factors, and reveal factor interactions. In this study, we use the function of the factor and interaction detectors to clarify the explanatory strength of each influencing factor on the spatial

distribution of tourism scenery and to detect the interaction between each influencing factor indicator.

$$q = 1 - \frac{\sum_{h=1}^L N_h \sigma_h^2}{N \sigma^2}. \quad (3)$$

Here, q is the intensity detection value of the influencing factor on the spatial pattern, N and N_h are the number of samples contained in the whole area and sub-region of the detection factor, respectively, and σ_h^2 and σ^2 denote the variance of the value of the sub-element layer h and the whole area Y , respectively. L is the number of sub-regions. q has a value ranging between 0 and 1, and if stratification is generated by the independent variable X , a larger q -value indicates a stronger explanatory power of the independent variable X on attribute Y . When q is 1, it indicates that factor X completely controls the spatial distribution of tourist attractions and *vice versa*. The q -value indicates that factor X explains $100 \times q\%$ of the spatial variation in tourism.

2.3 Theoretical framework

The point-axis theory was proposed by the Chinese geographer Lu Daodao in 1984. Based on the central place theory, spatial diffusion theory, and growth pole theory, this theory illustrates the objective rules of spatial development of geographical elements. The point-axis theory provides a theoretical basis for the study of regional tourism development and planning, and the optimization of tourism spatial patterns. Spatiotemporal thinking is one of the characteristics of geography research. The organic combination of spatial thinking and temporal thinking reflects the unity of ephemerality and co-occurrence. This paper uses spatiotemporal thinking to help improve the depth and science of research on issues such as spatial evolution and chronological studies. In 1980, Butler proposed a model of the life cycle evolution of tourist places, which helps study the development stages of tourist places, predicts the development trend of tourist destinations, and guides the optimization of the spatial pattern of high-level scenic spots and the formulation of tourism development ideas.

In order to study the spatial pattern evolution characteristics and influencing factors of high-level scenic areas, this study first puts forward hypothesis H1H2 based on the point-axis theory, spatiotemporal thinking theory, and tourism place life cycle theory. Second, the correctness of hypothesis H1H2 is verified by using geospatial statistical methods, correlation analysis, and geographic probes (Figure 2).

H1. The high-level scenic spots in the Qing–Gan–Ning area of the Yellow River Basin have significant divergent characteristics in spatial and temporal distribution.

H2. Natural, economic, and social factors have a significant impact on the spatial pattern of high-level scenic spots.

3 Spatial distribution characteristics of tourist attractions and their evolution

3.1 Spatial distribution types of tourist attractions and their evolution

The mean nearest neighbor analysis tool was used to calculate the NNI of high-level tourist attractions in the area (Table 1); the NNI values of the spatial distribution of HLTAs from 2009 to 2021 were all less than 1, passed the Z-test and confidence test, and had a clustered spatial structure type. The NNI value first showed growth and then declined, indicating that the spatial agglomeration of HLTAs was first mildly weakened and tended to be uniformly distributed, and then, the agglomeration was strengthened.

To eliminate the interference of administrative boundaries (Weng et al., 2021), the coefficient of variation (CV) of the Tyson polygon was used to measure the degree of agglomeration. The C_v values of the Tyson polygon were 131.8%, 161.4%, and 203.5% from 2009 to 2021, and the C_v value increased steadily during the period. When the C_v values are all greater than 64%, it shows an aggregation distribution, and higher C_v s represent a more obvious aggregation (Duyckaerts et al., 2000). The C_v values based on the Voronoi diagram area further verified the conclusion that the HLTAs in the area showed a clustered distribution trend.

3.2 Density of spatial distribution of tourist attractions and their evolution

After using ArcGIS 10.8 to analyze the Kernel density of HLTAs, the resultant values were graded, and distribution maps were generated according to the natural break method. The Kernel densities of HLTAs in the area were 2.7, 4.4, and 7.4 per 10,000 km² in 2009, 2015, and 2021, respectively. The Kernel density gradually increased, and the degree of agglomeration continued to improve (Figure 3).

The areas with the highest Kernel density in 2009 were near Lan-Xi-Yin and Pingliang. The Kernel density was highest in Lanxi along the yellow urban agglomeration area, the southeast area of Gansu, and the northern area of Ningxia, and it was lower in other areas. In 2015, the core cities were further strengthened and the Kernel density of secondary centers was extended to the southeast and northeast. The areas in Lanxi along the yellow urban agglomeration area and the southeast area of Gansu were connected as one and tended to be connected with the area of Ningxia. In 2021, with a further increase in the number of HLTAs, the three areas were concentrated and connected into one large area. In particular, along the yellow urban agglomeration area, the Kernel density grows rapidly. Overall, the spatiotemporal pattern of high-level tourist attractions shows a spatiotemporal evolution, with the provincial capital city as the core, key cities as sub-centers, and the Yellow River as the axis, with point-like clustering and belt-like extension coexisting.

The distribution of the Kernel density of HLTAs in the area had a more evident hierarchical nature. Lanzhou, Xining, and Yinchuan form the three cores, whereas Pingliang, Linxia, and Haidong in

TABLE 1 NNI index and spatial structure type of HLTAs in the area from 2009 to 2021.

Year/year	Number of high-level scenic spots	Observations/km	Expected value/km	NNI	Type of spatial structure
2009	114	22.095	31.59	0.699	Clustered
2015	178	17.651	25.081	0.704	Clustered
2021	298	12.01	19.427	0.618	Clustered

TABLE 2 Slice high-level landscape municipal county-scale global Moran's I Index from 2009 to 2021.

	Year	Moran's I	Z-score	p-value
Municipalities	2009	−0.0868	−0.3520	0.7248
	2015	−0.0522	−0.0645	0.9485
	2021	0.0863	0.9001	0.3677
County	2009	0.1121	2.0256	0.0428
	2015	0.1864	3.2689	0.0011
	2021	0.1218	2.3555	0.0185

Qinghai, and Zhongwei in Ningxia form several sub-centers. The core area core density was above 43 per 10,000 km², and the sub-center distribution density was above 30 per 10,000 km². In addition, the medium-value area was distributed along the Yellow River and its tributaries, with a distribution density of more than 14 per 10,000 km². The low-value areas are mainly distributed in the Yushu and Guoluo provinces of Qinghai Province, Dingxi City, Qingyang City of Gansu Province, and the loess hills and ravines of southeastern Ningxia Province. This may be related to the distribution of nature reserves, fragile natural geographical environments, ecological protection policies, transportation accessibility, population density, and socioeconomic development levels in some areas.

3.3 Spatial distribution center of gravity of tourist attractions and their directional evolution

The spatial distribution of HLTAs in the area from 2009 to 2021 was analyzed using standard deviation ellipse analysis to study the changes in their shapes, distribution directions, and the mobility of the center of mass (Figure 4). In 2021, the mean center of mass shifted to the east by approximately 16' and to the north by approximately 6'. The center of mass is now located in Lanzhou City within Yuzhong County. Considering the Qing-Gan-Ning region of the Yellow River Basin as a whole, the distribution of HLTAs extends in the northeast direction as a whole; in other words, the development of HLTAs is faster in the northeastern part of the study area. The standard deviation ellipse has some significance for the balanced development of regional tourism and for avoiding bifurcation.

From 2009 to 2021, the area of the standard deviation ellipse decreased annually from 190,864 km² to 174,647 km². When the area of the ellipse decreases, the same proportion of high-level tourist attractions is distributed in smaller ellipses and the clustering of scenic spots in the ellipse increases. From 2009 to 2021, the long axis of the ellipse shortened from 320,969 km to 291,141 km, and the short axis remained almost the same. When the flatness of the standard deviation ellipse was smaller, the polarization in the direction of the long axis was weaker, and the standard deviation ellipse tended to be more

TABLE 3 Analysis of the number of HLTAs in the region and economic factors, and correlations from 2009 to 2021.

	Economic base	Income level	Industry development level
2009	0.640**	0.421*	0.715**
2015	0.536*	0.366	0.565**
2021	0.639**	0.499*	0.562**

* indicates significant correlation at 0.05 level (two-sided).

** indicates significant correlation at 0.01 level (two-sided).

TABLE 4 Detection results of factors influencing the distribution of HLTAs in the Qing-Gan-Ning region of the Yellow River Basin from 2009 to 2021.

Year	X1	X2	X3	X4	Y1	Y2	Y3	Y4	Z1	Z2	Z3	Z4
2009	0.336	0.336	0.608	0.661	0.31	0.82	0.48	0.416	0.273	0.877	0.491	0.449
2015	0.295	0.365	0.134	0.599	0.765	0.743	0.419	0.299	0.361	0.608	0.542	0.602
2021	0.690	0.62	0.642	0.600	0.336	0.619	0.608	0.496	0.598	0.538	0.433	0.51
Average	0.440	0.440	0.461	0.620	0.470	0.727	0.502	0.404	0.411	0.674	0.489	0.520

TABLE 5 Interaction detection results of factors influencing the spatial distribution of HLTAs in the Qing–Gan–Ning region of the Yellow River Basin from 2009 to 2021.

	X1	X2	X3	X4	Y1	Y2	Y3	Y4	Z1	Z2	Z3	Z4
X1	0.690											
X2	0.977	0.620										
X3	0.857	0.961	0.642									
X4	0.845	0.996	0.818	0.600								
Y1	0.930	0.898	0.961	1.000	0.336							
Y2	0.953	1.000	0.996	0.981	0.984	0.619						
Y3	0.992	0.996	0.984	0.899	0.922	0.969	0.608					
Y4	0.981	0.988	0.919	0.977	0.996	0.984	0.771	0.496				
Z1	0.981	0.996	0.961	0.965	0.934	0.930	0.922	1.000	0.598			
Z2	0.984	0.965	0.965	0.903	0.938	0.984	1.000	1.000	0.981	0.538		
Z3	0.919	0.984	0.925	0.965	0.806	0.965	1.000	0.860	0.915	1.000	0.433	
Z4	0.996	0.996	0.965	0.868	0.981	0.733	0.833	0.991	0.996	0.996	0.995	0.510

Bold value indicates nonlinear enhanced type.

positive; thus, the directionality of the distribution of the HLTAs was weaker. From the angle of deflection of the standard deviation, the angle of deflection of the ellipse decreased from 83.169° to 78.768° and then increased to 80.282°; the angle of deflection first decreased and then increased. The overall distribution pattern of the high-level tourist attractions was first deflected toward the northeast and then southeast. In general, the standard deviation of the elliptical area changed significantly; however, the morphology did not. The distribution direction of HLTA was northeast–southwest, which is consistent with the flow direction of the Yellow River in the region. It is assumed that the spatial distribution direction of HLTAs may be closely related to the flow direction of the Yellow River and the distribution of the water systems, which will be discussed later.

3.4 Spatial distribution linkage mechanism of tourist attractions and their evolution

The prefectural and county scales from 2009 to 2021 were subjected to ESDA exploratory spatial analysis (Table 2). The global Moran's *I* index of HLTA in this area was obtained. At the prefectural scale, HLTAs are not statistically significantly spatially autocorrelated under the municipal unit. Under the county unit, Moran's *I* indices for 2009, 2015, and 2021 were 0.1121, 0.1564, and 0.1218, respectively. Indices > 0, *p*-values passing the 0.05 significance test, and normal statistical Z-scores > 1.96 indicate that at the 95% confidence level, HLTAs have spatial autocorrelation under the county unit. From 2009 to 2015, Moran's *I* index increased from 0.1121 to 0.1864, indicating that the spatial agglomeration of tourism tourist attraction neighborhoods increased, and spatial differences gradually became significant. From 2015 to 2021, Moran's *I* index decreased to 0.1218, indicating that the spatial agglomeration of

tourism tourist attraction neighborhoods weakened. The overall inter-neighborhood differences were first enhanced and then weakened. Spatial autocorrelation and neighborhood agglomeration in HLTAs are closely related to the development status of the tourism industry in the region and in each domain area, which will be discussed later.

Using the Anselin Local Moran's index, a local indicator of spatial association (LISA) clustering map of the HLTA at the county scale was obtained (Figure 5). H–H areas from 2009 to 2021 were mainly concentrated in Xining City and Yinchuan City. After 2015, L–L areas began to appear, especially in the Qilian Mountains, Sanjiangyuan, and Gannan regions. The distribution of negatively correlated types was low, and the H–L areas showed a decreasing trend from 2009 to 2021, whereas the L–H areas showed an increase and then a decrease. The positively correlated H–H and L–L zones exhibited clustering and were widely distributed. The negatively correlated L–H and H–L zones show a point distribution that is more dispersed and smaller in scope.

The local spatial autocorrelation of eight counties, including Qinghai Huzhu County, changed from significant to non-significant, indicating that the spatial autocorrelation between the counties and surrounding counties weakened. Chongxin County in Gansu changed from an H–H area to an L–H area, and Ping'an District in Qinghai changed from a non-significant area to an L–H area, indicating that the surrounding HLTAs developed faster and lagged behind the surrounding areas due to the siphoning effect. Pingluo County and Yongning County in Ningxia changed from non-significant areas to H–H areas, indicating that the spatial distribution of HLTA in these two areas developed rapidly. Xinghai County of Qinghai changed from a non-significant area to an H–L area, indicating that the HLTA is developing well but does not significantly drive the development of the surrounding areas. The change from non-



FIGURE 1

Yellow River Basin Qing-Gan-Ning region map.

significant to L-L in Gangcha, Tianjun, Maduo, and Qumalai counties in Qinghai and Minxian in Gansu indicates that the density of HLTAs in and around the region is low and the development of HLTAs is lagging in relation, which may be related to the ecological protection measures implemented in Sanjiangyuan National Park, Qilian Mountain National Park, and other nature reserves (Hao et al., 2022).

4 Influencing factor selection

This study explored the influencing factors, aiming to address the following questions: (1) “why is the distribution along the Yellow River?” (2) “Why does it show spatial and temporal divergence?” and (3) “Why does it show spatial autocorrelation?”. Many factors affect the spatial distribution of HLTAs in the Yellow River Basin area of Qing, Gansu, and Ningxia. The basin is a special geographical unit. Based on Wu et al. (2017), Zhang et al. (2018), Zhang S. et al. (2020), Li et al. (2020), and Wang et al. (2020), the following three major categories were selected as the factors affecting the distribution of HLTAs to reflect the common features and individual characteristics of the influencing factors. Natural factors are difficult for humans to change and are the basic and limiting factors in the spatial distribution of HLTAs. Areas with superior natural conditions are excellent for the development of HLTAs, and this study explored the influencing factors from three perspectives: river hydrology, resource endowment, and topography. Social and economic factors are important driving factors for the spatial pattern of HLTAs and their evolution, as well as one of the important factors for spatiotemporal pattern divergence. Examples include economic development, transportation accessibility, and visitor markets.

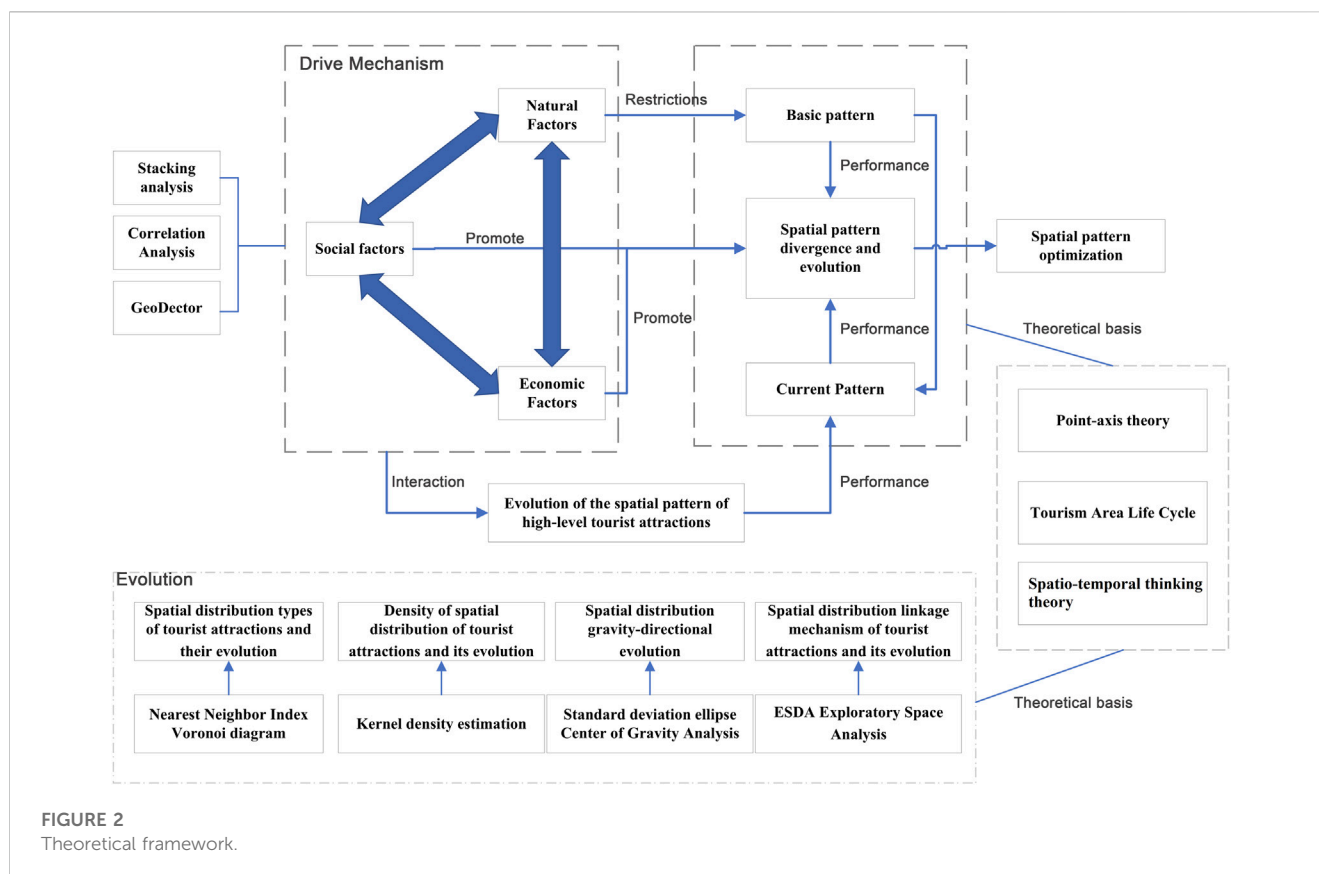
4.1 Natural factors

4.1.1 River system

The river system is an important element in the landscape and is the circulatory system of the watershed. Diverse water distribution conditions offer advantages as important carriers of tourism development in the Yellow River Basin. Tourism in the Yellow River Basin in Qing-Gan-Ning has developed and flourished because of water, which not only provides for the life and productivity of the coastal population but also provides high-quality resources for nature and humans. ArcGIS 10.8 was used to analyze the buffer zone of the main stream of the Qing-Gan-Ning Yellow River and its main tributaries (Duan et al., 2021). The analysis showed that the number of tourist attractions falling within the 3 km buffer zone was the highest, and the least number of locations fell within the 5-km buffer zone. From 2009 to 2021, 84, 140, and 204 locations fell into the three-level buffer zone on both sides of the main Yellow River and its major tributaries, accounting for 73.68%, 77.78%, and 68%, respectively. The remaining tourist attractions did not fall within the 10-km buffer zone. Combined with the nuclear density analysis in Figure 2 and the buffer zone analysis in Figure 6, it can be concluded that the spatial distribution of HLTAs in the Yellow River Basin has a strong connection with the distribution of river systems, which reflects a certain “hydrophilicity” and is one of the factors for the distribution of HLTAs along the Yellow River and the linear expansion along the Yellow River (Duan et al., 2019).

4.1.2 Resource endowment

Tourism resource endowment is the basis for the high-quality development of tourism in the Yellow River Basin. The spatial pattern of the HLTAs is an objective reflection of the elements of



tourism resources in a region (Qin et al., 2022). The Yellow River Basin in Qing-Gan-Ning is located in the transition zone between the second and the third terrain in China, with mountains, hills, and plains. The area has 155 basic types of distribution: grasslands, forests, lakes, rivers, wetlands, deserts, glaciers, and other crisscrossed natural landscapes. It is also the intersection area of multi-ethnic and multi-cultural heritage with deep historical and cultural heritage. The tourism resources of the three regions have continuity, correlation, and complementarity in spatial distribution with better resource endowment. There are primarily world natural cultural heritage sites, national parks, national natural parks, national tourist attractions, national historical and cultural cities, and other high-quality tourism resources. Resource endowment is also an important factor influencing the spatial and temporal patterns of HLTAs, as shown by the possible spatial clustering of HLTAs of the same type.

4.1.3 Topographical features

Topography is the basic skeleton of tourism tourist attractions (Qiu et al., 2021) and determines the type and distribution of tourist attractions to a certain extent. In ArcGIS 10.8, 2009, 2015, and 2021 high-level tourist attraction data were superimposed onto the watershed area digital elevation model (DEM) to obtain elevation and slope data for each high-level tourist attraction (Figure 6). In terms of slope, HLTAs are mostly distributed in areas with a slope of 0° – 10° , accounting for 67.34% of all HLTAs. In terms of altitude, 88.55% of HLTAs are distributed in areas with an altitude of 1,000 m–3,000 m, and only 11.11% are distributed in high-altitude

areas above 3,000 m. In other words, HLTAs are mostly distributed in areas with relatively low altitudes and flat terrain in the Loess Plateau, Qinghai-Tibet Plateau, and Loop Plain. The flat terrain is conducive to the layout and development of HLTAs.

4.2 Economic factors

4.2.1 Economic basis

Tourism is an economic activity that is directly impacted by the level of economic development. First, the economic base is important for the stable and healthy development of HLTAs. The economic base provides the necessary financial support for the planning, operation, product system construction, infrastructure, and talent introduction to the HLTA. In contrast, the rapid development of the regional tourism economy promotes the emergence of HLTAs and spatial agglomeration, which helps bring into play the radiation-driven role of tourism and deepens regional tourism cooperation, thus accelerating the growth of high-quality tourist attractions. The development and construction of HLTAs, and their spatial agglomeration, in turn, drive the development of the regional tourism economy.

4.2.2 Income level

The income level provides material guarantees for residents to travel and is an important driving force for the evolution of tourism spatial patterns. Between 2009 and 2021, with the rapid economic development of the Qing-Gan-Ning region, the living standards of residents improved significantly, and people had a higher pursuit of

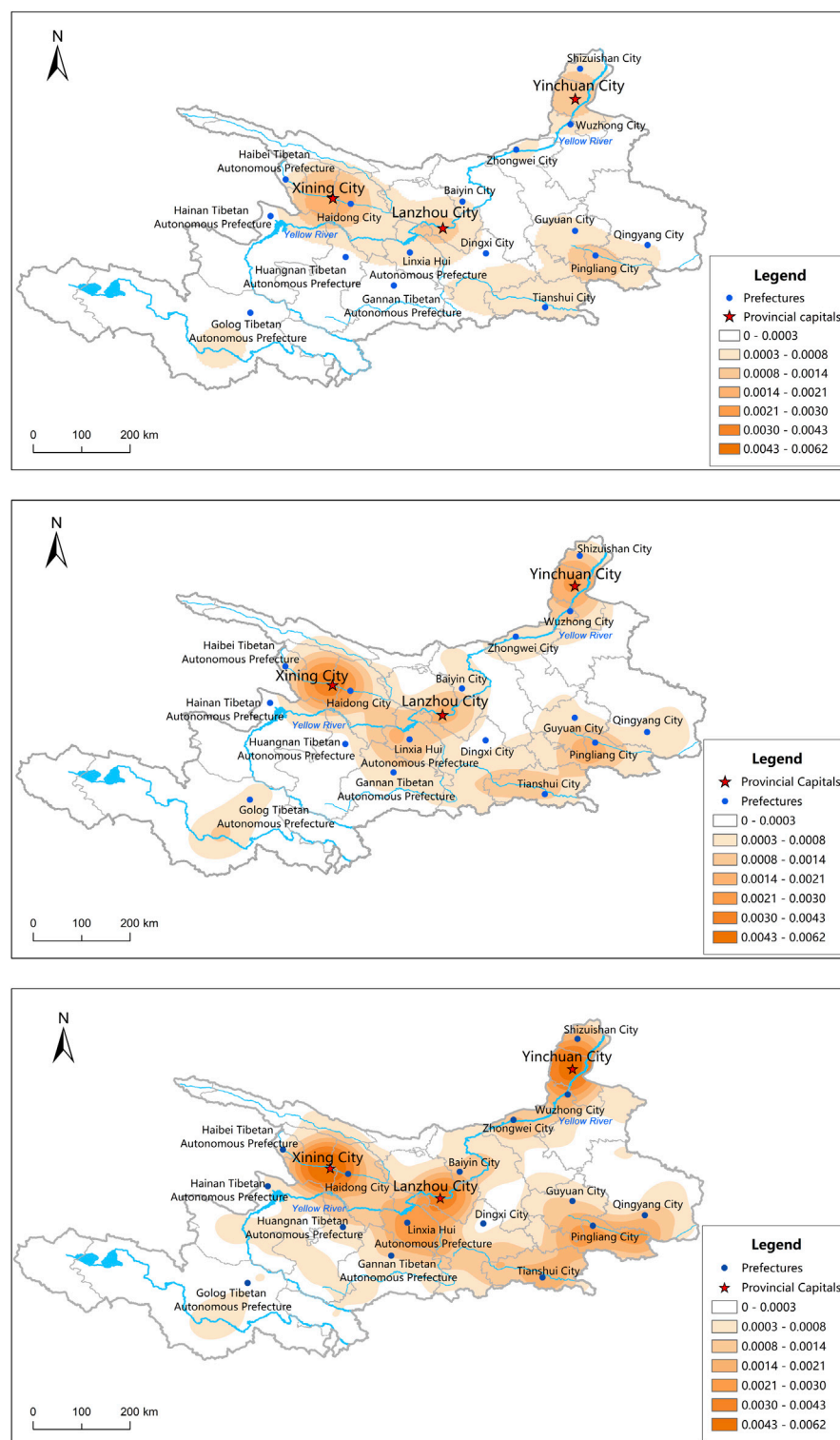


FIGURE 3

(A) is 2009's distribution of high-level tourist attractions kernel density in the region. (B) is 2015's distribution of high-level tourist attractions kernel density in the region. (C) is 2021's distribution of high-level tourist attractions kernel density in the region.

spiritual and cultural life. This brings about a change in consumption, which increases tourism demand, the willingness to travel, and tourism consumption expenditure to significantly

increase and promote the development of tourism. In the context of mass tourism, the income level of residents has a profound impact on the layout of HLTAs and tourism development.

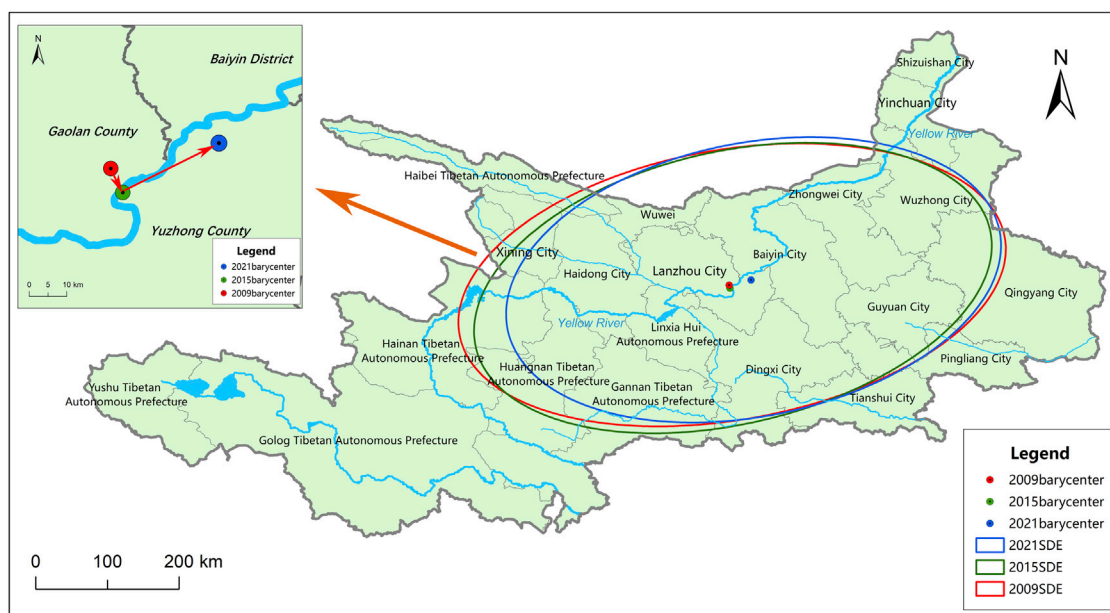


FIGURE 4
2009–2021 slice of high-level scenic spatial distribution of the center of mass and standard deviation ellipse.

4.2.3 Industry development level

The tourism industry's development level is an external expression of the evolution of regional tourism spatial patterns (Gan and Wang, 2021) and an important factor that constrains the high-quality development of tourism. The tourism development level is an important indicator of the level of utilization of tourism resources in a region. A good tourism industry foundation can promote the development of regional food, housing, transportation, tourism, shopping, entertainment, and related industries, which drive each other and, thus, promote the benign development of tourist attractions and bring about industrial agglomeration. In addition, a HLTA has high recreational value and attractiveness and often develops into key tourism development nuclei, which further influence the spatial pattern characteristics of tourist attractions. The level of industrial development is also an important factor affecting the spatial autocorrelation in HTAs. When the industrial development of each region is separate and lacks linkage, the industrial development status is further stretched, and there is no positive correlation in space.

Table 3 Using GDP *per capita*, disposable income *per capita*, and tourism income as measurement factors, the results show that the Pearson correlation was ≥ 0.3 and passed the significance test. The selected factors show moderate or higher correlation with the number of HTAs. In summary, the spatiotemporal pattern of HTAs is significantly influenced by economic factors.

4.3 Social factors

4.3.1 Policy support

Government orientation is an external regulatory force for the evolution of the tourism spatial structure. On one hand, the

dynamic management mechanisms and policy guidance of tourist attractions have a direct impact on the spatial pattern of HTAs. On the other hand, dynamic management mechanisms and policy guidance exert an impact by making tourism development plans, improving tourism-supporting facilities, broadening tourism investment and financing channels, deepening regional tourism cooperation, helping to create a diversified HLTA, providing policy support for tourism development, and realizing high-quality tourism development. The number of HTAs is increasing, the types of HTAs are becoming richer, the spatial layout is more reasonable, and financial investment and policy support from governments at all levels are indispensable.

4.3.2 Traffic network

The transportation network is a channel linking tourist sources and destinations, which enhances the accessibility of tourist locations by reducing the spatial and temporal distance effects, and, thus, the psychological distance of tourists from tourist locations, enhancing tourists' willingness to travel (38). It also has an important impact on the development and construction of tourism resources and the spatial distribution of HTAs, and is the "blood vessel" for the evolution of the spatial and temporal patterns of HTAs. Improving transportation networks improves the spatial agglomeration and spatial diffusion of HTAs, and promotes the transformation of HTAs into "point-line surfaces." Buffer zone analysis was conducted on the main national and provincial roads in the area. Buffer zone analysis showed that the number of HTAs within the buffer zone of major highways in 2009, 2015, and 2021 was 97, 151, and 257, respectively, accounting for 84.9%, 83.8%, and 85.6% of all HTAs in the area (Figure 7).

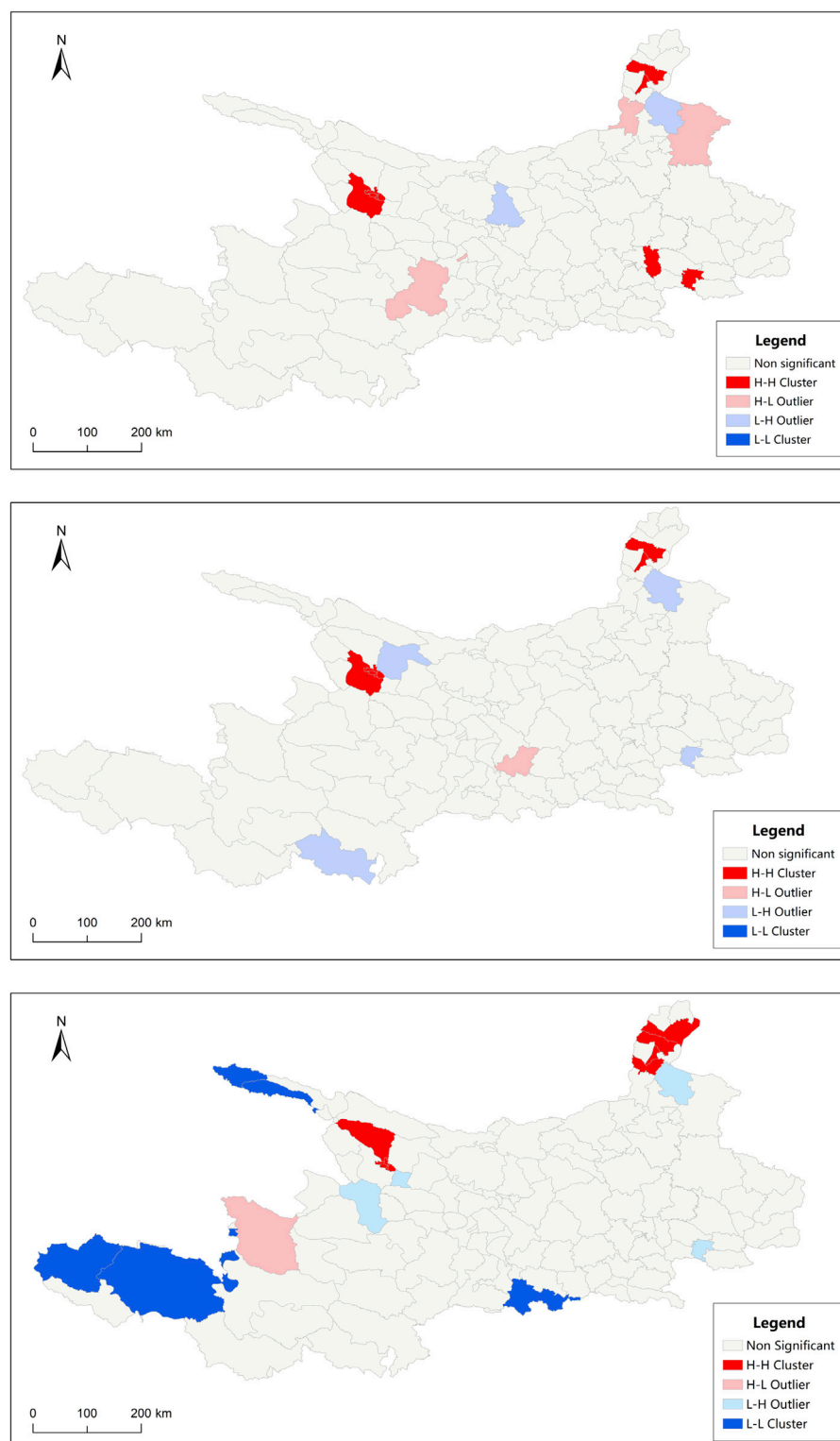


FIGURE 5

(A) is 2009's local spatial autocorrelation LISA map of the slice counties. (B) is 2015's local spatial autocorrelation LISA map of the slice counties. (C) is 2021's local spatial autocorrelation LISA map of the slice counties.

4.3.3 Guest market

Tourists influence the production and development of tourist attractions. As an important tourist destination, the spatial layout

of the HLTA is closely related to the source market and population distribution. With the development of mass tourism and tourism demand, residents of tourist attractions

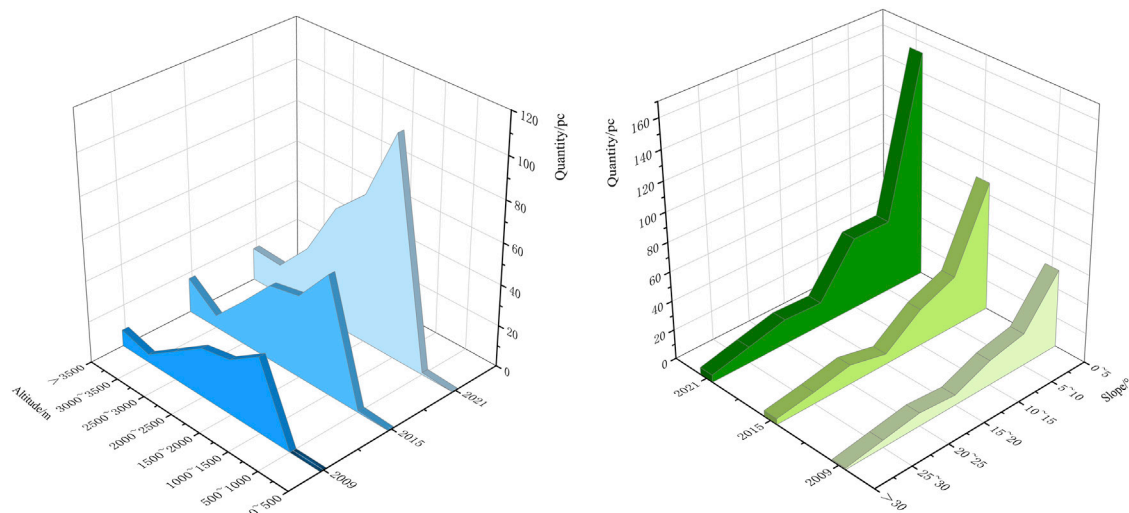


FIGURE 6

Elevation and slope distribution of HLTAs in the Qing-Gan-Ning region of the Yellow River Basin.

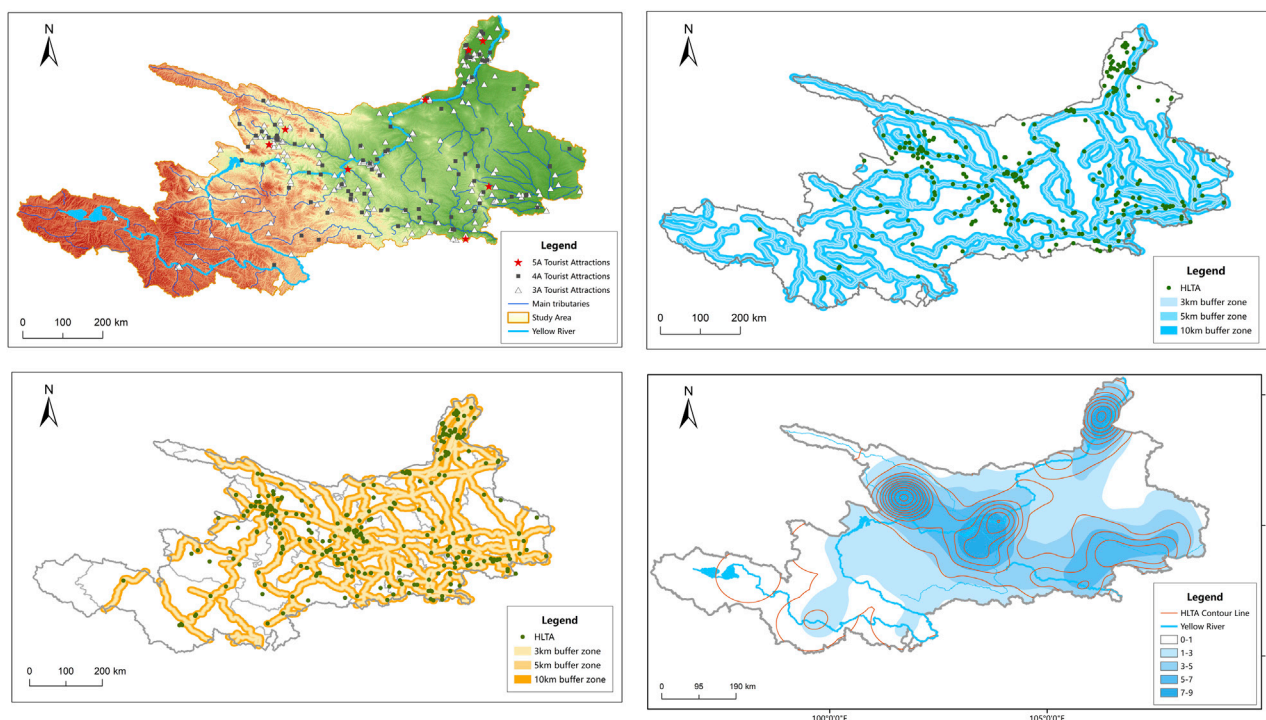


FIGURE 7

(A) is landforms overlay analysis of the impact factors of HLTAs. (B) is water system overlay analysis of the impact factors of HLTAs. (C) is road network overlay analysis of the impact factors of HLTAs. (D) is cities overlay analysis of the impact factors of HLTAs.

have become an important source of tourists for such locations. The resident population influences the scale of the local tourism market and the scale of related tourism practitioners to meet the operational needs of tourist attractions and also brings consumer groups and passenger flow support for tourist attractions. Represented by urban areas with a high population size and

consumption levels in the area, contours are generated based on the spatial distribution density of HLTAs and superimposed with the distribution density of municipal and county administrative centers in the area. The area with a high tourist attraction value distribution density has significant spatial coupling characteristics with the area with a high town distribution



FIGURE 8
Spatial pattern of tourism in the Qing-Gan-Ning region of the Yellow River Basin.

density. The trend of HLTAs in the Yellow River Basin relying on the town source market distribution is obvious. In addition, the distribution of towns and populations tends to be water-based and mostly distributed along rivers.

5 Geo-probe-based impact factor detection and interaction detection

5.1 Factor detection

These factors are verified using a GeoDetector. The data were clustered and discretized using the Jenks natural break method to generate the data type, and the influencing factors were introduced into the geographic probe to measure the influence of q -values and analyze the explanatory power of the factors influencing the spatial distribution pattern of HLTAs in Qing-Gan-Ning. Referring to the research results of scholars and the actual situation in the Qing-Gan-Ning region (Tang et al., 2019; Yao et al., 2019; Min et al., 2021), three major categories and 12 index systems were established. For this approach, X , Y , and Z are natural, economic, and social factors, respectively; X_1 is the resource endowment, X_2 is the altitude of the tourist attractions, X_3 is the distance from rivers, X_4 is the slope of the tourist attractions, Y_1 is the proportion of the three industries, Y_2 is the tourism income, Y_3 is the *per capita* disposable income, Y_4 is the urbanization rate, Z_1 is the resident population, Z_2 is tourism trips, Z_3 is fiscal policy support, and Z_4 is the distance from the traffic line. Yellow River Basin 2009 to 2021 HLTAs factors in the order of the size of explanatory factor q are tourism industry income (0.7274) > tourism trips (0.6743) > scenic slope (0.62) > scenic distance from road (0.52) > *per capita* disposable income of residents (0.5) > fiscal policy support (0.489) > tertiary industry share (0.471) > distance from river (0.462) > resource endowment (0.441) > tourist attraction elevation (0.44) > resident population (0.411) > urbanization rate (0.404). After classification,

economic (0.5257), social (0.5235), and natural factors (0.491) were identified (Table 4).

The q -values varied from year to year. From 2009 to 2021, the q -values of nine out of 12 factors affecting the spatial distribution of HLTAs showed an increase, indicating that the explanatory power of the influencing factors on the number of HLTAs is increasing. Three factors show a decline in both the q -value and the X_4 slope factor, indicating that the topography of the HLTAs is becoming richer and more diverse. The Y_2 disposable income of residents has less explanatory power for HLTAs, indicating that an increasing number of groups with average income participate in tourism, and the trend of mass tourism is significant. Z_2 tourist trips show a decline in the q -value, indicating that more tourists are no longer consuming tickets, and the consumption per unit tourist increased, indicating the gradual development of in-depth tourism that emphasizes the experience and the feeling.

5.2 Interaction detection

Interaction detection mainly analyzes whether there is an interaction effect between factors in the spatial distribution of HLTAs. When $q(x_1 \cap x_2) < \min(q(x_1), q(x_2))$, the interaction shows nonlinear weakening; if $\min(q(x_1), q(x_2)) < q(x_1 \cap x_2) < \max(q(x_1), q(x_2))$, the interaction shows single-factor nonlinear weakening; when $q(x_1 \cap x_2) > \max(q(x_1), q(x_2))$, the interaction shows one-factor nonlinear weakening; when $q(x_1 \cap x_2) > \max(q(x_1), q(x_2))$, the interaction shows one-factor nonlinear weakening. When $q(x_1 \cap x_2) > \max(q(x_1), q(x_2))$, the two show a two-factor enhancement, when $q(x_1 \cap x_2) = q(x_1) + q(x_2)$, they show independence, and finally, when $q(x_1 \cap x_2) > q(x_1) + q(x_2)$, they show a nonlinear enhancement.

Among the combinations of interaction probes (Table 5), the four groups that showed nonlinear enhancement were ($X_4 \cap Y_1$),

(Y1∩Y4), (Y1∩Z2), and (Y1∩Z4), where Y1 showed nonlinear enhancement with the other four factors. The interactions among the remaining 74 groups of factors showed a two-factor enhancement.

The results of interaction detection show that there is an interaction between any two influencing factors, which enhances the explanation of the spatial distribution of HLTAs. This indicates that the spatial and temporal evolution of the spatial pattern of HLTAs in the area is not only influenced by the natural environment, society, and economy but also that each factor interacts with the others to form the spatial distribution pattern of HLTAs.

6 Discussion

- (1) From the viewpoint of natural influencing factors, the spatial distribution pattern of HLTAs is influenced by natural factors such as resource endowment, topography, geomorphology, and hydrology. Therefore, regarding tour operators and tourist attractions, scientific and systematic planning and development of HLTAs should be conducted, and the development mode of tourist attractions should be changed to promote the rational allocation of resources oriented to the resource-product-market brand (Xiao et al., 2011).
- (2) From the perspective of economic and social factors, governments and policy-making authorities should first improve the construction of tourism-supporting infrastructure, establish a hierarchical transportation network, strengthen spatial connections, and enhance the accessibility and convenience of tourist attractions, continuing to promote overall economic and societal development. We should also raise income levels to increase the potential for residents' tourism consumption and provide a source market for HLTAs. Simultaneously, high-quality and comprehensive talent should be cultivated in the fields of culture and tourism to enhance the level of tourism services.
- (3) From the current regional development, the H-H areas can adopt the agglomeration-line diffusion development mode to create a high-standard demonstration area. The L-H and H-L areas can adopt the growth pole diffusion mode with bigger and more advantageous tourist attractions. The L-L areas can adopt the ecological-common promotion development mode with ecological priority and cross-area cooperation, a point to lead the line, a point to become a line, and a line to lead the surface, and break the low-low agglomeration situation, promoting the upgrade of tourism scenic spots to high-level tourism scenic spots (Chang et al., 2023).
- (4) We should establish cross-regional linkage development and tourism cooperation mechanism, give full play to the advantages of complementary resources, geographical proximity, and cultural commonality, and strengthen the linkage development between provinces, high-level scenic spots, and high-level scenic spots in the upper, middle, and lower reaches of the Yellow River. At the same time, we should actively cultivate the Internet + new tourism industry, accelerate the construction of high-level scenic site informationization, actively build intelligent scenic spots, and optimize intelligent

information systems. In addition, we should actively explore the creation of the Yellow River National Cultural Park brand, digging deeper into the local characteristics of culture, the Yellow River culture, ethnic culture, and promote the organic integration of cultural tourism.

- (5) Taking the Silk Road Economic Belt as an opportunity, with "one axis, two wings, three cores, and ten districts" as the blueprint, we suggest building the Yellow River Basin into a world-class golden cultural tourism belt to achieve high-quality tourism development (Yu and Chen, 2022).

"One axis" is the main development axis of the Yellow River. The Yellow River was used as a link to establish a cross-regional cooperation mechanism. The linkage development between provinces, HLTAs, and HLTAs on the Yellow River should be strengthened to realize the complementary advantages of regional tourism resources and the mutual delivery of tourists.

The "two wings" of the Yellow River are formed by its four first-class tributaries (i.e., Huangshui-Datong River and Weihe-Daxia River development wings). We suggest building the Yellow River-Silk Road intelligent tourism belt, including online and offline synergistic promotion and active cultivation of the "Internet + tourism" industry, enrichment of online tourism activity, and actively carrying out online and offline multiple image shaping, marketing, and intelligent tourist attraction construction (Figure 8).

The "three cores" are the provincial capitals of Qinghai, Gansu, and Ningxia (the capital). Xining, Lanzhou, and Yinchuan are the three major growth poles. The central city played a leading role in enhancing the radiation functions of the core area. In contrast, secondary tourism cities, such as Qinghai Haidong, Gansu Linxia, and Tianshui, should be developed to achieve an orderly and efficient tourism node in the hierarchical system.

The "ten districts" form the Qing-Gan-Ning 10 key tourism function board. We suggest enrichment and improvement of the product system. The Yellow River-theme tourism brands include Chinese civilization exploration, world heritage, ecological culture, non-foreign heritage culture, red gene inheritance, Yellow River peace, grotto culture, ancient capital new cities, and rural revitalization.

There are some shortcomings and uncertainties in this study. First, we selected the Qing-Gan-Ning region of the Yellow River Basin as the research area and the scope of the research area is relatively small. Future work should compare and analyze the HLTAs in the upper, middle, and lower reaches of the Yellow River. From the data source perspective, the social statistics are mostly from the municipal level, and the accuracy of the research on the micro level is poor. In terms of the influencing factors, the factors selected in this paper are not broad enough, and the influencing factors will vary from time to time and place to place. This study shows that the spatial pattern of high-level tourist attractions is formed by the interaction of natural, economic, and social factors, so there is uncertainty whether the high-level tourist attractions in the Qing-Gan-Ning region will continue to maintain the evolution of "point-like clustering and belt-like extension" in the next 6 years. Second, this study abstracts all the tourist attractions as "point-like elements," and there is uncertainty whether the abstraction as point-like elements will affect the accuracy of the research conclusions.

In the future, we will further study the influence mechanism based on microscale data, such as counties, to improve the accuracy of the research results and provide a scientific reference for the high-quality development of HLTAs in the Yellow River Basin.

7 Conclusion

This study investigated the spatial distribution and influencing factors of premium tourist attractions in the Qing–Gan–Ning region of the Yellow River Basin from 2009 to 2021. The main findings are the following. (1) Distribution type: in the nodal years, the premium scenic spots in the basin exhibited a cohesive distribution pattern. The nearest neighbor index values were 0.699, 0.70, and 0.618, with a coefficient of variation of Tyson polygons ranging from 131.8% to 203.5%. (2) Density and evolutionary trend: the density of premium sites per 10,000 km² during the nodal years was 27, 44, and 74, respectively. These sites showed a trend of point-like clustering and linear expansion, with the provincial capital and the Yellow River as the central elements. (3) Distribution center of mass and direction: the distribution center of mass for premium scenic spots was located in Yuzhong County, Gansu Province. The deflection angles ranged from 83.169° to 80.282°, aligning with the flow direction of the Yellow River. (4) Spatial autocorrelation: at the county scale, the distribution of premium scenic spots exhibited a piecewise pattern. The positively correlated areas had a wide distribution range, while the negatively correlated areas showed a point-like distribution. (5) Influencing factors: economic factors (0.5257) had the greatest impact on the spatial distribution of high-level scenic spots, followed by social factors (0.5235) and natural factors (0.491). The interaction among these factors demonstrated two-factor enhancement and nonlinear enhancement, shaping the final spatial distribution pattern of premium tourist attractions.

Data availability statement

The raw data supporting the conclusion of this article will be made available by the authors, without undue reservation.

References

- Bao, Y. F., Jiang, H. J., Ma, E., Sun, Z., and Xu, L. H. (2023). A longitudinal spatial-temporal analysis of ancient village tourism development in zhejiang, China. *Sustainability* 15, 143. doi:10.3390/su15010143
- Chang, B. R., Ding, X. J., Xi, J. C., Zhang, R. Y., and Lv, X. H. (2023). Spatial-temporal distribution pattern and tourism utilization potential of intangible cultural heritage resources in the yellow river basin. *Sustainability* 15, 2611. doi:10.3390/su15032611
- Chen, H., Lu, L., and Zheng, S. T. (2011). The tourism spatial pattern evolution of the pearl river delta. *Acta Geogr. Sin.* 66, 1427–1437. doi:10.3724/SP.J.1011.2011.00415
- Cheng, Z. H., and Niu, L. Q. (2016). Measurement on the attitude of ecotourists towards the management means of scenic resort based on the environmental cognition. *Hum. Geogr.* 31, 136–144. doi:10.13959/j.issn.1003-2398.2016.02.021
- Duyckaerts, C., and Godefroy, G. (2000). Voronoi tessellation to study the numerical density and the spatial distribution of neurons. *J. Chem. Neuroanat.* 20, 83–92. doi:10.1016/S0891-0618(00)00064-8
- Duan, W. L., Chen, Y. N., Zou, S., and Nover, D. (2019). Managing the water-climate-food nexus for sustainable development in Turkmenistan. *J. Clean. Prod.* 220, 212–224. doi:10.1016/j.jclepro.2019.02.040
- Duan, W. L., Maskey, S., Chaffe, P., Luo, P. P., He, B., Wu, Y., et al. (2021). Recent advancement in remote sensing technology for hydrology analysis and water resources management. *Remote Sens.* 13, 1097. doi:10.3390/rs13061097
- Fyall, A., Leask, A., Barron, P., and Ladkin, A. (2017). Managing Asian attractions, generation y and face. *J. Hosp. Tour. Manag.* 32, 35–44. doi:10.1016/j.jhtm.2017.04.006
- Gan, C., and Wang, K. (2021). Spatial distribution pattern and influencing factors of high-quality tourist attractions in wuling moun-tains area. *Resour. Environ. Yangtze Basin* 30, 2115–2125. doi:10.11870/cjlyzyyhj202109007
- Grayson, K., and Martinec, R. (2004). Consumer perceptions of iconicity and indexicality and their influence on assessments of authentic market offerings. *J. Consumer Res.* 31, 296–312. doi:10.1086/422109
- Gu, Y. Q., Yang, J., Feng, X. L., Li, C., and Li, X. M. (2015). Spatial differentiation of human settlement environment suitability in Chinese typical tourist cities. *Sci. Geogr. Sin.* 35, 410–418. doi:10.13249/j.cnki.sgs.2015.04.410
- Guedes, A. S., and Jiménez, M. I. M. (2015). Spatial patterns of cultural tourism in Portugal. *Tour. Manag. Perspect.* 16, 107–115. doi:10.1016/j.tmp.2015.07.010

Author contributions

Conceptualization: RS. Formal analysis: RS. Methodology: RS and YY. Investigation: RS. and YY. Writing—original draft preparation: RS and YY. Writing—review and editing: JX and XK. Visualization: RS and YY. Supervision: JX. Funding acquisition: JX. All authors contributed to the article and approved the submitted version.

Funding

This research was supported by the Social Science Planning Project of Qinghai Province (grant No. 2022Y012), the Social Science Planning Project of Qinghai Province (grant No. 2022ZCY033), and the Applied Basic Project of Qinghai Science and Technology Department (grant No. 2018-ZJ-789).

Acknowledgments

The researchers would like to express their gratitude to the reviewers. Their valuable suggestions to improve the quality of this paper are appreciated. We thank Editage for its linguistic assistance during the preparation of this manuscript.

Conflict of interest

The authors declare that the research was conducted in the absence of any commercial or financial relationships that could be construed as a potential conflict of interest.

Publisher's note

All claims expressed in this article are solely those of the authors and do not necessarily represent those of their affiliated organizations, or those of the publisher, the editors, and the reviewers. Any product that may be evaluated in this article, or claim that may be made by its manufacturer, is not guaranteed or endorsed by the publisher.

- Guo, Q., Zhong, Y., Li, J., Wang, Q., and Huang, Z. (2012). The research on the spatial structure of a-grade tourist districts in poyang lake eco-economic zone. *J. Jiangxi Normal Univ. Sci. Ed.* 36, 646–652. doi:10.16357/j.cnki.issn1000-5862.2012.06.002
- Hao, Z., Ye, D., Hui, W., Han, Z. L., and Wang, H. Y. (2022). An empirical analysis of tourism eco-efficiency in ecological protection priority areas based on the dpsir-sbm model: A case study of the yellow river basin, China. *Ecol. Inf.* 70, 101720. doi:10.1016/j.ecoinf.2022.101720
- Jaafar, M., Noor, S. M., and Rasoolimanesh, S. M. (2015). Perception of young local residents toward sustainable conservation programmes: A case study of the lenggong world cultural heritage site. *Tour. Manag.* 48, 154–163. doi:10.1016/j.tourman.2014.10.018
- Kang, S., Lee, G., Kim, J., and Park, D. (2018). Identifying the spatial structure of the tourist attraction system in South Korea using gis and network analysis: An application of anchor-point theory. *J. Destination Mark. Manag.* 9, 358–370. doi:10.1016/j.jdmm.2018.04.001
- Li, D. H., Zhang, X. Y., Lu, L., Zhang, X., and Li, L. (2020). Spatial distribution characteristics and influencing factors of high-level tourist attractions in the yellow river basin. *Econ. Geogr.* 40, 70–80. doi:10.15957/j.cnki.jjdl.2020.05.008
- Li, Y., Caixia, S., and Binggeng, X. (2019). Temporal and spatial pattern evolution characteristics and driving factors of national wetland parks in the yangtze river basin. *Econ. Geogr.* 39, 194–202. doi:10.15957/j.cnki.jjdl.2019.11.023
- Li, Y. J., Chen, T., and Wang, J. (2013). Spatial structure of tourism attractions in qiangdongnan prefecture. *Resour. Sci.* 35, 858–867.
- Liao, Z. J., and Zhang, L. J. (2021). Spatial distribution evolution and accessibility of a-level scenic spots in guangdong province from the perspective of quantitative geography. *Plos One* 16, e0257400. doi:10.1371/journal.pone.0257400
- Lin, C. H., Chen, J. Y., Hsu, S. S., and Chung, Y. H. (2014). Automatic tourist attraction and representative icon determination for tourist map generation. *Inf. Vis.* 13, 18–28. doi:10.1177/1473871612472177
- Liu, D. J., Hu, J., and Chen, J. Z. (2014). The spatial structure and disparities of leisure tourism destinations in wuhan. *Econ. Geogr.* 34, 176–181. doi:10.15957/j.cnki.jjdl.2014.03.028
- Ma, L., Ma, Y. F., and Lin, Z. H. (2013). A comparative study of the spatial structure of 100 tourism attractions. *Resour. Sci.* 35, 296–303.
- Ma Xf, Y. X. (2019). Spatio-temporal distribution of high-level tourist attractions and spatial heterogeneity of its influencing factors in Western hunan. *J. Nat. Resour.* 34, 1902–1916. doi:10.31497/zrxyxb.20190908
- Min, W., Mei, H., Guozhong, C., Lixin, T., and Xianglun, K. (2021). Spatial distribution changes and influencing factors of A-level tourist attractions based on geodetector. *Chinese J. Popul. Resour. Environ.* 31 (8), 166–176. doi:10.12062/cpre.20210436
- Qin, J. X., Duan, W. L., Chen, Y. N., Dukhovny, V. A., Sorokin, D., Li, Y., et al. (2022). Comprehensive evaluation and sustainable development of water-energy-food-ecology systems in central Asia. *Renew. Sustain. Energy Rev.* 157, 112061. doi:10.1016/j.rser.2021.112061
- Qiu, Y. H., Yin, J., Zhang, T., Du, Y. M., and Zhang, B. (2021). Spatiotemporal dynamic analysis of a-level scenic spots in guizhou province, China. *Isprs Int. J. Geo-Information* 10, 568. doi:10.3390/ijgi10080568
- Samitas, A., Asteriou, D., Polyzos, S., and Kenourgios, D. (2018). Terrorist incidents and tourism demand: Evidence from Greece. *Tour. Manag. Perspect.* 25, 23–28. doi:10.1016/j.tmp.2017.10.005
- Tang, C. C., Sun, M. Y., and Wan, Z. W. (2019). Spatial distribution characteristics of high-level scenic spots and its influencing factors in beijing-tianjin-hebei urban agglomeration. *Econ. Geogr.* 39, 204–213. doi:10.15957/j.cnki.jjdl.2019.10.025
- Wang, T., Wang, L., and Ning, Z. Z. (2020). Spatial pattern of tourist attractions and its influencing factors in China. *J. Spatial Sci.* 65, 327–344. doi:10.1080/14498596.2018.1494058
- Weber, J., and Sultana, S. (2013). Why do so few minority people visit national parks? Visitation and the accessibility of “America’s best idea”. *Ann. Assoc. Am. Geogr.* 103, 437–464. doi:10.1080/00045608.2012.689240
- Weng, G. M., Shen, K., and Pan, Y. (2021). Spatial differentiation characteristics and formation mechanism of rural tourism destinations in China: based on 1000 key rural tourism villages. *Geogr. Geo-Information Sci.* 37, 99–105. doi:10.3969/j.issn.1672-0504.2021.04.014
- Wu, L. M., Huang, Z. F., Zhou, W., and Fang, Y. L. (2013). The spatiotemporal evolution and dynamic mechanism of a-grade tourist attractions in jiangsu province. *Econ. Geogr.* 33, 1158–1164. doi:10.15957/j.cnki.jjdl.2013.08.027
- Wu, Q., Li, X. G., Wu, L., and Chen, S. (2017). Distribution pattern and spatial correlation of a-grade tourist attractions in hunan province. *Econ. Geogr.* 37, 193–200. doi:10.15957/j.cnki.jjdl.2017.02.026
- Wu, T. H., Zhang, J., and Li, W. J. (2009). The spatial pattern evolution of the inbound tourism economic development level and the causes in China—Based on the inbound tourism economic entropy analysis. *J. Arid Land Resour. Environ.* 23, 189–194. doi:10.13448/j.cnki.jalre.2009.05.037
- Wu, X. Y., and Chen, C. Y. (2022). Spatial distribution and accessibility of high level scenic spots in inner Mongolia. *Sustainability* 14, 7329. doi:10.3390/su14127329
- Xiao, J., Cao, G., Hou, G., Zhao, R., Fang, Y., Gao, R., et al. (2011). The development of geopark ecotourism in the Qinghai-Tibet Plateau: A case study of the kanbula national geopark. *Acta Geosci. Sin.* 19, 225–234. doi:10.1007/s10577-011-9192-9
- Xiaoxiao, L., Peiji, S., and Ruidong, Z. (2018). Spatial network structure and optimization of self-help tourism in gansu-qinghai-ningxia region. *J. Arid Land Resour. Environ.* 32, 197–203. doi:10.13448/j.cnki.jalre.2018.387
- Xinyue, W., and Juanjuan, H. (2016). Spatial distribution features and influence factors of rural leisure tourism destinations in shandong province. *Sci. Geogr. Sin.* 36, 1706–1714. doi:10.13249/j.cnki.sgs.2016.11.013
- Yang, Z., Tian, J., Li, W., Su, W., Guo, R., et al. (2021). Spatio-temporal pattern and evolution trend of ecological environment quality in the yellow river basin. *Acta Ecol. Sin.* 41, 7627–7636. doi:10.5846/stxb202012083131
- Yang, Z., Yin, M., Xu, J., and Lin, W. (2019). Spatial evolution model of tourist destinations based on complex adaptive system theory: A case study of southern anhui, China. *J. Geogr. Sci.* 29, 1411–1434. doi:10.1007/s11442-019-1669-z
- Yao, Y. J., Jing, H., and Liu, D. J. (2019). Spatial evolution and influence mechanism of a-level scenic spots in urban agglomeration in the middle reaches of the yangtze river. *Econ. Geogr.* 39, 198–206. doi:10.15957/j.cnki.jjdl.2019.01.024
- Yu, X., and Chen, H. X. (2022). Study on coupling coordination of the human settlement environment and tourism industry in the yellow river basin. *Front. Environ. Sci.* 10. doi:10.3389/fev.2022.1016839
- Yuan, C., Hou, Z., and Chen, J. (2015). Biocompatibility of Mn_{0.4}Zn_{0.6}Fe₂O₄ magnetic nanoparticles and their thermotherapy on VX2-carcinoma-induced liver tumors. *Areal Reseach Dev.* 32, 74–84. doi:10.1166/jnn.2015.9150
- Zha, A., and Qiu, J. (2015). Recreational value assessment on hangzhou west lake scenic area based on travel cost. *Tour. Sci.* 29, 366–373. doi:10.16323/j.cnki.lykx.2015.05.004
- Zhan, M. S., and Zhu, J. H. (2019). Spatial planning of qingyun mountain scenic spot in benxi, northeast China based on ecological sensitivity assessment. *Ying Yong Sheng Tai Xue Bao = J. Appl. Ecol.* 30, 2352–2360. doi:10.13287/j.1001-9332.201907.037
- Zhang, C., Weng, S., and Bao, J. (2020a). The changes in the geographical patterns of China’s tourism in 1978–2018: Characteristics and underlying factors. *J. Geogr. Sci.* 30, 487–507. doi:10.1007/s11442-020-1739-2
- Zhang, H., Duan, Y., and Han, Z. (2021). Research on spatial patterns and sustainable development of rural tourism destinations in the yellow river basin of China. *Land* 10, 849. doi:10.3390/land10080849
- Zhang, J. S., and Wang, F. F. (2007). Principles and application of using entropy-weight-based multiple-destination travel cost method to evaluate the tourism value of recreation resources: A case study of wuyishan. *J. Nat. Resour.* 22, 28–36. doi:10.3321/j.issn:1000-3037.2007.01.004
- Zhang, S., Zhang, G., and Ju, H. (2020b). The spatial pattern and influencing factors of tourism development in the yellow river basin of China. *Plos One* 15, e0242029. doi:10.1371/journal.pone.0242029
- Zhang, X., Cheng, S., and Sun, Y. (2018). Spatial distribution characteristics and influence factors of high-grade tourism resources in yangtze river economic belt. *Areal Res. Dev.* doi:10.3969/j.issn.1003-2363.2018.05.017
- Zhu, H., and Chen, X. L. (2008). Space distribution structure of a-grade scenic spot in China. *Sci. Geogr. Sin.* 28, 607–615. doi:10.13249/j.cnki.sgs.2008.05.607
- Zhu, S. D., Bai, Z. Y., Gan, Z. T., Jin, S. L., Zhang, C., and Wang, J. (2022). Simulation of the spatial pattern of scenic spots combining optimal scale and deep learning. *Front. Earth Sci.* 10. doi:10.3389/feart.2022.887043
- Zhu, Y., Halik, W., and He, C. (2017). Spatial heterogeneity and optimization strategies of tourism attractions in xinjiang based on the gwr mode. *J. Nat. Sci. Hunan Normal Univ.* 40, 1–8. doi:10.7612/j.issn.1000-2537.2017.06.001



OPEN ACCESS

EDITED BY

Cletah Shoko,
University of the Witwatersrand,
South Africa

REVIEWED BY

Aliya Baidourela,
Xinjiang Agricultural University, China
Sheng Hu,
Northwest University, China

*CORRESPONDENCE

Jiang Wu
✉ dbwujiang@126.com

RECEIVED 16 March 2023

ACCEPTED 21 July 2023

PUBLISHED 25 August 2023

CITATION

Wu J, Han S, Shi L and Hui Q (2023)
Study on the spatial variability of
thermal landscape in Xi'an based on
OSM road network and POI data.
Front. Ecol. Evol. 11:1187591.
doi: 10.3389/fevo.2023.1187591

COPYRIGHT

© 2023 Wu, Han, Shi and Hui. This is an
open-access article distributed under the
terms of the [Creative Commons Attribution
License \(CC BY\)](https://creativecommons.org/licenses/by/4.0/). The use, distribution or
reproduction in other forums is permitted,
provided the original author(s) and the
copyright owner(s) are credited and that
the original publication in this journal is
cited, in accordance with accepted
academic practice. No use, distribution or
reproduction is permitted which does not
comply with these terms.

Study on the spatial variability of thermal landscape in Xi'an based on OSM road network and POI data

Jiang Wu^{1*}, Shenshan Han¹, Leijie Shi² and Qun Hui³

¹College of Geography and Environment, Xianyang Normal University, Xianyang, China,

²Urban Planning and Design Research Institute, The Engineering Design Academy of Chang'an University Co. Ltd., Xi'an, China, ³R&D and Quality Inspection Department, Shaanxi Dibo Jingyuan Surveying and Mapping Geographic Information Co., Ltd, Xi'an, China

As the primary contributor to the urban heat island effect, the construction land can be used to understand the spatial variation characteristics of the thermal landscape within the city at the microscopic scale. Taking the main urban area of Xi'an as the study area, this paper divides the minimum urban land unit by using OpenStreetMap (OSM) road network data and employs the kernel density analysis method based on Point of interest (POI) data to construct seven types of urban functional blocks. Furthermore, this paper also establishes a thermal landscape footprint characterization model to investigate the impact range of thermal landscape footprint for various types of functional blocks and quantitatively evaluate the spatial variation characteristics of urban thermal landscape, which is of great significance to the enhancement of urban ecological environment. The study indicates that: (1) The spatial distribution of urban functional blocks presents highly coupled characteristics with POI kernel density. (2) The surface thermal landscapes of seven types of urban functional blocks are predominantly medium-temperature and sub-high-temperature pixels, with the mean values of thermal fields ranked as logistics and storage blocks > industrial development blocks > transportation hub blocks > comprehensive service blocks > residential and living blocks > commercial and business blocks > strategic reserved blocks. (3) Apart from the strategic reserved blocks, the remaining urban functional blocks can produce thermal diffusion phenomena to the surrounding areas, and their thermal landscape footprints are obviously differentiated, with their influence ranges ranked as industrial development blocks > logistics and storage blocks > comprehensive service blocks > residential and living blocks > commercial and business blocks > transportation hub blocks. The findings of the study can provide scientific guidance for both the enhancement of urban ecological environment as well as the rational planning and layout of the city.

KEYWORDS

POI, OSM, thermal landscape, urban functional blocks, spatial variation

1 Introduction

The fundamental concept of “urban heat island” is defined as a phenomenon in which the temperature inside the city is significantly higher than that in the surrounding suburbs, and is mainly influenced by both natural and anthropogenic factors (Manley, 1958). As global warming intensifies over the years and urbanization continues to increase, the emergence of a series of issues such as resource shortage, environmental degradation, traffic congestion, and excessive population density has had a remarkable negative impact on urban development. In this regard, the “13th Five-Year Plan” for National Ecological Protection has pointed out that one of the major ecological issues faced by China is the limited role of urban ecosystems in mitigating the thermal environmental effects of cities. Furthermore, the “14th Five-Year Plan” also explicitly proposed to improve the planning and coordination mechanism in the field of ecological civilization, to build an ecological civilization system, and to promote the comprehensive green transformation of economic and social development. Against this background, mitigating the urban heat island effect has already become a critical link in promoting the well-being of humankind, new urbanization construction as well as green economic development.

Cities are the geospatial carriers of production and social activities conducted by human in the process of social development. Consequently, various ecological and environmental issues that arise in the urbanization process are closely related to the anthropogenic role of urban landscape patterns. Geographically, urbanization can be manifested as a change in the structure and function of land use/surface cover types, which is specifically characterized by the transformation of natural landscapes such as vegetation and water systems into artificial underlying surface composed of elements such as cement, asphalt and metals (Zhuang et al., 2019). During this process, the evapotranspiration of vegetation is diminished, the ground heat radiation, heat transfer and heat storage are changed, combined with the release and transmission of anthropogenic heat from human activities, resulting in significant effects on the spatial distribution of the urban thermal environment (Li et al., 2012; Chen et al., 2013; Yue and Xu, 2013; Rossi et al., 2014). As an interdisciplinary research field of geography, ecology and economics, urban thermal environment mainly involves various directions such as quantitative methods (Wan and Li, 1997; Qin et al., 2001), spatial and temporal evolution characteristics (Yao et al., 2017; Qiao et al., 2019), driving factors (Giorgio et al., 2017; Singh et al., 2017; Zheng and Weng, 2018) and different scales (Orlanski, 1975) according to the differences in the emphasis of each research direction. This paper mainly discusses the spatial variation of urban thermal landscape based on microscopic scale.

Abundant research findings have been achieved by a large number of scholars both domestically and internationally around the impact of land use/cover change on the urban thermal environment. Estoque et al. (2017) analyzed the relationship between surface temperature and impervious surface and greenfield spatial patterns in metropolitan areas such as Bangkok, Jakarta, and Manila. The findings indicated that the

average surface temperature showed a significant positive correlation with impervious surfaces and was about 3 degrees Celsius higher than that of greenfield areas (Estoque et al., 2017). Singh et al. (2017) explored the effect of land use change on the urban thermal field, and the findings indicated that the temperature in areas with dense buildings was significantly higher than that in areas covered by vegetation and water bodies, and the ecological index was worst in highly urbanized areas in the central part of the city. Through analyzing the dynamic change characteristics of urban heat island effect and the relationship between heat island effect and land change in Wuhan City in the last 10 a, Liu et al. (2017) showed that the heat island area presented a trend of expansion from the old city to the new city, and the increase in the area of construction land was an important influencing factor for the expansion of urban heat island intensity area. According to the investigation of the relationship between the distribution of heat island effect grades and land cover types in three cities of Jinan, Wuhan and Chongqing by Yi et al. (2018), it was found that urban construction land was the major contributor to the urban heat island effect, however, the land cover types that could best mitigate the urban heat island effect were not exactly the same. Guo et al. (2020) revealed that NDBI was highly correlated with surface temperature *via* analyzing the relationship between changes in different land use types and surface temperature in Ganjingzi District, Dalian City, and that the expansion of urban areas had a greater role in influencing the thermal environment. By using Xi'an city as the study area, Huang et al. (2022) conducted a systematic analysis of the relationship among changes in land use scale, structure and morphology and changes in the thermal environment, whose findings pointed out that changes in the area share of arable land and construction land were positively correlated with changes in surface temperature, and that the high dominance and agglomeration of the patchy landscape of these two was a critical factor in the increase in surface temperature and the deterioration of the thermal environment, while forest and grassland as well as water bodies had a significant cooling effect (Huang et al., 2022). Qiao et al. (2022) proposed an algorithm for the contribution of urban thermal environment change based on land use type, and quantified the contribution of land use type change to urban thermal environment change for each city in the Beijing-Tianjin-Hebei urban agglomeration on this basis. Furthermore, the study also pointed out that the contribution of arable land, urban construction land and rural settlements to urban thermal environment change was more significant, and the unit contribution intensity of human activities to urban thermal environment change was much higher than that of natural climate (Qiao et al., 2022). To summarize, as a collection containing various types of land (residential land, public administration and public service land, commercial and service land, industrial and mining land, etc.), the significant influence of construction land on the spatial distribution of urban thermal environment is self-explanatory. By studying the influence of different types of construction land on the urban thermal landscape, the spatial variation characteristics of the thermal landscape within the city can be learned at the microscopic scale, which provides scientific guidance for the improvement of the

urban ecological environment and the rational planning and layout of the city.

Over recent years, numerous scholars have been using point-of-interest (POI) (Zhang et al., 2021; Li et al., 2022), social media data (Chen et al., 2018; He et al., 2020), mobile phone signaling data (Zhong et al., 2017; Wang et al., 2020), vehicle trajectory data (Yang et al., 2020) and other massive amounts of big data for “urban computing” (Zheng, 2015), to achieve urban functional block identification, population movement characteristics research, and so forth. In particular, the POI is a point-like spatial data for representing geographical entities (government, schools, hospitals, shops, neighborhoods, etc.) in GIS, each of which consists of objective attribute features (name, address, type, etc.) and location features, and the geographical entities it represents are mostly the primary places of human activities in the city. By recording the precise geographical coordinates of urban facilities and quantitative information on human activities, this data can reflect the intensity and type of human activities at a fine scale. According to existing studies on urban heat island effect, POI data can reflect the heat source intensity of human activities in cities, and can be complemented with remote sensing imagery as an effective data source for fine-scale studies on the urban heat island (Han et al., 2017). On this basis, this paper identifies different types of functional blocks in the city based on POI data, and studies the spatial variability characteristics of the thermal landscape of different functional blocks in the city. The identification of urban functional blocks requires the acquisition of the minimum urban land unit, and in urban planning and design, the land unit formed by road network connections is generally taken as the fundamental urban unit. The land unit divided on the basis of the road network takes into account the actual distribution of urban roads and, for the identification of urban functional blocks, units with the same socio-economic function are more meaningful and the block division is more reasonable.

With the main urban area of Xi'an as the study area, this study uses Landsat 8 remote sensing imagery to invert the urban surface

temperature and divides the minimum urban land unit by using OpenStreetMap (OSM) road network data. Meanwhile, this study also combines the urban zoning standards of territorial spatial planning, constructs seven types of urban functional blocks by using the kernel density analysis method based on POI data, and creates the thermal landscape footprint characterization model. Moreover, this study also investigates the impact range of the thermal landscape footprint of each type of functional blocks, quantitatively evaluates the spatial variation characteristics of the urban thermal landscape, and achieves the exploration of the urban thermal landscape from the whole to the local and from the macro to the micro, which is of great significance to the enhancement of the urban ecological environment.

2 Data and methods

2.1 Overview of the study area

The study area of this paper covers the main urban area of Xi'an, which is mainly the area within the Xi'an Ring Expressway, including seven districts within Xi'an (Xincheng District, Beilin District, Lianhu District, Weiyang District, Yanta District, Baqiao District and Chang'an District) as well as a small part of Qindu District in Xianyang City, with a total area of about 457km². Located in the Guanzhong Basin in the central Weihe River Basin, Xi'an is characterized by a warm-temperate semi-humid continental monsoon climate with warm and dry springs, hot and rainy summers, mild autumns, and cold and foggy winters. The schematic diagram of the study area is shown in Figure 1.

With the rapid development of the city in recent years, Xi'an has faced increasingly serious ecological and environmental issues, with high temperatures in summer hitting record levels several times. In 2017, Xi'an became the first provincial capital city whose high temperature in summer exceeded 40°C and ranked among the top three cities in China in terms of the number of high temperature

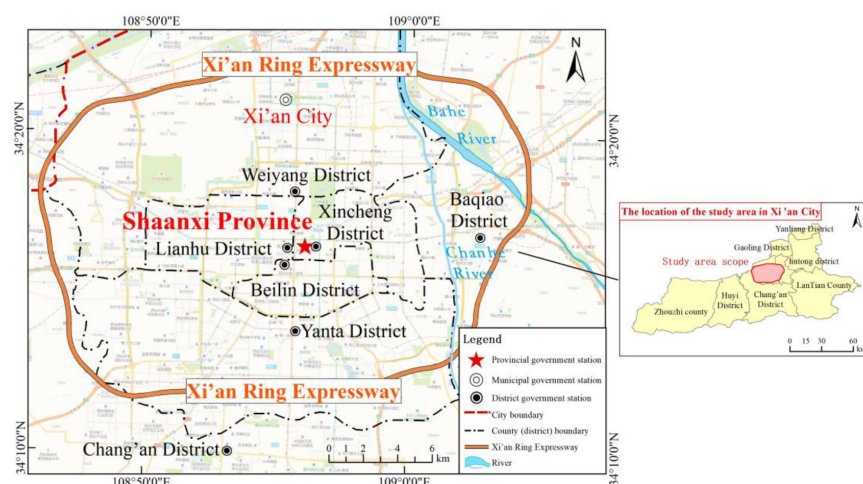


FIGURE 1
Overview of the study area.

days in a row. Hence, it is of great significance to study the evolutionary characteristics of the thermal landscape in the main urban area of Xi'an and propose mitigation measures.

2.2 Data sources

2.2.1 Remote sensing data

This paper used the Landsat 8 remote sensing imagery data (satellite orbit number Path&Row: 127-365) to perform the inversion of the surface temperature of Xi'an City. Based on the imaging, this study selected the imagery of May 30, 2021, with the satellite transit time around 03:19 (GMT+8). The imagery data were of high quality at this time and were basically cloud-free within the study area, which could better reflect the actual conditions of the surface. The Landsat imagery data were downloaded from the United States Geological Survey (USGS) website (<https://glovis.usgs.gov>) and were pre-processed for radiometric calibration and atmospheric correction.

This article selects MODIS land surface temperature product MOD11A1 to verify the accuracy of the surface temperature retrieved from Landsat data. Its spatial resolution is 1km, and its temporal resolution is 1 day, including daytime and nighttime temperatures. MODIS data is downloaded from the United States Geological Survey website (<https://glovis.usgs.gov>).

2.2.2 POI data

The POI data (including name, type and coordinate attributes) used in this paper were all programmatically captured through the application programming interface provided by Baidu Maps and were obtained on June 1, 2021. A total of 165,739 POI data in JSON format of 28 types, including restaurants, shopping centers, schools, residences, and others, were captured under the coordinate system of Baidu Maps. After analyzing the JSON data, this study obtained the POI point vector data in ESRI Shape format and established the geographic coordinate system.

OSM road network data: OSM is designed to provide users with free and easily accessible digital map resources, and is the most preferred spontaneous geographic information at present. OSM road data has high accuracy in positioning and topology, and can be downloaded from the official website of OpenStreetMap.

2.3 Methods

2.3.1 Surface temperature inversion

The mono-window algorithm was derived by Qin et al. (2001) as an algorithm to invert the surface temperature using the Landsat TM/ETM+ 6th band data based on the surface thermal radiation transport and conduction equation, which requires three parameters: the average atmospheric operating temperature, the atmospheric transmittance, and the surface emissivity. The calculation formula is as follows:

$$T_s = [a(1 - C - D) + (b(1 - C - D) + C + D)T_6 - DT_a]/C \quad (1)$$

Where T_s is the actual surface temperature (K); a and b are constants, being -67.355351 and 0.458606 , respectively; C and D are intermediate variables, $C = \epsilon\tau$ and $D = (1 - \tau)[1 + (1 - \epsilon)\tau]$, in which ϵ is the surface emissivity and τ is the atmospheric transmittance; T_6 is the brightness temperature (K) of the pixel detected by the sensor at the satellite altitude; T_a is the average atmospheric operating temperature.

In order to verify the surface temperature results obtained from inversion, this paper used MODIS data from the corresponding time period, with imaging time on the same day as Landsat data. Meteorological station data is discrete data, and there are few stations with uneven distribution. Considering the difficulty and practicality of data acquisition, this article does not use meteorological station data as the verification object. Due to the MODIS data resolution of 1km and the Landsat inversion of surface temperature data resolution of 30m, the study area was divided into a grid of 3000m×3000m using fishing net tools in ArcGIS software, and the average MODIS surface temperature values and Landsat surface temperature values within each grid were calculated and compared for their differences.

2.3.2 Urban thermal landscape grading

The mean-standard deviation method classifies urban thermal landscape grades by using the combination of the mean value of surface temperature and different standard deviation multiples. The thermal landscape grades in this paper are divided into 6 levels, namely: low temperature zone, sub-medium temperature zone, medium temperature zone, sub-high temperature zone, high temperature zone and extra-high temperature zone, which are assigned with values of 1–6 respectively. The classification criteria are shown in Table 1.

TABLE 1 The grade classification of urban thermal landscape.

Thermal landscape pixel value	Thermal landscape grade	Calculation formula
1	Low temperature zone	$T < T_{mean} - 2.5T_{std}$
2	Sub-medium temperature zone	$T_{mean} - 2.5T_{std} < T \leq T_{mean} - 1.5T_{std}$
3	Medium temperature zone	$T_{mean} - 1.5T_{std} < T \leq T_{mean}$
4	Sub-high temperature zone	$T_{mean} < T \leq T_{mean} + 1.5T_{std}$
5	High temperature zone	$T_{mean} + 1.5T_{std} < T \leq T_{mean} + 2.5T_{std}$
6	Extra-high temperature zone	$T > T_{mean} + 2.5T_{std}$

2.3.3 Classification of urban functional blocks

2.3.3.1 Classification of the minimum urban unit based on OSM road network

The irregular grid composed by the road network was used as the fundamental unit to undertake urban functions. Since the original OSM road network data was too redundant and the trunk roads were bi-directional, there were some topological errors and invalid data, so it was necessary to optimize the original OSM road network data. In this study, the highways, trunk roads, first-class roads, second-class roads and third-class roads in the OSM road network data were extracted, and the topology of the road network was processed, which mainly included extending the unconnected roads and trimming the suspended roads, and the centerline of the original two-lane trunk roads were extracted and simplified to form a clearly connected urban road network, as well as generating the minimum urban unit surface. After visual interpretation and comparison of the optimized OSM road network data with the Gaode map, the overall consistency is high and can be used for subsequent analysis. The OSM road network before and after optimization is shown in Figure 2.

2.3.3.2 Kernel density analysis

The kernel density analysis method derived from the Tobler's First Law of Geography, that is, the closer the location to the core elements the greater the density expansion value it obtains (Wang et al., 2019), which reflects the characteristics of spatial heterogeneity and the decay of central intensity with distance. Not only can this method reflect the detailed features, but also can avoid the interference of subjective disturbing factors in a limited way (Yu et al., 2016), and it is widely used in the field of density estimation of geographic phenomena with typical continuous geographic characteristics, such as urban infrastructure services and risk assessment of traffic sections (Elgammal et al., 2002). The kernel density analysis is calculated as follows:

$$f(s) = \sum_{i=1}^n \frac{1}{h^2} \varphi\left(\frac{s-c_i}{h}\right) \quad (2)$$

Where $f(s)$ is the kernel density estimation function located at position s , h is the attenuation value, also known as the bandwidth; c_i is the position of the i th POI point; n is the number of POI points whose path distance from position s is no more than h ; and φ is the predetermined kernel function.

According to the different distribution conditions of each POI point, the formula of bandwidth h can be deduced as follows:

$$h = 0.9 \times \min(SD, \sqrt{1/\ln 2 \times D_m}) \times N^{-2} \quad (3)$$

Where SD is the standard distance between the average center of the point and all points, which is calculated as formula (4); D_m is the median distance between the average center of the point and all points; N is the total number of POIs.

$$SD = \sqrt{\sum_{i=1}^n (x_i - \bar{X})^2 / N + \sum_{i=1}^n (y_i - \bar{Y})^2 / N} \quad (4)$$

Where SD and N have the same meaning as above; x_i and y_i are the coordinates of the i th POI point; \bar{X} and \bar{Y} are the average central point coordinates of the POI point, respectively.

2.3.3.3 Quantitative identification of urban functional blocks

This paper divided the POI data into the following seven categories of functional blocks according to the "Guidelines for the Preparation of Municipal Land and Space General Planning" and the "Guidelines for the Land and Space Survey, Planning & Use Control and Classification of Land and Sea Use". Furthermore, this paper also combined with AMAP for fine optimization, and supplemented the information of some block units in the suburbs of cities where POI was not captured. The specific classification criteria are shown in Table 2.

The kernel density of POIs with different densities was segmented according to the urban unit divided by OSM data, and then the proportion of the kernel density for each type of POI within the road network unit was calculated for identifying each functional block. The calculation formula is as follows:

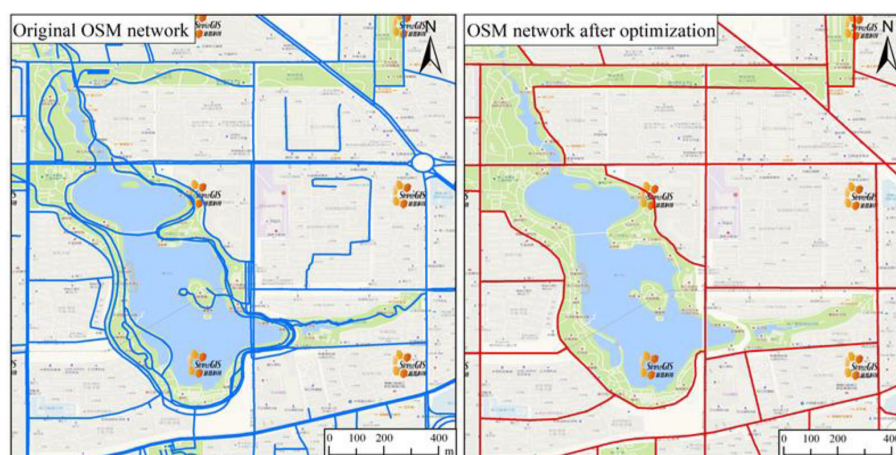


FIGURE 2
The comparison chart before and after OSM road network data optimization.

TABLE 2 POI data classification.

Urban functional zoning	Definition	POI category
Residential and living blocks	Areas with the primary functional orientation of residential buildings and residential support facilities.	Residential communities, villas, community centers
Comprehensive service blocks	Areas with the primary functional orientation of providing administrative offices, cultural, educational, medical and comprehensive commercial services.	Supermarkets, shopping centers, restaurants, hotels, government agencies, hospitals, schools, etc.
Commercial and business blocks	Areas with the primary functional orientation of providing commercial and business offices and other employment opportunities.	Office buildings, banks, insurance companies, etc.
Industrial development blocks	Areas with the primary functional orientation of industry and its supporting industries.	Factories, industrial estates, etc.
Logistics and storage blocks	Areas with the primary functional orientation of logistics and storage and their supporting industries.	Logistics parks, warehouses, etc.
Transportation hub blocks	Areas with the primary functional orientation of large-scale transportation facilities such as airports, ports, and railroad passenger and freight stations.	Train stations, high-speed railway stations, bus stations, etc.
Strategic reserved blocks	Areas reserved for the control of significant strategic functions of the city.	

$$M_i = N_i / D \times 100 \% \quad (5)$$

Where M_i is the frequency density of type i POI; N_i is the sum of the kernel density of type i POI; D is the sum of all kernel densities.

When the frequency density of a certain type of POI is $\geq 50\%$, the unit is identified as a single functional block; when the frequency density of a certain type of POI is $< 50\%$, the block is subdivided in combination with AMAP; and when the frequency density of all types of POI is 0, which means that the block has no POI data temporarily and is generally an area to be developed, then it is identified as a strategic reserved block.

2.3.4 Thermal landscape footprint characterization model

The actual impact area in the high temperature urban areas covered by construction land often exceeds its physical coverage boundary. The concept of urban heat island effect footprint was first proposed by Zhou et al. (2015). It was defined as a continuous distribution area with significant urban heat island effect on a gradient from urban built-up areas to rural or suburban areas. By developing an urban thermal landscape footprint characterization model, this paper investigates the impact range of thermal landscape footprint of different types of urban functional blocks. The multi-ring buffer zone (ring spacing is 500m and the number of rings is 10) was established based on various types of urban functional blocks obtained from OSM road network and POI data, and the gradient change characteristics of thermal landscape on various types of blocks were quantitatively analyzed. The calculation formula is as follows:

$$\Delta T_i = \frac{\sum_{k=1}^N T_{ik}}{N} - \frac{\sum_{k=1}^M T_{ak}}{M} \quad (6)$$

Where ΔT_i is the difference of thermal field averages between the i th ring buffer of the urban functional block and the whole study area; T_{ik} is the k th pixel thermal landscape level of the i th

ring buffer of the urban functional block; N is the total number of pixels in the i th ring buffer; T_{ak} is the k th pixel thermal landscape level in the study area; M is the total number of pixels in the study area. ΔT_i can reflect the impact range of the thermal landscape footprint of the urban functional block; when $\Delta T_i > 0$, the average value of the thermal field within the buffer area i is larger than the average value of the whole area, then the buffer area belongs to the impact range of the thermal landscape footprint of the urban functional block; when $\Delta T_i < 0$, it is considered that the thermal landscape footprint of the urban functional block cannot affect this area.

2.4 Study framework

This article takes the main urban area of Xi'an as the research area, uses OSM road network data to divide the minimum urban land use units, constructs 7 types of urban functional blocks based on POI data of interest points, and establishes a thermal landscape footprint characterization model to study the impact range of thermal landscape footprints of various functional blocks, and finally quantitatively evaluates the spatial differentiation characteristics of urban thermal landscape. The overall research framework of this study is shown in Figure 3.

3 Spatial distribution characteristics of urban thermal landscape

The surface temperature of the study area on May 30, 2021 was obtained in this study based on Landsat imagery data with the inversion of the above-mentioned mono-window algorithm developed by Qin Zhihao. The blue area in the figure indicates the area with lower surface temperature, and the gradual change from blue to red indicates the progressive increase of surface temperature, as shown in Figure 4. According to the inversion

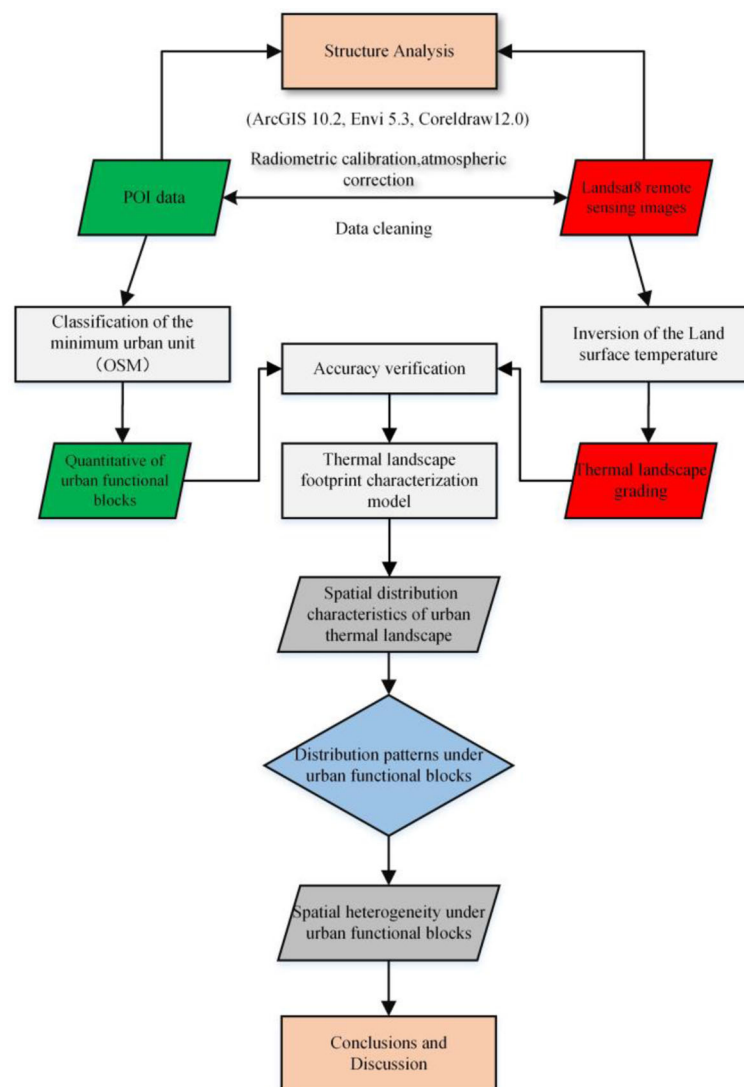


FIGURE 3
Research framework diagram.

results, the average surface temperature in the study area was 38.93°C, with the lowest being 23.34°C and the highest being 55.19°C. After statistics, the average difference between the land surface temperature retrieved based on Landsat and the land surface temperature of MODIS products is 0.16°C, which indicates that the land surface temperature retrieved by Landsat has a high accuracy and is suitable for the study of urban thermal landscape. Simultaneously, the mean-standard deviation method was used to classify the thermal landscape grades, as shown in Figure 5A. Since water bodies, woodlands, and others can cover the influence of construction land on the surface temperature (Zhu et al., 2017), it is necessary to remove the woodlands and water bodies and other pixels when calculating and analyzing the thermal landscape footprint, as shown in Figure 5B.

Among the six types of thermal landscapes, the sub-high temperature zone, high temperature zone and extra-high temperature zone are the dominant factors in the urban heat island, and these three types of thermal landscapes jointly

constitute the “urban heat island landscape”. As can be observed from Figure 5B, a large number of low and sub-medium temperature zones in the original thermal landscape are found near water bodies (Ba River, Chan River, Hancheng Lake, etc.) and green land parks (Tang Paradise, Qujiang Pool Relic Park, Xi’an Botanical Garden, etc.). The “urban heat island landscape” is formed in the center of the city, in particular, the industrial and logistic parks in the western and northern suburbs of the city gather a large number of pixels from extra-high temperature zones. After eliminating the pixels of water bodies, woodlands and grasslands, the spatial distribution characteristics of the thermal landscape changed significantly. Statistics of the thermal landscape pixels before and after elimination (Table 3) indicated that the number of pixels in the low and sub-medium temperature zones decreased significantly, the urban heat island landscape pixels changed slightly, and the percentage of high temperature pixels all increased. After the quantitative statistics of the mean value of thermal landscape pixels, it was found that the mean value of the

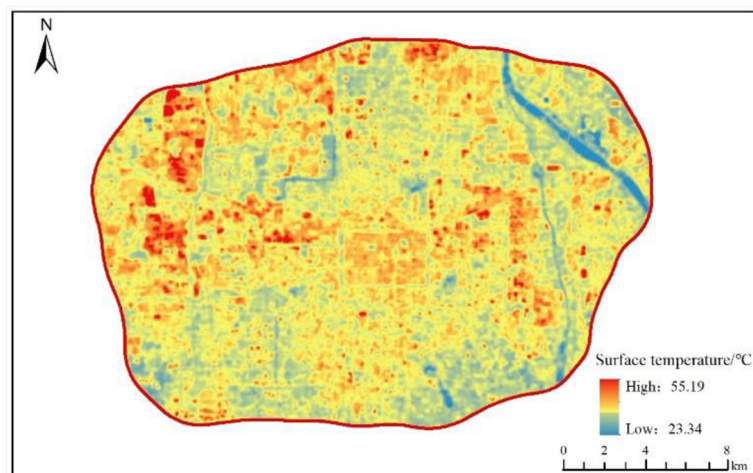


FIGURE 4
Surface temperature inversion results.

original thermal landscape pixels was 3.50, and the mean value of the thermal landscape pixels after eliminating water bodies and woodlands was 3.58. Consequently, water bodies, woodlands and other surfaces have a certain covering effect on the urban thermal landscape, and the elimination of these pixels can make the subsequent study more precise.

4 Spatial distribution characteristics of urban thermal landscape

4.1 Distribution characteristics of urban functional blocks

This paper divided different types of functional blocks in the study area based on OSM road network and POI data, and compare the identification results of urban functional blocks with the planning map of the “Xi’an Overall Plan (2008–2020)”, indicating a high overall consistency as shown in Figure 6. This paper divided

different types of functional blocks in the study area based on OSM road network and POI data, as shown in Figure 6. Among the seven types of functional blocks, the relationship of area share is residential and living blocks (59.78%) > comprehensive service blocks (16%) > strategic reserved blocks (12.44%) > industrial development blocks (6.20%) > commercial and business blocks (3.35%) > logistics and storage blocks (1.42%) > transportation hub blocks (0.82%). Among them, the residential and living blocks have a wide coverage and are densely distributed, and are the major functional blocks of the study area; the comprehensive service blocks mainly provide supporting services to the residential and living blocks, and thus form a spatial pattern of continuous distribution in the center and small blocks with multiple cores near the residential and living blocks; as the Hi-tech Industries Development Zone is the economic and industrial center of Xi’an, it is also a gathering place for commercial and administrative enterprises, and thus the commercial and business blocks present a spatial pattern with the Hi-tech Industries Development Zone as the core and other areas as the scattered distribution; the industrial

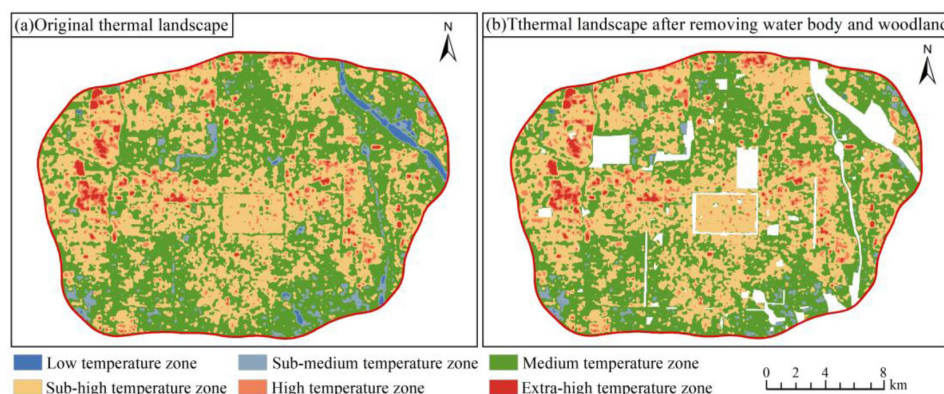


FIGURE 5
The spatial distribution of the thermal environment landscape. (A) Original thermal landscape. (B) Thermal landscape after removing water body and woodland.

TABLE 3 The grade classification of urban thermal landscape.

	Original thermal landscape		Thermal landscape after excluding water bodies, woodlands, etc.	
	Number of pixels (pcs)	Percentage (%)	Number of pixels (pcs)	Percentage (%)
Low temperature zone	5069	1.00	181	0.04
Sub-medium temperature zone	18942	3.73	9547	2.06
Medium temperature zone	240867	47.43	216811	46.68
Sub-high temperature zone	211516	41.65	206520	44.47
High temperature zone	23246	4.58	23175	4.99
Extra-high temperature zone	8195	1.61	8194	1.76
Total	507835	100.00	464428	100.00

development blocks, logistics and storage blocks as well as the strategic reserved blocks have similar distribution characteristics and are far away from the densely populated areas of the downtown, mainly distributed in the relatively less densely populated areas around the Ring Expressway, with more distribution in Weiyang District and the western part of Yanta District.

4.2 Spatial pattern characteristics of thermal landscape in different urban functional blocks

This paper categorized and obtained the distribution pattern of thermal landscape under various types of urban functional blocks based on the data of urban thermal landscape and functional blocks, and counted the thermal landscape grade data under various types of urban functional blocks. As shown in Table 4, the average values of surface thermal landscape of different types of urban functional blocks are significantly different, and the relationship of their sizes is logistics and storage blocks (4.19) > industrial development blocks (4.15) > transportation hub blocks (3.73) > comprehensive service blocks (3.69) > residential and living blocks (3.53) > commercial and business blocks (3.48) > strategic reserved blocks (3.33). The surface thermal landscape within the seven types of urban functional blocks is dominated by the medium temperature and sub-high temperature zone pixels, and the distribution of thermal landscape pixels in the low temperature zone is not significant. Among them, the percentage distribution of surface thermal landscape grade in residential and living blocks, commercial and business blocks, and strategic reserved blocks is relatively similar, and the percentage of urban heat island landscape pixels all exceed 50% and the percentage of medium temperature zone pixels is higher. This can be attributed to the fact that most of the residential communities are internally covered with landscaping (the national standard is not less than 30%), while the strategic reserved blocks are basically undeveloped bare land or grassland, so the ground cover as green land provides a certain degree of cooling effect to the city. Industrial development blocks, logistics and storage blocks and transportation hub blocks are covered by more high temperature pixels, and industrial production activities with high energy

consumption and high emission are the dominant activities inside the industrial estates, whose daily production of exhaust gas and wastewater have a greater impact on the urban thermal environment. At the same time, as the most significant and basic activity in logistics, a large number of logistics vehicles in transportation emit greenhouse gases, including carbon dioxide. For this reason, the high temperature phenomenon on the surface of the logistics and storage blocks is more remarkable. Inside the transportation hub blocks are the railway station, high-speed railway station and long-distance bus station, which are responsible for the external transportation of the city, and the daily flow of people is large and crowded, so the heat generation is also relatively high.

As shown in Figure 7, in terms of spatial pattern distribution, the residential and living blocks, the comprehensive service blocks and the commercial and business blocks form a more significant heat island landscape pattern, basically presenting a distribution pattern of high temperature in the center and gradually lower in the periphery. The high temperature pixels of the industrial development blocks and the logistics and storage blocks are in the area around the Ring Expressway, which coincides with the distribution pattern of industrial POI within their functional blocks. The thermal landscape pixels at all grades in the transportation hub blocks and the strategic reserved blocks are relatively well distributed, with no significant differences in spatial structure.

5 Characteristics of thermal landscape footprint variability under urban functional blocks

The actual impact range of the high temperature area on the surface of urban construction land is generally larger than its physical boundary, where thermal diffusion phenomenon exists. This paper generated a multi-ring buffer zone of 300–3000m (with a spacing of 300m and a total of 10 rings) with seven types of urban functional blocks as the core, constructed a thermal landscape footprint characterization model, and explored the variability characteristics of the surface thermal landscape footprint of

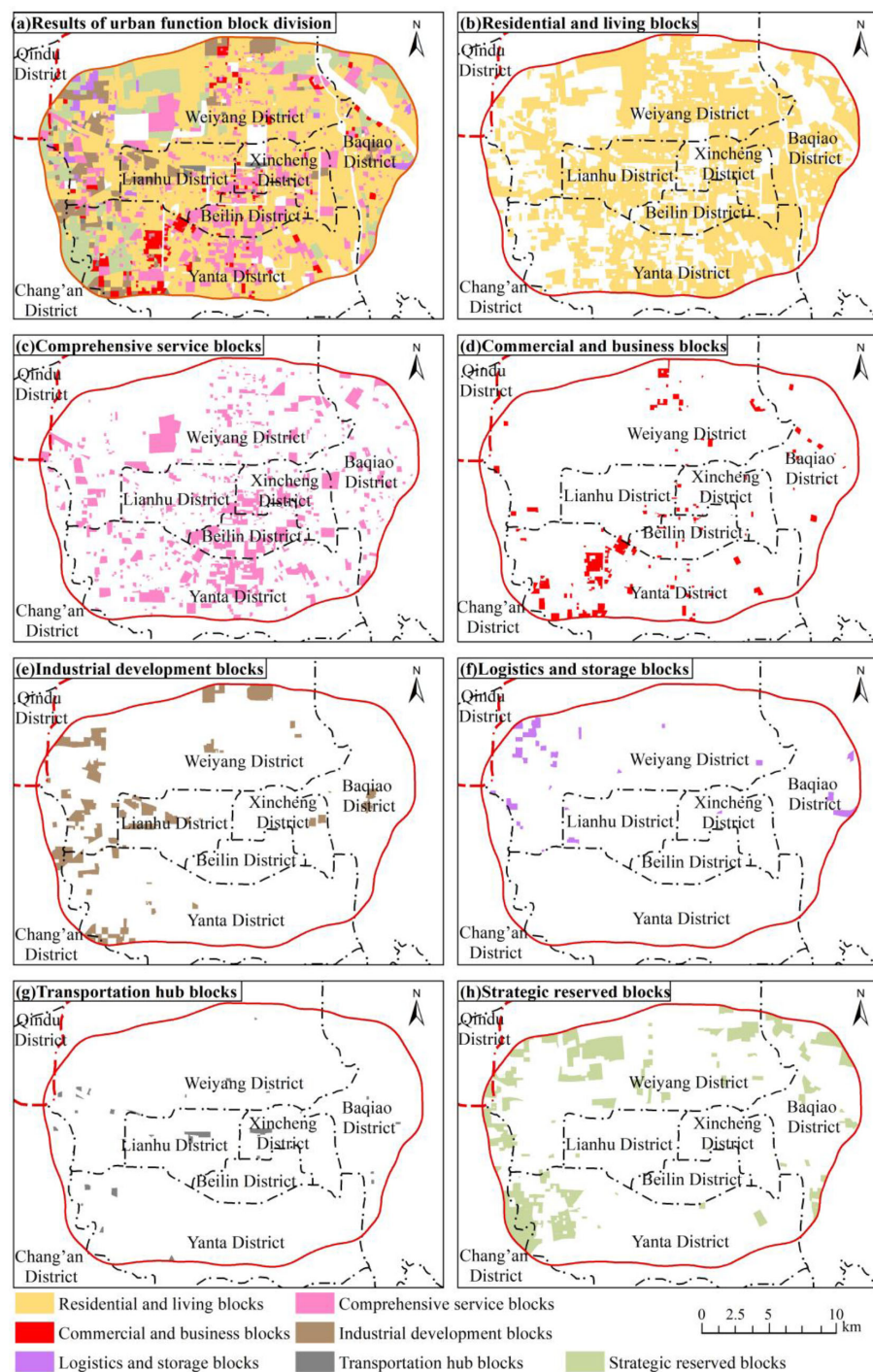


FIGURE 6

The spatial distribution of urban functional blocks. (A) Results of urban function block division. (B) Residential and living blocks. (C) Comprehensive service blocks. (D) Commercial and business blocks. (E) Industrial development blocks. (F) Logistics and storage blocks. (G) Transportation hub blocks. (H) Strategic reserved blocks.

various types of urban functional blocks. The mean value of surface thermal field under each ring buffer was statistically calculated for each urban functional block, and its changing trend was analyzed as shown in Table 5 and Figure 8.

As the distance of the buffer zone increases, the mean value of thermal field in the buffer zone of all urban functional blocks, excluding the strategic reserved blocks, tends to decrease

progressively, and the decreasing rate is basically from fast to flat. Among them, the mean value of the thermal field of the industrial development block decreases the most in the 2nd ring buffer zone, reaching 0.41, and then the decrease tends to be stable, fluctuating around 0.2, and the overall decrease of the mean value of the thermal field reaches 0.58, which is much higher than that of other urban functional blocks; under the logistics and storage blocks as

TABLE 4 The grade classification of Urban thermal landscape.

Type of urban functional blocks	Average value of thermal landscape pixel	Percentage of each type of thermal landscape pixel (%)					
		Low temperature zone	Sub-medium temperature zone	Medium temperature zone	Sub-high temperature zone	High temperature zone	Extra-high temperature zone
Residential and living blocks	3.53	0	1.6	49.73	43.9	4.08	0.69
Comprehensive service blocks	3.69	0.06	1.53	39.40	49.99	6.15	2.87
Commercial and business blocks	3.48	0	0.34	58.08	36.64	3.36	1.58
Industrial development blocks	4.15	0.02	0.10	21.61	51.25	17.52	9.50
Logistics and storage blocks	4.19	1.03	0.79	21.94	46.73	12.97	16.53
Transportation hub blocks	3.73	0	1.2	32.38	59.84	5.7	0.88
Strategic reserved blocks	3.33	0.11	6.58	54.59	37.55	1.11	0.05

well as the comprehensive service blocks, the decreasing rate of the mean thermal field of the buffer zone reaches the peak in the 4th ring buffer zone and decreases significantly, after which it gradually stabilizes; the decreasing rate of the mean value of the thermal field in the buffer zone of the residential and living blocks, the commercial and business blocks and the transportation hub blocks reaches the highest in the 5th ring buffer zone. The mean value of thermal field in the buffer zone of the strategic reserved blocks tends to increase due to the relatively low temperature of its internal thermal field, and basically shows a fast and then steady growth trend. The above quantitative analysis reveals that the surface thermal landscape within the seven types of urban functional blocks can have significant impacts on the surrounding areas, yet their impact range varies and the thermal landscape footprint has obvious heterogeneity. When comparing the mean value of thermal field in the 10th ring buffer zone of six types of urban functional blocks (except the strategic reserved blocks), it is indicated that the industrial development blocks have the largest mean value of thermal field, which means that their thermal landscape footprint may have the widest impact.

The mean value of the thermal field in the study area is 3.58. It is determined that when the mean value of the thermal field in the buffer zone is greater than that in the study area, the buffer zone is still within the impact range of the thermal landscape of the urban functional blocks at that time. The mean value of the thermal field in the buffer zone of the industrial development blocks is always higher than the mean value of the thermal field in the study area, as shown in Figure 8, indicating that its thermal landscape footprint has a wider impact and the thermal diffusion to the outside is obvious. Both the residential and living blocks and the comprehensive service blocks have a mean value of thermal field larger than 3.58 in the 4th ring buffer zone, and the mean value of

thermal field of the comprehensive service blocks is slightly larger than that of the residential and living blocks, so the impact range of the thermal landscape footprint of the comprehensive service blocks is slightly larger than that of the residential and living blocks; the thermal landscape footprint of the logistics and storage blocks is impacted up to the 5th ring buffer zone, second only to the industrial development blocks; in the 3rd ring buffer zone of the commercial and business blocks and the transportation hub blocks, the mean value of their thermal fields is larger than that of the study area, and the impact range of the thermal landscape footprint of the transportation hub blocks is smaller, with less obvious effect of thermal diffusion outward. Based on the above quantitative analysis, the impact range of thermal landscape footprint of six types of urban functional blocks (except strategic reserved blocks) is ranked as industrial development blocks > logistics and storage blocks > comprehensive service blocks > residential and living blocks > commercial and business blocks > transportation hub blocks.

6 Conclusion and discussion

6.1 Conclusion

This paper inverts the urban surface temperature based on Landsat 8 remote sensing imagery, and uses OpenStreetMap (OSM) road network data to divide the minimum urban land unit, and constructs seven types of urban functional blocks based on POI data using the kernel density analysis method. Meanwhile, this paper also establishes the thermal landscape footprint characterization model to study the impact range of thermal landscape footprint of various types of functional blocks and quantitatively evaluates the

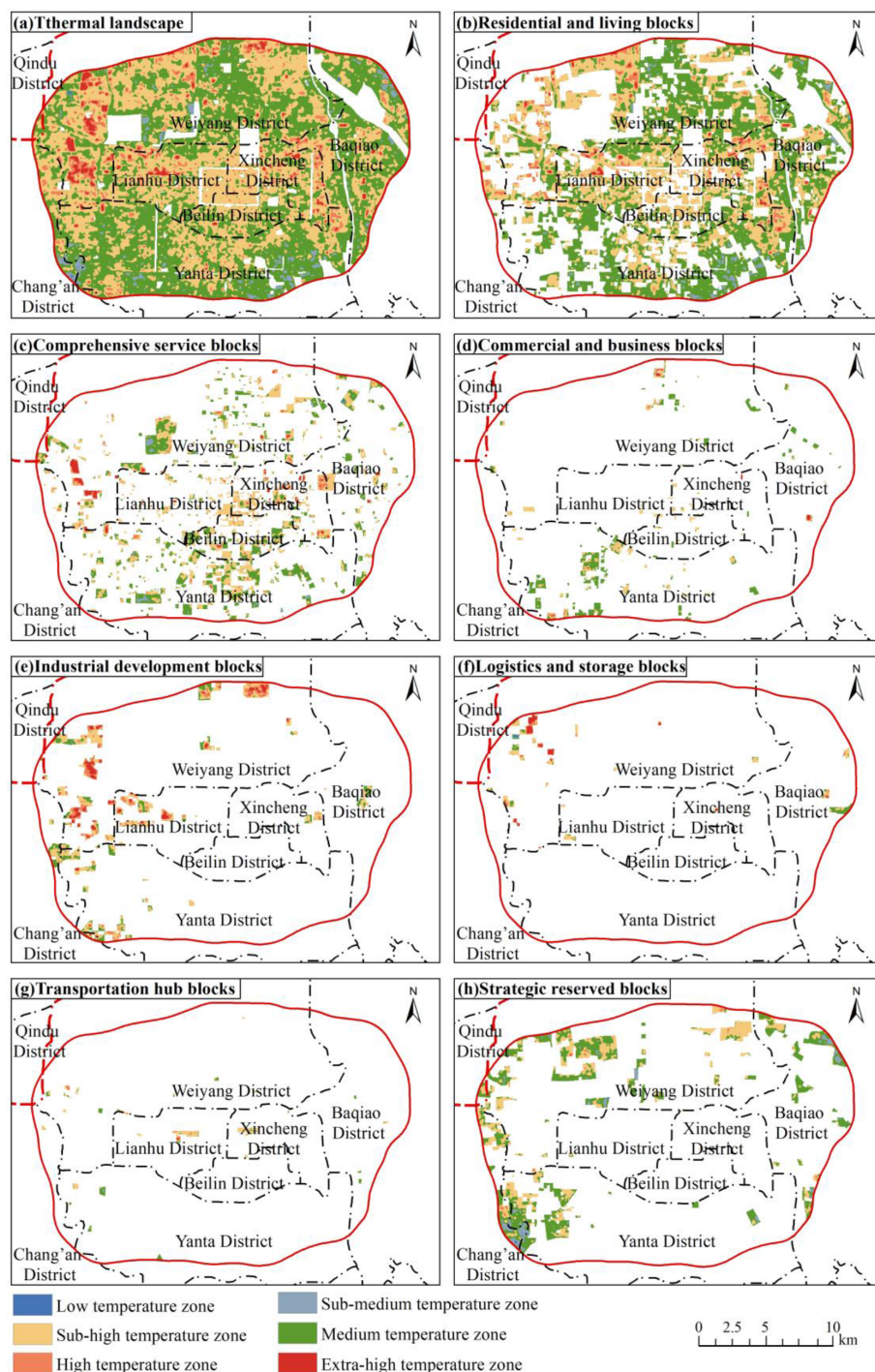


FIGURE 7

The spatial distribution of thermal landscape of various urban functional blocks. (A) Results of urban function block division. (B) Residential and living blocks. (C) Comprehensive service blocks. (D) Commercial and business blocks. (E) Industrial development blocks. (F) Logistics and storage blocks. (G) Transportation hub blocks. (H) Strategic reserved blocks.

spatial variation characteristics of urban thermal landscape. The following conclusions are mainly drawn from this study:

(1) The spatial distribution of urban functional blocks identified based on POI data presents a high coupling with the POI kernel density, and the area share of seven types of urban functional blocks in the study area is ranked as residential and living blocks >

comprehensive service blocks > strategic reserved blocks > industrial development blocks > commercial and business blocks > logistics and storage blocks > transportation hub blocks.

(2) The surface thermal landscape of the seven types of urban functional blocks is dominated by the pixels of medium and sub-high temperature zones, while the distribution of thermal landscape

TABLE 5 The statistical table of the average value of surface thermal field under the buffer zone of urban functional blocks.

Buffer zone distance (m)	Average value of surface thermal field						
	Industrial development blocks	Logistics and storage blocks	Comprehensive service blocks	Residential and living blocks	Commercial and business blocks	Transportation hub blocks	Strategic reserved blocks
300	4.17	3.85	3.8	3.78	3.72	3.7	2.8
600	3.76	3.73	3.71	3.7	3.68	3.65	2.97
900	3.72	3.72	3.67	3.67	3.64	3.59	3.1
1200	3.72	3.64	3.6	3.59	3.54	3.53	3.17
1500	3.68	3.61	3.54	3.48	3.42	3.38	3.21
1800	3.66	3.58	3.55	3.48	3.40	3.32	3.25
2100	3.65	3.58	3.5	3.44	3.40	3.31	3.27
2400	3.64	3.56	3.5	3.43	3.35	3.30	3.38
2700	3.6	3.56	3.48	3.41	3.37	3.31	3.58
3000	3.59	3.50	3.45	3.37	3.34	3.27	3.6

pixels of low temperature zones is not significant. The mean values of surface thermal landscape of different types of urban functional blocks are significantly dissimilar, and the relationship among their sizes is logistics and storage blocks > industrial development blocks > transportation hub blocks > comprehensive service blocks > residential and living blocks > commercial and business blocks > strategic reserved blocks.

(3) Apart from the strategic reserved blocks, the surface thermal landscape within the other six types of urban functional blocks can produce thermal diffusion to the surrounding areas, yet the impact range varies and the thermal landscape footprint has obvious heterogeneity. The impact range of the thermal landscape footprint is ranked as industrial development blocks > logistics and storage blocks > comprehensive service blocks > residential and

living blocks > commercial and business blocks > transportation hub blocks.

6.2 Discussion

This paper integrates OpenStreetMap (OSM) and POI data to divide urban functional blocks, which breaks through the limitation of traditional land classification using remote sensing imagery, constructs a thermal landscape footprint characterization model, and achieves a fine quantitative analysis of the surface thermal environment affected by different construction lands.

As the political and cultural center of Shaanxi Province, as well as the core area of the “the Belt and Road” and the heart of the

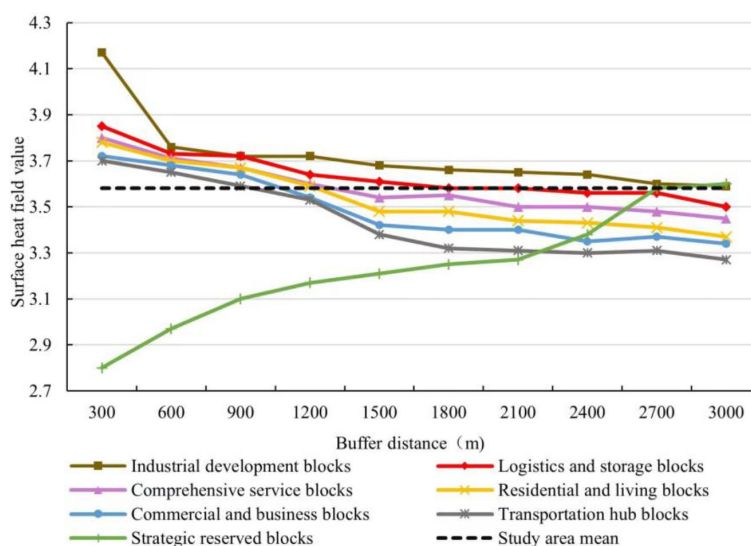


FIGURE 8

The variation trend of the mean value of surface thermal field with buffer distance.

Eurasian Continental Bridge Economic Belt, Xi'an's rapid urbanization has not only provided rapid GDP growth, but also caused a series of environmental problems. Therefore, in this context, this paper explores the impact mechanism and spatial pattern of urban spatial structure on urban thermal environment from a small scale, which is of great significance for scientific guidance of urban planning and construction, mitigation of Urban heat island effect, and promotion of sustainable urban development. At the same time, it provides scientific reference for the planning and management of urbanization development in other regions of Shaanxi Province with Xi'an as the center.

The innovation of this article mainly lies in the accurate division of urban functional blocks by combining OSM road network data and POI data. Based on this, constructing a thermal landscape footprint characterization model to explore the spatial differentiation characteristics of urban thermal landscape is more refined, which can quantify the spatial pattern of urban thermal environment from a smaller scale, providing more accurate support for related research in this field. Furthermore, this paper reveals that the thermal environmental effects of different subtypes of construction lands have obvious differences, as manifested in the mean value of thermal landscape, grade distribution and the impact range of thermal landscape footprint significantly varied within different types of urban functional blocks. The impact range of the thermal landscape footprint of industrial development blocks and logistics and storage blocks is relatively wide, which is mainly related to their high energy-consuming and high-emission production activities, and the heat emission is obvious and concentrated in the surrounding area, making the local surface thermal environment change to form the heat island effect. The surface heat comes not only from industrial energy emissions, but also from anthropogenic heat emissions from residential life and human's own metabolism, and it is greatly influenced by population density and intensity of human activities, hence the surface thermal environment of residential and living blocks and comprehensive service blocks, which are closely related to human life, changes significantly.

Although this paper has a certain degree of scientific and innovative study on the surface thermal landscape effect of different types of construction lands at the microscopic scale, some issues still exist for further consideration and improvement due to the complex formation mechanism and influencing factors of urban heat island effect. With the development of network technology, the POI database is still in the process of continuous expansion, and the data accuracy and information richness are also upgraded accordingly, and the rich information in POI data of users still needs to be further explored. For instance, the impact of human activities on the surface thermal field cannot be reflected in some remote mountainous areas due to the lack of POI data. Therefore, it is necessary to further enrich the POI data and to consider adding other factors to improve the validity of the model for thermal landscape analysis. Meanwhile, the surface thermal field has the

characteristics of dynamic changes of day-night and seasonal, and has periodic changes even on both weekdays and non-weekdays. In the subsequent work, the study of spatial variability of urban thermal landscape under different time scales should be deepened.

Data availability statement

The original contributions presented in the study are included in the article/supplementary material. Further inquiries can be directed to the corresponding author.

Author contributions

JW is responsible for the original idea. JW performed the experiments and wrote the paper. LS and QH contributed to analysis of the data. SH contributed to revising the paper. All authors contributed to the article and approved the submitted version.

Funding

This study is funded by the Xianyang Normal University Research Initiation Fund (2022XSYB031).

Acknowledgments

The authors are grateful to the editor and reviewers for spending their valuable time on constructive comments and suggestions that improved the quality of the manuscript considerably.

Conflict of interest

Author QH was employed by the company Shaanxi Dibo Jingyuan Surveying and Mapping Geographic Information Co., Ltd.

The remaining authors declare that the research was conducted in the absence of any commercial or financial relationships that could be construed as a potential conflict of interest.

Publisher's note

All claims expressed in this article are solely those of the authors and do not necessarily represent those of their affiliated organizations, or those of the publisher, the editors and the reviewers. Any product that may be evaluated in this article, or claim that may be made by its manufacturer, is not guaranteed or endorsed by the publisher.

References

- Chen, L., Sun, R., and Liu, H. (2013). Eco-environmental effects of urban landscape pattern changes: progresses, problems, and perspectives. *Acta Ecologica Sin.* 33 (4), 1042–1050. doi: 10.5846/stxb201205070659
- Chen, X., Zhang, Z. A., Hu, X., Huang, Z., and Lv, L. (2018). Characteristics of tourists flow in scenic spots based on Weibo Check-in big data: A case study of zhongshan scenic spot in Nanjing city. *Economic Geogr.* 2018 (9), 206–214. doi: 10.15957/j.cnki.jjdl.2018.09.024
- Elgammal, A., Duraiswami, R., Harwood, D., and Davis, L. S. (2002). Background and foreground modeling using nonparametric kernel density estimation for visual surveillance. *Proc. IEEE* 90 (7), 1151–1163. doi: 10.1109/JPROC.2002.801448
- Estoque, R. C., Murayama, Y., and Myint, S. W. (2017). Effects of landscape composition and pattern on land surface temperature: An urban heat island study in the megacities of Southeast Asia. *Sci. Total Environ.* 577, 349–359. doi: 10.1016/j.scitotenv.2016.10.195
- Giorgio, G. A., Ragosta, M., and Telesca, V. (2017). Climate variability and industrial-suburban heat environment in a Mediterranean area. *Sustainability* 9 (5), 775. doi: 10.3390/su9050775
- Guo, A., Yang, J., Sun, W., Xiao, X., Cecilia, J. X., Jin, C., et al. (2020). Impact of urban morphology and landscape characteristics on spatiotemporal heterogeneity of land surface temperature. *Sustain. Cities Soc.* 63, 102443. doi: 10.1016/j.scs.2020.102443
- Han, S., Wei, S., Zhou, W., Zhang, M., Tao, T., Qiu, L., et al. (2017). Quantifying the spatial pattern of urban thermal fields based on point of interest data and Landsat images. *Acta Ecologica Sin.* 37 (16), 5305–5312. doi: 10.5846/stxb201605301037
- He, L., Pan, J., and Dong, L. (2020). Study on the spatial identification of housing vacancy. *Remote Sens. Technol. Appl.* 35 (4), 820–831.
- Huang, X., Song, T., Wang, B., Zheng, D., and Qi, M. (2022). Study on the influence of land use evolution of scale, structure and pattern on urban thermal environment: A case study of Xi'an. *Scientia Geographica Sin.* 42 (5), 926–937. doi: 10.13249/j.cnki.sgs.2022.05.018
- Li, J., Qi, X., and Yuan, W. (2022). Spatial differentiation of multi-functional mixed use of construction land based on points of interest. *Prog. Geography* 41 (2), 239–250. doi: 10.18306/dlkxjz.2022.02.005
- Li, Y., Zhang, H., and Kainz, W. (2012). Monitoring patterns of urban heat islands of the fast-growing Shanghai metropolis, China: Using time-series of Landsat TM/ETM+ data. *Int. J. Appl. Earth Observations Geoinformation* 19, 127–138. doi: 10.1016/j.jag.2012.05.001
- Liu, H., Shen, G., and Huang, Q. (2017). Evolution of urban heat island effect and its relationship with land use change in Wuhan in recent 10 years. *Resour. Environ. Yangtze Basin* 26 (9), 1466–1475. doi: 10.11870/cjlyzyyhj201709019
- Manley, G. (1958). On the frequency of snowfall in metropolitan England. *Q. J. R. Meteorological Soc.* 84 (359), 70–72. doi: 10.1002/qj.49708435910
- Orlanski, I. (1975). A rational subdivision of scales for atmospheric processes. *Bull. Am. Meteorological Societ.* 527–530. doi: 10.1234/12345678
- Qiao, Z., He, T., Lu, Y., Sun, Z., Hu, X., and Yang, J. (2022). Quantifying the contribution of land use change based on the effects of global climate change and human activities on urban thermal environment in the Beijing-Tianjin-Hebei urban agglomeration. *Geographical Res.* 41 (7), 1932–1947. doi: 10.11821/dljy020210787
- Qiao, Z., Huang, N.-Y., Xu, X., Sun, Z., Wu, C., and Yang, J. (2019). Spatio-temporal pattern and evolution of the urban thermal landscape in metropolitan Beijing between 2003 and 2017. *Acta Geographica Sin.* 74 (3), 475–489. doi: 10.11821/dlxb201903006
- Qin, Z.-H., Zhang, M.-H., Karnieli, A., and Berliner, P. (2001). Mono-window algorithm for retrieving land surface temperature from Landsat TM6 data. *Acta Geographica Sin.* 56 (4), 456–466. doi: 10.1142/S0252959901000401
- Rossi, F., Pisello, A. L., Nicolini, A., Filippini, M., and Palombo, M. (2014). Analysis of retro-reflective surfaces for urban heat island mitigation: A new analytical model. *Appl. Energy* 114, 621–631. doi: 10.1016/j.apenergy.2013.10.038
- Singh, P., Kikon, N., and Verma, P. J. S. C. (2017). Impact of land use change and urbanization on urban heat island in Lucknow city, Central India. *A Remote Sens. based estimate.* 32, 100–114. doi: 10.1016/j.scs.2017.02.018
- Wan, Z., and Li, Z.-L. (1997). A physics-based algorithm for retrieving land-surface emissivity and temperature from EOS/MODIS data. *IEEE Trans. Geosci. Remote Sens.* 35 (4), 980–996. doi: 10.1109/36.602541
- Wang, B., Wang, L., Liang, Y., Yang, B., Huang, X., and Yang, M. (2020). Characteristics of jobs-housing spatial distribution in Beijing based on mobile phone signaling data. *Prog. Geogr.* 39 (12), 2028–2042. doi: 10.18306/dlkxjz.2020.12.006
- Wang, J., Ye, Y., and Fang, F. (2019). A study of urban functional zoning based on kernel density estimation and fusion data. *Geogr. Geo-Information Sci.* 35 (3), 66–71.
- Yang, W., Meng, F., Li, Y., and Tang, M. (2020). Research on passenger travel characteristics based on OD data analysis of vehicle trajectory. *GEOMATICS&SPATIAL Inf. Technol.* 43 (1), 144–147,150. doi: 10.3969/j.issn.1672-5867.2020.z1.044
- Yao, R., Wang, L., Huang, X., Niu, Z., Liu, F., and Wang, Q. (2017). Temporal trends of surface urban heat islands and associated determinants in major Chinese cities. *Sci. Total Environ.* 609, 742–754. doi: 10.1016/j.scitotenv.2017.07.217
- Yi, C., Hu, J., and Li, X. (2018). Response analysis of land cover type to urban heat island effect. *Bull. Surveying Mapp.* 2018 (1), 72–76. doi: 10.13474/j.cnki.11-2246.2018.0013
- Yu, W., Ai, T., Yang, M., and Liu, J. (2016). Detecting “Hot Spots” of facility POIs based in kernel density estimation and spatial autocorrelation technique. *Geomatics Inf. Sci. Wuhan Univ.* 41 (2), 221–227. doi: 10.13203/j.whugis20140092
- Yue, W., and Xu, L. (2013). Thermal environmental effects of typical urban water landscape. *Acta Ecologica Sin.* 33 (6), 1852–1859. doi: 10.5846/stxb201112141915
- Zhang, J., Shi, W., and Xiu, C. (2021). Urban research using points of interest data in China. *Scientia Geographica Sin.* 41 (1), 140–148. doi: 10.13249/j.cnki.sgs.2021.01.015
- Zheng, Y. (2015). Introduction to urban computing. *Geomatics Inf. Sci. Wuhan Univ.* 40 (1), 1–13. doi: 10.13203/j.whugis20140718
- Zheng, Y., and Weng, Q. (2018). High spatial-and temporal-resolution anthropogenic heat discharge estimation in Los Angeles County, California. *J. Environ. Manage.* 206, 1274–1286. doi: 10.1016/j.jenvman.2017.07.047
- Zhong, W., Wang, D., Xie, D., and Yan, L. (2017). Dynamic characteristics of Shanghai's population distribution using cell phone signaling data. *Geographical Res.* 36 (5), 972–984. doi: 10.11821/dljy201705013
- Zhou, D., Zhao, S., Zhang, L., Sun, G., and Liu, Y. (2015). The footprint of urban heat island effect in China. *Sci. Rep.* 5 (1), 1–11. doi: 10.1038/srep11160
- Zhu, X., Wang, X., Zhou, Y., Wu, W., and Liu, Z. (2017). Spatial variability of thermal environment in Xi'an under the build-up area expansion. *Chin. J. Ecol.* 36 (12), 3574–3583. doi: 10.13292/j.1000-4890.201712.015
- Zhuang, Y., Xue, D., Kuang, W., Chi, W., and Pan, T. (2019). Study on the pattern of land cover hierarchy in Hohhot-Baotou-Ordos cities in the Semi-arid region of China. *Remote Sens. Technol. Appl.* 34 (1), 197–206. doi: 10.11873/j.issn.1004-0323.2019.1.0197

Frontiers in Ecology and Evolution

Ecological and evolutionary research into our natural and anthropogenic world

This multidisciplinary journal covers the spectrum of ecological and evolutionary inquiry. It provides insights into our natural and anthropogenic world, and how it can best be managed.

Discover the latest Research Topics

[See more →](#)

Frontiers

Avenue du Tribunal-Fédéral 34
1005 Lausanne, Switzerland
frontiersin.org

Contact us

+41 (0)21 510 17 00
frontiersin.org/about/contact



Frontiers in Ecology and Evolution

